UNIVERSITY OF CALIFORNIA
SANTA CRUZ

UNLOCKING THE NEXT ERA OF EXOPLANET DIRECT IMAGING THROUGH TARGETED HIGH-CONTRAST IMAGING OBSERVATIONS AND ADAPTIVE OPTICS DEVELOPMENT

A dissertation submitted in partial satisfaction of the
requirements for the degree of

DOCTOR OF PHILOSOPHY

in

ASTRONOMY AND ASTROPHYSICS

by

Rachel Bowens-Rubin

June 2024

The Dissertation of Rachel Bowens-Rubin
is approved:

Dr. Phil Hinz, Chair

Dr. Andrew Skemer

Dr. Rebecca Jensen-Clem

Dr. Mark Chun

Peter Biehl
Vice Provost and Dean of Graduate Studies

Table of Contents

List of Figures

List of Tables

Abstract

Unlocking the Next Era of Exoplanet Direct Imaging through Targeted High-Contrast Imaging Observations and Adaptive Optics Development

by

Rachel Bowens-Rubin

While the majority of exoplanets are currently detected using indirect methods of observation, the direct imaging method offers a way to characterize an exoplanet's atmosphere, chemical composition, density, temperature, and orbit. However, the use of direct imaging has so far been limited to studying a population of young ($\leq 500Myr$), hot ($\geq 600K$), massive ($\geq 2M_{jup}$) gas giants and brown dwarfs. In this thesis, I present my work to expand the set of directly imaged companions through observation and instrumentation development. The introduction provides an overview of the promise, challenges, and motivation for conducting exoplanet direct imaging. The inner chapters of the thesis are divided by subject area into two parts. Each observation/instrumentation module contains three chapters following the same format: (I) An "emerging techniques" introductory section that gives an overview of the sub-field; (II) Original research into the current performance capabilities and limitations of our methods and technologies; and (III) A "futures" section where I discuss the natural next steps of the sub-field.

In Part 1, I introduce the strategies and tools available for conducting targeted direct imaging observations – a method to use supporting data to curate a direct imaging observation. I demonstrate how this targeted approach is implemented by conducting an HCI/RV survey of our fifth closest neighbor, Wolf 359. I use this data to quantify the current limits of conducting high-contrast imaging with Keck-NIRC2 in the M-band (4.7μm). I complete Part 1 by outlining a future JWST survey that could enable the direct detection of sub-Jupiter mass exoplanets down to ice-giant size.

In Part 2, I present the state of the development of an emerging large-format deformable mirror technology for adaptive optics. The Netherlands Organization of Applied Scientific Research (TNO) recently developed a new style of high-efficiency hybrid-variable reluctance actuator that is the basis of an emerging large-format deformable mirror technology. I present my performance testing of this technology using two lab prototypes and compare my results against the needs for future ELT adaptive optics systems. I close Part 2 by reviewing the designs of five in progress adaptive secondary mirrors that incorporate the TNO technology for the NASA IRTF, UH-2.2m, Automated Planet Finder, the European Solar Telescope, and the W.M. Keck Observatory.

I conclude by sharing my perspectives on the near future of the field of exoplanet direct imaging. I add a final appendix in the form of a 10-minute science play, commemorating the experience of searching for direct imaging companions.

For all those embarking on unusual, complex, and ambitious searches for companions.

Acknowledgments

I would first like to thank my MIT mentor Richard P. Binzel for helping me me summon the grit to apply to PhD programs over so many application cycles. This thesis would not have existed without his belief in my potential as a scientist and his encouragement to keep pursuing my dreams of becoming a space explorer. His kindness is a vital part of where I am today.

I am profoundly grateful to my advisor, Phil Hinz, for being so gracious in lending me his time and expertise in teaching me how to find my own way through whatever puzzles I brought to him. I feel honored to have had the opportunity to learn so much from Phil and to have received such abundance of support both in and out of the lab.

I would like to thank the reading members of my committee for their encouragement through the years: Becky Jensen-Clem, Mark Chun, and Andy Skemer. Their mentorship has shaped both this thesis and my academic success. I have always appreciated having their ear and getting to understand their take on the field.

I extend my heartfelt thanks to the members of the UCSC Lab for Adaptive Optics, many of whom have been my coauthors and close collaborators: Maïssa Salama, Jules Fowler, Dominic Sanchez, Ben Gerard, Maaike Van Kooten, Deno Stelter, Nour Skaf, Vincent Chambouleyron, Aditya Sengunta, Jordan Diaz, Claire Max, Don Gavel, Bruce Macintosh, Amanda Mohr, Klaus Stephenson, and Cesar Laguna. I'd like to extend special thanks to the LAO staff who have mentored me and so many other grad students

from start to finish, Daren Dillon and Reni Kupke.

Two postdoctoral researchers outside of the LAO became my role models and played an integral part of my growth during my time in graduate school. I would like to extend my gratitude to Aarynn Carter for opening the door to observing with JWST by mentoring me in all things python-JWST-direct-imaging analysis related and always making time for early career researchers first. Thank you to Melodie Kao for teaching me the techniques of scientific question asking and how to find balance in what is most important in life, health, and the pursuit of science.

I would like to acknowledge the following colleagues who provided input, coauthorship and/or scientific expertise to particular chapters of this document beyond my advisor and reading committee:

- Chapter 1: Anne Dattilo
- Chapter 2: Maïssa Salama
- Chapter 3: Joseph Murphy, Mary Anne Limbach, Andreas Seifahrt, Rocio Kiman, Maïssa Salama, Sagnick Mukherjee, Madison Brady, Aarynn Carter, Maaike A.M. van Kooten, Howard Isaacson, Molly Kosiarek, Jacob Bean, David Kasper, Rafael Luque, Gudmundur Stefansson, Julian Sturmer, Mikko Tuomi, Ignasi Ribas, Olivier Absil, Ester Linder, Jonathan Fortney, Andrew Skemer, Jorge Llop-Sayson, Andrew Howard, Caroline Morley, Kevin McKinnon, Kevin Wagner, Steve Ertl, Jules

Fowler, Jason Wang, and Zack Breismeister

- Chapter 4: Many previously thanked folks from Chapter 3; Mary Anne and Andrew Vandenburg for sharing the week of the JWST C3 proposal crunch with me

- Chapter 5 - 7: Arjo Bos, Stefan Kuiper, Max Baeten, Wouter Jonker, Matthew Maniscalco, Daren Dillon, Abraham Marsh, Caesar Laguna, Brad Holden, Matt Radovan

- Chapter 8: Mikayla Wilson

- Appendix A: Zara Barryte, E. Rosser, Isabel Kain, and the cast who volunteered (or who were volunteered by others) to read the script aloud at the post-defense party

In addition to those already named, I'd like to thank the broader set of early career researchers, faculty, and other collaborators who have helped me grow as a scientist through their collaboration, discussions, and support: Maddy Broome, Brittany Miles, Callie Hood, Amanda Quirk, Maggie Thompson, Brynna Downey, Nicholas Scarsdale, Evan Davis, Arcelia Hermosillo Ruiz, Alex Mannings, Sunil Simha, Jayron Aclan, Lisette Birch, Luca O'Shea, Sam Rosales, Sarah Blunt, Kyle E Franson, Jayke Nguyen, Yiting Li, Logan Pearce, Natasha Batalha, Briley Lewis, Elisabeth Matthews, Emily Rickman, Ruth Murray-Clay, Natalie Batalha, Connie Rockosi, and Steph Sallum.

My deep gratitude goes to the people in my life who supported me like chosen family across the years completing this work. These folks include the members of the Hebard Street co-op who I lived with – Dani Etchegaray, Ken Prola, Willow Gibney-Jones, Dan Berman, Chase Larue & Clare DePew – as well as Zara Barryte, E. Rosser, Andrea Meister, Sid Creutz, Kevin Hwang, Tauntaun Danbee Kim, Quinn Shemet, Evan Peairs, Andrew Wimmer, Alana Fitts, Kirsten Olson Pappas, Julie Henion Richardson, and Jules Fowler. I would like to extend an extra thanks in these regards to Adrienne Mueller who supported me through the most critical weeks of finishing writing this document (and for reviewing every single one of my postdoc applications last fall).

A portion of the data presented in this thesis were obtained at the W. M. Keck Observatory, which is operated as a scientific partnership among the California Institute of Technology, the University of California, and the National Aeronautics and Space Administration. The Observatory was made possible by the financial support of the W. M. Keck Foundation. I would like to acknowledge the Keck staff who supported the Wolf 359 observations including the observing assistants, Arina Rostopchina and Julie Renaud-Kim, and the instrument scientists, Carlos Alvarez and Greg Doppmann. Thank you to Charlotte Bond and Sam Ragland who supported operation of the pyramid wavefront sensor and the following observers for their contribution in collecting the HIRES velocities: Isabel Angelo, Corey Beard, Aida Behmard, Sarah Blunt, Fei Dai, Paul Dalba, Benjamin Fulton, Steven Giacalone, Rae Holcomb, Emma Louden, Jack Lubin, Andrew Mayo, Daria Pidhorodetska, Alex Polanski, Malena Rice, Emma Turtelboom, Dakotah

Tyler, Lauren Weiss, and Judah Van Zandt.

I wish to recognize and acknowledge the very significant cultural role and reverence that the summit of Maunakea has always had within the indigenous Hawaiian community. We are most fortunate to have the opportunity to conduct observations from this mountain.

Chapter 1

Introduction

1.1 The joy of studying exoplanets

Space, the final frontier...

I would like you, dear reader, to appreciate before anything else that we are the first generation to have access to the tools and methods needed to scientifically answer questions about alien worlds! The practice of discovering exoplanets is a little younger than I am, and I've grown up alongside it. The oldest paper in the Astrophysics Data System to use the term "exoplanet" to refer to a planet orbiting around a distant star is from 1992. I was six years old when the first planet outside of our Solar System was discovered around a Sun-like star (51 Peg b, [160]). In my first research position as an undergraduate, I was tasked to take the observatory's first measurement of a transiting

planet at a time when we only knew of a couple dozen transiting systems. I've watched as the number of discovered exoplanets ticked higher and higher thanks to the Kepler and TESS exoplanet transit space missions, alongside the multitude of discoveries coming from the dozens of radial velocity instruments. Soon, I'll get to PI a survey using JWST to directly image exoplanets orbiting some of our nearest neighboring stars. We have discovered over five-thousand exoplanets, and we're just at the beginning.

I am drawn to studying exoplanet science because there is still so much to explore. I love the feeling of wonderment that comes from making a good plot to reveal an important connection. I am in awe that this sort of science is even possible, let alone so close to helping us answer some of the biggest philosophical questions we face, *What else is outside Earth? How unique is the planet we're living on and the Solar System that we are a part of? What's our place and context - not just in our friendships, families, workplace, and societies - but in the whole dang universe??* I feel such a privilege to get to be an astronomer who has the job to ask the questions that could lead us to a minuscule more of understanding of what's really out there.

1.2 How have we been finding exoplanets so far?

Our continuing mission to explore strange new worlds...

Over the past 30-years, the field of exoplanet science has developed a multitude of techniques for discovering and characterizing planets. I reference five detection methods

in the main chapters of this thesis: direct imaging, radial velocity, astrometry, transit, and microlensing. These methods are introduced below and summarized in Table 1.1.

Each of these exoplanet detection techniques are based around one or more of the three fundamental measurements you can perform in observational astronomy:

- Photometry - measures the *brightness*
- Astrometry - measures the *position*
- Spectroscopy - measures the *spectra* to understand the difference in the brightnesses at different wavelength colors

There's a trend in astronomy to apply these same fundamental measurements over and over again but with increasing fainter objects, closer resolution, and more precision as our telescopes get bigger and our instruments become more sensitive. For example, the measurements done in exoplanet direct imaging today have little fundamental difference to what Galileo did when he looked through the first telescope with his eye to see Jupiter's four moons and plot their orbits over time.

We categorize the exoplanet discovery techniques into one of two types depending on what we are measuring to study the exoplanet. For *indirect* methods of observation, we perform photometry, astrometry, or spectroscopy on a star in order to infer the presence of an exoplanet. For *direct* methods of observation, we measure the light from the exoplanet directly.

The ***direct imaging method*** is a direct method of observation where we image the

photons coming directly from the exoplanet itself to measure the planet's *relative astrometric motion* and *photometry* directly (overviewed in Figure 1.2; example in Figure 1.3). The majority of direct imaging surveys completed so far have been performed in the thermal infrared. In thermal infrared direct imaging, the heat emitted from a companion is imaged, similar to looking through night-vision googles.[1] It is the best method for discovering hot, massive exoplanets/brown dwarfs orbiting at wide separations and long periods. By quantifying the relative astrometric motion the planet with respect to its star, we can measure its precise dynamical mass. By measuring the photometry, we can measure it temperature. If the age of the system is known, we can also infer the companions radius and some basic properties about its atmosphere (clouds versus no clouds). Once a planet has been directly imaged, follow-up *direct spectroscopy* may also be performed in order to more fully characterize the planet's atmosphere and chemical composition. While a powerful technique, few exoplanets have yet to be directly imaged because of the challenges associated with reaching a sufficient instrument contrast to see dim exoplanets next to bright stars. The technical details of this challenge and how we may overcome them are the focus of this thesis.

The ***radial velocity method*** is an indirect method of observation where we perform *spectroscopy* of a star over time to infer the motion of a planet (overviewed in 1.4). While the radial velocity method is bias towards massive planets on short edge-on orbits, some long-duration radial velocity surveys are beginning to reach the maturity needed

[1] It is also possible to do reflected light direct imaging in the visible band. Reflected light observing is not discussed in detail in this thesis but will play a critical role in the future characterization of exoplanets using direct imaging.

to detect giant planets in the outer regions of their systems (i.e., [87, 202, 208]). The population of radial velocity planets and direct imaging planets are beginning to merge. I discuss how radial velocity data can be applied to tailor direct imaging characterization observations in Chapter 2.

The ***astrometry method*** is an indirect method of observation where we measure the *astrometry* of a star over time to infer the motion of a planet 1.5). While also bias to short-orbit massive exoplanets, the astrometry method is complementary to the radial velocity method because it is able to detect the face-on motion in a system. Thanks to the incredible data volume being released by the *Gaia* survey [90, 91] on the precise position of stars, it is expected that within the next decade the number of exoplanets discovered using astrometry will increase by orders of magnitude [186]. The use of supporting absolute astrometry for tailoring direct imaging observations is discussed in Chapter 2.

The ***transit method*** is an indirect method of observation where we perform *photometry* on a star over time to see if a planet shadows-out part of its star (Figure 1.6).[2] This technique requires the planet to be in precise geometric alignment on an orbit that crosses between its star and our point of view. This special alignment is most likely to occur for large planets on short orbits, and very unlikely to occur for an Earth-like planet orbiting a Sun-like star ($\sim$0.5% [226]). Because of this bias towards short orbit planets,

[2]Transit spectroscopy is another form of direct detection method where the light from the star passing through the planets atmosphere is measured. While it is a form of direct detection and can be used to characterize planets atmospheres, it is not relevant in later chapters so is not discussed in detail.

the exoplanet populations discovered through transit and direct imaging are distinct. However, the two methods are complementary when studying planetary architecture in a system as a whole because the transit method can provide insight into the interior of the system.

The ***microlensing method*** is an indirect method of observation that requires a chance alignment between a foreground star hosting an exoplanet with a background star (Figure 1.7). The star (and planet) in front gravitationally bend the light from the background star, creating a unique pattern in the brightness change. This discovery method is more agnostic to the mass of the planet than other detection methods, so it excels at probing the occurrence rates of planets on wider orbits with lower masses that are tricky to see with other techniques. However, because this method requires a one-off chance alignment, individual planet discoveries cannot be followed-up. In Chapter 4, I apply the statistics we have learned from microlensing surveys [53, 189, 230] to estimate the yield of performing a direct imaging search for ice-giant exoplanets of nearby stars with JWST.

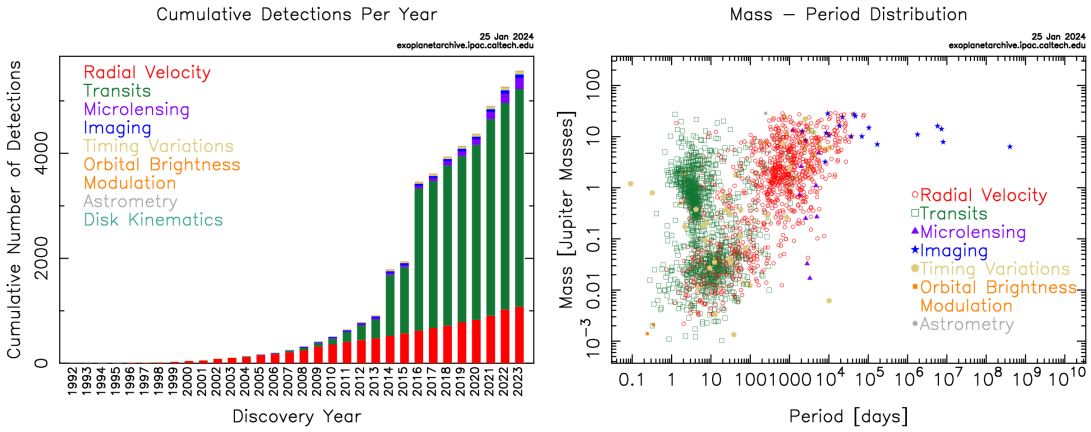

(a) Exoplanets Discovered Over Time (b) Current Population of Exoplanets

Figure 1.1 **The Development of the Field of Exoplanet Science.** We have discovered more than 5000 exoplanets in the past three decades. The majority of exoplanets are currently found using indirect detection techniques like radial velocity and transit. *(Figure credit: NASA Exoplanet Archive)*

Table 1.1 **Summary of Exoplanet Detection Methods Covered in this Thesis**

Exoplanet Detection Method	**Indirect/ Direct**	**Description**	**Weakness**
Direct Imaging	Direct	Image the light from an exoplanet directly to measure the brightness and position of the planet	Requires hard to achieve contrast with host star and the detectability of objects with dim flux
Radial Velocity	Indirect	Measures the spectra of the star to quantify the doppler shift from the star's movement due to the planet	Small planet on wide orbits have tiny signal; stellar activity is hard to detangle; Can't measure planet radius, orbit inclination, or precise mass
Astrometry (absolute)	Indirect	Measures the absolute position of the star to see the star's movement due to an orbitting planet	Small planet on wide orbits have tiny signal; Can't measure planet radius orbit inclination, or precise mass
Transit	Indirect	Measures the change in brightness of a star that occurs when a planet eclipses the star	Needs precise geometric alignment to have the planet occult the star; Can't measure mass
Microlensing	Indirect	Measures the brightness of two stars going through a chance alignment where the front star (and planet) bend the light from the back star	Can never do follow-up since measurement occurred during chance event

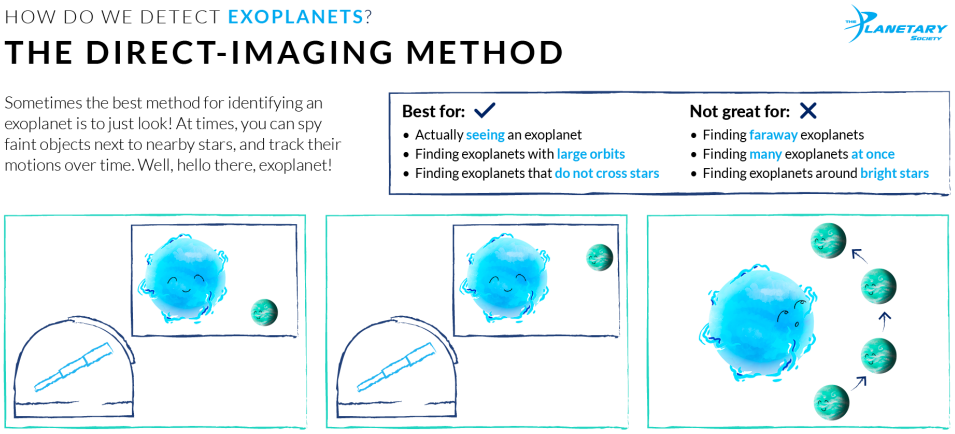

Figure 1.2 **An Overview of the Direct Imaging Method.** This graphic focuses on the benefits/weaknesses of thermal emission direct imaging (not reflected light). (*Figure Credit: The Planetary Society*)

1.3 The growing need for exoplanet characterization

To seek out new life and new civilizations...

The majority of exoplanets found so far were discovered using one indirect method of observing – mostly either transit photometry or radial velocity (see Figure 1.1). Because the light from the planet is not resolved in these techniques, the information we gather in the initial discovery of an exoplanet is limited.

Let's imagine a scenario where we're onboard the *USS Starship Enterprise D* when the crew pulls up to an exoplanet. Captain Picard tells Science Officer Data to scan the planet, and Data replies, "The planet's orbital period is about two weeks." Data would probably get a lot of blank stares from the crew if he gave such an ambiguous of a reply.

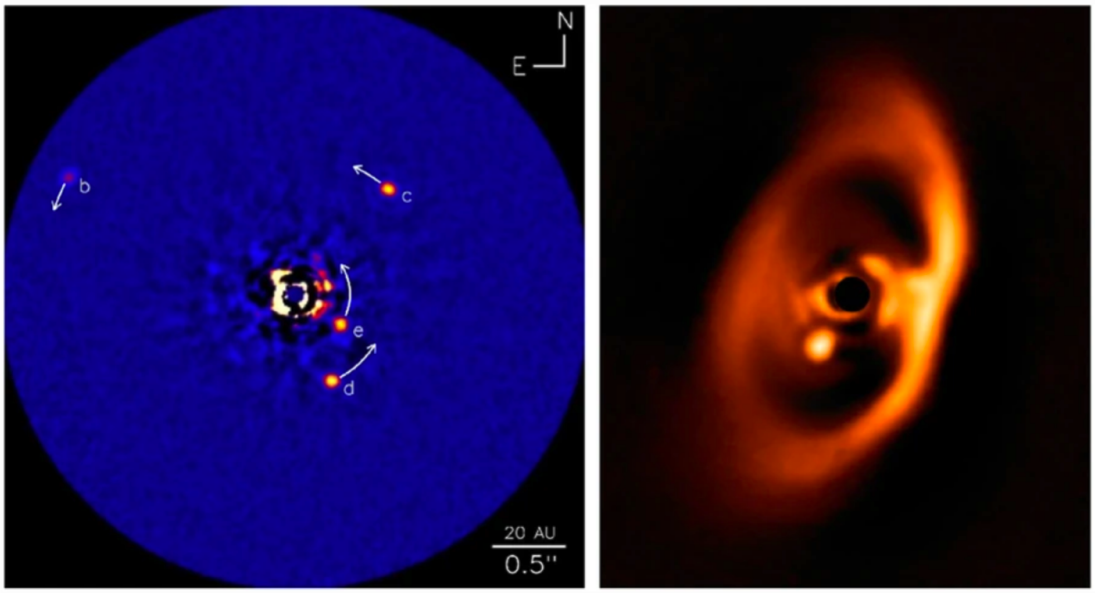

Figure 1.3 **Examples of Direct Imaging.** *(Left)* The HR 8799 system as imaged by Keck-NIRC2 [157]. *(Right)* PDS 70 taken at SPHERE in K-band [174].

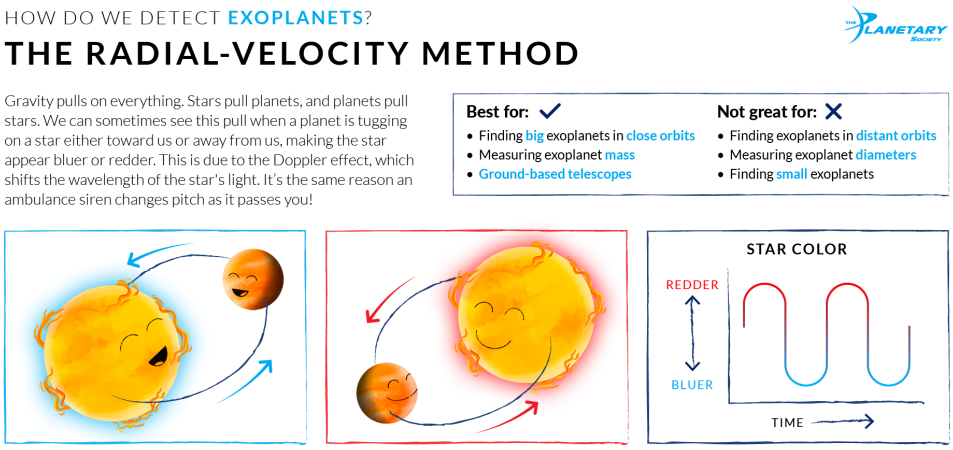

Figure 1.4 **An Overview of the Radial Velocity Method.** (*Figure Credit: The Planetary Society*)

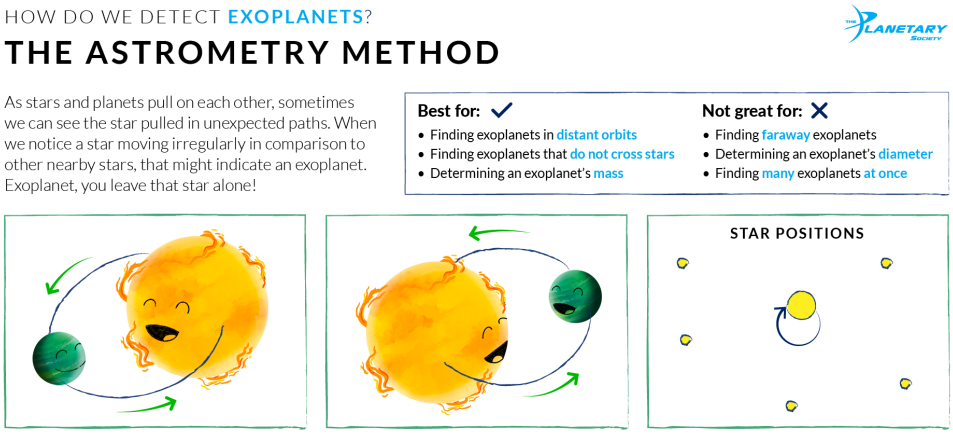

Figure 1.5 **An Overview of the Astrometry Method.** I refer to this detection method as "absolute astrometry" throughout the thesis to distinguish it from measuring the "relative astrometry" position of a planet as compared to its star. (*Figure Credit: The Planetary Society*)

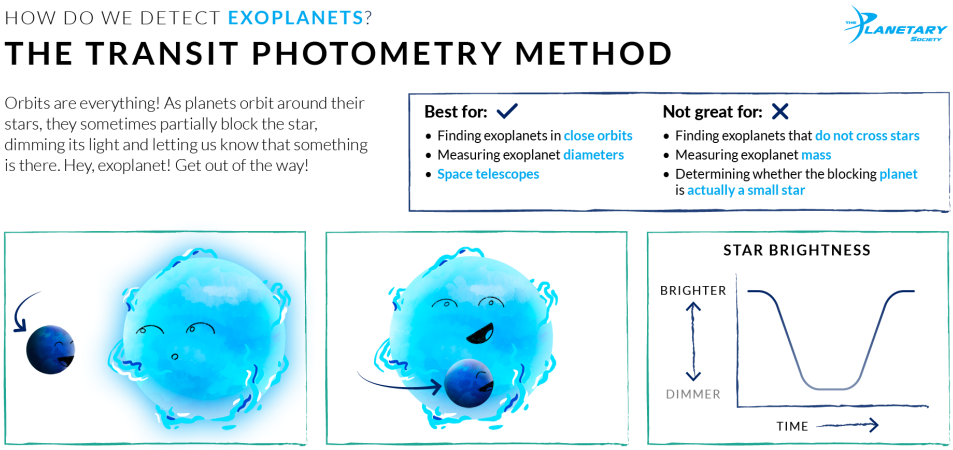

Figure 1.6 **An Overview of the Transit Method.** (*Figure Credit: The Planetary Society*)

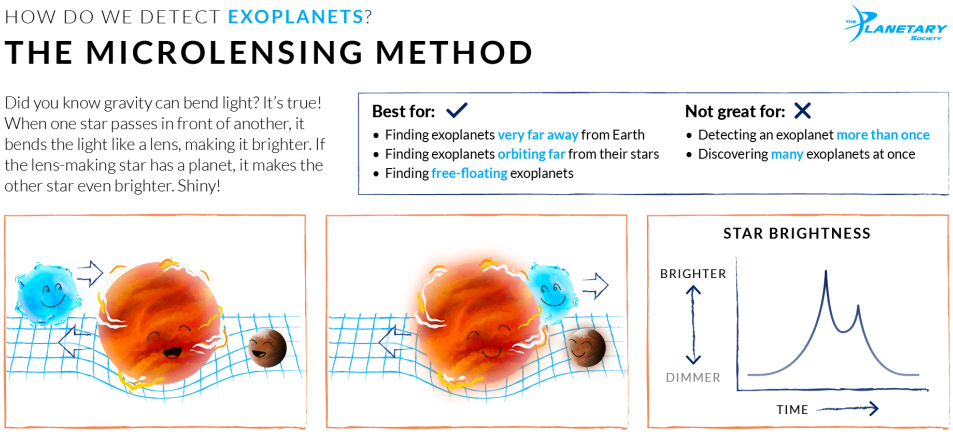

Figure 1.7 **Overview of the Microlensing Method.** (*Figure Credit: The Planetary Society*)

Or worse, Data could say something like, "It appears to have a minimum mass limit of 2 Jupiter masses. It might be bigger though!" This is about where we're at in terms of understanding the exoplanets that we have discovered. While measuring some basic planetary properties has been helpful for identifying trends and provides a first-pass of understanding, we need more ways to characterize individual planets and understand their place in their solar system architecture. We want our metaphorical Data's to be able to report back the status of the gases in the atmosphere, what sorts of geology might exist on a planet, what the weather is like, and even if there might be other life forms on the surface.

Table 1.2 summaries the properties of an exoplanet that we currently measure and the detection methods able to measure them. Combining multiple indirect detection techniques offers one solution to validate exoplanet candidates and conduct more detailed

characterization of a planet. For example, collecting radial velocity measurements of a planet that also transit can reveal both a planet radius and inclination angle (from transit) and a mass estimate (from radial velocity) (i.e. [2, 126]). However, there is no combination of indirect observation methods that can measure a planet's atmosphere.

Direct imaging/spectroscopy offers a solution to characterize of all the properties listed in Table 1.2 from density/bulk composition to atmospheric dynamics.[3] Thermal infrared direct imaging is uniquely capable of probing the deepest layers in exoplanetary atmospheres to understand the chemical equilibrium where biosignitures are more likely to be present (see Figure 1.8; [151]). For example, direct imaging/spectroscopy observations have been used to detect water methane ammonia and carbon monoxide (see Madhusudhan et al 2019 [151] for full summary of these observations). Direct imaging has also been used to measure chemical abundances ratios that can reveal clues to how the planet was formed [167], such as the C/O ratio [102, 166].

If we someday hope to characterize the full diversity of exoplanets (particularly those on wide-orbits that include the habitable-zone), it is imperative that we continue to expand our abilities to perform direct imaging/spectroscopy.

[3] Measuring the spectrum of an exoplanet as it transits ("transit spectroscopy") offers another solution to measure the atmosphere of a planet and is also considered a direct method of observation. However, it's use is limited to planets that transit (mostly on short periods) and cannot reach the precision of direct spectroscopy. Transit spectroscopy/direct spectroscopy should be considered complementary because transit spectroscopy is best used for short-period highly-irradiated planets while direct spectroscopy is best used for longer-period self-luminous planets.

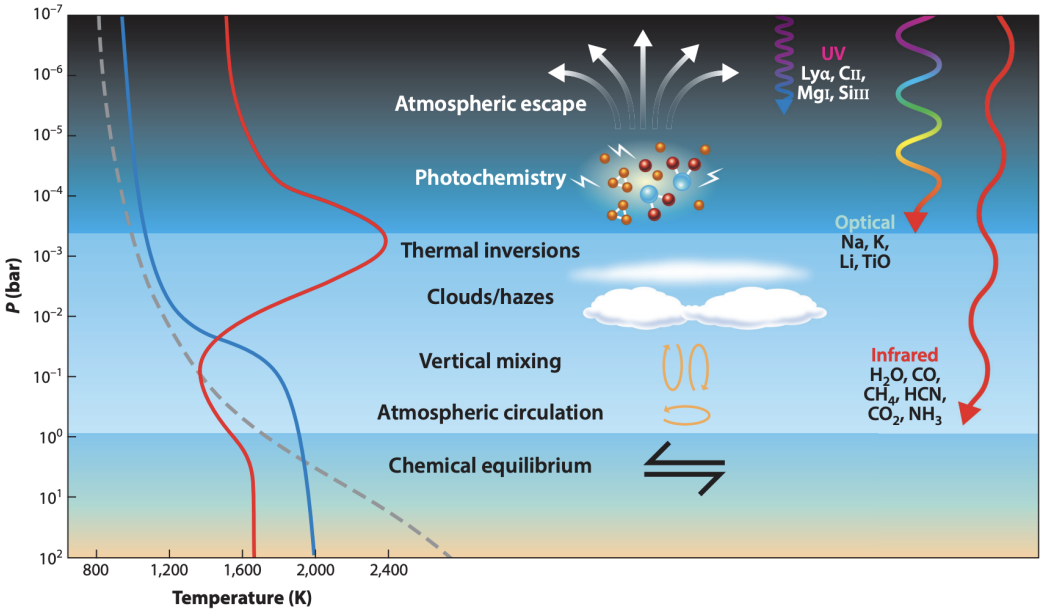

Figure 1.8 **Processes that are active in exoplanet atmosphere by the wavelength which can probe them.** Thermal direct imaging can uniquely be used to probe the area of the atmosphere closest to the surface where chemical equilibrium is occurring and biosignatures may emerge. (*Figure credit: Madhusudhan et al 2019;* [151])

Table 1.2 **Summary of Methods to Characterize Exoplanets**

Property	**Technique(s) that can be used to get measurement**	**Could be inferred using models/ additional info**
Orbital period/ separation	Direct imaging, RV, Astrom, or Transit	–
Mass	Direct imaging can provide precise mass; RV + astrom can provide precise mass	RV or astrom alone can provide a min mass
Planet Radius	Transit	Direct imaging (if age is known)
Density/ Bulk Composition	RV + Transit	Direct imaging (if age is known)
Orbit Inclination	Direct imaging Transit RV + Astrom	–
Atmospheric Composition	Direct imaging*	–
Temperture	Direct imaging	–
Full Planetary System Architecture	Requires combo of methods with the abilities to probe a range of orbit separations	See Chap 2

* transit spectroscopy can also reveal a planet's atmosphere, but is not discussed in future chapters of this thesis so has not been included

1.4 The challenges of exoplanet direct imaging

These are the voyages of...

Directly imaging an exoplanet is technologically challenging. Stars are orders of magnitude brighter than planets, a comparison often described by "looking for a firefly near a lighthouse."

When quantifying the sensitivity of an exoplanet direct imaging observation, astronomers plot the *contrast curve* to denote the detection threshold of a potential companion by separation[4] (example shown in Figure 1.9). Direct imaging observations become more sensitive to fainter companions as the separation from the star increases because the influence of the bright star diminishes. Because of this trend, it is common to discuss the contrast curve in two divided parts that limit the performance as the "contrast limited regime" and the "background limited regime." In the following subsections, I describe the nuances of what is enabling our current sensitivity for each of the two parts of the contrast curve.

[4] 1, 3, and 5σ contrast curves are common in the literature, but any value can be chosen. Ultimately, the choice of the observer what value they would like to plot their contrast curves in.

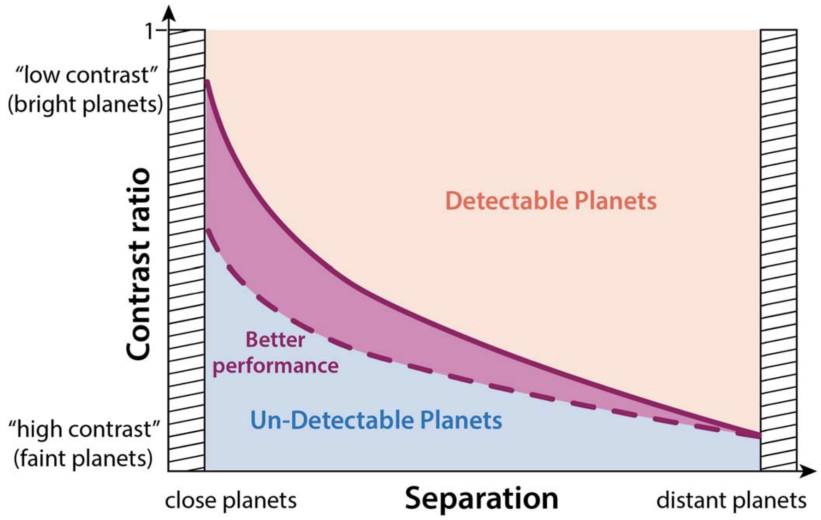

Figure 1.9 **How to Read a Contrast Curve.** The sensitivity of direct imaging observations are reported in terms of the contrast of a theoretical companion with its host star at a given detection threshold. A potential exoplanet with a brightness above the contrast curve will be bright enough and at sufficient separation to be detected. The units of a contrast curve can either be plotted from the observers perspective (flux ratio/delta magnitude vs arcsec) or the planetary system perspective if the distance to the system and age are known (planet mass vs AU). The sensitivity of a direct imaging observation progresses from being "contrast limited" to being "background limited" the farther the performance is evaluated from the host star. *(Figure credit: Follette et al 2023; [82])*

Table 1.3 Peak of Blackbody Flux for Example Planets

Planet	Effective Temperture	Peak flux of blackbody (μm)
HR 8799 b	1200 K [29]	2.4
51 Eri b	700 K [196]	4.1
Mercury	440 K [178]	6.6
COCONUTS-2b	430 K [254]	6.7
Earth	254 K [178]	11.4
Jupiter	110 K [178]	26.3
Neptune	47 K [178]	61.7

1.4.1 Seeing the firefly: detecting the planet in the background limited regime

Detecting the flux from a planet, even without the influence of the star, is no easy feat. If we ignore the atmosphere of a planet and consider it to be a blackbody, the energy emitted by a planet will follow the Planck's law of blackbody radiation. Figure 1.10 shows examples of the blackbody curve of objects within the range of temperatures that could belong to an exoplanet (50K - 1200K). As we consider colder temperatures, the flux diminishes and the peak shifts further to longer wavelengths following Wein's Displacement Law,

$$\lambda_{peak} = \frac{b}{T} \tag{1.1}$$

where λ_{peak} represents the peak of the blackbody curve, b is Wein's displacement constant, and T is the temperature. Table 1.3 lists examples of known planets with their effective temperatures and the wavelength that their blackbody would expect to peak.

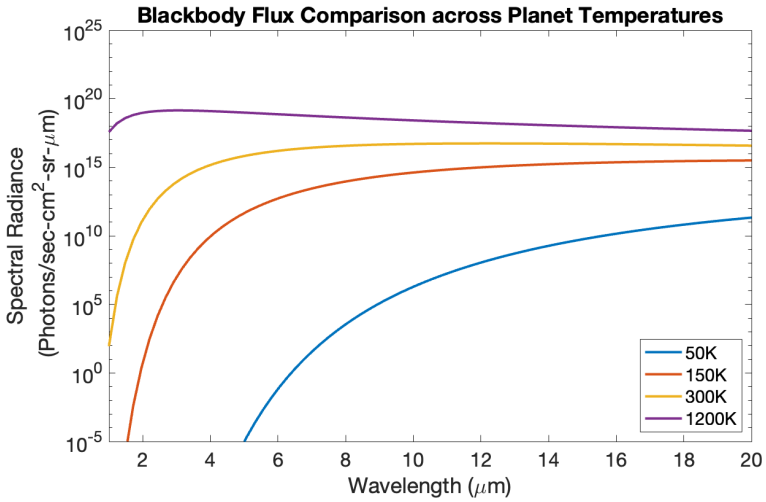

Figure 1.10 **Blackbody Curves for Planet Temperature Range**. While planets are not simple blackbodies, understand the blackbody flux at planet tempertures is useful for gaining intutiion for understanding the observing challenges. The flux emitted by cold planets ($<$ 300K) is accessible only in long infrared wavelengths ($>$ 5μm). This figure was generated using online tools from `https://www.opticsthewebsite.com/OpticsCalculators`.

The current set of directly imaged planets peak in the near to mid infrared. Our Solar System planets are colder, and thus peak in the mid to far infrared. As a consequence, observers must turn to observing in the infrared in order to be able to capture sufficient flux from a planet to be seen when trying to measure its energy emitted. These sorts of infrared observations include their own set of challenges:

Challenge 1: When observing from the ground, gases in the atmosphere glow at infrared wavelengths which increases the sky background counts. While some IR wavelengths can still be measured through atmospheric seeing windows (see Figure 1.11), infrared observing is still plagued with increased and variable sky background conditions.

Challenge 2: The telescope and instruments themselves also both glow in the infrared. Every optic that the light passes through will add its own thermal noise if it is not being actively cooled.

Challenge 3: When performing science that is resolution limited such as exoplanet direct imaging moving to longer wavelengths increases the size of the PSF shape. This farther limits the inner working angle when we are trying to view as tight of a separation as possible.

Challenge 4: The options for infrared detectors are limited, particularly in the mid to far infrared, which can make building new instrumentation challenging. Infrared detector technology can often be classified and inaccessible for use in astronomy.

Even with all these observing challenges, there is a small set of companions that are bright enough to be observed with our current instrumentation. These companions are hot and nearby. A self-luminous companion will be hot if it still retains its heat from formation by being young ($\sim<$ 1 Gyr) and/or massive ($\sim>$ $2M_{jup}$). Proximity in stellar distance boosts the apparent magnitude of the companion logarithmically,

$$m = 5\log_{10}(d/10) + M \tag{1.2}$$

where m is the apparent magnitude, M is the absolute magnitude, and d is the distance in parsec. The trade among these three factors (age, mass, and proximity) controls the observed brightness of our little firefly planets.

In Chapter 3.5, I quantify the background limited regime of the Keck-NIRC2 imager as applied to the detectablity of the exoplanet candidate Wolf 359b. In Chapter 4, I consider the background limit of JWST NIRCam and MIRI observations, and apply this to evaluate the detectablity of an ice-giant exoplanet. In chapter 7, I discuss how adopting an adaptive secondary mirror can better the background limit for large ground based telescopes in the infrared.

1.4.2 Beating the lighthouse: improving the contrast

In addition to being able to detect the flux from the planet, it is essential to be able to distinguish the signal from the star from the planet.

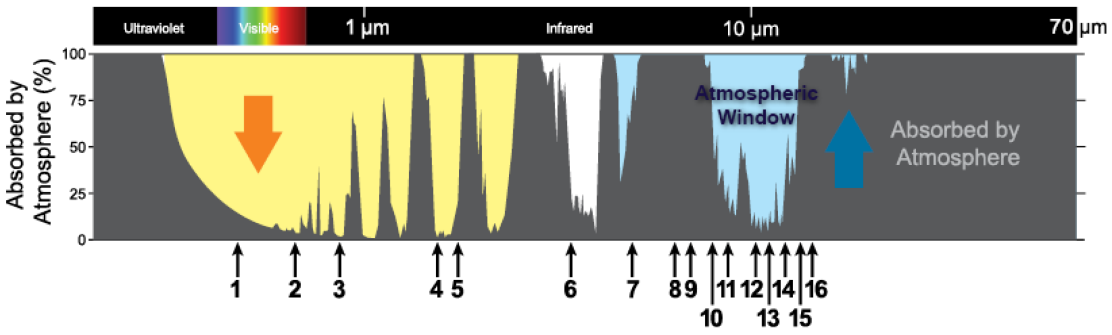

Figure 1.11 **Atmospheric Observing Windows.** Water vapor in the Earth's atmosphere absorbs infrared radiation, leaving only tight bandpasses where astronomical observing is possible from the ground. *(Figure credit: NOAA)*

Two key technologies enable our ability to perform high-contrast imaging and mitigate the flux difference between the planet and star:

1. **Adaptive optics:** When light enters the atmosphere, it becomes distorted by the air. An *adaptive optics* system is used to correct this blurring effect, enhancing the image and maintaining the resolution to resolve different astrophysical sources. The goal is to restore the PSF to its original diffraction-limited size.
2. **Coronagraph**: A *coronagraph* is a specialized optic designed to block the light from a star when it is in the center of the image, functioning somewhat like an advanced version of shading the Sun with your hand to see a flying bird. A coronagraph aids in imaging faint exoplanets without overwhelming the camera with excessive starlight.

The adaptive optics system concentrates the light from the star behind the coronagraph.

If the performance of your adaptive optics system is strong, the better the suppression of the starlight will be by the coronagraph. If the performance is not perfect (as is the case with most observations), speckles will appear that can mascaraed as planets. To reduce the the impact of these speckles, the community has adopted specific observing strategies (i.e. angular differential imaging [157]) and developed a multitude of sophisticated post-processing techniques [82]. I explain the role of adaptive optics in high-contrast imaging in greater depth in Chapter 5 and introduce the technology development related to a new style of large-format deformable mirror in Chapters 6 and 7.

If selecting nearby targets, proximity will naturally make companions appear at proportionally wider separation angles for a given orbit, relaxing the contrast requirements for planets on shorter orbits. This relationship can be expressed as,

$$\theta_{sep} = \frac{a}{d} \tag{1.3}$$

where θ_{sep} is the angular separation between the star and planet (arcsec), a is the orbital position of the planet (AU), and d is the stellar distance (pc).

Another option to better your contrast is simply to chose to image companions orbiting fainter stars. In these cases, using a coronagraph may not be necessary. I explore the tradeoffs of using the vector vortex coronagraph with Keck-NIRC2 in M-band in Chapter 3 and JWST in Chapter 4.

1.5 The aims of this thesis

To boldly go where no one has gone before!

In this thesis, I aim to give an overview on the state of the field of exoplanet direct imaging, explore the current limitations facing observers/our instrumentation, and offer some near-future solutions to how we may soon use direct imaging to unlock new science cases. My goal with this text is to equip a late-stage undergraduate or early-stage graduate student to take on the research that will benefit the field in observational exoplanet direct detection and the development of large-format deformable mirror adaptive optics technology.

I cover both my observation-based and instrumentation-based research. I have divided the inner chapters of the thesis into these two parts. Each observation/instrumentation module of the thesis contains three chapters following the same format: (I) an "emerging techniques" introductory section that gives an overview of that sub-feild, (II) original research into the current performance capablities and limitations of our methods/technologies, and (III) a futures section where I overview the technical details and projects in progress.

Overview of Part I: Observation

- Chapter 2: Emerging techniques and resources for conducting tailored direct imaging observations

- Chapter 3: Current performance and limitations: Hunting for companions in the fifth-closest system using combined high-contrast imaging and radial velocity analysis.
- Chapter 4 The Future: Prospects for the direct detection of cold ice giants and gas giants orbiting young low-mass neighbors

Overview of Part II: Instrumentation

- Chapter 5: Emerging technologies and resources for building adaptive secondary mirror based adaptive optics systems
- Chapter 6: Current performance and limitations: Laboratory testing of HVR-actuator based large-format deformable mirror technology
- Chapter 7: The Future: Future development of the HVR-based large-format deformable mirror technology and in-progress adaptive secondary mirrors

Chapter 8 offers concluding thoughts and four perspectives on the future of exoplanet direct imaging. Appendix A contains a 10-minute science play for the enjoyment of the direct imaging community.

Part I

Observation

Chapter 2

Emerging techniques and resources for conducting tailored direct imaging observations

"The real secret is turning disadvantage into advantage."

2.1 The motivation for conducting targeted direct imaging campaigns

The heritage of detecting exoplanets via the direct imaging technique has been to conduct blind surveys of hundreds of star systems using 8-10m class telescopes. More than a dozen surveys [22,23,35,39,56,57,92,106,118,133,137,175,179,197,236,237,240,249] have

revealed approximately 40 wide orbit (> 10AU) brown dwarf/large gas giant companions ($> 2M_{jup}$) [33]. The majority of these substellar companions are in the brown dwarf mass regime.

These early surveys have revealed that these massive, wide-orbit companions are rare (< 4%; [34]). Figure 2.1 shows the currently discovered exoplanet population in conjunction with the occurrence rates measured for planets orbiting outside of > 1AU using direct imaging, radial velocity, and/or microlensing.[1] The past sensitivity of direct imaging has been limited to the upper right corner of this plot ($Mjup > 2$, a >10AU). While the direct detections of these larger companions have enabled the study of brown dwarfs and the boundary between stars/planets, it cannot yet be used to study the differences between different planet populations.

Moving to a targeted observing strategy offers the direct imaging community a solution for expanding the types of exoplanets we image using our current set of instruments and detect new planets more efficiently. By applying some initial knowledge, we can tailor the high-contrast imaging follow-up observation for choice of candidate, best suited instrument, observing filter, observation window, and integration time to optimize the chance of a detection. This targeted approach allows for the selection of a small number of systems to observe as deeply as possible. It does not allow for occurrence rate studies because there is not a homogeneous unbiased sample.

[1] The source code to generate your own version of the occurence rate figure can be retrieved online at `https://github.com/logan-pearce/occurrence-rate-plot/tree/main`

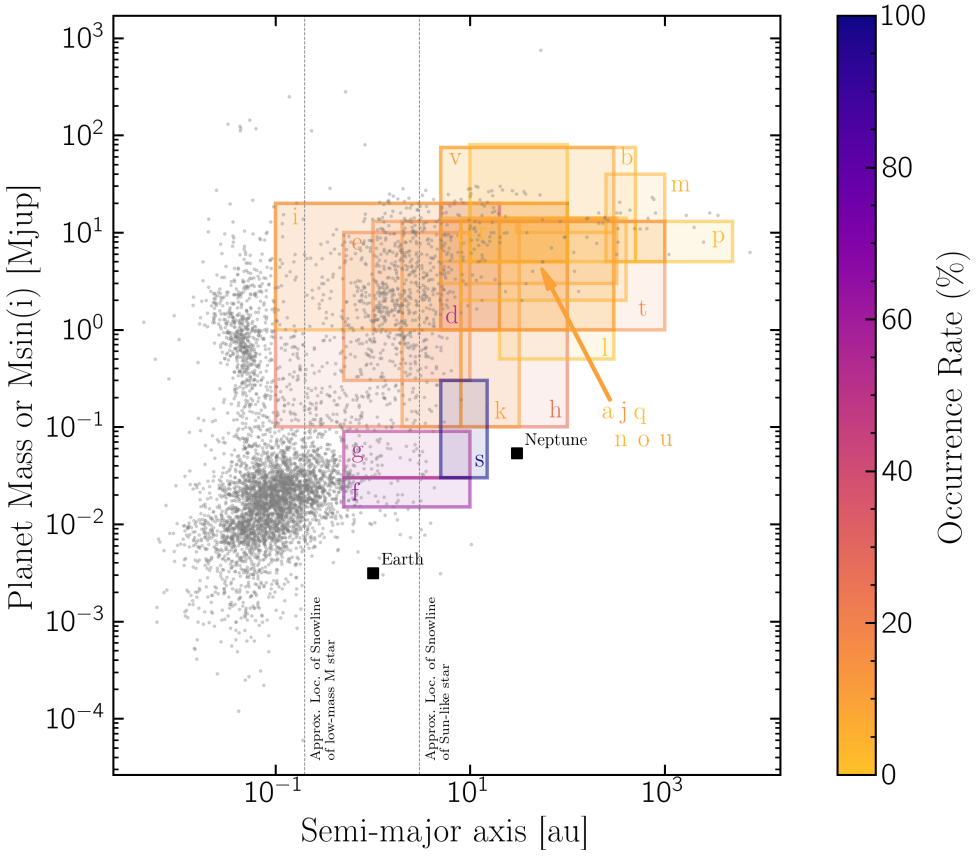

a: Bowler 2016
30-300AU, 10-13Mjup, $2.8^{+3.7}_{-2.3}$%
b: Bowler+ 2018
5-500AU, 13-74Mjup, 1-4%
c: Bowler+ 2018
5-500AU, 5-13Mjup, 1%
d: Bryan+ 2016
5-20AU, 1-20Mjup, 52±5%
e: Cassan+ 2012
0.5-10AU, 0.3-10Mjup, 17^{+6}_{-9}%
f: Cassan+ 2012
0.5,10AU, 0.015-0.03Mjup, 62^{+35}_{-37}%
g: Cassan+ 2012
0.5-10AU, 0.03-0.09Mjup, 52^{+22}_{-29}%

h: Fernandes+ 2019
0.1-100AU, 0.1-20Mjup, $26.6^{+7.5}_{-5.4}$%
i: Fernandes+ 2019
0.1-100AU, 1-20Mjup, $6.2^{+1.5}_{-1.2}$%
j: Fulton+ 2021
2-8AU, 0.1-13Mjup, 14%
k: Fulton+ 2021
8-32AU, 0.1-13Mjup, $8.9^{+3.0}_{-2.4}$%
l: Galicher+ 2016
20-300AU, 0.5-14Mjup, $1.05^{+2.80}_{-0.70}$%
m: Lafreniere+ 2014
250-1000AU, 5-40Mjup, $4.0^{+3.0}_{-1.2}$%
n: Lannier+ 2016
8-400AU, 2-14Mjup, $2.3^{+2.9}_{-0.7}$%

o: Meshkat+ 2017
10-100AU, 5-20Mjup, $6.27^{+3.49}_{2.59}$%
p: Naud+ 2017
500-5000AU, 5-13Mjup, $0.84^{+6.73}_{-0.66}$%
q: Nielsen+ 2019
10-100AU, 5-80Mjup, $0.8^{+0.8}_{-0.5}$%
r: Nielsen+ 2019
10-100AU, 5-13Mjup, $3.5^{+1.9}_{-1.4}$%
s: Poleski+ 2021
5-15AU, 0.03-3Mjup, 1.5 ice giants per star%
t: Rameau+ 2013
1-1000AU, 1-13Mjup, $16.1^{+26.3}_{-11.2}$%
u: Vigan+ 2012
5-320AU, 3-14Mjup, $8.7^{+19.6}_{-6}$%
v: Vigan+ 2021
5-300AU, 1-75Mjup, $5.7^{+3.8}_{-2.8}$%

Figure 2.1 **The Measured Occurrence Rates of Exoplanets on Orbits > 1AU.** Brown dwarfs and giant exoplanets beyond 10 AU have been found to be rare through direct imaging surveys. The frequency of long-period planets increases for sub-Jupiter mass planets and tighter separation (1-10 AU) as measured by RV and microlensing. *This figure was made in collaboration with Logan Pearce. [183]*

In this chapter, I review the current state of strategies, resources, instruments, and analysis tools available to observers who wish to conduct tailored direct imaging. My goal is to build a "starter guide" for new observers as well as provide helpful resources for more experienced observers who are less familiar with the targeted HCI strategies and tools.

2.2 Overview of the Process of Targeted Direct Imaging

After establishing the science case, the first step of conducting a tailored direct imaging observation is to identify supplemental data that may be of use to you. Once these datasets are retrieved, the observer then needs to identify the tools/code that can be applied to help sort through the data (or build their own). In Section 2.3, I present options for incorporating radial velocity, absolute astrometry, and transit measurements. I often describe these tools with a focus on identifying small giant exoplanets, but the same strategies can be applied for hunting for companions of many types (i.e. white dwarfs, brown dwarfs, stars, etc).

Once a set of candidates are identified, you must estimate the range of angular separations possible and predict the brightness. If the companion's mass can be predicted using supplemental data, the absolute magnitude of the companion can be predicted using evolutionary cooling models. To do this, the age must be estimated. The age estimate can often stand as a hurdle for making good brightness estimates before the

observation or setting accurate survey non-detection limits after the observation. These estimates for each candidate can then be compared with the predicted contrast curve for your instrument. I describe more detail on how to perform each of these steps in the following subsections.

After the candidates are identified, it's time to identify the instruments, observing modes, and timing best suited to making the detection. Making decisions surrounding instrument choices often include questions like: Would space-based observing be needed to make this detection? What telescopes do I have access to? What instruments are available on those telescopes and are any optimized for the observing I think would be best? The observing mode decisions can include questions like: What is the best filter choice for this observation? Should a coronagraph be used? Is this detection at a tight enough separation angle that aperture masking is required? Timing decisions include questions like: When will the candidate be likely to be at its maximum separation during its orbit? When will the system be up in the sky?

After these decisions are made, it's time to write a proposal and observe. If the candidate is detected, excellent! The photometry and relative astrometry of the candidate can be measured in order to estimate its mass and orbital properties. The observation would also pave the way for future follow-up observations where the position needs to be known more precisely in order to obtain spectra or even more precise astrometry. If a non-detection is made, upper limits can be set on a candidate's mass using evolutionary cooling models, an age estimate of the system, and the measured contrast between the

star and the background.

Figure 2.2 shows a flow chart for my vision of the field for moving through the process of identifying brown dwarf/exoplanet candidates for direct measurement through their characterization. In this diagram, I specifically call out JWST as a telescope that is more capable of detecting dim ($M > 16$), wide orbit (> 0.5 arcsec) companions that ground-based facilities cannot see. When discussing astrometic followup, I suggest using the ExoGRAVITY [131] interferometric instrument for its unprecedented ability to perform astrometic measurements with a precision $10 - 100$x better than non-interferometric imagers like Keck-NIRC2, NACO, or GPI.

2.2.1 Estimating the contrast curve

The final contrast curve will be specific to the instrument and its configuration (i.e. telescope diameter, filter, integration time, coronagraph choice, etc), the target (the brightness of the star in your chosen filter), and the observing conditions at the time of observation (adaptive optics performance, weather, etc). Because there are so many factors that affect the final contrast sensitivity, simulating a contrast curve it is not straightforward. Every target may require its own estimation, and the tools that do exist for these predictions tend to only be relevant for specific modes of operation.

Finding a published contrast curve of a similar observation in the literature and adapting it to your target can be a good starting point. If you are making this adjustment,

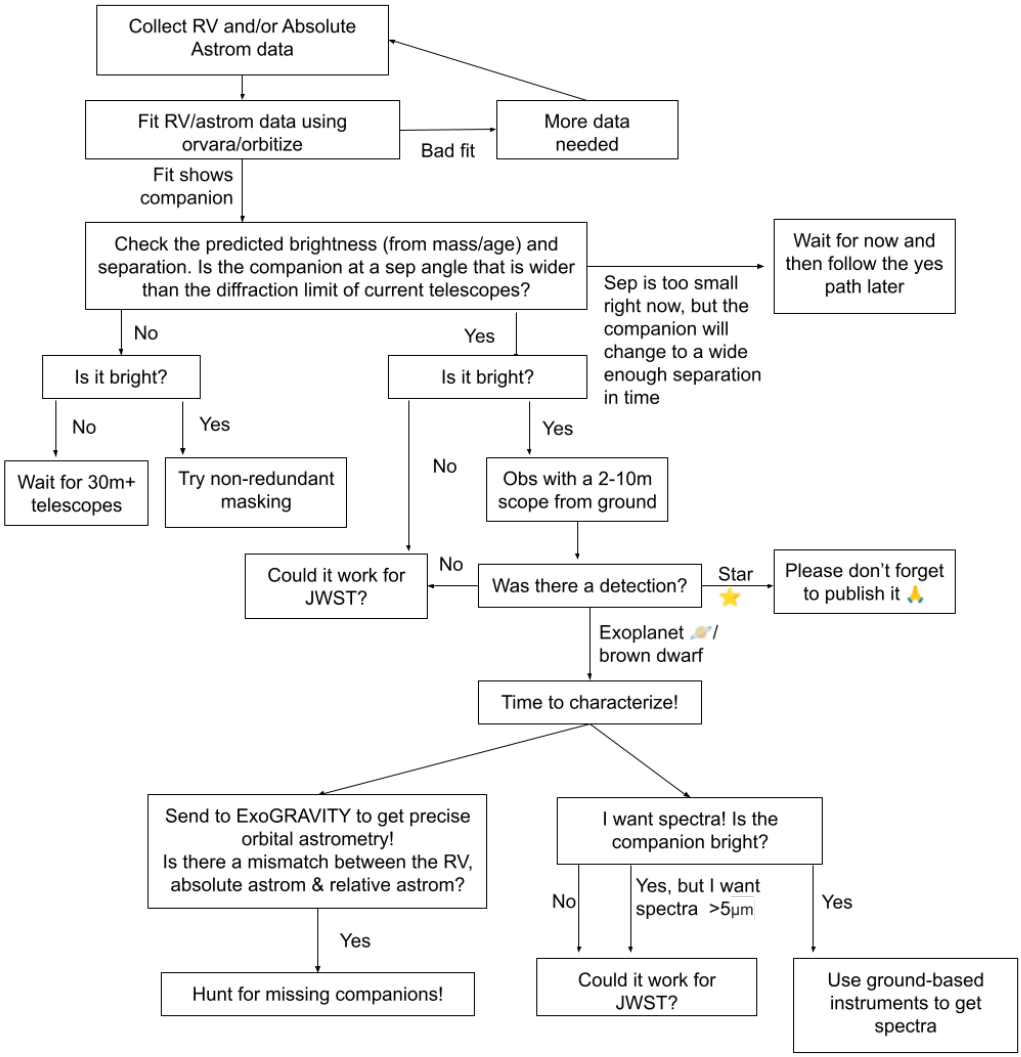

Figure 2.2 **Flowchart of the steps to perform targeted direct imaging and follow-up characterization.** This chart was created in the landscape of instrumentation in 2024.

remember that sensitivity in the background-limited regime of the contrast curve (where you are sufficiently far away from the star to not be affected by the influence of the starlight) will likely not change with different targets or with your observation.

The *Keck NIRC2 SNR and Efficiency Calculator* provides observers with estimates for the expected background-limited sensitivity of NIRC2 observations.[2] However, this calculator is not compatible with coronagraphic observations at Keck. The NIRC2 electronics were upgraded in 2023 to make the readout efficiency $> 90\%$, and at the time of this writing, the calculator efficiency had yet to be updated accordingly.

The *Vortex Imaging Contrast Oracle* (VICO) predicts the contrast for targets observed with Keck-NIRC2 with the vortex coronagraph in L-band [248].[3] VICO was trained using 3 years of Keck-NIRC2 HCI imaging data. The tool assumes an ADI reduction. The user inputs the target's W1 mag, R mag, total integration time, and the expected PA rotation. This tool was trained before the NIRC2 electronics upgrade, so expect the sensitivity predicted by VICO to be an underestimate of the performance likely now.

`PanCAKE` [51, 185] is the go-to simulation code for predicting JWST contrast curves for high-contrast imaging with NIRCam coronagraphy. To run a `PanCAKE` simulation, the user specifies their target's brightness, spectral type, filter, integration time, and type of KLIP strategy (ADI/RDI/ADI+RDI). While the accuracy of `PanCAKE` has been verified against measurements by NIRCam, it has yet to be deemed reliable for use with MIRI

[2] The Keck NIRC2 SNR and Efficiency Calculator can be accessed here: `https://www2.keck.hawaii.edu/inst/nirc2/nirc2_snr_eff.html`

[3] VICO can be accessed at `https://wxuan.shinyapps.io/contrast-oracle/`

coronagraphy (as of time of writing).

2.2.2 Predicting the planet's brightness

The mass, age, and distance dependence:

Substellar companions (like exoplanets and brown dwarfs) radiatively cool over time, releasing the energy that they generated during their formation. The starting temperature due of the planet is mass dependant ($T \propto GM/R$) and emits energy following the relationship,

$$L_{bol} \propto \frac{M^{5/2}}{t^{5/4}} \tag{2.1}$$

where L_{bol} is the bolometric luminosity of the planet, t is the age, and M is the mass [33]. The implications of this relationship is that 1) higher mass planets are brighter in the infrared, 2) younger planets are brighter than older planets, and 3) the brightness is more affected by mass than age.

The proximity of the system to us will also affect how bright the planet appears. The evolutionary cooling models provide planet brightness in absolute magnitude. To convert these values to the apparent magnitude (m) follows the relationship,

$$m = 5\log_{10}(d/10) + M \tag{2.2}$$

where M is the absolute magnitude and d is the distance to the system in parsec. Favoring nearby systems has a logarithmic dependant advantage. For example, the same planet at 100 pc instead of 10 pc will appear 5 magnitudes dimmer.

Age dating:

Exoplanet direct imagers typically adopt the age of the star as a proxy for the age of its exoplanets, however age dating the star can still be challenging. There are multiple methods for obtaining age estimates of a system (kinematic, rotation period, UV flux excess, color-magnitude isochrone tracks, etc.) which may not yield the same answer for each system. I opt not to go into the details of each of these age dating methods as they are the subjects of full PhD thesis (i.e. [18, 125])

The NASA exoplanet archive does not currently provide ages in its data listing. Selecting targets from young moving groups may provides an option if the exact age is necessary to conduct the science case, but relying on young moving groups is not always possible. Tedious literature searches do not always yield an answer for particular star systems. Low-mass stars can be particularly difficult, and many indicators that work for higher mass stars only reveal relative maturity (young/old) [74, 180, 190]. For those seeking the age estimate of a target, here is my short list of starting resources:

- The UltracoolSheet contains resources on 4000+ Ultracool Dwarfs and Imaged Exoplanets. It recently added an age dating tab, accessible here: `https://docs.google.com/spreadsheets/d/1i98ft8g5mzPp2DNno0kcz4B9nzMxdpyz5UquAVhz-U8/edit#gid=1544744403`

- Ages for discovered planet are sometimes listed on `https://exoplanet.eu/`
- I started a public NASA ads library to collect papers containing age estimates. This *age bank* library has 6 papers at the time of writing: [13, 104, 152, 181, 211, 218].

Evolutionary Cooling Models:

A variety of evolutionary cooling models have emerged to provide the expected brightness for an object of a given age and mass. The different evolutionary models have variations in factors like starting metallicity, clear/cloudy atmospheres, handling of mixing and equations of state, opacity, temperatures, and applicable mass ranges.

The `Species` python package has excellent integrated quick tools to help calculate isochrones and provide the estimated brightness of an object.[4] The package is compatible with the following evolutionary models:

- AMES-Cond [11] - Original cool brown dwarfs and giant planet models (<1400K)[5]
- AMES-Dusty [55] - Low-mass stars and brown dwarfs with dusty atmospheres (<1700-3000K)
- ATMO isochrones (CEQ, NEQ weak, NEQ strong) [187] - cool T-Y brown dwarfs and giant exoplanets
- Baraffe et al. (2015) [12] - low-mass stars modeled with 2D/3D radiative hydro-

[4] You can find more info on using Species to estimate the magnitude from the mass here: `https://species.readthedocs.io/en/latest/tutorials/read_isochrone.html`. Many of the models listed can be accessed directly without going through the `Species` package here: `https://perso.ens-lyon.fr/isabelle.baraffe/`

[5] This COND models are publicly available at:`http://perso.ens-lyon.fr/isabelle.baraffe/?C=M;O=D`

dynamics simulations, superseding the BCAH98 models (>3000K)

- Linder et al. (2019) [146] - cloudless cold sub-Jupiter mass exoplanets from $5M_{earth} - 2M_{jup}$.
- Saumon & Marley (2008) [213] - cloudy low mass stars, brown dwarfs, and giant planets
- Sonora Bobcat (2021) [156] - cloudless substellar objects with $3.25 \leq logg(cgs) \leq 5.5$ and $200 \leq T_{eff} \leq 2400$K
- The Phoenix grids [3] - stars $T_{eff} > 1500$K across a variety of metallicities and surface gravities

To provide the reader with a better intuition of the relationship between the mass/age/distance on the brightness of small giant planets, I've included Figure 2.3 which shows the Linder 2019 models for the NIRCam F444 filter for Neptune and Jupiter mass planets. A Neptune sized planet ($0.05M_{jup}$) of 100 Myr of age is comparable in brightness to a Jupiter mass planet of 5 Gyr in age.

2.3 Strategies for applying data from indirect methods of observation

2.3.1 Radial Velocity

In many cases, we only need a hint to a companion's existence to curate an HCI observation using RV data. As high-precison RV instruments like ESO-HARPS, Keck-HIRES,

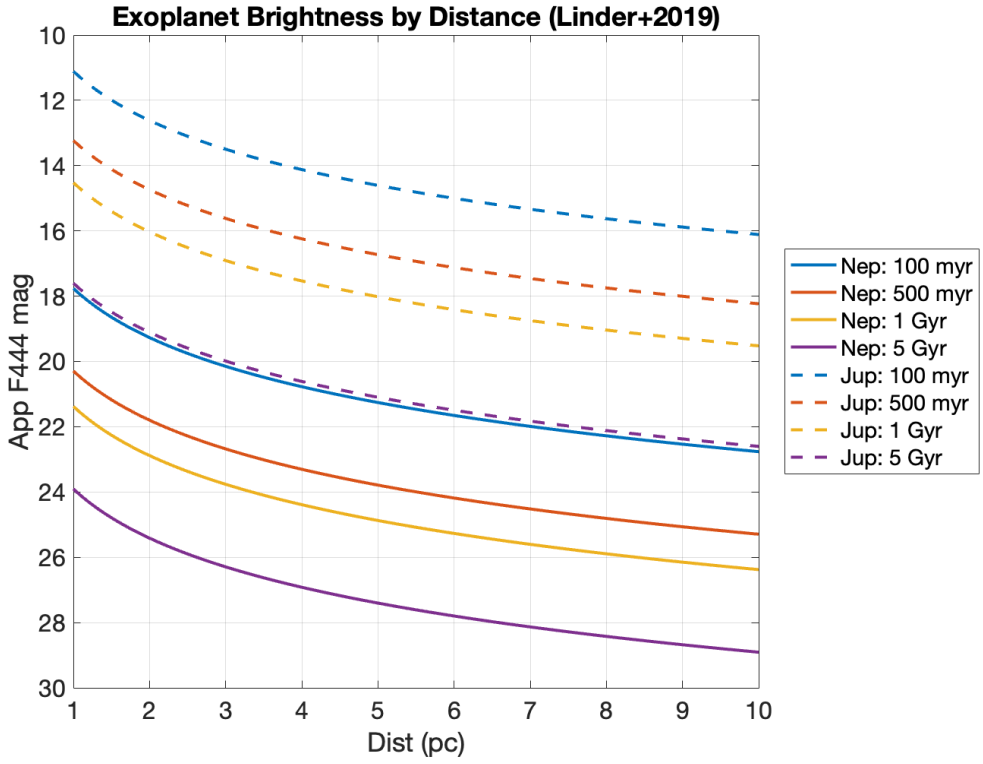

Figure 2.3 **Planet apparent magnitude by distance as estimated by the Models in Linder et al 2019** [146]. The apparent magnitudes are shown in the JWST NIRCam F444 filter (4.44μm), which is similar in wavelength to Keck-NIRC2 M-band (4.6μm). The mass, age, and distance to a system will effect its companion's apparent brightness.

and CORALIE extend beyond a decade of operation, the established long-term baseline allows for the detection of long-period companions ($> 2AU$) that may overlap with the sensitivity space of direct imaging.

Cheetham et al 2018 [58] demonstrated this by leveraging RV data to directly image an ultra-cool brown dwarf, HD 4113C. Based on the the CORALIE survey's detection of long-term RV trends [235], Rickman et al 2019 [205] conducted targeted direct imaging resulting in the discovery of three giant planets and two brown dwarfs. The TRENDS high-contrast imaging survey used long-baseline velocities from Keck-HIRES to target their survey for white dwarf and substellar companions (e.g., [65,66]).

Analyzing radial velocity data to get the data products requires technical expertise, and thus it is hard for newcomers to build their own pipelines. Each RV instrument team tends to develop and maintain their pipeline (or set of pipelines) as a community. Examples of these sorts of pipelines are described in papers include the HARPS-SERVAL pipeline [233], the CARMENES pipeline [202], the HIRES pipeline [45], and more.

Collecting RV data unfortunately becomes complicated for the youngest stars that make the best direct imaging targets. Young stars display high stellar activity which will scatter the RV measurements unless the stellar activity is accounted for through a cross analysis with activity indicators or high-cadence data collection [251].

For those seeking RV data, you may wish to begin by checking the following resources:

- The **Data & Analysis Center for Exoplanets** (DACE) has tools for accessing

public RV data: https://dace.unige.ch/dashboard/

- ***Jump*** is the California Planet Search teams proprietary website for accessing data from Keck-HIRES, the Automated Planet Finder, and select other telescopes. You need special access to search Jump; contact Andrew Howard, Howard Isaccson, or a member of the California Planet Search team to discuss getting access if needed: https://jump.caltech.edu/
- As an alternative to Jump, Paul Butler continues to run a version of the Keck-HIRES data pipeline and releases the data products publicly (with some time delay). As of the time of this writing, they have publicly released the data products through March 2020. The RV data products can be retrieved in a tar file at this address: https://ebps.carnegiescience.edu/data/hireskeck-data
- I started an **ADS library** to collect papers with RV data products. At the time of this writing, there were 6 papers in the *radial velocity bank* library: [14, 45, 81, 202, 208, 233]:

  https://ui.adsabs.harvard.edu/public-libraries/5AGgzppMSD2srEw2sHDCsg

The radial velocity community has many tools to perform orbit fitting once the data products are made. The following is a sample of the RV fitting tools available that may be of interest for helping plan HCI observations:

- The **Data & Analysis Center for Exoplanets** (DACE) has tools for performing RV fits. It is possible to upload your own data and perform custom fits to data that has yet to be released publicly if it is not in the DACE archive. The DACE

fitting tools are excellent for newcomers: https://dace.unige.ch/dashboard/

- `RadVel: The Radial Velocity Fitting Toolkit` is a python package that is the go to fitting tool for the RV community. It perform a maximum-likelihood fit based off of priors given by the user [86]: https://radvel.readthedocs.io/en/latest/
- `orbitize_radvel_utils` is a small piece of python code made by Sarah Blunt that can employ the output of a `radvel` fit to calculate the expected separation on a specified epoch. https://github.com/sblunt/orbitize_radvel_utils/tree/main

- `Show me the orbit` is jupyter notebook made by Sarah Blunt that was created to help users of orbitize visualize their planet's orbit. While not designed for it, the code can be used to help visualize a planets orbit with respect to its RV signal.

2.3.2 Absolute Astrometry

Measuring the position/velocity change of a star can reveal the orbit of unseen companions as they both orbit a common center of mass. The astrometric signal in arcsec (S) caused by a companion is dependant on the mass of the companion (m), the mass of the central star (M), the semimajor axis of the companion's orbit in AU (r), and the distance to the system in pc (d),

$$S = \frac{mr}{Md} \tag{2.3}$$

Thus, massive, nearby, close-in planets orbiting low-mass stars will create the strongest astrometric signal. For reference, the Jupiter-Sun system would create a 1 milliarcsec signal if seen at a distance of 5pc [198], which is achievable with our current instrumentation.

Two space missions have been vital in achieving the necessary astrometric precision to detect giant exoplanets and brown dwarfs. The Hipparcos space satellite was operated by ESA from 1989-1993 to measure the precise locations (median precision 1 milliarcsec) of over 120,000 celestial objects [78]. Twenty years later, ESA launched a successor mission called *Gaia* which has already provided the precise location of more than 1.8 million stars with a precision 100 times better than *Hipparcos* [90, 91]. These missions have been transformative by the unprecedented amount of data provided that can be utilized in nearly all subfeilds of astrophysics.

In 2018, Tim Brandt created a cross-calibrated catalog of the Hipparcos and Gaia astrometry in order to measure the accelerations of the stars across the more than 20 year time baseline between the two missions [37, 38]. This catalog was published under the name *Hipparcos-Gaia Catalog of Accelerations* (HGCA) and was transformative for observers trying to conduct targeted direct imaging observations of exoplanets/brown dwarfs. Figure 2.4 describes the principle behind the HGCA, which uses the proper motion measurements to measure the change in the stars velocity. Nearly all instruments capable of performing high-contrast imaging observations have been used by observers run programs to search out substellar companions by favoring the HGCA accelerators.

For example, the now famous AF Lep b giant planet companion was discovered this way ([71,84,162]; see Figure 2.4, right), along with brown dwarfs companion examples like HD 176535 A [140], HIP 99770 b [67], HIP 39017b [231], HIP 21152 B [26,83,130], HIP 29724 B [26], HD 60584 B [26], and HIP 63734 B [26]. The COPAINS survey reported a detection rate of 6 stellar and 4 substellar detections in 25 targets when relying on the HGCA to help with target selection [26].

Pierre Kervella [121] produced a similar catalog to the HGCA called the *Catalog of Hipparcos-Gaia EDR3 proper motion anomalies*. This catalog can be accessed on VizieR or at `https://sites.lesia.obspm.fr/pierre-kervella/` Kervella also has released a public python script accessible at the same link that can be used to generate the predicted mass as a function of orbital radius of a companion based on its acceleration. This tool makes an excellent option for evaluating the potential mass/separation space of a candidate companion.

Both of the presented catalogs are currently limited to targets which were bright enough to be observed with Hipparcos. Whiting et al 2023 [243] created an extension of the HGCA called the *Gaia Nearby Accelerating Star Catalog* (GNASC) which incorporates machine learning training on the HGCA, the Gaia Data Release 2, and Gaia Early Data Release 3. Because of the use of multiple Gaia data releases, this catalog contains a limited set of nearby accelerating stars that were not part of the original Hipparcos survey.

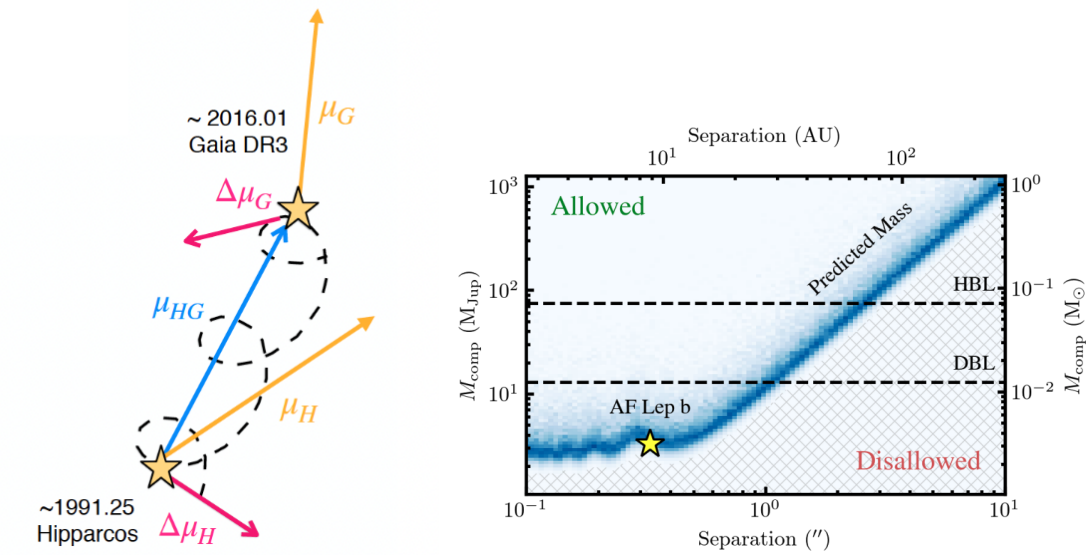

Figure 2.4 **The principle behind the Hipparcos-Gaia catalog of acceleration.** *(Left)* The star's proper motion is measured by both Hipparcos and Gaia, creating two velocity measurements with a 20-30 year baseline. By measuring the difference in these velocities, the local acceleration of the star from an unseen companion can be measured. (*Figure retrieved from Zhang et al 2024 [253]*) *(Right)* Because the acceleration is derived from only two measurements, there is a range of possible masses and orbital periods which could cause the acceleration. An example of this degeneracy for AF Lep is shown as the blue line. AF Lep b was discovered to be in the giant planet portion of this degeneracy (*Figure retrieved from Franson et al 2023 [84]*).

In the upcoming Data Release 4, Gaia will release its time series data. This will enable the discovery of exoplanets using astrometry without the limits of the cross-calibration with Hipparcos. It is expected to discover approximately 20,000 high-mass $(1-15M_{jup})$ long-period planets within 500pc using high-precision stellar astrometry using data from five years of operation [186].

Software tools that allow direct imagers to incorporate the HGCA into their observing planning are discussed in the orbit fitting section, Section 2.5.2.

2.3.3 Transits

He et al 2023 [105] found that Kepler transiting systems with at least three small inner transiting planets (< 1AU) that showed highly irregular spacing have a correlation with the presence of an outer giant planet $(50M_e \leq M_p \sin(i) \leq 13M_{Jup}$. The outer giant planets in their sample were sourced from the Kepler Giant Planet Search catalog which were found using radial velocity. While irregular spacing indicated the presence of a giant planet, not all giant planets caused irregular spacing in the inner planets.

The authors quantify the spacing between the transiting planets using a term called "gap complexity." They define high gap complexity as $C > 0.32$ and calculated the quantity using Equations 13 & 14 (and the values of C_{max} from Table 2) from Gilbert & Fabrycky 2020 [97]. Figure 2.5 shows the system architecture of the Kepler planets used to identify this correlation in He et al 2023 [105].

While there is promise in this method of tailoring, there have not been any attempts to employ gap complexity to curate a direct imaging search for outer giant planets as far as I can find published. This may not have been attempted yet because many of the currently discovered transiting exoplanet systems are from the Kepler survey and are located hundreds of parsecs from us. This distance makes even the youngest targets unobtainable to detect a giant planet with our current instrumentation. As TESS continues to reveal transiting exoplanets around nearby stars, there may emerge a few young TESS systems that are good candidates for detecting gas giant exoplanets with deep high-contrast imaging.

2.4 Observing Strategies and Tools

2.4.1 Differential imaging

To boost our ability to separate the light from star and companion, high-contrast imaging surveys typically employ one or more differential imaging strategies. These techniques work by establishing a set of images where the stellar PSFs remain the same while something about the the companion's PSF changes. The images can then be differences against to remove the stellar contribution and reveal the companion. The two most common differential imaging strategies employed are angular differential imaging (ADI) and reference differential imaging (RDI).

In angular differential imaging, the companion will appear at different angles around

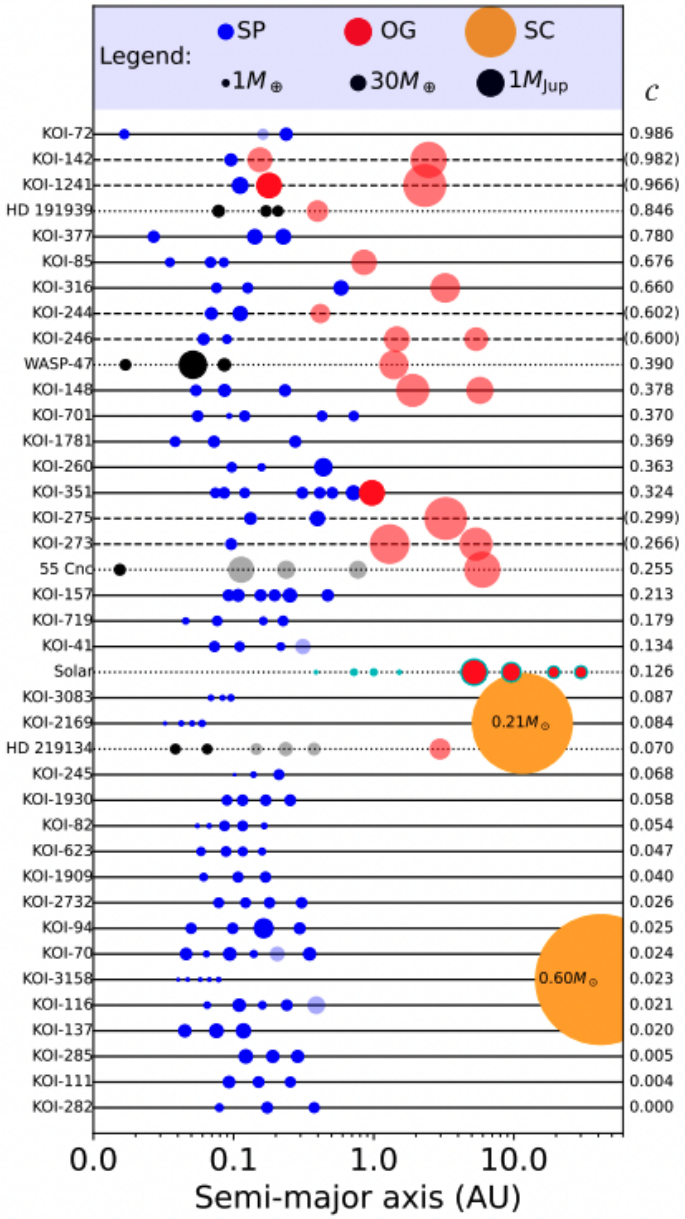

Figure 2.5 **Example of the correlation between transiting planets with irregular spacing and outer giant planets.** High "gap complexity" ($C > 0.32$) can be used as a predictor of an outer giant planet existing in the system. This figure and prediction was created by He et al 2023 [105] using the Kepler sample.

the stellar PSF. From the ground, this is typically done by locking the vertical angle of the telescope so the sky appears to rotate across the night. The most angle change will occur when the target is crossing the meridian, when the greatest change in parallatic angle is occurring. To use ADI with space telescopes, the spacecraft must perform extra rolls. Figure 2.6 show an overview of the steps performed in an ADI analysis.

In reference differential imaging, a set of reference stars similar to the science target is observed under the same conditions. The PSFs of the references stars are normalized and then subtracted from the science images to reveal the companion. The stellar PSFs must be stable to perform this technique, so RDI is often best utilized by space telescopes where the conditions are changing on slower timescales.

2.4.2 Instruments used by the exoplaent direct imaging community

Table 2.1 lists the adaptive optics enabled imaging instruments currently available to the high-contrast imaging community. This table leaves off decommissioned and upcoming instruments.

The Gemini Planet Imager (GPI) was operating on Gemini South from 2014 - 2019. GPI 2.0 will soon be commissioned on Gemini North.

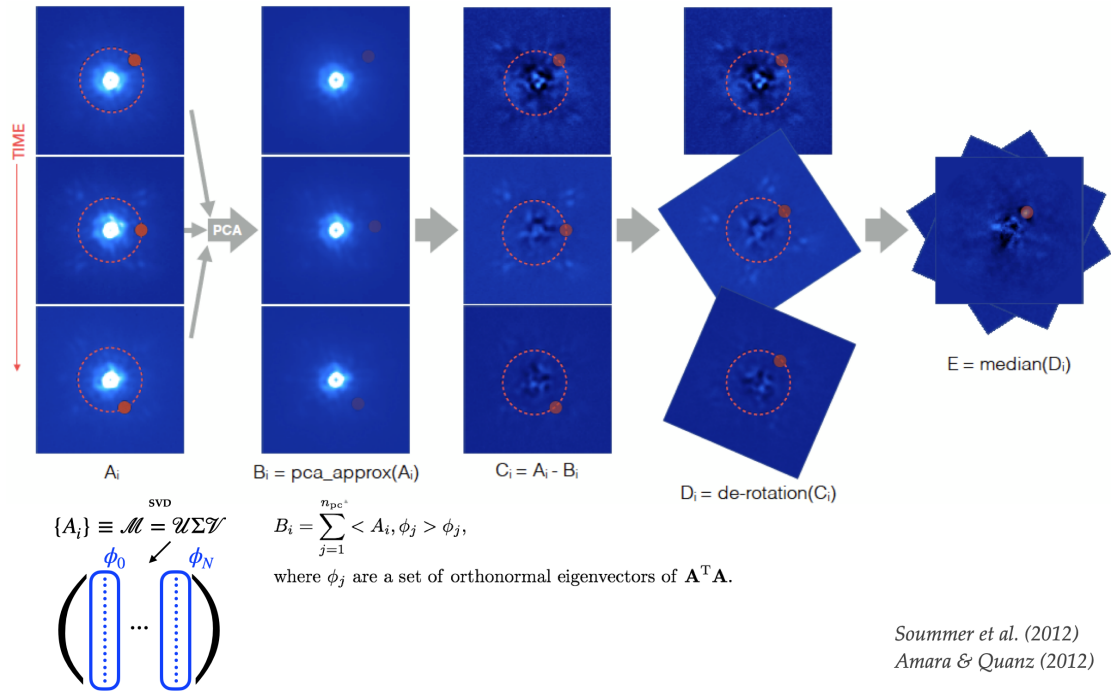

Figure 2.6 **Steps of conducting the angular differential imaging analysis using principle component analysis.** A PCA library is built and then used to subract the contribution of the stellar PSF. The images are then derotated and stacked to reveal the companion. *This figure was retrieved from the VIP tutorial website.*

Table 2.1 **Instruments used by the HCI community that are on sky at time of writing**

Instrument	Telescope	Wavelength (m)	Operations Start
NaCo	VLT	1–5	2002
ALTAIR-NIRI	Gemini N.	1.1–2.5	2003
NIRC2	Keck	1–5	2004
PALM-3000	Palomar 200"	1.1–1.65	2009
LMIRCam	LBT	3–5	2012
SPHERE	VLT	0.5–2.3	2014
SCExAO / VAMPIRES	Subaru	0.5–2.2	2015
MagAO-X	Magellan Clay	0.6-1	2019
NirCAM / MIRI	JWST	0.6 - 25.5	2022

This table was adapted from Milli et al 2016 [165]

2.5 Analysis tools available

2.5.1 Image processing

A vital part of high-contrast imaging analysis involves incorporating a strategy to remove the signal from the host star which is orders of magnitude brighter than the companion. Two open-source code packages are currently availbile to the community to perform the PSF post-processing and subtraction needed: the `Vortex Image Processing (VIP)` and `pyKLIP`. Both can utilize principal component analysis to run the PSF subtraction.

`VIP`[6] [100] is a python package dedicated to high-contrast imaging analysis. It was built originally to analyze ground-based ADI observations with the vortex coronagraph in the optical train. It is capable of performing PSF subtraction using a variety of algorithms (pairwise frame difference, full frame PCA [4, 223], annular PCA, non-negative matrix

[6]VIP: `https://vip.readthedocs.io/en/v1.4.0/`

factorization [101, 201], LLSG [99], ect) on images both with and without a coronagraph in place. `VIP` also has a set of metrics tools which can calculate contrast curves, measure the signal-to-noise ratio of a detection, and automated source detection.

`PyKLIP`[7] [241] is a python implementation of the Karhunen-Loève Image Projection (KLIP) algorithm. It has many of the same metric and PCA subtraction features as `VIP` in addition to a characterization module to measure the photometry and astrometry of a detected source. `PyKLIP` is built to support data from multiple instruments including P1640, GPI, SPHERE, CHARIS, MagAO/VisAO, Keck-NIRC2. `SpaceKLIP`[8] [48, 120] uses the `pyKLIP` code as a base to provide a data reduction pipeline for JWST NIRCam and MIRI.

2.5.2 Orbit fitting

Three software tools are available that can be used to fit an exoplanet's orbit: `orbitize!`, `orvara`, and `octofitter`. These three packages are compatible with radial velocity data, the Hipparcos-Gaia Catalog of Accelerations from astrometric measurements, and/or relative astrometry of the companion from direct imaging. They can be used to explore targets of interest for HCI followup or be used after a detection is made of the companion to measure the dynamical mass and improve the orbit fit.

The development of the `orbitize!` python package[9] [24] is led by Sarah Blunt. It

[7] PyKLIP: `https://pyklip.readthedocs.io/en/latest/index.html`
[8] spaceKLIP: `https://github.com/kammerje/spaceKLIP`
[9] orbitize!: `https://orbitize.readthedocs.io/en/latest/`

was originally designed to fit the orbits of directly imaged exoplanets, and is capable of doing so through an MCMC or the Orbits for the Impatient algorithm. `Orbitize!` has a reputation for being friendly for new users and is viewed by the community as a robust and versatile orbit fitter. As of the writing of this thesis, it has been cited in more than 80 papers. For new users installing both python and `orbtize!`, I recommend following the instructions listed on the Code/Astro webpage. `Orbtize!` makes an excellent choice of package for conducting final orbit fits for publication.

The `Orbits from Radial Velocity, Absolute, and/or Relative Astrometry` (orvara) python package[10] was created by Tim Brandt to run orbit fits with a combination of data sources quickly. It was the first orbit fitting package to integrate in the acceleration information from the HGCA and has tools for the direct imaging community that plot a likelihood map of the planet's predicted location at a given epoch. Its underbelly is written in C, and installations of `orvara` can be tricky pending your operating system. The best application for `orvara` is for fitting a large number of targets with limited data before observations are made in order to curate your target list.

`Octofitter`[11] is a Julia package written by William Thompson and is the newest of the three packages presented here. It can use RV and HGCA acceleration data to increase the SNR of direct imaging observations. It can be used even if there are no planets detected in a single epoch of direct imaging observations, and so this tool is particularly valuable for finding faint companions with multi-epoch HCI observations. Because of its

[10] `orvara`:`https://github.com/t-brandt/orvara`
[11] `Octofitter`: `https://github.com/sefffal/Octofitter.jl`

implementation in Julia, `octofitter` is fast to converge. It has been shown to run in approximately 1/10 of the time of `orvara` and 1/100 of the time of `orbitize!`.

One software tool has been released that can be used to determine if a detection is a physically associated companion or is a background object. The `backtracks` python package[12] can accept a list of relative positions of the candidate source around the host and fit a stationary, infinite distance background track.

2.5.3 Quantifying the survey sensitivity

Quantifying the survey sensitivity of your observations is necessary in order to make occurrence rate measurements. The standard way to measure the survey sensitivity is to run an injection-recovery test, where fake signals of a specific masses/separations are injected into the dataset and the fitter attempts to recover it.

The `Exoplanet Detection Map Calculator (Exo-DMC)`[13] was built by Mariangela Bonavita to help observers calculate the survey sensitivity of direct imaging observations/surveys. It is a variation on the Multi-purpose Exoplanet Simulation System (MESS) code [25]. The user inputs a contrast curve specified in separation (AU) versus the planet mass detectable (must assume an age and evolutionary cooling model).An example of a survey sensitivity map created with `Exo-DMC` can be found in the next Chapter, Figure 3.7.

[12] `backtracks`:`https://github.com/wbalmer/backtracks`
[13] Exo-DMC: `https://github.com/mbonav/Exo_DMC?tab=readme-ov-file`

`RVSearch`[14] can be used to calculate the survey sensitivity of an RV dataset. `RVSearch` is a planet search pipeline based on `RadVel` and was built by the California Planet Search team. An example of a survey completeness map created with `RVSearch` can be found in the next Chapter, Figure 3.9).

The unreleased `Mess3` [72] package can be used to calculate the survey sensitivity given the combination of RV data, HGCA astrometry, and high-contrast imaging data. This tool would be ideally suited for working with multiple data sources should it be released publicly.

2.6 Summary

An opportunity has been unlocked for the field of exoplanet direct imaging thanks to the growing abundance of data collected from all exoplanet detection methods. Over the past decade, the community is growing the set of tools available that can help observers curate their high-contrast imaging observations to accomplish new scientific aims. In overview, the basic steps of using this targeted direct imaging strategy is the following:

1. Collect the supplemental data of your choice that you would like to apply.
2. Apply the supplemental data to make predictions for the planetary architecture of each system by conducting orbit fitting, making planetary mass/brightness predictions, etc. This step may involve building new software if some is not publicly available for your needs.

[14] RVSearch: `https://california-planet-search.github.io/rvsearch/`

3. Make a set of predicted contrast curves for the instrument/modes you intend to use. Compare the brightness and separation estimates of your targets to the contrast curve to check their potential observability.
4. Select the targets of interest for your science case, the instrument, observing mode, and timing that would be the most likely to yield a detection.
5. Write your proposals and observe!
6. Conduct your analysis to reveal a companion or set limits from the non-detection.

There are a variety of software tools that can be used to help conduct targeted direct imaging across all steps:

- Estimating planet brightness from evolutionary models: `species`
- Using RV data: DACE, `RadVel`, supporting code in `orbitize!`, `RVSearch`
- Using Gaia-Hipparcos astrometric accelerations: Pierre Kervella's PMa_sensitivity plotter, `orvara`
- Companion Orbit fitting/combining multiple data types: `orbitize!`, `orvara`, `octofitter`
- Background star vetting orbit fitting: `backtracks`
- High-contrast imaging processing: `VIP`, `pyKLIP/SpaceKLIP`
- Estimating Survey Completeness: `Exo-DMC`, `RVSearch`, `Mess3`

Chapter 3

Current performance and limitations: Hunting for companions in the fifth-closest system using combined high-contrast imaging and radial velocity analysis.

"Starfleet reports it has engaged the Borg at Wolf 359"

ADAPTED FROM

A Wolf 359 in Sheep's Clothing: Hunting for Substellar Companions in the Fifth-closest System Using Combined High-contrast Imaging and Radial Velocity Analysis.

Rachel Bowens-Rubin, Joseph M. Akana Murphy, Philip M. Hinz, Mary Anne

Limbach, Andreas Seifahrt, Rocio Kiman, Maissa Salama, Sagnick Mukherjee, Madison Brady, Aarynn L. Carter, Rebecca Jensen-Clem, Maaike A. M. van Kooten, Howard Isaacson, Molly Kosiarek, Jacob L. Bean, David Kasper, Rafael Luque, Gudmundur Stefansson, and Julian Sturmer.

Astronomical Journal, 166(6):260, December 2023

3.1 Abstract

Wolf 359 (*CN Leo, GJ 406, Gaia DR3 3864972938605115520*) is a low-mass star in the fifth-closest neighboring system (2.41 pc). Because of its relative youth and proximity, Wolf 359 offers a unique opportunity to study substellar companions around M stars using infrared high-contrast imaging and radial velocity monitoring. We present the results of Ms-band (4.67 μm) vector vortex coronagraphic imaging using Keck-NIRC2 and add 12 Keck-HIRES velocities and 68 MAROON-X velocities to the radial velocity baseline. Our analysis incorporates these data alongside literature radial velocities from CARMENES, HARPS, and Keck-HIRES to rule out the existence of a close ($a < 10$ AU) stellar or brown dwarf companion and the majority of large gas-giant companions. Our survey does not refute or confirm the long-period radial velocity candidate, Wolf 359 b ($P \sim 2900$ d) but rules out the candidate's existence as a large gas-giant ($> 4M_{jup}$) assuming an age of younger than 1 Gyr. We discuss the performance of our high-contrast imaging survey to aid future observers using Keck-NIRC2 in conjunction with the vortex coronagraph in the Ms-band and conclude by exploring the direct imaging capabilities

with JWST to observe Jupiter-mass and Neptune-mass planets around Wolf 359.

3.2 Introduction

Over 70% of the stars in our galaxy are M-dwarfs, yet we know little about the exoplanets that exist in these systems beyond the snow line ($\geq$0.5 AU, [173]). Most exoplanet detection methods and surveys are blind to this discovery space. The geometric probability of an exoplanet transit occurring for an exoplanet orbiting an M-dwarf beyond 1 AU is less than 0.1%. Astrometry and radial velocity surveys of M-dwarfs require lengthy baselines in order to observe a planet's full orbit because planets orbiting low-mass stars have longer periods for an equivalent separation.

Microlensing surveys have provided the first hint that cold gas giants, ice giants, and super-Earths could be common outside the snow line of M-dwarfs with increasing prevalence for smaller planets. A survey from [53] estimated that the majority of low-mass stars host a giant planet between 0.5–10 AU, with Jupiter-like planets ($0.3-10\ M_{\rm Jup}$) at an occurrence rate of 17^{+6}_{-9}%, Neptune-like planets ($10-30\ M_{\oplus}$) with a rate of 52^{+22}_{-29}%, and super-Earths ($5-10\ M_{\oplus}$) with a rate of 62^{+35}_{-37}%. A microlensing survey by the Microlensing Observations in Astrophysics collaboration is consistent with these results and concluded that Neptune-sized planets are one of the most common types of planet seen outside the snow line [230]. Poleski et al. 2021 [189] used data from the Optical Gravitational Lensing Experiment to determine that nearly every star could host an

ice-giant planet from 5-15 AU, measuring an occurrence rate of $1.4^{+0.9}_{-0.6}$ ice giants per system.

Exoplanet direct imaging—where photons from an exoplanet are spatially resolved from their host star—is the only exoplanet detection technique that offers a pathway for characterizing the atmosphere, composition, and formation history for exoplanets orbiting beyond the snow line that are unlikely to transit. When directly imaging the closest set of stellar neighbors ($d < 5$ pc), the current generation of high-contrast imaging systems on 8–10 m telescopes can probe comparatively colder planets at angular separations corresponding to where the prevalence of exoplanets outside the snow line is expected to peak (1–10 AU; [80]). Proximity in stellar distance makes companions appear at proportionally wider separation angles from their host star for a given orbit ($\theta_{\rm sep} \propto a/d$) and boosts the apparent magnitude of the companion logarithmically ($m = 5\log_{10}(d/10$ pc$) + M$). This makes companions that are dimmer in absolute magnitude and closer in orbital separation easier to detect than if they were in a more distant analogous system.

The heritage of detecting exoplanets via the direct imaging technique has been to conduct blind surveys of hundreds of young-star systems in search of a rare set of large gas giant planets on long-period orbits that are bright enough to detect using short integration times. Thanks to the growing abundance of long-baseline exoplanet radial velocity (RV) data (e.g., [202,208,233]), we can now use RV data in tandem with high-contrast imaging (HCI) observations to tailor our imaging observations to conduct lengthier measurements around fewer systems. Information from RV data can be applied to select viable targets

for imaging, choose the optimal imaging filters, predict how much integration time is required, and predict when a companion will be at its maximum separation from its host star. This targeted approach to HCI observing motivates the use of extended observing sequences which can expand our abilities to directly image colder ($< 500\,\mathrm{K}$) companions.

In many cases, we only need a hint to a companion's existence to curate an HCI observation using RV data. Cheetham et al. 2018 [58] demonstrated this by leveraging RV data to directly image an ultra-cool brown dwarf, HD 4113C. Based on the the CORALIE survey's detection of long-term RV trends [235], Rickman et al 2019 [205] conducted targeted direct imaging resulting in the discovery of three giant planets and two brown dwarfs. The TRENDS high-contrast imaging survey used long-baseline velocities from Keck-HIRES to target their survey for white dwarf and substellar companions (e.g., [65], [66]). Hinkley et al. 2022 [107] used the VLTI/GRAVITY instrument to discover HD 206893 c by utilizing long-baseline RV data from European Southern Observatory's High Accuracy Radial velocity Planet Searcher (HARPS, [159]; [184]) and correlating it with the *Gaia-Hipparcos* astrometry accelerations ([37]) and orbital astrometry of the system's outer companion.

Conducting targeted HCI observations of nearby systems that span multiple nights is becoming an increasingly common observing strategy to probe for sub-Jupiter mass exoplanets. The surveys from Mawet et al. 2019 [158] and Llop-Sayson et al. 2021 [147] completed multi-night HCI campaigns of the nearby, youthful ε Eridani system ($d = 3.22$ pc, age $= 600 \pm 200$ Myr) with the goal of directly detecting the RV-discovered exoplanet,

ε Eridani b. Combined, the 2017 and 2019 surveys collected nearly 16 hours of 4.67μm imaging data over nine nights using the W. M. Keck Observatory's NIRC2 Imager [245] but were not able to make an imaging detection of the planet. By combining the mass upper-limits from HCI with RV and *Gaia* accelerations, [147] constrained the mass of ε Eridani b to be in the sub-Jupiter mass domain, $0.66^{+0.12}_{-0.09}$ $M_{\rm Jup}$. [239] also demonstrated the advantage of searching for companions around nearby stars by performing a 100 hr HCI survey at 10–12.5 μm of the α Centauri system ($d = 1.3$ pc, age $= 5.3 \pm 0.3$ Gyr). They imaged one candidate and demonstrated that it was possible to achieve survey sensitivities down to warm sub-Neptune mass planets through the majority of the α Centari habitable zone. While these surveys were not able to make definitive direct detections, they demonstrated the possibilities of future ground-based mid-infrared HCI campaigns of nearby stars.

3.2.1 The Wolf 359 System

Wolf 359 is a solar-metallicty M6V star [188] and one of our nearest stellar neighbors[1] (2.41 pc; [91]). Table 3.1 summarizes Wolf 359's stellar parameters.

Radial velocity surveys have been monitoring Wolf 359 for more than two decades. A preprint paper presented by [234] identified two exoplanet candidates orbiting Wolf 359 using 63 RV measurements from Keck-HIRES and HARPS spanning 13 years. These planet candidates are summarized in Table 3.2. The shorter-period candidate (Wolf

[1] As one of our nearest neighbors, this system has captured the public's interest and is a setting in many fictional stories including the Wolf 359 podcast and several episodes in the *Star Trek* franchise.

359 c) was refuted by [132] after determining that the RV signal matched the star's rotation period. The RV signal for the Wolf 359 b candidate could correspond to a cold, Neptune-like exoplanet on a wide orbit of approximately 8 years [234] (P_{orb} = 2938 ± 436 d, $a = 1.845^{+0.289}_{-0.258}$ AU).

Wolf 359 has conflicting age estimates in the literature, but most indicate that the star is young (< 1 Gyr). The star is highly active, with stellar flares that occur approximately once every 2 hr [145]. Wolf 359 has strong flare activity even among flaring M dwarfs [144], which is consistent with a youthful age estimate. An age estimate by Pavlenko et al. 2006 [182] made by modeling the spectral energy distribution predicts that Wolf 359 could be as young as $100 - 350$ Myr, which is consistent with its high activity. Wolf 359 also has a fast rotation period ($P_{\rm rot} = 2.705 \pm 0.007$; [103]), as confirmed with photometry from *K2* [112], among other observatories. The combination of the gyrochronological relationship from Engle et al. 2018 [76] and Wolf 359's stellar rotation period suggests an age estimate of < 500 Myr. However, the star lies at the edge of the Engle rotation–activity–age relationship for M0-6 stars, and the rotation period cannot act as a direct proxy for age in this system in this context.

The combination of Wolf 359's proximity and potential youth make it an ideal system for searching for companions using infrared direct imaging. An exoplanet candidate like Wolf 359 b would not be possible to directly image around most star systems. However, because Wolf 359 is one of our nearest neighbors, the parameters of the Wolf 359 b candidate can be constrained using our current generation of HCI instruments operating

Table 3.1 **Properties of Wolf 359**

Property	Value
RA J2000	10 56 28.92 $^{(a)}$
DEC J2000	+07 00 53.00 $^{(a)}$
Distance	2.4086 ± 0.0004 pc $^{(a)}$
Parallax	415.18 ± 0.07 mas $^{(a)}$
Spectral Type	solar-metallicity M6 $^{(b)}$
Mass	0.110 ± 0.003 $M_{\odot}$ $^{(c)}$
Teff	2749^{+44}_{-41} K $^{(c)}$
Radius	0.144 ± 0.004 $M_{\odot}$ $^{(c)}$
log(g)	5.5 cgs $^{(d)}$
V mag	13.5 $^{(e)}$
R mag	11.684 $^{(e)}$
H mag	6.482 $^{(f)}$
MKO Ms mag	5.85 ± 0.06 $^{(g)}$
Rotation Period	2.705 ± 0.007 d $^{(h)}$
Age range	100 Myr–1.5 Gyr $^{(f)}$

(a) GaiaDR3 [91]; *(b)* Kesseli et al. 2019 [122]; *(c)* Pineda et al. 2021 [188]; *(d)* Fuhrmeister et al. 2005 [85]; *(e)* Landolt et al. 2009 [136]; *(f)* Cutri et al. 2003 [69]; *(g)* Leggett et al. 2010 [138]; *(h)* Guinan et al. 2018 [103]; *(f)* The lower estimate is from Pavlenko et al. 2006 [182] and the upper estimate is from the kinematic age estimated in Section 3.4.1 of this work.

at 8-10 m telescopes.

3.3 Observations and Data Reduction

3.3.1 Keck-II NIRC2 Vortex Coronagraphy

We conducted high-contrast imaging observations of the Wolf 359 system with the W.M. Keck Observatory NIRC2 imager coupled with the vector vortex coronagraph [216]. We completed our observations over three nights, as summarized in Table 3.3.

Table 3.2. **Exoplanet Candidates Identified by Tuomi et al. 2019** [234]

Candidate	Period (d)	$m \sin i (M_\oplus)$	a (AU)	Status	Note
Wolf 359 b	2938 ± 436	$43.9^{+29.5}_{-23.9}$	$1.845^{+0.289}_{-0.258}$	possible cold-Neptune	investigated in this work
Wolf 359 c	$2.6869^{+0.0004}_{-0.0003}$	$3.8^{+2.0}_{-1.6}$	0.018 ± 0.002	false positive†	RV signal is due to star rotation

† Wolf 359 c was refuted by Lafarga et al. 2021 [132].

We conducted HCI observations using the fixedhex pupil stop with Keck's L/M-band vortex coronagraph. The telescope was operated in the vertical angle rotation mode (Sky PA = 4.43°) to enable angular differential imaging (ADI) analysis methods. The centering of the vortex was controlled using the in-house QACTIS IDL software package [113]. Each QACITS sequence consisted of a set of (1) three calibration images to acquire an off-axis star PSF and sky images, (2) three optimization images to center the star on the vortex and stabilize the tip/tilt in the adaptive optics system, (3) a series of science images.

We operated the Keck-II adaptive optics system with the recently commissioned near-infrared pyramid wavefront sensor (PyWFS) [28] in natural guide star mode. We selected the PyWFS over the facility Shack–Hartmann wavefront sensor because it is better suited for performing adaptive optics corrections when using an M-dwarf as a natural guide star because it operates in H-band (1.633μm, NIRC2 Filters) rather than R-band (0.641

μm, [19]). Wolf 359 is 5.2 magnitudes brighter in the H-band versus R-band [69, 136], thus we were able to take advantage of the improved AO quality with the significantly more flux available for wavefront correction.

Our HCI survey spanned three nights in 2021: February 22, February 23, and March 31 (UT). We collected images using the Ms filter (4.670μm, NIRC2 Filters) with NIRC2 operated in narrow mode. The science images had a frame size of of 512 x 512 pixels (5.090"x5.090"; pixel scale = 0.009942 $\pm$ 0.00005 arcsec/pixel, Keck General Specs). The frames were taken with an integration time of 0.3 s with 90 coadds. We obtained a total of 664 science frames over 14 QACTIS sequences, totaling 4.98 hr of science integration time.

We performed our data reduction using the *VIP: Vortex Imaging Processing* python package (`VIP`); [100]). We pre-processed the NIRC2 data for bad pixels, flat-field correction, and sky background correction using the automated pipeline described in Xuan et al. 2018 [248] using `VIP version 0.9.9`. Sky subtraction was completed using the PCA-based approached described in Hunziker et al. 2018 [115] using `VIP` version 1.3.0. After pre-processing the science images, we removed 5% of the lowest-quality science frames using `VIP`'s Pearson correlation bad-frame detection from each night.

To establish an anchor for our reported contrast, we measured the flux of Wolf 359 using the unobstructed PSF images taken at the start of the QACTIS sequence. We created a PSF template by combining and then normalizing the 14 PSF images taken on 2021

March 31 (UT). The PSF frames were collected using an integration time per coadd of 0.015s with 100 coadds. We performed the stellar photometry using the `fit_2dgaussian` function, as outlined in the `VIP` tutorial. We measured the full width half max of the NIRC2 Ms PSF to be $FWHM = 9.67$ pixel (0.0962).

We created the final reduced image using the combined image set from the three nights with the 631 images that passed bad-frame detection. We applied a highpass filter to each individual image using a `VIP`'s Gaussian highpass filter with size 2.25 $FWHM$. The images were then derotated using the parallactic angle and median combined. We subtracted the stellar point spread function (PSF) using full-frame angular differential imaging principle component analysis (PCA) using `VIP`'s `pca` module (following the methods of Soummer et al. 2012 [223] and Amara et al. 2012 [4]). We performed PCA optimization by injecting a fake companion 100 pixels from the star to determine the number of principle components that yielded the max signal-to-noise of the fake companion. The three-night combined image set had an optimal number of principal components of PC = 18 (PC = 4 when highpass filtering was applied). While performing PCA stellar point spread subtraction, we adopted a center masking of 2 $FWHM$ and a parallactic exclusion angle the size of 1 $FWHM$. The final reduced image from the highpass-filtered three-night combined image set is shown in Figure 3.1 along with its accompanying signal-to-noise threshold map. We detected no point source signals above a 2σ threshold using VIP's built in detection function in log mode. We thus conclude that we did not detect any companions in the direct imaging portion of this survey.

We calculated contrast curves using `VIP`'s `contrast_curve` function, which calculates the $\sigma * noise/throughput$ using fake planet injection with a student-t distribution correction. We found that applying a highpass filter had little affect on our final sensitivity, so our contrast curves are reported using the images with no applied high-pass filtering. The combined-night contrast curve was calculated by first processing the sensitivity by separation for each night separately. The combined-nights sensitivity was then calculated using a weighted variance at each separation, $\sigma_{comb}(sep) = \sqrt{1/(\sigma_{n1}(sep)^{-2} + \sigma_{n2}(sep)^{-2} + \sigma_{n3}(sep)^{-2})}$. The overall sensitivity of the HCI survey of Wolf 359 is plotted in Figure 3.2.

3.3.2 Radial Velocity Observations

3.3.2.1 Keck-HIRES

We present an additional 12 Keck-HIRES high-precision RV measurements gathered by the California Planet Search (CPS) team between Dec 25 2017 and Jan 13 2022 (UT). The Keck-HIRES velocities are available online in a machine readable format in Bowens-Rubin et al 2023 [31]. These measurements extend the baseline of the Keck-HIRES post-2004 velocities to over 17 years when combined with the 40 Keck-HIRES RVs included in [234]. The new Keck-HIRES exposures were collected with the C2 decker (14"x0.86", R = 45,000) and had a median integration time of 1800 s, corresponding to a median SNR of 65 pix^{-1} at 5500 Å.

Observations were taken with a warm (50° C) cell of molecular iodine at the entrance

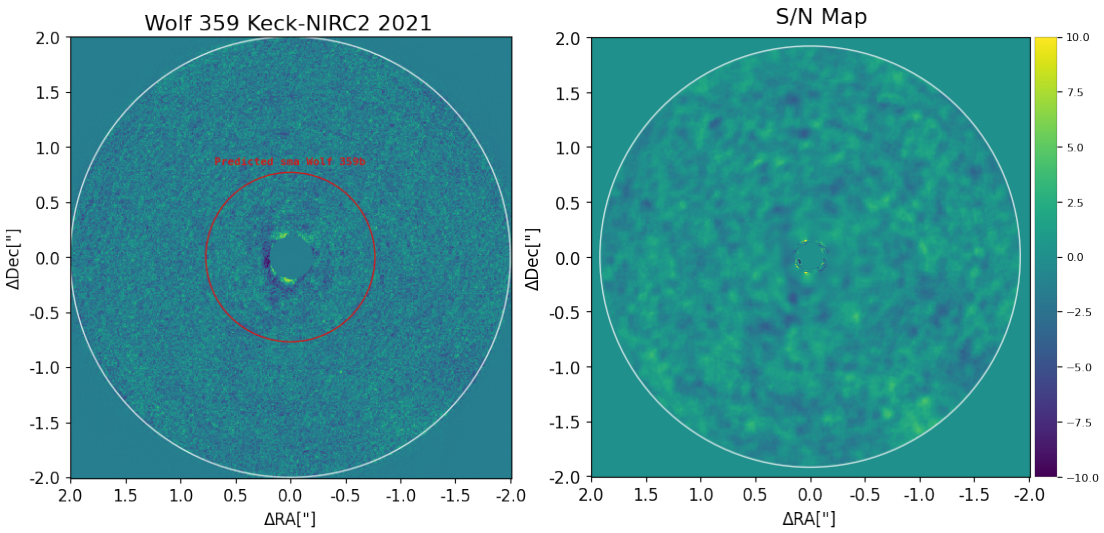

(a) The final reduced image

(b) SNR Map

Figure 3.1 **Final reduced image of the Wolf 359 system from the Keck-NIRC2 high-contrast imaging survey**: Our final reduced image of the Wolf 359 system was created using the the highpass-filtered three-night combined image cube. The corresponding S/N map is shown in (b). The red circle shown in (a) corresponds to the predicted semi-major axis of the Wolf 359 b candidate. The stellar PSF was subtracted using full-frame PCA with `VIP`. No companion-like point sources were detected to more than 2σ above the background using `VIP`'s built-in detection function.

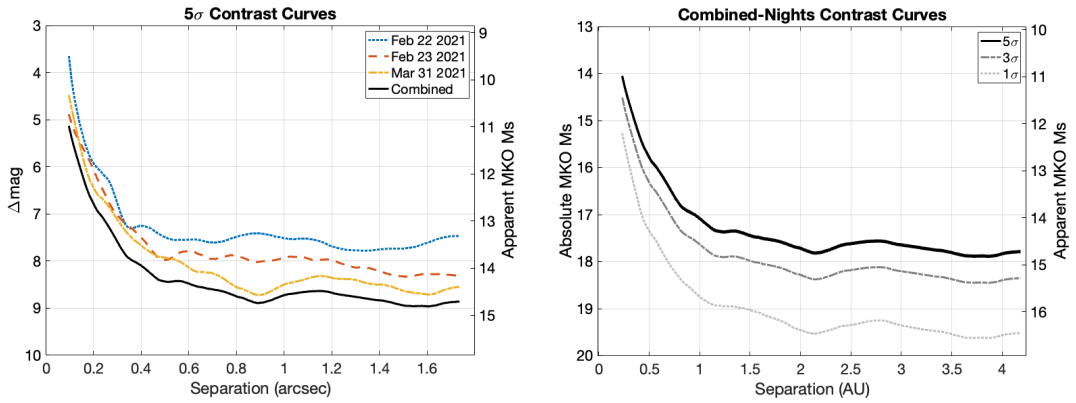

(a) 5σ contrast curves by observing night with the combined-image contrast

(b) The planet sensitivity of the 3-night combined survey

Figure 3.2 **Contrast curves from the Keck-NIRC2 imaging survey**: The contrast curves were created using the fullframe PCA algorithm in `VIP` with the images that were not highpass filtered. The solid black line represents the 5σ sensitivity achieved with the combined-nights cube.

Table 3.3 **High-Contrast Imaging Keck-NIRC2 Observing Summary**

Date (UT)	# **Frames**	**Total Int Time (hr)**	**PA Change**	**PWV opacity**	**Opt. PC full fr.**	$5\sigma\Delta Mag$ **0.2"**	$5\sigma\Delta Mag$ **0.98"**	$5\sigma\Delta Mag$ **1.7"**
2021 Feb 22	181	1.36	77.35°	0.08-0.20	8	6.0	7.3	7.5
2021 Feb 23	200	1.50	76.88°	0.06-0.10	28	6.1	7.5	8.3
2021 Mar 31	283	2.12	126.29°	0.10-0.16	14	6.4	7.7	8.6
Combined Nights	664	4.98	–	–	18	6.8	8.2	8.9

All science images were collected using the MKO Ms filter, $tint = 0.3s$, $coadd = 90$, and $subframesize = 512 \times 512$ with NIRC2 in narrow mode. The precipitable water vapor opacity was measured at 225 GHz by the Submillimeter Array and retrieved at `http://www.eao.hawaii.edu/weather/opacity/mk/archive/`. The optimal PC and 5σ contrast is reported for the image sets with no highpass filter applied. To convert the listed ΔMag to MKO Ms apparent magnitude, add 5.85.

slit [43] and RVs were determined following the procedures of Howard et al. 2010 [111]. The superposition of the iodine absorption lines on the stellar spectrum provides both a fiducial wavelength solution and a precise, observation-specific characterization of the instrument's PSF. Each RV spectrum was then modeled as the product of the deconvolved template spectrum and the FTS molecular iodine spectrum which is convolved with the point-spread function. The chi-squared value of this model is minimized with the RV (Z) as one of the free parameters.

Radial velocities computed via the iodine cell method require a high-SNR iodine-free "template" of the stellar spectrum. Ideally, CPS aims for template spectra to have an SNR of about 200 pix^{-1} at 5500 Å in order to properly deconvolve the spectrum with the instrument's PSF, which is measured by observing rapidly rotating B stars immediately before and after the template exposure(s). In the case of Wolf 359, CPS acquired three consecutive iodine-free exposures of the star on 2005 Feb 27 with the B1 decker (3.5"×0.574," R = 60,000). Each observation had an exposure time of 400 s corresponding to a combined SNR of 40 pix^{-1} at 5500 Å. Because Wolf 359 is relatively faint in V-band (V = 13.5 mag [136]), high SNR Keck-HIRES exposures quickly become prohibitively expensive (SNR of $\sim$ 100 pix^{-1} would take well over an hour of integration). Rather than attempt to acquire another, higher SNR template of Wolf 359, we searched for a best-match template from a library of over 300 stars with high-SNR, iodine-free Keck-HIRES spectra and bracketing B star observations following the methods of [70]. Recomputing the RVs using the best-match template that we identified increased the

RV errors by a factor of ~ 2, so we chose to continue to use the original CPS template. The poor match might be a consequence of Wolf 359's late spectral type—the library from Dalba et al 2020 [70] contains stars with $T_{\rm eff} > 3000$ K. Using the CPS template, RVs taken before the Keck-HIRES detector upgrade in 2004 have a median measurement error of 8.2 m/s and post-upgrade RVs have a median measurement error of 3.9 m/s.

3.3.2.2 MAROON-X

We publish 68 measurements of Wolf 359 made with the MAROON-X spectrograph at Gemini Observatory. The MAROON-X velocities are available online in a machine readable format in Bowens-Rubin et al. 2023 [31]. The MAROON-X data were acquired with both the red (649–920 nm) and blue (491–670 nm) arm simultaneously during 34 observing nights. These observations were taken over 5 observing runs during February 2021, April 2021, May 2021, November 2021, and April 2022.

Spectra were taken with a fixed exposure time of 30 min and showed an average peak SNR of 90 pix^{-1} in the blue arm and 460 pix^{-1} in the red arm. The data were reduced by the instrument team using a custom `python3` data reduction pipeline to produce optimum extracted and wavelength calibrated 1D spectra. The radial velocity analysis was performed using SERVAL [252], a template matching RV retrieval code in a custom `python3` implementation. On average, the RV uncertainty per datum was 1.0 m/s for the blue arm and 0.3 m/s for the red arm. MAROON-X uses a stabilized Fabry-Perot etalon for wavelength and drift calibration [215] and can deliver 30 cm/s on-sky RV precision

over short timescales [232] but suffers from inter-run RV offsets with additional per-epoch uncertainties ranging from 0.5–1.5 m/s, corresponding to increased uncertainties of 1.4 m/s for the blue arm and 0.9 m/s for the red arm for signals on timescales longer than one month.

3.4 Analysis

3.4.1 Stellar Age Estimation

We provide an updated analysis of the age of Wolf 359 in order to constrain the sensitivities of our high-contrast imaging survey. We correlate our age estimates to our HCI survey sensitivity using evolutionary cooling models in order to determine the maximum mass of an unseen companion in Section 3.4.2.

Gyrochronology: The relation between rotation period, age, and mass has been studied extensively for low-mass stars (e.g. [15, 68, 117, 222]). It has been shown that stars begin their life with a fast rotation period and spin down with time via magnetic braking. The particular shape of this relation and the time it takes a star to spin down depends on its mass. The gyrochronology relation for Sun-like stars is calibrated, so the rotation period can be used to estimate an age. However, this gyrochronology relationship for Sun-like stars does not hold for M dwarfs [6]. While the relationship for low-mass stars has not been calibrated, it has been shown that rotation correlates with relative maturity [75, 180, 191].

We calculated Wolf 359's Rossby number to be $R_0 = 0.02$ using the convective turnover time computed from [247]. We then compared our R_0 value to Figure 6 of [176]. We find that Wolf 359 lies in the magnetically saturated portion of this plot. For Sun-like stars, being in the saturated regime means the star is young (< 100 Myr). However M dwarfs stay rotating fast longer, thus a fast rotation period does not always mean the star is as young [117, 161]. Medina et al. 2022 [161] estimated that fully convective M dwarfs transition between the saturated to the unsaturated regime at around 2.4±0.3 Gyr, which provides an approximate upper limit to the age of Wolf 359 but is not informative. Below we combine rotation period with kinematics to estimate a more constrained upper limit on the age of Wolf 359.

CMD age dating: We compared the color magnitude diagram position of Wolf 359 against the 100 pc sample of M dwarfs from *Gaia* and empirical sequences based on bona fide members of young associations of several ages [88]. From Figure 3.3, we conclude that Wolf 359 has already converged into the main sequence. This analysis suggests that Wolf 359 is older than the age of the Pleiades cluster (112 Myr) as the lowest mass stars in this cluster have not converged into the main sequence. From the CMD analysis, we conclude the age of Wolf 359 is older than 112 Myr.

Isochrone age dating: We used the MESA Isochrones and Stellar Tracks (MIST) [59, 73] to estimate Wolf 359's age using a color-magnitude diagram. We adopt the MESA models associated with an M6 star ($0.11 M_{\odot}$) with a metallicity of [Fe/H] = 0.25 dex [153] and rotation of $0.4 v/v_{\rm crit}$. We used *Gaia* photometry (apparent magnitude

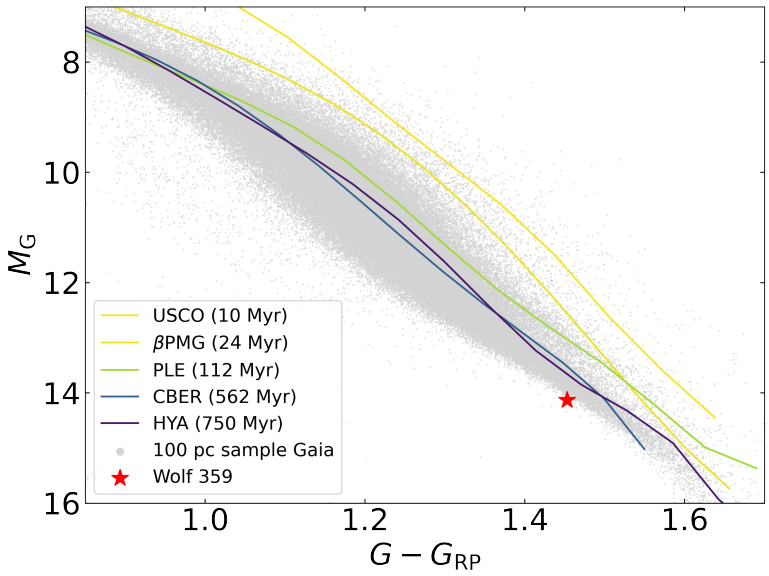

Figure 3.3 **CMD comparison of Wolf 359 with young moving groups**: We plot the color-magnitude diagram for Wolf 359 with empirical sequences from young associations of ages 10 Myr, 24 Myr, 112 Myr, 562 Myr, and 750 Myr [88] and the *Gaia* 100 pc sample of M dwarfs. The red star represents the position of Wolf 359. The color-magnitude position of Wolf 359 is not in agreement with the youngest moving groups of 10–112 Myr. We find that Wolf 359 is in better agreement with the Coma Berenices (562 Myr) and Hyades (750 Myr) moving groups and the field sample. We conclude that Wolf 359 has converged on to the main sequence and that its age is older than 112 Myr. *(Figure Credit: Rocio Kiman)*

$g = 11.038 \pm 0.003$, absolute magnitude $G = 14.130 \pm 0.003$, apparent magnitude $g_{\rm bp} = 13.770 \pm 0.005$) to compare with the MIST isochrones (Figure 3.4). Our iscohrone age estimate is largely driven by the measurement of the *Gaia* G magnitude.

While the MIST models can be unreliable for low-mass stars, they were recently shown to provide a good fit for stars like Wolf 359 with masses below $0.25\,M_{\odot}$ and a metallicity of [Fe/H]=+0.25 using the Hyades single star sequence [36]. We predict an age of $\sim 400\,$Myr using the MIST models.

Kinematic age dating: We estimated Wolf 359's kinematic age to be $1.53 \pm 0.3\,$Gyr following the methods outlined in Lu et al. 2021 [149]. Briefly, this method consists of estimating the vertical velocity dispersion of a group of stars with similar temperatures and similar rotation periods. Assuming that the evolution of rotation period for stars with similar temperatures is the same, the stars in this group should have similar ages. Therefore we can use an age-velocity relation to estimate the average age of the group from the vertical velocity dispersion. We obtained a group of stars with similar mass and rotation period as Wolf 359 from the MEarth sample in Newton et al 2018 [177]. We combined their reported rotation periods, mass, and radial velocities with their proper motions and parallaxes retrieved from *Gaia* eDR3 [90] in `galpy`[2] [30] to calculate their vertical velocities. We then created a bin in mass and rotation period around Wolf 359, selecting similar stars with similar ages. To define the size of the bin, we used a group of stars with similar mass and rotation period as one M dwarf in the MEarth sample

[2] `Galpy`: `https://github.com/jobovy/galpy`

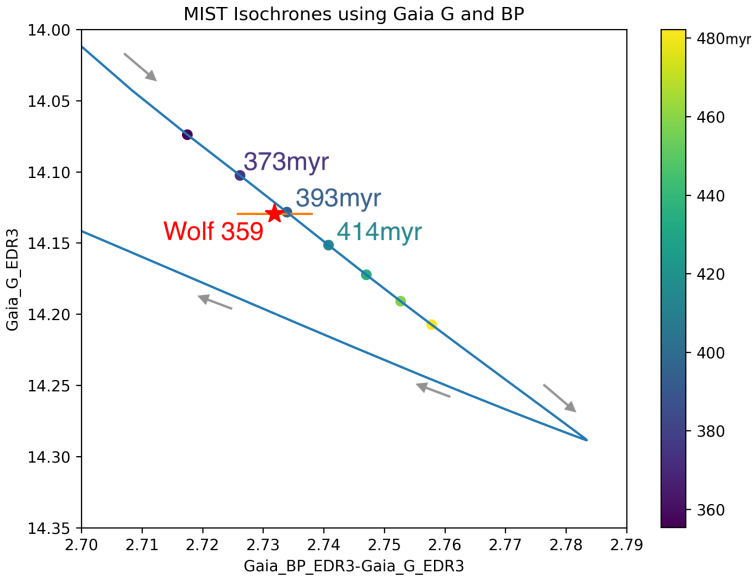

Figure 3.4 **Isochrone age dating**: We used the MIST isochrone models with the *Gaia* eDR3 photometry in G and BP to estimate an age for Wolf 359. The blue line represents the MIST isochrone track for a star of 0.11 $M_{\odot}$ with metallicity of $[Fe/H] = +0.25$ dex. Wolf 359 is represented by the red star, which lies closest to the isochrone point with an age of 393 Myr (between 373 Myr and 414 Myr). We estimate an age of 400 Myr from isochrone dating.

which is co-moving with a white dwarf. We used `wdwarfdate` [124] to get the age of the white dwarf from its effective temperature and surface gravity (retrieved from [95]), and set the bin size so the kinematic age of the group reproduced that age. We used the age-velocity relation from [250] to correlate the vertical velocity dispersion with ages and then performed a Monte Carlo propagation of the vertical velocity uncertainties to determine the uncertainty in the kinematic age of Wolf 359. The resulting distribution from the Monte Carlo simulation is shown in Figure 3.5. We obtained a kinematic age of 1.5 ± 0.3 Gyr. However, as most of the stars in the bin are in the saturated regime, their rotation period still depends on their initial rotation period, making the dispersion in age larger. Therefore, we adopt an age of 1.5 Gyr as an upper bound for Wolf 359's age.

Age summary: Our age estimate from the MIST isochrone comparison (400 Myr) is consistent with our young association comparison (> 112 Myr). Our CMD comparison with young moving groups shows it is probable that Wolf 359 has converged on to the main sequence. While the 2.7 d rotation period cannot be used to provide an exact age using gyrochronology, Wolf 359's fast rotation is a relative indicator of youth (< 2.4 Gyr). We provide a better constrained upper bound estimate using the kinematic age dating of $\sim 1.5 \pm 0.3$ Gyr.

For completeness through the remainder of this chapter, we consider ages for Wolf 359 between 100 Myr - 1.5 Gyr in our HCI analysis. However, our analysis suggests that the ages estimated by Pavlenko et al. 2006 [182] using the spectral energy density

distribution ($\sim 100 - 350$ Myr) seem less likely due to Wolf 359's suspected convergence with the main group. If we someday measure the dynamical mass and temperature of an exoplanet companion around Wolf 359 using infrared direct imaging, we may then be able to apply planetary-mass isochrones to refine this age estimate.

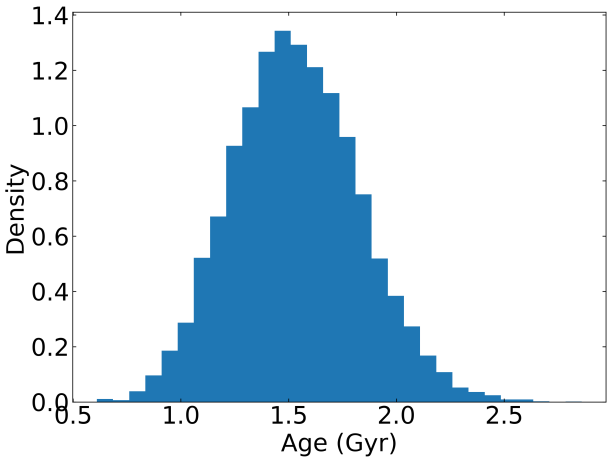

Figure 3.5 **Kinematic age dating:** Wolf 359's kinematic age was measured using the methods outlined in [123]. The results of the Monte Carlo simulation shown here finds the kinematic age to be 1.53 ± 0.3 Gyr. We adopt this kinematic age as our age upper-bound for Wolf 359. *(Figure Credit: Rocio Kiman)*

3.4.2 High-Contrast Imaging Analysis

We used the Keck-NIRC2 contrast curves (Figure 3.2) to determine the final 5σ sensitivity of our imaging survey across separations between 0.23 AU and 4.18 AU. We cannot make constraints on companions orbiting beyond separations of 4.18 AU on the night of observation because the field of view of the camera was limited to 5.1" $\times$ 5.1" (512$\times$512

pixel) to increase the speed of camera readout.

We then applied published isochrone models to predicted the upper mass limits for companions ruled out by the HCI observations. In Figure 3.6a, we applied the isochrone models created by Isabelle Baraffe[3] to place constraints in the speckle-limited region at the tightest angular separations (< 1 AU). We used the BHAC15 models for the stellar regime $T_{eff} > 3000$ K [12], the DUSTY models for the brown dwarf regime 1700 K $< T_{eff} < 3000$ K [54], and the COND models for the planetary regime $T_{eff} < 1400$ K [10]. The Baraffe models predict that companions with masses above the deuterium burning limit (> 13 $M_{\rm Jup}$) with ages younger < 1.5 Gyr will be brighter than $M_s = 14.0$. Our survey reached a greater than 5σ sensitivity to companions with $Ms = 14$ at separations greater than 0.25 AU. We therefore rule out any stellar and brown dwarf companions orbiting outside of 0.25 AU to 4.18 AU at the time of observation.

In Figure 3.6b, we used the isochrone models presented by Linder et al. 2019 [146] to set the mass upper limit in the background-limited regime from 1–4.18 AU (Figure 3.6b), where the sensitivity is limited by the sky background rather than the stellar contrast. Our combined-night contrast curve averages a sensitivity of $Ms = 17.7$ in this region. This sensitivity rules out companions with a mass bigger than 2.1 $M_{\rm Jup}$(667 $M_{\oplus}$) for ages younger than 1.5 Gyr. We cannot rule out companions to 5σ with masses smaller than 0.4 $M_{\rm Jup}$(127 $M_{\oplus}$) for any adopted age older than 100 Myr.

[3]The Baraffe isochron models were retrieved at `http://perso.ens-lyon.fr/isabelle.baraffe/`.

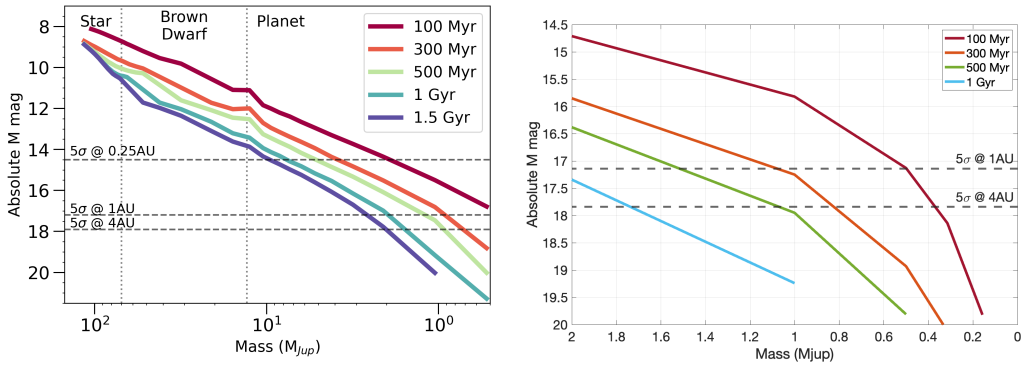

(a) Baraffe Isochrones for stellar, brown dwarf, and planetary cooling regimes

(b) Linder+2019 low-mass planetary cooling curves

Figure 3.6 **Isochrones overlaid with the 5σ constraints from the Keck-NIRC2 survey**: The horizontal lines represent our imaging survey's 5σ sensitivity at 1 and 4 AU of separation. (a) We use the BHAC15/DUSTY/COND models ([12], [54], [10]) to rule out all tight stellar and brown dwarf companions ($> 13\,M_{\rm Jup}$) outside of 0.25 AU (0.1"). *(Figure Credit: Maïssa Salama)* (b) From 1–4.18 AU of separation, we apply the Linder et al. 2019 low-mass planetary cooling models to place upper mass limits on planetary companions. We rule out planets with masses $> 1.5 M_{\rm Jup}$ to 5σ if Wolf 359 is younger than 500 Myr in this region.

In order to estimate the completeness by mass and orbital semi-major axis of the high-contrast imaging survey, we utilized the Exoplanet Detection Map Calculator (`Exo-DMC`) package [27] (Figure 3.7). We converted the combined-night 5σ Keck-NIRC2 contrast curves from apparent M mag into upper mass estimates adopting four ages: 100 Myr, 300 Myr, 500 Myr, 1 Gyr (Figure 3.7a). We used the Linder and Ames-COND isochrone models for this conversion and averaged the estimated masses in areas where the models overlapped. The Ames-COND isochrones[4] were accessed using the `species` package [227].

The greater than 10% survey coverage spans from a semi-major axis range of 0.2 AU to 10 AU. We find the best survey coverage ($> 95\%$) of semi-major axis between 1-3 AU. Assuming an age younger than 1 Gyr, we rule out companions with a semi-major axis of 1-3 AU above 10 M_{jup}. While the semi-major axis predicted for the Wolf 359 b candidate ($a = 1.8 \pm 0.2$ AU) is within this range, we do not reach the sensitivity to probe to the minimum mass predicted ($m \sin i \sim 0.14\, M_{jup}$) regardless of age. For an age of 1 Gyr, we rule out that the Wolf 359 b candidate as described by [234] cannot be bigger than $4M_{jup}$. For an age of 100 Myr, we rule out that the Wolf 359 b cannot be bigger than $1M_{jup}$.

[4]The Ames-COND models can be found at `https://phoenix.ens-lyon.fr/Grids/AMES-Cond/`

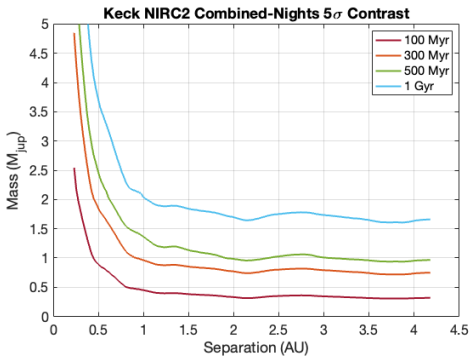

(a) Keck NIRC2 Combined Night

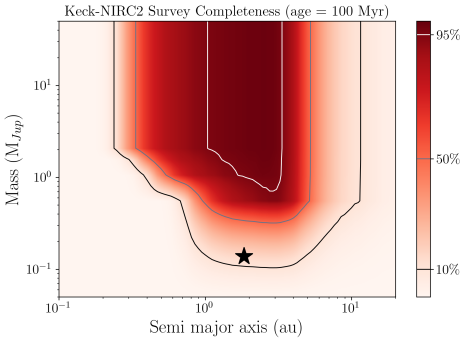

(b) Completeness for age of 100 Myr

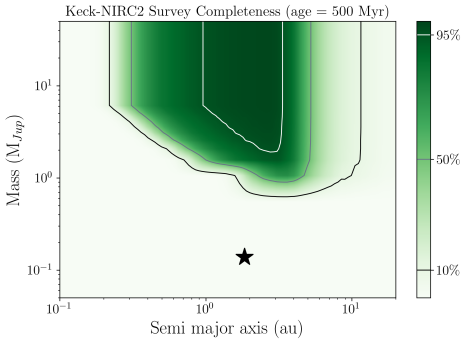

(c) Completeness for age of 500 Myr

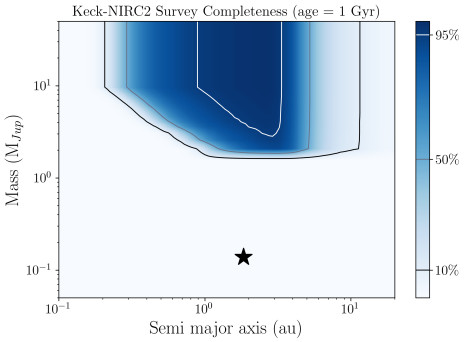

(d) Completeness for age of 1 Gyr

Figure 3.7 **Keck-NIRC2 High Contrast Imaging Survey Completeness**: (a) The NIRC2 combined-nights 5σ contrast was converted to mass space using the Linder+2019 and Ames-COND isochrone models. (b-d) The NIRC2 survey completeness maps for the ages 100 Myr, 500 Myr, 1 Gyr were estimated using the Exoplanet Detection Map Calculator (`Exo-DMC`) python package from the mass-space combined-nights 5σ contrast curves. Our imaging survey has 10% coverage to companions with a semi-major axis of 0.2-10 AU and reaches 95% coverage for companions with a semi-major axis between 1-3 AU. The black star represents the Wolf 359 b semi-major axis and minimum mass as predicted by [234].

3.4.3 Radial Velocity Analysis

Our RV analysis incorporates 275 velocities from four instruments: Calar Alto Observatory's CARMENES [194], ESO-HARPS [159], Keck-HIRES, and Gemini-MAROON-X. The RV instruments and measurements used in our analysis of Wolf 359 are summarized in Table 3.4 and are available in full in machine readable format online. The CARMENES data were retrieved from the DR1 release which spans from 2016–2020 [202]. The MAROON-X, HIRES, and HARPS data were provided directly by the observing teams.

We elected to use the HARPS data as analyzed with the TERRA pipeline [5] in order to remain consistent with the analysis presented in Tuomi et al. 2019 [234]. The 77 HARPS-TERRA velocities used in this analysis incorporate the velocities presented in the 2019 announcement.

The MAROON-X RVs were computed using both the red and blue arms of the spectrograph, producing two RV measurements per observation. We treat each the MAROON-X red-arm and blue-arm measurements as being from different instruments to account for different instrumental offsets and RV jitter amplitudes. We do the same for the Keck-HIRES velocities collected before and after a detector upgrade in 2004. Within each instrument, we bin observations collected within 0.1 d of one another.

We used the `RVSearch`[5] python package [208] to perform a blind planet search within

[5] `RVsearch`: `https://github.com/California-Planet-Search/rvsearch`

our RV timeseries data (Figure 3.8). We detected the known signal associated with the rotation period of the star (2.71 d). Once the stellar-rotation activity signal was removed, we detected no signals over a False Alarm Probability of 0.1%. We used the injection-recovery tools built into `RVSearch` to estimate the sensitivity of our RV survey to planets of specified $m \sin i$ and semi-major axis to create the completeness contour shown in Figure 3.9. The probability of detection for a planet with a minimum mass equivalent to a Neptune-mass, Jupiter-mass, and the Wolf 359 b candidate is also shown in Figure 3.9. `RVSearch` yielded a 32% completeness to an equivalent $m \sin i$ and semi-major axis as the Wolf 359 b candidate. Because we do not have a significant completeness in this space, we are not able to confirm or deny the candidacy of Wolf 359 b using `RVSearch` with our RV dataset.

To further explore the candidacy of Wolf 359 b, we used the open-source software package `radvel`[6] [86] to model the RV data. We used the Tuomi et al. 2019 [234] results for Wolf 359b listed in Table 3.2 as priors. We employed fits with and without the Gaussian Process Fitting module which can be used to fit and remove signals due to stellar activity. We ran our `radvel` MCMCs using $N_{walkers} = 50$, $N_{steps} = 10000.0$, $N_{ensembles} = 6$, and $MinAutoFactor = 30.0$. In all `radvel` fits, the chains did not pass the convergence test to indicate that the walkers were well mixed. The convergence criteria could not be met, so we draw no conclusions about the properties of the Wolf 359b candidate from our `radvel` fits. We detected no new candidates. At 95% confidence, our RV

[6] `Radvel`: `https://github.com/California-Planet-Search/radvel`

analysis excludes planets with a minimum mass bigger than $m_{\rm p} \sin i > 13.5\ M_{\oplus}$(0.04 $M_{\rm Jup}$) for $a = 0.1$ AU and planets with a minimum mass bigger than $m_{\rm p} \sin i > 147\ M_{\oplus}$(0.46 $M_{\rm Jup}$) for $a = 1$ AU. We have over 50% completeness to exclude planets with an $m_{\rm p} \sin i$equivalent or bigger than $1 M_{\rm Jup}$within 5.3 AU and 1 Neptune-mass within 0.52 AU. Our RV survey has little coverage to companions orbiting with a semi-major axis larger than $a > 10$ AU for all masses.

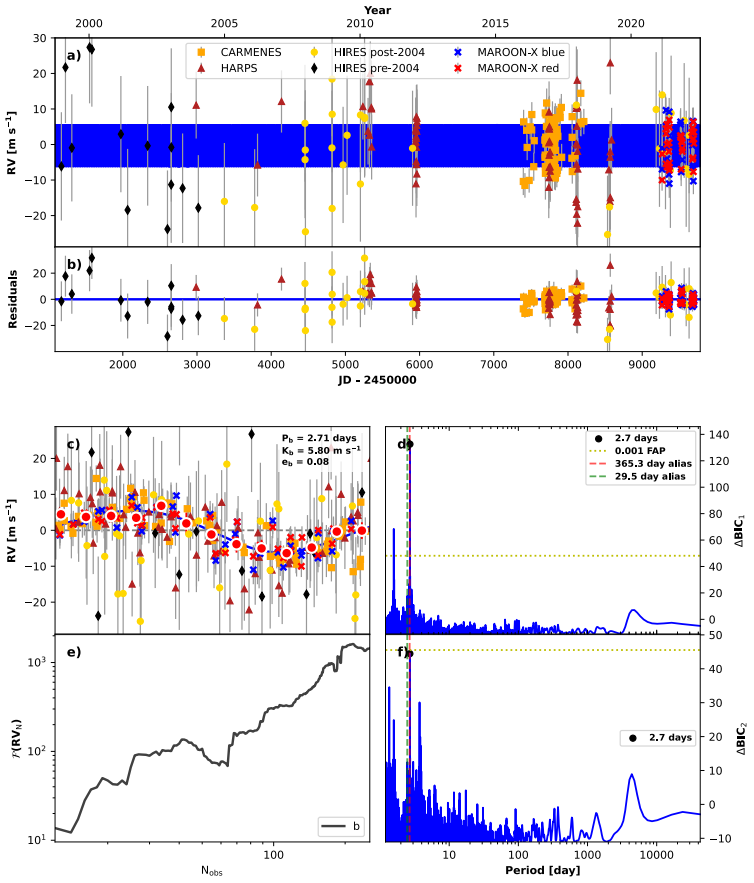

Figure 3.8 **RV timeseries & periodograms from RVSearch** *(a)* The RV timeseries. The blue represents the signal from the known rotation period (2.71 d; [103]). *(b)* The time series residuals. *(c)* The folded timeseries for the rotation period signal (2.71 d). *(d)* The periodogram before removing the rotation period signal. The peaks correspond to the rotation period signal (2.71 d), and half the rotation period (1.4 d). *(e)* The quantification of the detection for the 2.7 d signal monotonically increases as expected. *(f)* The periodogram of the residuals after removing the 2.71 d signal. We do not find evidence for additional candidates above the False Alarm Probability threshold (0.1%).

Figure Credit: Joey Murphy

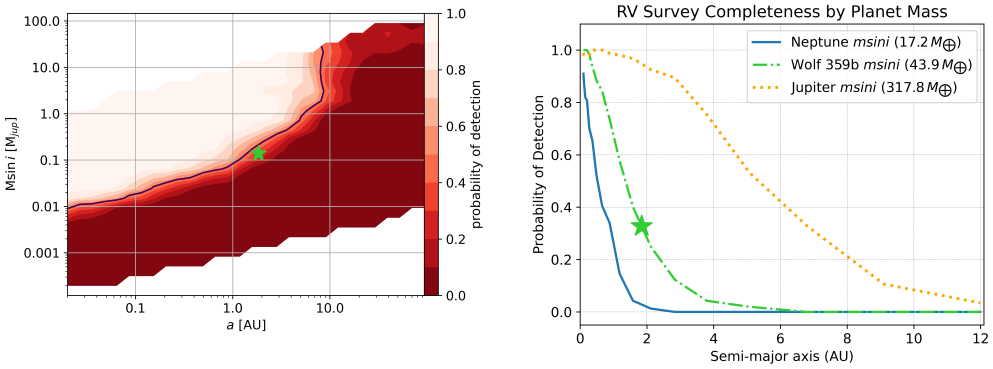

(a) Wolf 359 Radial Velocity Survey Completeness Contour

(b) Probability of Detection by Minimum Mass

Figure 3.9 **Radial Velocity Survey Completeness**: We used the injection-recovery function within `RVSearch` to determine the completeness of our Wolf 359 RV survey as a function of the minimum planet mass and semi-major axis. Our analysis methods yield a 32% chance of recovering a signal that matched the Wolf 359b candidate as described by Tuomi et al. 2019 [234] (green star).

Table 3.4. **Wolf 359 RV data summary**

Instrument	Source	Spectral Range (nm)	# Meas.	Baseline	Avg. RV Precision	Inst. Offset*
CARMENES	[202]	550-1700	78	2.23 yr	1.99 m/s	0.05 m/s
ESO-HARPS	M. Tuomi	378-691	77	15.3 yr	3.09 m/s	-3.22 m/s
HIRES Pre-04	CPS	300-1000	14	5.05 yr	8.09 m/s	-9.68 m/s
HIRES Post-04	CPS	300-1000	38	17.14 yr	4.26 m/s	-3.28 m/s
MRN-X blue	MRN-X	499-663	34†	1.17 yr	1.39 m/s	-6.47 m/s
MRN-X red	MRN-X	649-920	34†	1.17 yr	0.88 m/s	-5.62 m/s

Data from all but the CARMENES instrument were provided to us through direct communications with the source listed. CPS stands for the California Planet Search team in direct communication with Howard Isaacson. MRN-X stands for the MAROON-X instrument/team in communication with Jacob Bean.

†The MAROON-X blue and red data were collected simultaneously

* The instrument offsets were calculated from the fit made using `RVSearch` when detecting the signal from the stellar rotation period.

3.5 Discussion

3.5.1 Performance of the direct imaging survey with Keck-NIRC2

Few Keck-NIRC2 HCI observations have been published that span multiple nights that utilize the Ms filter (4.67μm) in conjunction with the vector vortex coronagraph. Previous published deep surveys of this type have so far limited to the Eps Eri results from Mawet et al. 2019 [158] and Llop-Sayson et al. 2021 [147]. However, it is expected that surveys similar to the work presented here will become more common as data from indirect methods of exoplanet detection become more widely available and drive targeted direct imaging surveys towards studying colder companions. We document the expected performance of our imaging survey as compared to our measured performance to aid in the planning of future multi-night Keck-NIRC2 HCI surveys that are completed with the Ms filter with the vortex coronagraph.

We report that our measured efficiency on the night with the greatest number of images (2021 March 31 UT) was 52%. This excludes the setup time and used the observing configuration described in Section 3.3.1. After our initial setup, we observed Wolf 359 for 4.05 hr and totalled 2.12 hr of science integration time. We ran the majority of QACITS sequences with 50 science images (22.5 min total integration time) and experienced no significant QACITS centering issues while collecting science data.

We adopt the predictions produced by the Keck Observatory's online NIRC2 SNR and Efficiency Calculator to quantify the expected SNR in the background limited regime

of our contrast curves. These equations for the NIRC2 SNR Calculator are outlined in subsection 3.5.1.1. We do not consider the speckle-limited regime of our contrast curves from this comparison ($sep < 0.8$) as the NIRC2 SNR calculator cannot quantify the SNR in the speckle-limited region.

We evaluate the performance using one night of observations to avoid complications in the performance discussion from combining data across multiple nights. We elected to use 2021 March 31 (UT) because it is the night of our survey with the most available data. Our contrast curve for this night was generated using 269 of the 283 images taken with an exposure time of 0.3 s and coadd of 90, totalling approximately 2 hr of integration time. We measured an average 5σ contrast in the background-limited region of the contrast curve (> 0.8) to be $\Delta m_s = 8.53$ (apparent magnitude of $m_s = 14.38$).

Our measured 5σ detection limit from 2021 March 31 is consistent with the performance on individual nights of the Eps Eri survey where Llop-Sayson et al. 2021 [147] used the pyramid wavefront sensor (pyWFS) to collect approximately 2 hours of integration time. The best SNR achieved by Llop-Sayson et al. 2021 was between the separations of $1.5 - 1.75$ and corresponds to an apparent magnitude of $m_s = 14.4$ ($\Delta mag = 12.7$). Both this work and the Eps Eri surveys indicate it is improbable to detect a companions dimmer than $m_s = 14.4$ to 5σ with this instrument configuration in one half-night of Keck NIRC2 time when operating with the vortex coronagraph paired with the pyWFS.

We next checked our measured results against the prediction made by the NIRC2 SNR

calculator using the parameters that matched our observing setup: 0.3 s integration time with 90 coadds, narrow mode, 2 reads, 269 images, and no telescope nodding. We assumed a Strehl ratio of 0.85 which is a conservative estimate associated with 300 nm of wavefront error. The NIRC2 SNR calculator assumes that the background flux and flux from the source will follow Poisson statistics. We find that the calculator predicts the 5σ threshold to be at an apparent magnitude of $m_s = 16.07$, which is not consistent with with our observed results. Our measured SNR was 1.69 magnitudes brighter than the predicted performance by the NIRC2 SNR calculator, meaning we were more restricted in the companions that we could detect at the background-limited wide separations than was predicted by the calculator.

We expect that the prediction by the NIRC2 calculator would be somewhat inconsistent with our results because the NIRC2 SNR calculator was not designed to predict observations when the vortex mask is used. To better refine our predicted performance estimate, we modified the equations used by the NIRC2 SNR calculator. These modifications are documented in subsection 3.5.1.1 and incorporate a throughput penalty to the measured signal to account for the use of the fixhex pupil stop and the vortex mask at 4.7 μm (Total throughput penalty, 0.57 ± 0.03). We additionally offer a revision to the background flux counts when the vortex is used in M-band (17850 DN/s per pixel). When we apply our revised equations to estimate the predicted performance for our 2021 March 31 dataset, we find that our 5σ detection threshold is predicted to be at $m_s = 15.49$. While this estimate better aligns with our measured performance, this method still over-estimates

the brightness of the 5σ detection threshold by 1.11 magnitudes when comparing to our measured performance from that night ($m_s = 14.38$).

We ruled out the possibility that this performance gap was due to uncorrected non-uniform background counts spatially in the individual images through highpass filtering. We used `VIP`'s internal highpass filtering function to determine the optimal highpass filtering by injecting a fake planet into each individual image, running six types of highpass filters on each image, and then using stellar photometry to recover the SNR of the injected planet. The optimal highpass filtering method was `gaussiansubt` with size $2.25 * fwhm_{nirc2}$. We then edited `VIP`'s contrast curve function to include the highpass filtering step using the optimal highpass filter. The highpass filtering step was added after fake planet injection but before running PCA. There were slight differences between the contrast curves produced from the image sets with and without the highpass filter, but the differences did not affect the contrast achievable in the background limited region of the image. We thus conclude that the performance gap is not due to poorly corrected background structures in each frame.

To determine if the performance gap was due to the image background noise not obeying Poisson statistics temporally, we measured how the sky background noise over time compared to the statistics expected from photon noise. We measured the sky background noise by summing the counts inside four circular apertures with a diameter equal to the $fwhm_{NIRC2}$ using the 2021 March 31 image set before and after sky subtraction was completed. The apertures were located 1.76 arcseconds from the image center in the

direction of the image corners in order to avoid contamination from the star. We found our measured background noise value using 20 frames from the image cube after the sky subtraction was applied. The 20 frames were chosen from the full cube where the conditions were stable (no background drift, average background counts in the raw frames are consistent, and similar adaptive optics correction). We plotted the aperture sum counts of each aperture and then took the standard deviation of the counts over time. The corresponding photon noise value was determined using the image cube before the background subtraction was made. We measured the sum of photons inside each aperture, averaged the sums, and then took the square root of the average sum to act as the expected photon noise. The ratio between our measured-noise to photon-noise contribution was 1.9 from the subset of the 20 stable frames. Across the full image cube, we found the ratio of measured/theoretical-photon noise to be 3.0. This corresponds to a flux difference of 0.69 and 1.2 magnitudes respectively. This range of values is consistent with the performance gap we see after accounting for the throughput loss from the vortex and pupil stop ($\Delta mag = 1.1$).

We hypothesize that the background noise does not follow Poisson statistics because of short time-scale water vapor variations at timescales less than the length of our 30 s images. This hypothesis could be tested when upgrades to the NIRC2 electronics are completed in 2023 which will allow for faster readout and background corrections to be made at shorter timescales. If proven true, the limits of previous surveys may be improved upon by observing the target again using sub-second integration times in order

to improve background correction.

3.5.1.1 Revised SNR Estimations for Keck-NIRC2 with the Vortex Coronagraph in M-band

The W.M. Keck Observatory provides an online tool to help observers plan their NIRC2 observations, the NIRC2 SNR and Efficiency Calculator.[7] The NIRC2 Calculator does not provide performance estimates for using the vector vortex coronagraph mask, which is a common configuration for conducting high-contrast imaging observations to hunt for exoplanet and brown dwarf companions. In this section, we offer a method to modify the equations used by the NIRC2 Calculator to aid in the SNR prediction when using the L/M-band vortex [217] with the Ms filter.

We recommend that observers planning to use the Lp filter in conjunction with the L/M-band vortex use the Vortex Imaging Contrast Oracle (VICO)[8] [248] instead of the equations documented here. VICO produces a full contrast curve based off of user inputs for the host's magnitude, the survey's total integration time, and predicted spanned parallactic angle. VICO's performance and contrast predictions are based off a training set of 304 targets that were observed between 2015 to 2018 using the Shack-Hartmann wavefront sensor to perform adaptive optics correction.

We consider SNR predictions only and do not attempt to match the efficiency predictions

[7] https://www2.keck.hawaii.edu/inst/nirc2/nirc2_snr_eff.html
[8] https://wxuan.shinyapps.io/contrast-oracle/

made by the NIRC2 Calculator. The predictions offered by our modified equations are intended to predict the SNR in the background limited regions where light from the host star is negligible in comparison to the background flux. We do not attempt to predict the full contrast curve or the SNR in the speckle limited regions of the image.

Figure 3.10 shows the values defined internally to the NIRC2 SNR Calculator alongside our choices for the user defined parameters that are applicable to our observing mode. The calculator internally defines the read noise, gain, zero-point for each filter, and number of pixels within a full-width-half-max for each filter. The user is able to specify the object magnitude, Strehl ratio, time per exposure (tint), coadds, number of dithers, repeats per dither, camera mode (narrow versus wide), filter, number of reads, array window size, and adaptive optics mode (natural guide star versus laser guide star). We matched our user defined parameters to our 2021 March 31 (UT) dataset to compare the predicted performance to the measured performance on that night. Terms related to laser motion control were excluded because our observations were performed using natural guide star adaptive optics. We adopted a Strehl ratio of 0.85 for our predictions, which is a conservative estimate equivalent to 300 nm of error on the wavefront.

We began the modifications to the equations used in the NIRC2 SNR Calculator by adding a corrective factor for the throughput for using Keck-II's fixedhex pupil stop. The NIRC2 SNR calculator assumes that NIRC2 images will be taken with Keck Observatory's circular largehex pupil stop. However, when operating NIRC2 in conjunction with the vortex coronagraph, the fixedhex pupil is typically used. The fixedhex pupil was

specifically tailored for use with the vortex coronagraph at Keck, and its shape blocks the telescopes spiders and central obscuration. It has a throughput of 84% as compared to the largehex pupil. We assigned a 0.84 throughput penalty for this difference in pupil stop.

We further refined our throughput penalty by accounting for the throughput hit due to the absorption by the vector vortex coronagraph at $4.67\mu m$. The throughput of the Keck annular groove phase mask was measured in the lab to be $70 \pm 3\%$ ([119], AGPM-L9r2 in Table 4). We conducted on-sky testing to verify this throughput as observed with the full optical system in June 2022. We imaged HIP 74785 using the fixhexed pupil for all images. We moved the vortex coronagraph in-and-out of the optical path to create a direct comparison to measure the transmission of the vortex mask. When the vortex was in place, it was intentionally miscentered with respect to the stellar PSF to assure no flux from the star was blocked due to the coronagraphy properties of the vortex. The stellar photometry was then measured in each image using `photutils` within a circular aperture of 60 pixels in radius. The throughput ratio of the no-vortex to with-vortex stellar flux was measured to be $68 \pm 3\%$. While the vortex throughput measurement using on-sky images is consistent with laboratory tests, we note that we find that there was a slight defocus in the on-sky images when the vortex was in place such that a photometry aperture radius of $> 5\, FWHM$ needed to be used to achieve this consistency.

We document both the lab and on-sky testing values for the throughput penalty due to the vortex absorption in Figure 3.10 alongside our calculation for the total through-

put penalty. The total throughput penalty was calculated by multiplying the vortex throughput penalty by the fixhex throughput penalty. We adopted the more pessimistic value of the total throughput penalty (57%) when discussing the performance of NIRC2 in Section 3.5.

To quantify a correction factor for the background flux, we measured the background flux per pixel in each image for our full datacube from the three observing nights of Wolf 359. The NIRC2 calculator assumes a value of 18535 DN/s per pixel for the sky background contribution when observing in narrow mode with the Ms filter using no vortex with the largehex pupil. We measured the sky background in our images with the vortex and fixhex pupil by finding the median of each image cube. We then averaged those medians by night to find the average image median to be 17457 ± 4 on 2021 Feb 22, 17008 ± 7 DN/s on 2021 Feb 23, and 17850 ± 106 DN/s on 2021 March 31. These values indicate that there is a measurable excess background flux when the vortex optic is in place, as the background counts do not scale with the throughput penalty. We adopt the most pessimistic value for the background flux (2021 March 31) for our discussion of the NIRC2 performance in Section 3.5.

The equations outlined in this Chapter account for the throughput penalty of using the vortex only. When applied to the Wolf 359 2021 March 31 dataset, this method of prediction overestimated the 5σ performance capabilities by ~ 1 magnitude. We caution observers who are planning to detect a companion dimmer than $m_s = 14.4$ with Keck-NIRC2 using one or more half-nights approach the observation carefully and not rely

Parameter	Value	How defined?	Notes
Read noise in electrons (r_{noise})	56	Internal	
Gain in e- per DN ($gain$)	4	Internal	
The zero-point for Ms filter in narrow mode ($zeropoint$)	22.7	Internal	
Number of pixels in aperture (n_{pix})	490.8	Internal	
N Reads	2 (CDS)	User	2 reads is a standard readout mode
Array Window Size	512	User	512 x 512 is a standard img size for HCI imaging
AO Mode	NGS	User	Natural Guide star mode
Strehl	0.85	User	Conservative assumption assuming 300 nm of wavefront error
tint	0.3 s	User	Time per frame before coadd used in this survey
coadds	90	User	Num. frames added together before a full read used in this survey
Number of images (n_{exp})	269	User	Num. images collected on 2021 Mar 31 of this survey
Fixhex Throughput as compared to largehex pupil	0.84	Calculated	The ratio of the size of the fixedhex/largehex pupil at Keck
Vortex Throughput at 4.6 μm meas. in lab	0.70 ± 0.03	Measured	AGPM-L9r2 in Table 4 of Jolivet et al. 2019
Vortex Throughput at 4.6 μm meas. on sky	0.68 ± 0.03	Measured	Meas. using data shared by Keck Obs staff
Throughput Penalty using vortex value meas. in lab	0.59 ± 0.03	Calculated	$FixhexThrough * VortexThrouput_{lab}$
Throughput Penalty using vortex value meas. on sky	0.57 ± 0.03	Calculated	$FixhexThrough * VortexThrouput_{sky}$; Value adopted for NIRC2 performance discussion in Section 4.
Background flux using vortex with fixhex pupil at 4.6 μm	17850 DN/s	Measured	Average DN/s meas. on 2021 Mar 31 of this survey

Figure 3.10 **Parameters used in the modified NIRC2 Performance Calculation**

solely on the online NIRC SNR calculator or the equations listed in this section.

Equations to calculate the SNR:

The terms that deviate from the formulas used by the NIRC2 SNR calculator are highlighted in red.

$$
\begin{aligned}
n_{exp} &= coadds * n_{images} && \text{We assume no dithering} \\
m_{zero} &= zeropoint + 2.5 * \log_{10}(strehl) && \\
bg &= background * gain && \text{Meas. } background = 17850 \text{ DN/s per pix} \\
TputPenalty &= FixhexThroughput * VortexThroughput && \text{Meas. } ThroughputPenalty = 0.58 \\
signal &= TputPenalty * n_{exp} * tint * 10^{(0.4(m_{zero}-mag))} && \text{Signal after tput penalty applied} \\
\sigma^2_{read} &= n_{exp} * r^2_{noise} * n_{pix} && \text{Read noise} \\
\sigma^2_{skybg} &= n_{pix} * bg * n_{exp} * tint && \text{Photon-noise of sky background} \\
\sigma^2_{photon} &= signal && \text{Photon-noise of source} \\
\sigma_{tot} &= \sqrt{\sigma^2_{read} + \sigma^2_{skybg} + \sigma^2_{photon}} && \text{Total noise} \\
SNR &= signal/\sigma_{tot} && \text{Signal-to-Noise}
\end{aligned}
\tag{3.1}
$$

3.5.2 Prospects for Directly Imaging an Exoplanet around Wolf 359 using JWST

JWST offers an opportunity to directly image exoplanets in infrared wavelengths without the contamination from the Earth's atmosphere allowing for the telescope to probe for colder companions as compared to ground based telescopes. In this section, we present simulations to explore the potential of JWST to directly image a cold giant planet orbiting Wolf 359 using the Near Infrared Camera (NIRCam) Coronagraphic Imaging mode and Mid-Infrared Instrument (MIRI) imaging. MIRI and NIRCam can be used in

combination to span wider coverage for companions in orbital separations, cloudiness, and temperature. NIRCam can be used to achieve high contrasts at sub-arcsecond inner working angles at shorter infrared wavelenghts (0.6-5μm, [206]), which was demonstrated successfully during the Early Release Science Program to image the super-Jupiter mass exoplanet HIP 65426b [49]. MIRI operates at longer infrared wavelengths (5-28μm, [246]), giving greater sensitively to cold and cloudy companions.

Because of Wolf 359's proximity, a planet revealed through NIRCam or MIRI imaging has the potential to become the coldest directly image exoplanet that could be characterized with JWST spectroscopy. If such an exoplanet is detected, detailed characterization would allow the planet to become an anchor to test theories related to the atmosphere and formation of cold gas giant and ice giant planets.

3.5.2.1 NIRCam Coronagraphic Imaging

We explore the possibilities of using the NIRCam Coronagraphic Imaging mode to directly image companions orbiting Wolf 359 by simulating contrast curves using the Pandeia Coronagraphy Advanced Kit for Extractions (`PanCAKE`) python package[9] ([98], [185], [51]). We considered observations in the F444W filter, as the broadest band between the 4-5μm peak in brightness, in conjunction with the round coronagraphic mask MASK335R. We simulated integration times of 20 min, 1 hr, and 10 hr with ADI and RDI subtraction techniques. To simulate the ADI contrast curve, we assumed the total expo-

[9]Pandeia Coronagraphy Advanced Kit for Extractions; `https://github.com/spacetelescope/pandeia-coronagraphy`

sure time was split between two rolls (0° and 10°) when imaging the target. For the RDI simulations, we assumed a perfect reference with the same properties of Wolf 359 and used a 9-point circle dither pattern. PSFs were generated using the precomputed library over on-the-fly generation with wavefront evolution to reduce computational intensity. As such, these contrast curves represent an optimistic estimate of the achievable performance. We allowed PanCAKE to optimize the readout parameters for dither pattern, number of groups, and number of integrations.

To estimate what types of exoplanets may be detectable, we generated atmospheric models for companions with masses between 20 $M_{\oplus}$- 1 $M_{\rm Jup}$for ages spanning 100 Myr - 1.5 Gyr using the `PICASO 3.0`[10] [17,172] radiative–convective–thermochemical equilibrium model to simulate cloud-free 1D atmospheres for such companions. We assumed solar metallicity and C/O ratio for our simulated atmospheres. To estimate the $T_{\rm eff}$ and radius of a companion with a given mass at a certain age, we used the [146] evolutionary tracks and linearly extrapolated along the age axis when needed. The Phoenix stellar models [116] were employed to generate the stellar model for Wolf 359 using a spectral type of M5V and the Vega mag scaled to $2MASS\,k_s = 6.084$. An example of the set of thermal emission spectra from our generated atmospheric models are shown in Figure 3.11.

Our simulated NIRCam contrast curves are shown in Figure 3.12. Table 3.5 summarizes the detectability of theoretical cloudless exoplanets with varying masses using NIRCam

[10]Planetary Intensity Code for Atmospheric Spectroscopy Observations; `https://github.com/natashabatalha/picaso`

in ADI mode with 1 hour of total integration time. While our simulations span from 1-7 AU (0.4- 3), the full NIRCam field of view from the MASK335R inner working angle (0.57) to 20would correspond to 1.4 - 48.2 AU. We estimate that the region from 7-48.2AU will be background limited and have the same contrast as the result at 7AU for future observing planning purposes.

One hour of NIRCam integration time would provide sensitivity to a cloudless Jupiter-mass companion outside of 0.62(1.5 AU) at any predicted age range. Cloudless Saturn-mass exoplanets (0.3 $M_{\rm Jup}$) would be detectable at small separations if Wolf 359 is in the youngest part of its age range and at wider background-limited separations for ages up to ∼1 Gyr. A Neptune-like exoplanet (17 $M_{\oplus}$, 0.06 $M_{\rm Jup}$) will be visible if it is orbiting at wider separations and Wolf 359 is in the youngest part of its age range. The detection of a cloudless sub-Neptune exoplanet is unlikely with 1hr NIRCam ADI at any separations within Wolf 359's age range.

3.5.2.2 MIRI Imaging

Exoplanet gas giants with clear atmospheres are particularly bright in the emission band between 4-5μm, often making them detectable by the JWST NIRCam instrument. However, gas giants with cloudier atmospheres have muted emission from 4-5μm, instead emitting more at longer wavelengths (>15μm), as illustrated in Figure 3.13. This figure shows the emission differences between a cloudy (solid lines) and clear (dashed lines) young, sub-Saturn exoplanet (0.12$M_{\rm Jup}$). The cloudy and clear models used in this figure were generated using the method described in Limbach et al. 2022 [141]. This figure

Table 3.5. **NIRCam F444W Cornagraphic Imaging of Cloudless Companions**

Planet Mass	Age	Predicted apparent F444W mag	Sep. where Detectable by NIRCam 1 hr ADI
$1M_{jup}$	100 Myr	12.90	$> 0.6AU$
$1M_{jup}$	300 Myr	14.42	$> 0.8AU$
$1M_{jup}$	500 Myr	15.19	$> 0.9AU$
$1M_{jup}$	1200 Myr	17.05	$> 1.4AU$
$1M_{jup}$	1500 Myr	17.34	$> 1.5AU$
$0.5M_{jup}$	100 Myr	14.32	$> 0.8AU$
$0.5M_{jup}$	300 Myr	16.09	$> 1.1AU$
$0.5M_{jup}$	500 Myr	17.08	$> 1.4AU$
$0.5M_{jup}$	1200 Myr	19.51	$> 3.7AU$
$0.5M_{jup}$	1500 Myr	20.37	$> 4.7AU$
50 $M_{\oplus}$	100 Myr	17.06	$> 1.4AU$
50 $M_{\oplus}$	300 Myr	19.37	$> 3.6AU$
50 $M_{\oplus}$	500 Myr	20.85	$> 5.7AU$
20 $M_{\oplus}$	100 Myr	19.70	$> 3.9AU$

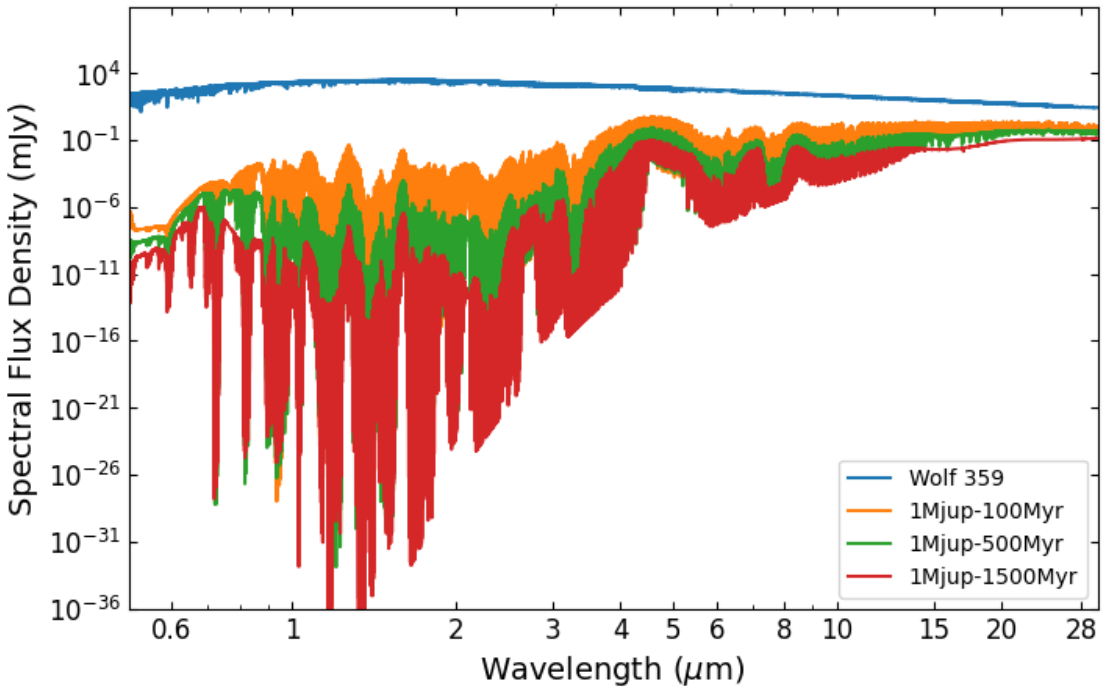

Figure 3.11 **Simulated atmospheric models for Wolf 359 and a cloudless $1 M_{\rm Jup}$ companion**: The modeled companion spectra shown correspond to ages of 100 Myr (orange), 500 Myr (green), and 1.5 Gyr (red). The simulated spectra of the Wolf 359 host star is shown in blue and were created by Sagnick Mukherjee. The estimates of the flux between $3.881\mu m - 4.982\mu m$ were used to determine the expected brightness and expected SNR for each companion type to simulate a NIRCam observation with F444W + MASK335R using `PanCAKE`.

demonstrates that exoplanets with cloudy atmospheres may be more easily detected through JWST Mid-Infrared Instrument (MIRI) broadband imaging at $21\mu m$, while clear atmospheres are more readily detected through direct imaging with NIRCam at

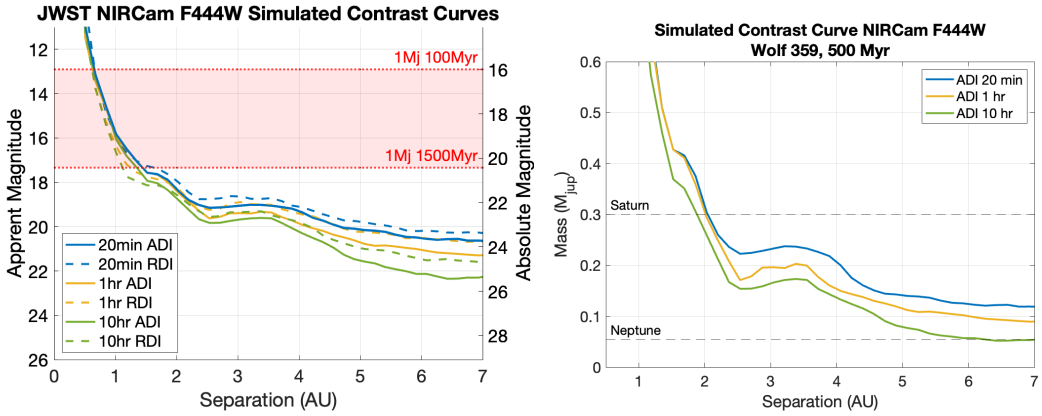

Figure 3.12 **Simulated JWST NIRCam Coronagraphic Imaging 5σ contrast curves at with F444W filter:** *(left)* We show contrast curves simulated using `PanCAKE` for three NIRCam exposure times in ADI and RDI mode. We predict that if a cloudless exoplanet existed with a mass greater than $1 M_{\rm Jup}$outside of ~ 1.5 AU, it would be detectable with 20 minutes of integration time. *(right)* The NIRCam F444W 5σ ADI contrast curves were converted to mass space using the [146] models with an adopted age of 500 Myr. We find that exoplanets larger than 1 Saturn mass will be detectable outside of 2 AU if Wolf 359 is in the younger part of its age range. A Neptune mass planet would be detectable beyond 6 AU if Wolf 359 is younger than 500 Myr and a $>$ 10 hr exposure was used.

4.5μm.

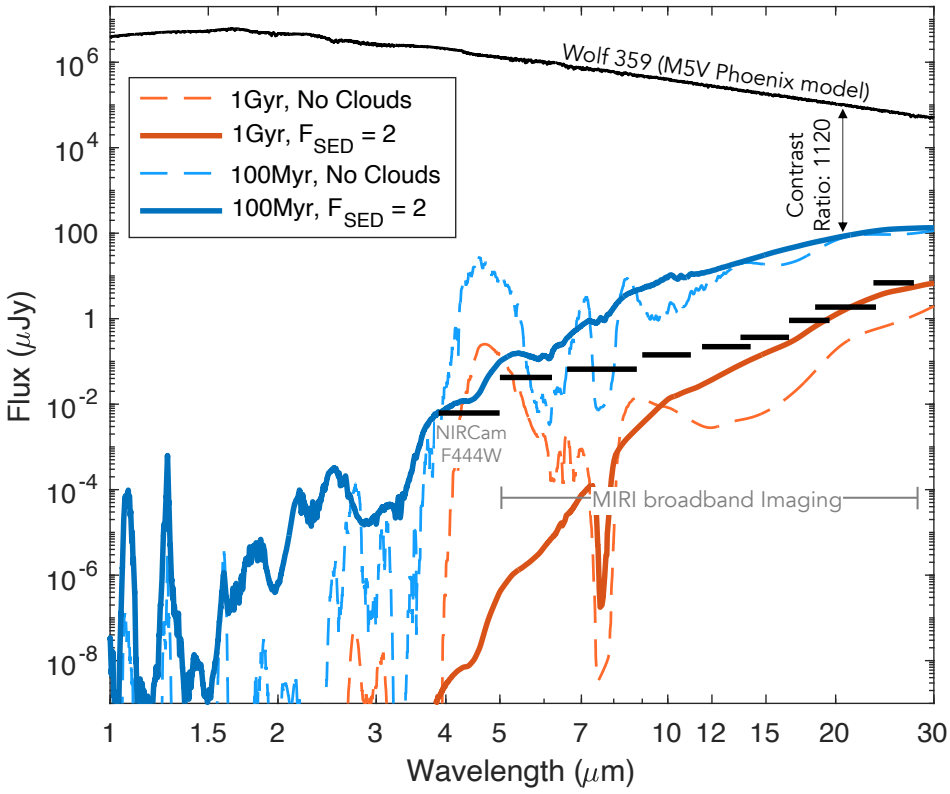

Figure 3.13 **Emission from a cloudy** (solid lines) a**nd clear** (dashed lines) **sub-Saturn** ($0.12M_{\rm Jup}$) at 100 Myr (blue) and 1 Gyr (red): The Black line shows the emission from Wolf 359 assuming a M5V spectral type. The black bars show the 3 hr, 5σ detection limits of NIRCam F444W and MIRI broadband imaging. At $21\mu m$, the contrast ratio between the star and a 100 Myr, $0.12M_{\rm Jup}$exoplanet is only 1120×. For the older exoplanet, the contrast ratio is 15,800×. *Figure Credit: Mary Anne Limbach*

We briefly explore the possibility of imaging exoplanets, like the Wolf 359b candidate

from [234], with MIRI. In the mid-IR, the planet's emission is increasing and the star's emission is decreasing. This results in a favorable contrast ratio of the planet to star of 1:1120 for an exoplanet that is 100 Myr, $0.12 M_{\rm Jup}$exoplanet with moderate cloud cover ($f_{SED} = 2$). However, the diffraction limit of JWST at 21 μm is 0.67" (6 pix) which is comparable to the separation between Wolf 359b and the host star. Using the coronagraphic mask at 23 μm, which has an inner working angle of 3.3λ/D, would block exoplanets at separations <2.16 arcsecs. Therefore, we instead consider directly imaging the system without a coronagraph and using KLIP [223] in post-processing to recover the exoplanet. KLIP has the potential to improve contrast by approximately $\sim$ 100 times [195].

Figure 3.14 shows the simulated MIRI contrast curve. To create this simulation, we used the pre-made set of point spread functions for JWST MIRI based on the in flight optical performance `WebbPSF` tool[11]. We used the F21000W PSF that includes geometric optical distortions. The contrast curve for KLIP was calculated assuming performance similar to that described in Rajan et al. 2015 [195].

In Figure 3.14, the shaded blue region above the black dashed line indicates the detectable exoplanet parameter space. With 3 hours of observation and using KLIP, a 0.12 $M_{\rm Jup}$planet with an age of 100 Myr with moderate cloud cover would be detectable at separations greater than 1.5 AU. With the same 3 hr integration time, an older (1 Gyr) exoplanet of this size would also be detectable if at wider separations (> 4 AU). This

[11] `jwst-docs.stsci.edu/jwst-mid-infrared-instrument/miri-performance/miri-point-spread-functions`

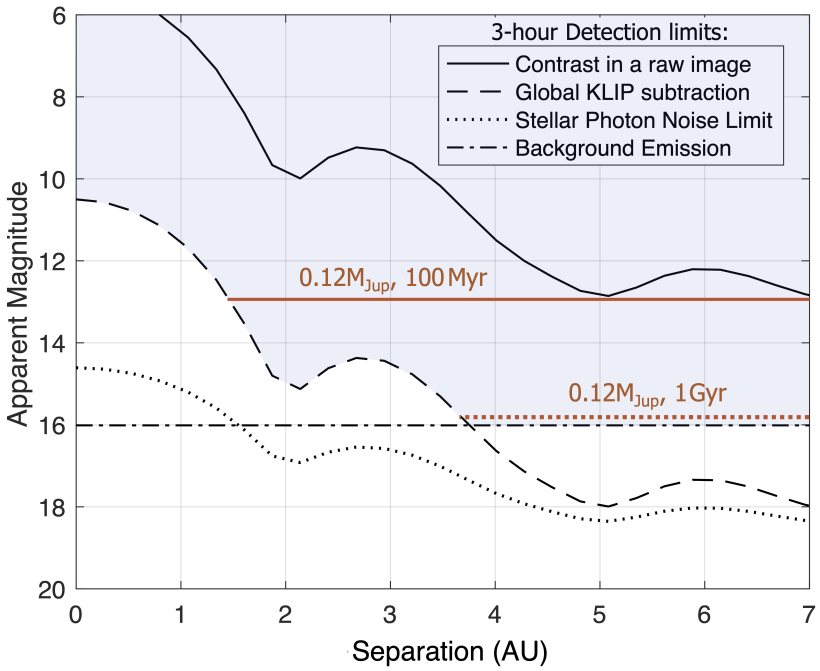

Figure 3.14 **Simulated contrast curve for JWST MIRI broadband imaging at 21μm.** The apparent magnitude of cloudy 100 Myr and 1 Gyr, 0.12$M_{\rm Jup}$exoplanets is shown by the red lines. A cloudy 100 Myr, 0.12$M_{\rm Jup}$exoplanet should be detectable at separations >1.5 AU, and a cloudy 1 Gyr, 0.12$M_{\rm Jup}$exoplanet is detectable at separations >4 AU. For this simulation, we assumed F2100W = 5.3 mag, based on the star's WISE band 4 (λ=22.2 μm) magnitude. *Figure Credit: Mary Anne Limbach*

approach requires an integration time which could fit into the JWST small proposals program and has the potential to detect nearby exoplanets to remarkably low masses.

3.6 Conclusions of the Wolf 359 Survey

We conducted a joint high-contrast imaging survey and radial velocity survey with the goal of constraining long-period companions around the nearby M-dwarf star Wolf 359. We do not rule out or confirm the Wolf 359 b RV candidate as presented by Tuomi et al. 2019 [234].

To define the companion mass upper limits placed by our imaging search, we performed an updated age analysis of Wolf 359 through kinematic age dating, CMD young moving group comparisons, and a MIST stellar isochrone comparison. We draw a conclusion of relative youth from the star's rotation period, and adopt the kinematic age of 1.53 ± 0.3 Gyr as the upper bound for Wolf 359's age. We rule out age estimates that are younger than 112 Myr through the comparison with young moving groups. Our MIST isochrone analysis produced an age estimate of 400 Myr.

We conducted a high-contrast imaging survey using Keck-NIRC2 with the Ms filter ($4.67\,\mu m$) in conjunction with the vector vortex coronagraph. We totalled 4.98 hr of integration time spread across 3 half-nights. The completeness of our imaging survey is highest (95%) for the semi-major axis range from 1-3 AU. Our HCI results rule out a stellar or brown dwarf companion with this semi-major axis range to 5σ, and companions

smaller than $0.4 M_{\rm Jup}$cannot be ruled out at any separation assuming an age older than 100 Myr. We compared our HCI survey's predicted performance as estimated by the NIRC2 SNR Calculator to our measured 5σ performance and found a discrepancy of 1.7 magnitudes for the night of 2021 March 31 (UT). This discrepancy can be partially accounted for by adjusting for the throughput loss when using the vortex at $4.7 \mu m$ and the fixhex pupil stop. Our analysis suggests that the remaining performance discrepancy may be due to the background noise exceeding the expected Poisson-noise level over time, indicating that it may be possible to improve the sensitivity of future surveys using faster image readout to better compensate for changes in the sky background.

We performed an updated radial velocity analyses of Wolf 359 with the `RVSearch` and `radvel` python packages with data from four RV instruments: CARMENES, HARPS, Keck-HIRES, and MAROON-X. After removing the known RV signal caused by the stellar rotation, we detect no signals above a false alarm probability of 0.1%. To 2σ, we exclude planets with a minimum mass bigger than $m_{\rm p} \sin i > 13.5\ M_{\oplus} (0.0425\ M_{\rm Jup})$ with a semi-major axis smaller than $a < 0.1$ AU and planets with a minimum mass larger than $m_{\rm p} \sin i > 147\ M_{\oplus} (0.46\ M_{\rm Jup})$ for a semi-major axis of less than $a < 1$ AU.

We simulated JWST NIRCam and MIRI observations to explore the potential of JWST to directly image ice giant and gas giant exoplanets orbiting Wolf 359. We predict that NIRCam Coronagraphic Imaging could detect a cloudless exoplanet with masses $> 1 M_{\rm Jup}$outside 1.5 AU and $> 0.5 M_{\rm Jup}$outside 4.7 AU with 1 hour of integration time (assuming an age younger than < 1.5 Gyr). Saturn and Neptune-mass exoplanets are

accessible to NIRCam in certain age/separation spaces, and it is unlikely that NIRCam could detect a sub-Neptune mass exoplanet. While MIRI imaging does not perform as well at smaller inner working angles, MIRI is capable of detecting cloudy exoplanets at smaller masses. We predict that a cloudy companion with a mass of $0.12 M_{\rm Jup}$could be directly imaged to 5σ if orbiting outside 4 AU using 3 hours of integration time (assuming an age of younger than 1 Gyr).

This survey of Wolf 359 further establishes the methods needed to comprehensively characterize exoplanet systems using the intersection of multiple measurement techniques. As our future direct imaging instrumentation and RV surveys gain an increased sensitivity to ice giant exoplanets and super-Earths, the Wolf 359 system will continue to be a compelling target for understanding the cold planet population and planet formation outside the snow line of low-mass stars.

Chapter 4

The Future: Prospects for the direct detection of cold ice giants and gas giants orbiting young low-mass neighbors

"You are about to move to an area of the galaxy containing wonders more incredible than you can possibly imagine... and terrors to freeze your soul."

ADAPTED FROM

JWST Cycle 3 Proposal *Cool kids on the block: The direct detection of cold ice giants and gas giants orbiting young low-mass neighbors*

Rachel Bowens-Rubin, Mary Anne Limbach, Aarynn Carter, Steve Ertel, Julien Girard, Philip M. Hinz, Elisabeth C Matthews, Caroline Morley, Sagnick Mukherjee,

Maissa Salama, Andrew Vanderburg, and Kevin Wagner

This program was approved as Cycle 3 GO 6122 as announced Feb 29 2024. https://www.stsci.edu/jwst/science-execution/program-information?id=6122

4.1 Abstract

Cold ice giant and gas giant exoplanets (<200 K, 0.03 - 10 M_{jup}) in systems orbiting low-mass stars (0.08 - 0.45 M_{sun}) could prove to be one of the most common types of exoplanets in the galaxy, yet we currently know of none that we can characterize through direct measurements. This survey presents an efficient pathway to utilize JWST's unique capabilities to accomplish a major objective in the exoplanet observing community: directly imaging a benchmark set of sub-Jupiter mass exoplanets. We propose a survey that has excellent coverage for detecting the under-studied population of ice-giant exoplanets (0.05 M_{jup}), which is out of reach for all but the most tailored JWST direct imaging observations.

We will observe six of the nearest (<6 pc), young (<1 Gyr) M-dwarfs to directly image exoplanets down to temperatures of 75K and as small as Neptune. We select nearby targets to optimize our coverage to the orbits where we expect giant planets to be the most prevalent (1-15 AU). We propose to use F444W NIRCam Coronagraphic Imaging in conjunction with F2100W MIRI Imaging to ensure the detection of clear and cloudy exoplanets. Based on our survey sensitivity and previously measured occurrence rates of

giant planets, we predict a discovery yield of 4.6 (+2.9 -1.9) planets, and nondetections would challenge the existing occurrence rates to 2.5-sigma. Exoplanets identified through this survey will be ideal candidates for JWST spectroscopic follow-up characterization to further understand the formation differences between gas giant and ice giant exoplanets and enable comparative planetology to the giant planets in our own solar system.

4.2 The case to conduct a search for cold sub-Jupiter mass exoplanets at the ice giant/gas giant boundary using JWST

The majority of the stars in our galaxy are M-dwarfs, yet we know little about the exoplanets that exist in these systems beyond the snow line (1 AU; [173]). The probability of an exoplanet transit occurring for an exoplanet orbiting an M-dwarf beyond 1 AU is less than 0.1%. Exoplanets orbiting low-mass stars have longer periods for the same semi-major axis, so astrometry and radial velocity surveys of M-dwarfs require lengthy time baselines to observer a planet's full orbit ($>$ 3 years for a exoplanet with $a = 1$AU around a $0.1 M_{\odot}$ star).

Key mysteries in planetary formation and exoplanet system architecture exist because we lack an observed sample of solar-system analog giant exoplanets to anchor our models. Giant planet formation plays a critical role in the development and the dynamics of the planetary system as a whole because the giant planets hold the majority of the mass.

The number and type of giant planets have been both correlated and anti-correlated with the chances of habitable-zone planets existing in the system [96]. The formation of our own ice giants (Neptune/Uranus) are the hardest solar system planets to explain because of their distance from the Sun [77]. While we have divided our own solar system giant planets into two categories ("ice giants" and "gas giants"), we do not know how artificial this boundary is and have yet to understand if is a typical architecture in other planetary systems. The current framework for understanding exoplanets that are akin to our solar system giant planets is based off of a combination of theoretical models [12, 146, 155] and direct imaging results from a few known cold ($T_{\rm eff} \sim 250$K) brown dwarfs [170, 220]. Characterizing even a small number of cold giant exoplanets could prove invaluable to understanding the intricacies of the role giant planets play in their systems and how our own giant planets impacted the formation of our own solar system [135].

The direct imaging method offers a solution for characterizing exoplanets orbiting outside their snow line. It is the only technique which can reveal a non-transiting exoplanet's atmospheric composition, thermal emission signatures, dynamical mass and precise orbit, surface gravity, and formation history. It can be used to measure chemical abundances ratios like the C/O, N/O, and N/C ratio to determine how the planet was formed (core accretion vs. gravitational collapse) [102, 167]. Direct imaging is also uniquely capable of probing the deepest layers in exoplanetary atmospheres to understand the chemical equilibrium where biosignitures are more likely to be present [151].

While a powerful tool, the use of direct imaging has so far been limited to studying a set

of young ($\leq 500 Myr$), hot ($\geq 600K$), massive ($\geq 2M_{jup}$) exoplanets at wide (> 10 AU) separations that lie on the planet/star boundary and occur rarely ($< 4\%$ occurrence rate; [34]). Thanks to its unprecedented mid-infrared capabilities, JWST offers an opportunity for a paradigm shift. We may now use direct imaging to characterize the cold giant exoplanets ($75 - 200$K) boarding the gas giants/ice giant divide.

Although cold giant planets are currently underrepresented in the set of discovered exoplanets, they are likely to occur in nature in abundance. Microlensing surveys have provided the first hint that ice-giant and small gas-giant exoplanets (0.01 - $3M_{Jup}$) could be extremely common ($1.4^{+0.9}_{-0.6}$ planet per system; [189]). The greatest prevalence is for smaller planets [53, 230] between 1-10 AU [80, 87]. The occurrence rate of Neptune-like planets beyond 10AU has yet to be well constrained, but direct imaging surveys have found that Jupiter-like planets become much more scarce ($\sim 2\%$ for $2-14M_{jup}$ between 8-400 AU, [137]; $< 4\%$ for $> 5-13M_{jup}$ between 30-300 AU [33]). We may expect the ice giant distribution to do the same and tail off outside of 10 AU. Thus, if we wish to design the most efficient survey to locate cold giant exoplanets suitable for characterization, we must focus our surveys between $1 - 15$ AU and favor systems that will give the most sensitivity to the smallest giant planets.

4.3 Survey Method: Observe 6 M-dwarfs with the ideal proximity, youthfulness, and contrast-with-the-host-star to reveal cold sub-Jupiter mass exoplanets

Fewer than two-dozen systems have the needed trifecta of proximity, youthfulness, and contrast-with-the-host-star to allow for JWST direct imaging to have the sensitivity to detect sub-Jupiter mass exoplanets at the orbital separations where they are expected to be most prevalent (1-10 AU; [53], [80]). Proximity makes an exoplanet appear at a wider angle from its host star and causes it to appear brighter from our perspective. A youthful target contains more residual heat-of-formation, and so it will appear brighter in the infrared. The light from an exoplanet orbiting a dim star is easier to detect because there is less of a difference in brightness. I have identified six of the most promising systems where these three factors align.

I present a survey that was simulated for F444W+MASK355R NIRCam Coronagraphic Imaging combined with F2100W MIRI imaging to explore 6 nearby M-dwarfs with known ages younger than 1 Gyr. We elect to simulate both NIRCam coronagraphic imaging and MIRI imaging to estimate the sensitivity to cold exoplanets with both clear and cloudy atmospheres. Exoplanet gas giants with clear atmospheres are bright in the emission band between 4-5μm. As a result, JWST NIRCam coronagraphic imaging will be able to detect exoplanets down to Neptune-like masses with clear atmospheres. However, gas giants with cloudy atmospheres have muted emission in the 4-5μm spectral range,

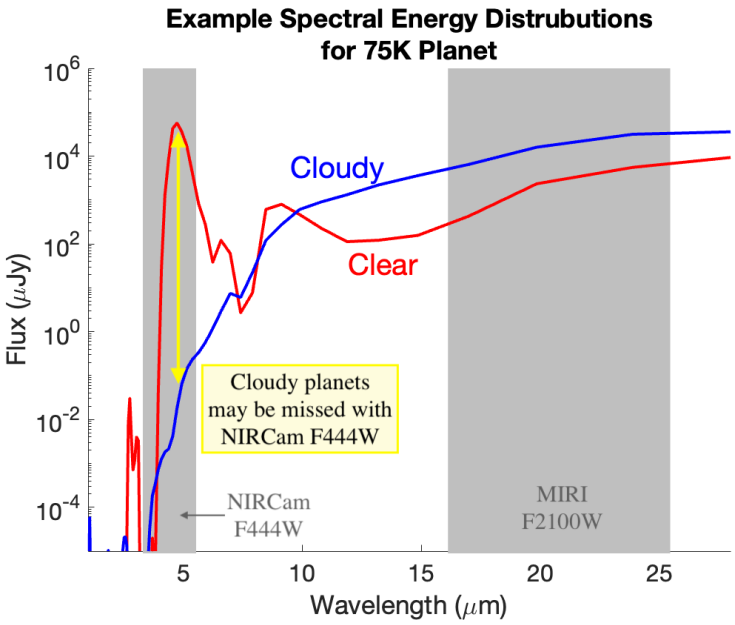

Figure 4.1 **Simulated Spectral Energy Distribution for a 75K Exoplanet**. When observing an exoplanet with a clear atmosphere (*red*), it is favorable to conduct the observation with NIRCam F444W. However, if the planet is cloudy (*blue*), the flux is suppressed at F444W and it is favored to use MIRI F2100W. By using both NIRCam and MIRI, a survey like that explored here can have sensitivity to both cloudy and clear 75K planets. *Custom models in this figure were provided by Caroline Morley.*

instead emitting more flux at longer wavelengths ($>15\mu m$). This is illustrated in Figure 4.1, which demonstrates that exoplanets with cloudy atmospheres can most efficiently be detected with MIRI F2100W imaging. The use of this sort of combined NIRCam/MIRI observing could provide occurrence constraints on giant exoplanets with all types of atmospheres, providing a complete picture for these exoplanet demographics.

Other direct imaging surveys such as those based from the young moving groups are not as sensitive to the ice-giant population ($0.01 - 0.3 M_{jup}$) as the observations explored here. For example, JWST GTO Proposal 1184 [214] and Cycle 2 GO Proposal 4050 [47] observed young M-dwarfs in order to study the cold giant planet population. However, they selected targets that are farther away ($6 - 60$ pc). This limits their ability to see within $a \leq$10 AU, missing the space most likely to host exoplanets outside the snow line.

4.4 Target Selection

We evaluated the six targets summarized in Table 4.1 for the survey. While any of these targets could make a compelling observation on its own, by combining these targets into a small survey, it would be possible to double each science target as a PSF calibrator to increase JWST's observing efficiency. This avoids extra observations of calibrator stars to perform reference differential imaging (RDI) post-processing.

Table 4.1 Target Summary

Common Name	dist. [90]	Type	Age in Lit.	NIRCam (AU) [a]	MIRI (AU) [b]
Wolf 359	2.41 pc	M6	400^{+1100}_{-300} Myr	1.4 - 48.2	2.4 - 47.6
Ross 154	2.98 pc	M3	<1 Gyr	1.7 - 59.6	3.0 - 58.8
DX Cancri	3.58 pc	M6.5	200 ± 100 Myr	2.0 - 71.6	3.6 - 70.7
AD Leo	4.69 pc	M3	25 - 300 Myr	2.7 - 93.8	4.7 - 92.6
EV Lac	5.05 pc	M3.5	25 - 300 Myr	2.9 - 101.0	5.1 - 99.7
YZ CMi	5.99 pc	M5	50 Myr, < 500Myr	3.4 - 11.4	6.0 - 118.2

[a] The AU range corresponding to the NIRCam MASK335R inner working angle (0.57") to 14".

[b] The AU range from 1" to the edge of the MIRI field of view with the SUB256 subarray (28.2").

Wolf 359 is the fifth closest star system to Earth (2.41 pc) and the closest in our sample.

This system was the subject of the ground-based survey discussed in detail in Chapter 3 of this thesis.

Ross 154 is the ninth closest star system to Earth (2.98pc). It is an M3V flare star and has been age dated to be < 1 Gyr using measurements of its rotation period [242]. Ross 154 has no disk or confirmed exoplanets but is being monitored using radial velocity with ESO/HARPS [234] and CARMENES [200]. Companions more massive than $35 \pm 4 M_{jup}$ orbiting between 4-30 AU were ruled out through the GTC/CanariCam observations [94].

DX Cancri is an M6.5Ve [150] located at 3.58 pc. It was identified as part of the Castor moving group (age 200 ± 100 Myr [139], [16]). DX Cnc has no disk or confirmed exoplanets. Companions more massive than $35 \pm 4 M_{jup}$ between 3-36 AU have been ruled out [94].

AD Leo is an active M3 star located at a distance of 4.97 pc. It has been age dated to 25-300 Myr based on the lack of Lithium in spectrum and its X-ray emission properties [218]. It was been monitored using radial velocity with ESO/HARPS and Keck/HIRES [234] and GIARPS [46] but has no confirmed disk or exoplanets.

EV Lac is a M3.5 flare star located at a distance of 5.05 pc. It has been age dated to 25-300 Myr based on the lack of Lithium in spectrum and its X-ray emission properties [218]. It is being monitored using CARMENES [200] but has no confirmed exoplanets.

YZ CMi is a M5 flare star located at a distance of 5.99 pc. It has been age dated to be

49 ± 1 Myr [133,163]. YZ CMi is a candidate member the Oceanus young moving group but shows a brightness excess confirming its youth relative to the moving group (age < 500 Myr) [89]. It is being monitored with CARMENES [200] but has no confirmed exoplanets.

4.5 Observation Mode

JWST provides the only platform to directly detect and characterize cold ice giant and gas giant exoplanets (< 200K). We elected to simulate NIRCam Coronagraphic Imaging in conjunction with MIRI imaging to explore the widest distribution of orbital semi-major axes possible for both cloudy and cloudless exoplanets.

We suggest that JWST conducts this search using two groups of non-interruptible sequences. Each grouping pairs the NIRCam and MIRI observations of three targets. This minimizes the JWST PSF drifts so that the targets can act as PSF references for each other for RDI post-processing. If a detection is made in only one of the NIRCam/MIRI images but not the other, this pairing also ensures that we are able to accurately locate the position of the companion in the opposite image.

4.5.1 NIRCam Coronagraphic Imaging

We explore using NIRCam with the F444W filter in conjunction with the MASK335R coronagraphic mask to estimate the sensitivity to clear-atmosphere exoplanets. We select

this mask because it has the best target acquisition performance [108] and provides a smaller inner working angle than the MASK430R. In JWST NIRCam observations, the observer gets to select both a short and long wavelength filter during single observations. We suggest F200W as the short wavelength filter because F200W will have the best contrast of the short filter options for cold exoplanets.

We simulated multiple observations with different exposure times using `PanCAKE` in F444. We found that a 50 min integration provided an average sensitivity to detect ice giants with a mass of $0.1 M_{jup}$ by a separation of 10 AU. Shorter integrations could not provide the sensitivities to detect exo-ice giants while longer integrations did not significantly affect the types of planets that would be detectable.

To increase JWST's observing efficiency, we assumed a survey that would double each science target as a PSF calibrator, thus the survey will be internally self-referencing. We simulated using the small grid dithering that was recommended by the ERS team [108], a 9-point dither pattern. We suggest the MEDIUM8 readout to reduce exposure times as compared to deeper readouts to avoid risks from cosmic ray hits. We elected to simulate 8 groups and 4 integrations to reach the desired exposure time. When dithered in 9 positions, this will produce 36 images, which is sufficient to form a PCA library for post-processing RDI PSF subtraction. This survey will adopt the Sub320A335R subarray as this program since it is focused on measuring the area of sky closest to the star and does not require a field of view beyond 20 arcsec.

4.5.2 MIRI Imaging

We elect to explore MIRI imaging to obtain sensitivity to cloudy-atmosphere exoplanets down to Neptune-like masses. Although the diffraction limit of JWST at 21 μm is 0.67 arcsec, the inner working angle of the 23 μm coronagraphic mask is 3.3λ/D. Even for our closest target, the coronagraph would block exoplanets at separations <2.16 arcsecs. Therefore, we instead examine F2100W direct imaging of the system without a coronagraph.

The implementation of referential differential imaging will allow for detection of cold giant planets close to the host, with the potential to improve our contrast by approximately $\sim 100\times$ [195]. At 1 arcsec, we expect a contrast ratio of 1:2500. Although this contrast ratio at first seems low, it corresponds to detection of a small gas giant with a median mass and separation of $0.25 M_{jup}$ at 4 AU for our sample. The contrast ratio between the host and cold exoplanet is low because in the mid-infrared, the planet's emission is increasing and the star's emission is decreasing.

We model observing each of the six systems with MIRI imaging for a total integration time of 50 min in the F2100W filter. This integration time was selected so that the average sensitivity of our survey would reach $0.1 M_{jup}$ by 10 AU. Our targets are very bright at F2100W, and the FULL detector array cannot be readout without saturation so we find we must use the SUB256 array. We model observations assuming a 2-point dither pattern and the FASTR1 readout pattern.

4.6 Predicted Sensitivity & Survey Yield

4.6.1 Modeling Synthetic Spectra for Stars and Planets

To evaluate the contrast of a theoretical exoplanet compared to its host star, we created synthetic spectral models from 0.5 to 30 microns. For stellar spectra, we adopted the *Phoenix stellar models* [3]. We generated models for exoplanets with masses between $0.06M_{Jup} - 1M_{jup}$ ($20M_e - 318M_e$) for ages spanning 100 Myr - 1 Gyr with both clear and cloudy atmospheres. To generate the clear models to simulate the NIRCam observations, we used the `PICASO 3.0`, [17] which are cloud-free 1D radiative-convective-thermochemical equilibrium models. We assumed solar metallicity and C/O ratio. We estimated the T_{eff} and radius using the Linder et al 2019 [146] evolutionary tracks and linearly extrapolated along the age axis when needed. To simulate cloudy exoplanets for our proposed MIRI F2100W imaging, we used custom cloudy models [142,154,168,169,213] to model the spectra of the planets.

4.6.2 Modeling the Expected Contrast

Because stars are orders of magnitude brighter than an orbiting exoplanet, exoplanets are less detectable via direct imaging when they are closer to their host star. To simulate the NIRCam Coronagraphic Imaging, we used the `PanCAKE` python package [52] to generate contrast curves with a 5σ detection threshold. `PanCAKE` is based on the official JWST exposure time calculator (ETC) `Pandeia` but allows the user to simulate contrast curves

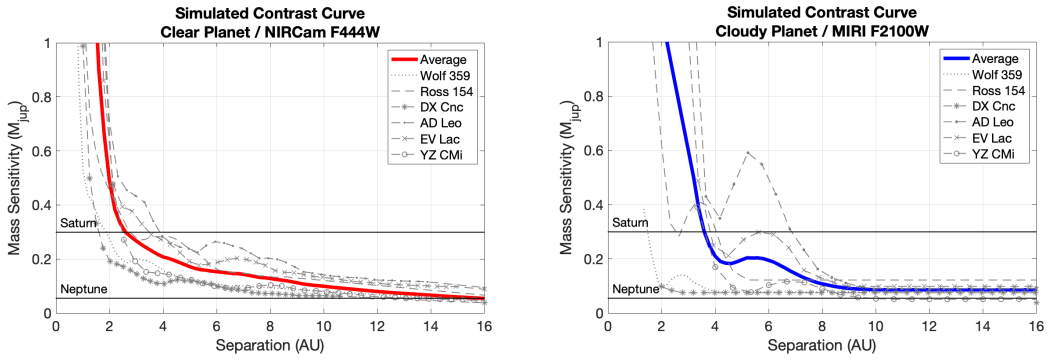

(a) Simulated NIRCam Contrast

(b) Simulated MIRI Contrast

Figure 4.2 **Sub-Saturn Detectability with NIRCam and MIRI:** The average 5σ sensitivity of our NIRCam coronagraphy observations could probe clear-atmosphere sub-Saturn exoplanets outside of 2 AU and reach $< 0.1 M_{jup}$ sensitivities by 10 AU on average. The simulations were made using `PanCAKE` and the mass sensitivities were calculated using the Linder et al. 2019 models. The 5σ sensitivity of our MIRI imaging observations could probe cloudy-atmosphere sub-Saturn exoplanets outside of 4 AU and reach $< 0.1 M_{jup}$ sensitivities by 8.5 AU. These observations reach sensitivity to sub-Saturn exoplanets in the regions where they are expected to be most prevalent (< 15 AU).

for coronagraphic imaging after inputting the specifics of the target acquisition, the parameters of the reference observations, the PSF subtraction style, and the expected wavefront error. Figure 4.2a shows our simulated contrast curves for our six NIRCam observations if probing a clear-atmosphere exoplanet. We adopted an integration time of 50 min total with a 9-point small grid dither and RDI PSF subtraction.

Figure 4.2b shows our simulated contrast curves for our six MIRI observations if probing a cloudy exoplanet. To generate the MIRI contrast curves, we used the pre-made set of PSFs for JWST MIRI based on the in flight performance `WebbPSF tool`. We used the F21000W PSF that includes geometric optical distortions. The contrast curve for RDI (KLIP) was calculated assuming performance similar to that described in Rajan et al. 2015 [195].

4.6.3 Survey completeness & planet yield

We calculated the completeness of the 6-star survey to detecting planets at an array of masses and orbit semi-major axes using the Exoplanet Detection Map Calculator (`Exo-DMC`) python package [27] (Figure 4.3). We find that the survey has the following average sensitivities to ice giant planets corresponding to the range quoted for the Poleski+2021 occurrence rate (5-15 AU, 0.01-0.3 M_{jup}; $1.4^{+0.9}_{-0.6}$ ice giants per star): clear-planets with NIRCam = 52%, and cloudy-planets with MIRI = 56%. If the microlensing occurrence rates are accurate, we estimate a discovery yield of $4.6^{+2.9}_{-1.9}$ planets found through these observations. If no planets are detected, our results will challenge the

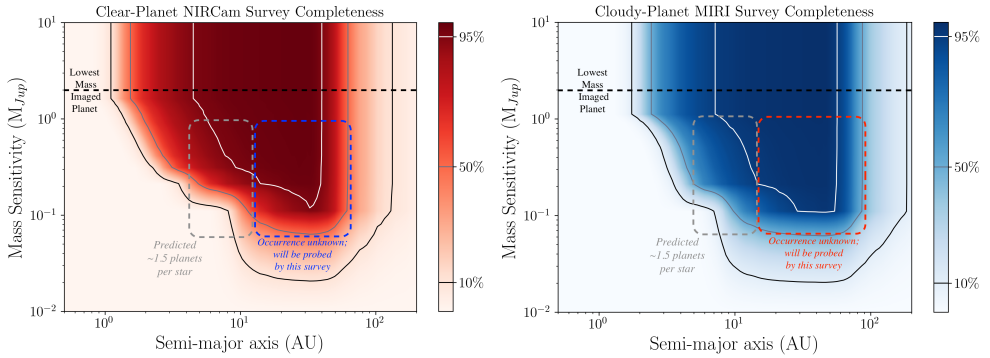

(a) Sensitivity to Clear Planets with NIRCam

(b) Sensitivity to Cloudy Planets with MIRI

Figure 4.3 **Survey Sensitivity:** We predict the survey sensitivity using our simulated 5σ contrast curves and the `Exo-DMC` python package for NIRCam and MIRI. We find our average survey coverage to be 54% for the area corresponding to the Poleski+2021 occurrence rates ($1.4^{+0.9}_{-0.6}$ planets per system; [189]) with a yield of $4.6^{+2.9}_{-1.9}$ planets. These observations could also probe the occurrence rate of the unexplored population of giant planets $0.05 - 1 M_{jup}$ from $15 - 50$ AU.

Poleski et al 2021 [189] microlensing occurrence rate to 2.5σ.

Outside of 15 AU, there are no occurrence rate measurements for sub-Jupiter exoplanets. Our survey is designed to probe the $0.1 - 1 M_{jup}$ mass space and $15 - 50$ AU semi-major axis space to $> 50\%$ completeness and will begin to establish the occurrence rates in this region.

False-Positive Vetting: Our first check to vet for false-positives will leverage our mutli-

color observing. In this proposal, we will observe using two NIRCam filters (F200W and F444W) and one MIRI filter (F2100W). This provides a basic check to see if the expected exoplanet spectral energy distribution is consistent with the measured photometry.

For future vetting, multi-epoch observations could be used to vet a candidate by repeating an observation at a later time. The nearby stars in our sample have very high proper motion and background objects will be stationary, so if the system is observed only a few months later, there will no longer be a chance alignment. The signal is unlikely to be caused by a background contaminant if the planet candidate's location remains consistent with respect to the host star.

4.7 Cycle 3 GO 6122

The *Cool Kids on the Block* program was approved as outlined in this chapter as part of JWST Cycle 3, General Observer 6122. The public pdf summarizing the observations can be found at `https://www.stsci.edu/jwst/science-execution/program-information?id=6122`. The survey will be performed by JWST between July 2024 - July 2025.

Part II

Instrumentation

Chapter 5

Emerging technologies and resources for building adaptive secondary mirror based adaptive optics systems

"There's theory... and then there's application. They don't always jibe."

5.1 The importance of adaptive optics to high-contrast imaging

Advanced ground based telescopes use adaptive optics (AO) to correct the blurs created by the atmospheric turbulence when the light travels through the air down to the telescope. Without adaptive optics correction, large telescopes would be limited to re-

solving objects at the separation of the atmospheric seeing at the site rather than the diffraction limit of the telescope. An ideal adaptive optics system can let its telescope on the ground take sharpened images as if it were imaging from space. Figure 5.1 shows a demonstration of the adaptive optics system at the W.M. Keck Observatory in use to correct the image of Uranus.

In an adaptive optics system, the light bounces off of a *deformable mirror*, which physically changes shape to correct the wavefront (Figure 5.2). The information for what shape the deformable mirror should morph into is collected by the *wavefront sensor* and then processed by a *real time control system*. The correction information is then fed back by the real time control system to the deformable mirror. To use a metaphor from Dr. Nour Skaf, the wavefront sensor is "the heart" which steers the system, the real-time control is "the mind" which computes what needs to be done and sends commands, and the deformable mirror is "the body" that performs the action.

The perfect adaptive optics system would completely correct the PSF shape to its ideal form.[1] If the telescope has a circular aperture with no central obscuration, the PSF shape that will be produced is an *Airy pattern* with a diffraction-limited core containing 84% of the light within the PSF radius of $1.22\lambda/D$, where D is the diameter of the telescope. [82]. When the AO system is not perfect (as no AO system is), some uncorrected residual seeing-limited halo is expected to fall in the radius of λ/r_0, where r_0 is the Fried parameter size of the air turbulence.

[1] The point spread function (PSF) is the image shape of a point-like source (like a star or a planet) after its passed through the telescope and instrument optics at a specified wavelength.

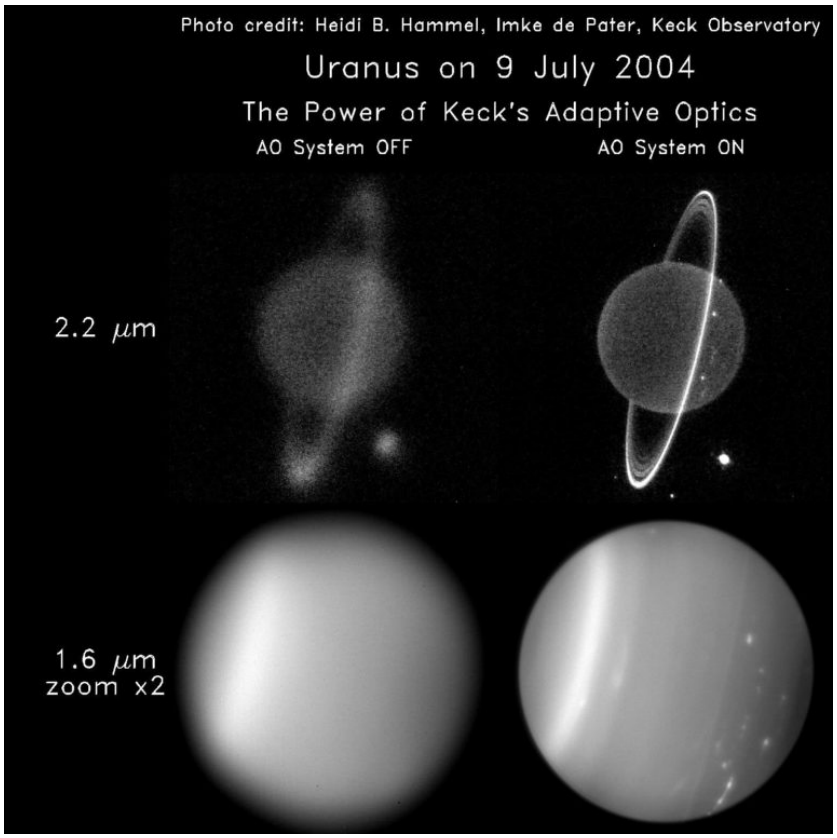

Figure 5.1 **Example of Adaptive Optics use at Keck**: *(Left)* Uranus is blurry without the Adaptive Optics system turned on. *(Right)* When you turn on the AO system, you can resolve feature in Uranus' rings and its atmosphere. (*Figure Credit: Heidi B. Hammel & Imke de Pater*)

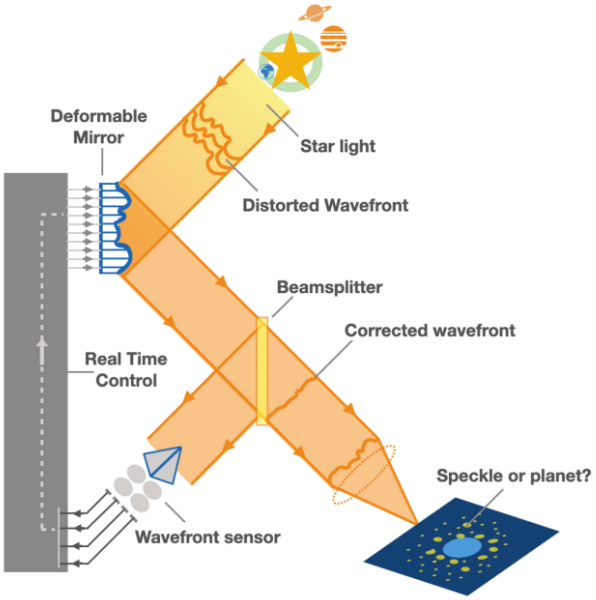

Figure 5.2 **Overview of an Adaptive Optics System**. An image is distorted as it passes through the atmosphere and the optical system of the telescope. A deformable mirror is used to correct the wavefront, restoring the shape of the PSF as closely as possible to its original form. *(Figure Credit: Nour Skaf; [219])*

Non-uniform uncorrected aberrations can also appear as speckles that can impersonate as a companion. These speckles are particularly troublesome when they appear on the timescale of the observation, as post-processing algorythms may not be sufficent to remove them. High wind speeds can also effect the PSF shape non-uniformly and cause a misshapen seeing-limited halo that is difficult to remove in post processing. If a coronagraph is being used, the amount of light concentrated within the PSF radius behind the central obscuration will affect the total suppression of the light and dictate the final contrast limits.

Our capabilities to perform exoplanet direct imaging is critically tied to the performance of the adaptive optic system. In summary, having a well performing adaptive optics system is important because:

1. The PSF of the exoplanet will be concentrated, helping the dim point source be detectable.
2. There will be less background light in the seeing-limited halo from the star.
3. Persistant speckles on the timescale of the observation will be less present. This decreases the chances of a false-positive detection.
4. If a coronagraph is in place, more light can be suppressed by the coronagraph improving the contrast limits.

5.2 The consequences of deformable mirror choice to the adaptive optics performance

When designing an adaptive optics system to meet our science needs, the community simulates and measures the performance using an error budget. The AO error budget is often expressed in *the total residual wavefront error* (σ_{tot}) which quantifies the optical path differences/changes in phase due to variations in the index of refraction from the air turbulence. The total wavefront error can be broken into different physical contributing factors and summed:

$$\sigma_{tot}^2 = \sigma_1^2 + \sigma_2^2 + \sigma_3^2 + ... \tag{5.1}$$

where σ_n represents the wavefront error from a physical effect.[2] There are two physical effects that are part of a standard adaptive optics error budget that depend on the performance of the deformable mirror: the *fitting error* and the *temporal error* [228]. The *drift error* can also affect long baseline observations (usually non-adaptive optics corrected).

The fitting error (σ_{fit}) represents how close the mirror can replicate the shape of the turbulence it is attempting to correct. It can be modeled by:

[2] For more information, see course notes by Claire Max for Astr 289 UCSC; https://www.ucolick.org/~max/289/

$$\sigma_{fit}^2 = k \left(\frac{D}{r_0} \right)^{5/3} N^{5/3} \tag{5.2}$$

where D is the telescope diameter, N is the number of actuators in the deformable mirror, k is the fitting parameter based on the surface type of your deformable mirror (continuous/segmented), and r_0 is the Fried parameter coherence length of the atmospheric turbulence that depends on the observing conditions. Typically, the projected actuator spacing on the primary mirror of the telescope should be smaller than the Fried parameter length to keep the fitting error term ignorable. The Fried parameter is wavelength dependant ($\propto \lambda^{6/5}$), decreasing with size with shorter wavelengths. Thus, a visible light adaptive optics system will require more actuators to get the same correction as compared to infrared.

The temporal error (σ_{temp}) is the error caused by the lag of your adaptive optics system and can be modeled by:

$$\sigma_{temp}^2 = \left(\frac{\tau}{0.314\, r_0/v} \right)^{5/3} \tag{5.3}$$

where τ is the time lag in the adaptive optics loop and v is the wind speed at your observing site. The time lag (τ) can be affected by how fast the actuators in a deformable mirror can move into a commanded position if the actuator speed is on the same order as the goal operation speed.

The drift error (σ_{drift}) represents the instability occurring over the duration of an observation due to an environmental change (i.e. shifting temperatures, changes in the gravity orientations of the telescope, etc). If the deformable mirror cannot hold its shape under conditions changing at the telescope to the precision required by the science, the optical drift could become a large contributor to the error budget. Drift may become most relevant in the cases where the observation is being conducted with the deformable mirror holding a static shape (operating without adaptive optics correction).

In addition to these AO error budget terms, the deformable mirror must be able to meet the basic operational requirements for existing at the observatory. These include but are not limited to the following:

- The deformable mirror must have the necessary mechanical stroke to be able to keep up with the tip/tilt corrections for the observing site (typically $<\sim 20\mu$m of stroke needed).[3]
- The DM must have a large operating range for temperature (-40F to 100F) and humidity or be placed inside a system to regulate these factors.
- The DM must be able to hold a static position in an open loop configuration when the wavefront cannot be measured.
- In the case where the deformable mirror is part of the telescopes main optics, the electronics/control cables for the DM must be simple enough to be wrapped through the telescope's cable wrap or be mounted to the telescope.

[3]The mechanical stroke length requirement can be calculated by $\frac{3\lambda\sqrt{l}}{2\pi}\left(\frac{D}{r_0}\right)^{5/6}$, where λ is the wavelength, D is the telescope diameter, r_0 is the Fried parameter, and $l = 1.03$ if the DM must compensate for the tip/tilt ($l = 0.134$ if there is a separate tip/tilt corrector). [228]

- The DM must be reliable and work across the lifetime of the observatory/science instrument (typically 5+ years)

To summarize, the deformable mirror must meet the basic operating requirements (listed above) as well as the science case's need for the number of actuators, temporal response, and drift conditions.

5.3 Why use an adaptive secondary mirror in your adaptive optics system for exoplanet direct imaging?

In a traditional AO system, the deformable mirror is added as part of a set of extra optical components post focal plane. In the example case of the W.M Keck Observatory's Keck-II Telescope, the AO system adds seven reflections after the tertiary mirror for a total of ten reflections. Each time the light interacts with one of the optics, it gains a small amount of thermal noise from the emissivity from the optic. For example, Hinz et al 2020 [109] estimated the emissivity of the Keck optical path to be ∼30%. At some infrared wavelengths, the background flux from the optical train dominates over the sky background (see Figure 5.3).

Replacing the static secondary mirror with an adaptive secondary mirror (ASM) provides a method to integrate the AO system directly into the telescope, removing the need for as many extra optics. Hinz et al 2020 estimates that an ASM based AO system could reduce the emissivity contribution to ∼12% at Keck.

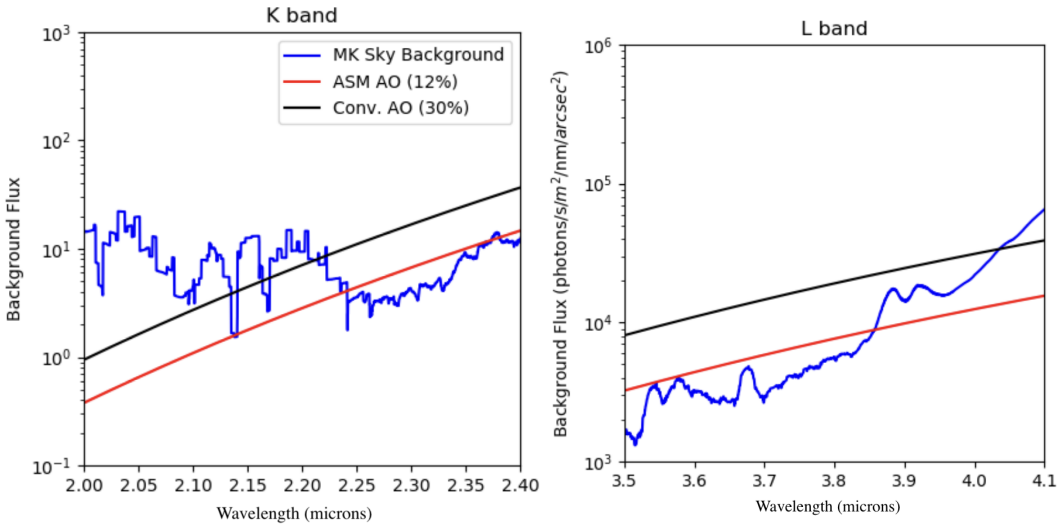

Figure 5.3 **Emission of the Maunakea sky background as compared to the emissivity of the current Keck AO system and an ASM based Keck AO system.** At some wavelengths, the emission of the adaptive optics system/telescope (*black*) dominate over the sky emission (*blue*). An ASM based AO system (*red*) offers a way to reduce the thermal noise added by the optical system. These plots are part of a simulation performed by Hinz et al 2020 [109].

For more broad use beyond the thermal background benefits, an ASM is also advantageous for building an AO system for wide-field/ground-layer correction. Incorporating an ASM can also be a method for moving to a higher actuator counts to reduce the fitting error because a larger area for actuator packing can reduce some engineering complexities.

5.4 The current generation of voice-coil based adaptive secondary mirrors

5.4.1 Overview

ASM based adaptive optics systems have been proven successful at telescopes like the Large Binocular Telescope [79], Magellan [63], the VLT Observatory [20], and the MMT Observatory [244]. These ASMs were built by AdOptica (Microgate/ADS) and are based around *voice-coil* style actuators.

The voice-coil actuators inside the ASMs operate by generating an electric current to control a magnetic field (via the Lorentz force) [228]. Each actuator is mounted across a small airgap from a corresponding magnet glued to the back of the mirror's facesheet (see Figure 5.4). The amount of applied current sets the position of the deformable mirror.

The feedback and control indentifies the position of the actuators using contactless ca-

pacitive sensors that are integrated with the mirror and real-time control software. The glass-facesheet is constructed to be relatively thin ($\sim$ 2mm) because of the limitations for the actuators to produce large amounts of force without generating excessive heat.

The AdOptica voice-coil based deformable mirrors have been the astronomical community's go to technology for building ASMs for the past decades. They currently hold the future contracts for building large-format deformable mirrors for the GMT [93] and the ELT [40].

5.4.2 Limitations

In the floating shell design for the voice-coil based technology, the facesheet and actuators have a contactless gap. The actuators provide no stiffness to damp out oscillations on the facesheet, making the shell analogous to a drumhead that can ring [203]. This can also be a safety concern if the mirror is trying to operate in high winds, as the facesheet can "ripped" from the actuators. The small gap is also a potential area of contamination in an observatory enviroment where dust, debris, and moisture is common.

The heat dissipation of the voice-coil actuators requires an active cooling system. Past AdOptica ASMs have incorporated glycol-based cooling systems. In February 2016, the Magellan ASM glycol cooling systems failed in a disastrous way that caused liquid to leak onto optics of the telescope [171]. LBT also experienced a leak when a wire overheated and melted the glychol cooling system tube. Recent AdOptica designs have now moved

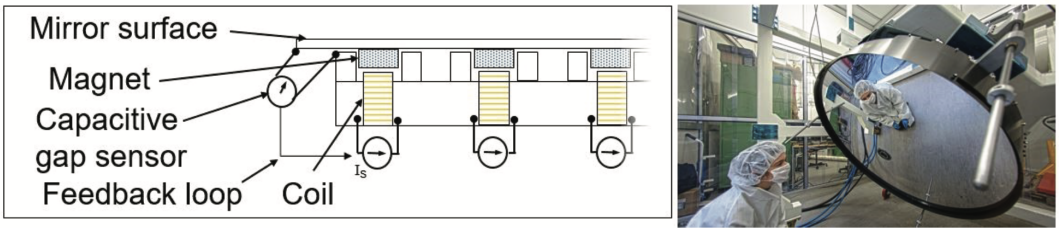

Figure 5.4 **Voice Coil Actuator Overview.** *(Left)* A diagram of the layout of a voice-coil based large-format deformable mirror from AdOptica *(Right)* The VLT ASM constructed by AdOptica. *(Figure retrieved from Strobele 2020; [228])*

away from glycol cooling towards an air-based CO_2 cooling system [93].

The mirror surface of the ASM at the LBT has been found to collect dust in patterns that resemble the magnet mounting. It is suspected that the magnets in the ASM attract magnetic dust due to being close to the surface of the shell.[4]

5.5 A growing alternative: hybrid-variable reluctance actuator based adaptive secondary mirrors

5.5.1 Overview

The Netherlands Organization for Applied Scientific Research (TNO) has made significant breakthroughs in large-format deformable mirror technology that could enable adaptive secondary mirrors to become simpler and less costly to operate. The key ad-

[4]This information was provided in direct correspondence with Amali Vaz.

vancement is a new style of hybrid variable reluctance (HVR) actuator that is ∼75 times more efficient than traditional voice-coil actuators (HVR actuator efficiency [128] $= 38N/\sqrt{W}$; MMT and LBT actuator efficiency [204] $= 0.5N/\sqrt{W}$).

A hybrid-variable reluctance actuator operates by combining variable reluctance and permanent magnet technologies to generate motion. The rotor moves towards positions of minimum magnetic reluctance, driven by the magnetic field created by current flowing through coils of wire around soft iron and enhanced by constant magnetic fields from the permanent magnets. Because magnetic flux passing through reluctance does not give rise to dissipation of heat like it does for a current encountering resistance, the heat generated in the HVR actuators is minimal.

The soft iron is attached to a strut that leaves the actuator and is bonded to the back of the mirror facesheet. The strut holds the facesheet in a fixed position (Figure 5.5), eliminating the air gap required with the voice-coil actuator technology. A diagram and photo of the 2020 generation TNO HVR actuator is shown in Figure 5.6. The force output of the 2020 HVR actuators is ±8N over a linear range (99.5%) before entering in magnetic saturation and can go up to a maximum force of ±14N when fully magnetically saturated.

Traditionally, the facesheets of adaptive secondary mirrors have been made by grinding a thick piece of glass into a thin shell of the correct optical prescription. This process is time consuming and costly. The facesheets for the HVR-based deformable mirrors

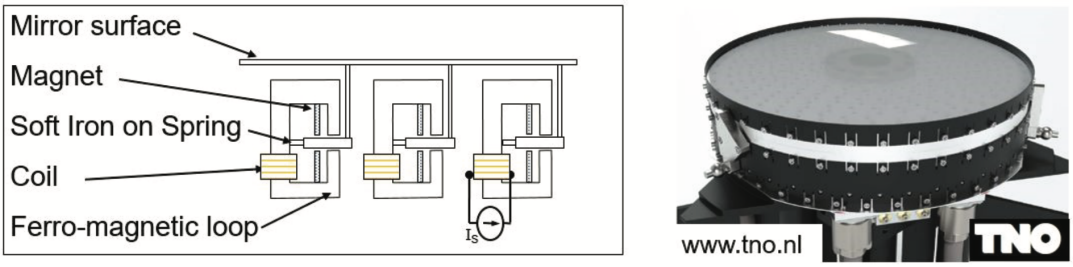

Figure 5.5 **Hybrid-Variable Reluctance Actuator Technology Overview.** *(Left)* Simplified diagram of the HVR actuator technology *(Right)* The CAD rendering of the UH2.2m ASM. *(Figure retrieved from Strobele 2020; [228])*

are being constructed using a different approach, starting with a flat piece of glass and slumping into the correct prescription using a hot thermal forming process. The University of California Observatories has been aiding in the development of this manufacturing process by experimenting with "free-form" glass slumping techniques that do not require the use of a mold [110]. Because the cost of flat glass blanks is low and there is no cost for manufacturing a mold, free form slumping could lower the costs significantly for making the specialized facesheets required.

TNO developed the procedure and tooling for replacing non-working actuators. This procedure was demonstrated by replacing an actuator in the FLASH mirror prototype in less than a day.

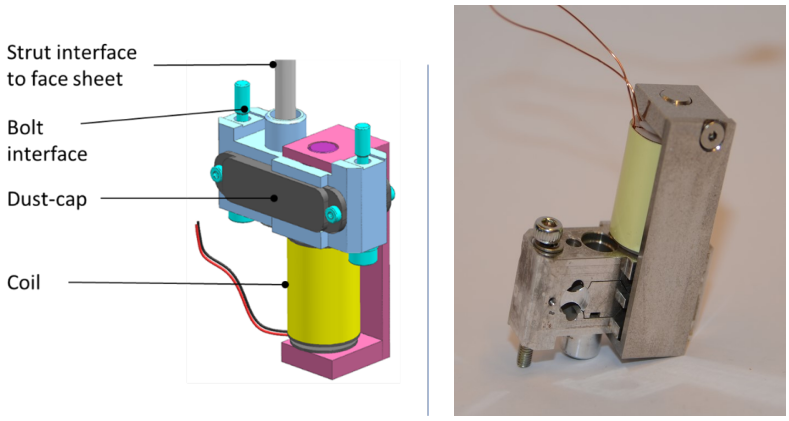

Figure 5.6 **TNO's 2020 version of the HVR Actuator** (*Left*) CAD model of the TNO HVR Actuator designed for FLASH and the UH2.2m adaptive secondary mirror. (*Right*) A picture of the realized FLASH actuator from the batch manufactured in November 2020.

5.5.2 Limitations

While the TNO large-format mirrors show great potential to make advanced adaptive optics systems accessible to a wide variety of observatories, they have yet to be proven to the astronomical community. At the time of this writing, the technology has not been deployed in an on-sky application. Delays in fabricating the ASMs have been experienced, and there is no guaranteed technology pathway to making an ASM at the size needed to fulfill the needs of the 8-10m class observatories. To help close this gap, a partnership has been formed between TNO, University of California Observatories, the University of Hawaii, and NASA to push the technology development.

In Chapter 6, I present my original research to conduct testing of the TNO deformable

mirror lab prototypes in order to explore the potential and limits of the technology. In Chapter 7, I review the HVR-based adaptive secondary mirrors in progress and discuss the planned pathway to the technology adopted at 8-10m class observatories. By increasing the technology readiness for the HVR-based deformable mirrors, observatories of all sizes may someday be able to adopt an adaptive optics system with the deformable mirror incorporated into its optical train.

5.6 Requirements for ASMs at major observatories

Figure 5.7 summarizes a comparison between the HVR based and voice-coil based technology. While the HVR technology shows potential to ease the building and implimentation of ASMs (particularly in the areas of cooling, shell manufacturing, and the control needed for shell damping), the HVR mirrors have yet to be proven on sky.

As we consider the technology tradeoffs between these two approaches for building large-format deformable mirror, it is worth considering what future science programs may need at major observatories. Ströbele et al 2020 [228] defines the requirements for a deformable mirror in a planet-hunting instrument at an 8m-class telescope as follows:

- Number of actuators: 700-4000
- Pitch: 0.4-30mm
- Mechanical Stroke: 2-10μm
- Control frequency: 1000-2000 Hz
- Actuators resolution: $<$ 0.1nm

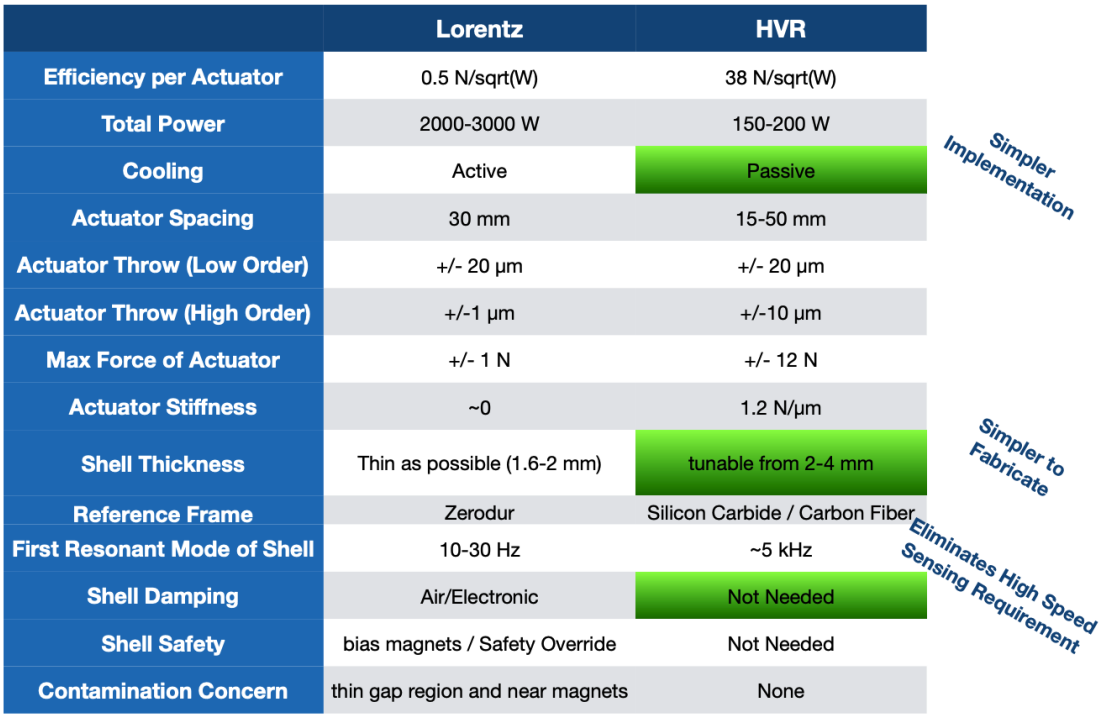

Figure 5.7 **Comparison of the contruction of the Lorentz Voice-Coil DMs with the Hybrid-Variable Reluctance DMs.** *(Figure Credit: Phil Hinz)*

Both technologies so far appear capable of meeting these needs. However, it should be noted that the TNO technology has yet to be proven to run at speeds greater than 1kHz.

The European Extremely Large telescope's (E-ELT; primary mirror 39.3m) M4 deformable mirror will require an evolution beyond the current large-format deformable mirror technology. Ströbele et al 2016 [229] presents the criteria for the performance of the E-ELT adaptive M4 mirror for two expected science cases (Figure 5.8; [229]). This study considered the requirements for a 'compact DM" where the DM will be controlled in open loop across many observing channels as well as a "XAO-DM" that can perform

extreme adaptive optics correction with high actuator count (11,000 to 20,000 actuators) at high speeds (> 1khz) to directly image exoplanets.

At the end of the next chapter, I will use the criteria provided by Ströbele to comment on the strengths and weaknesses of the performance of the TNO deformable mirrors.

Description	Specification value : Compact DM	Specification value : XAO-DM
DM clear aperture	Ø30mm-100mm, goal Ø45mm.	Ø150mm-450mm, goal Ø270mm. Annular shape with 24% central obscuration
Mirror surface Flatness	<15nm rms, stability of < 21nm rms within 1h	10nm rms, goal 5nm rms, after subtraction of few low order modes(Z4 to Z11)
Actuators count within the clear aperture	2800 to 5000	11 000, goal 20 000
Actuators pitch (derived information, no specification)	0.4mm-1.7mm	0.9mm – 3.7mm
Lowest mechanical resonance frequency (causing a mirror surface deformation)	>500Hz	>1000Hz, goal >2000Hz TBC
Actuators Stroke	>5µm (goal >8µm) (5by5)	>3µm (3by3)
Actuators resolution	-	<0.1nm goal < 0.06nm
Inter-actuator stroke	>1.3µm	>1.2µm
Small stroke settling time incl. latency of the drive electronics	250nm settling to ±10% within 700µs	50nm settling to ±10% within 150µs, goal 100µs
Hysteresis	Included in the linearity spec.	5%
Actuators non-linearity	<3% Goal <1%	<5% Goal <1%
DM surface temperature incl. Housing: deviation from ambient	<±1ºC	<±1ºC
Update frequency of the DM command	200Hz goal 500 Hz	2500Hz goal 4000 Hz
Nonfunctioning actuators. The exact numbers depend on the failure mode.	10-50, goal 0	5-30, goal 0

For both DM types the drive electronic is part of the development. In the following some key specifications are discussed in more detail.

Figure 5.8 **Summary of the DM requirements for the E-ELT as presented in Stroebele et al 2016** [229]. The "compact DM" and "XAO-DM" refer to two types of science cases for E-ELT instruments. XAO-DM refers to the extreme adaptive optics case for exoplanet direct imaging.

Chapter 6

Current performance and limitations: Laboratory testing of HVR-actuator based large-format deformable mirror technology

"Let's see what a Galaxy-class starship can do!"

ADAPTED FROM 3 PROCEEDINGS:

Performance of large-format deformable mirrors constructed with TNO variable reluctance actuators.

Rachel Bowens-Rubin, Philip Hinz, Wouter Jonker, Stefan Kuiper, Cesar Laguna, and

Matthew Maniscalco. *In Adaptive Optics Systems VII, volume 11448 of Society of Photo-Optical Instrumentation Engineers (SPIE) Conference Series, page 114485V, December 2020.*

Performance of large-format deformable mirrors constructed with hybrid variable reluctance actuators II: initial lab results from FLASH

Rachel Bowens-Rubin, Philip Hinz, Stefan Kuiper, and Daren Dillon.

In Techniques and Instrumentation for Detection of Exoplanets X, volume 11823 of Society of Photo-Optical Instrumentation Engineers (SPIE) Conference Series, page 118231R, September 2021.

Performance of large-format deformable mirrors constructed with hybrid variable reluctance actuators III: laboratory measurements of dynamic behavior

Rachel Bowens-Rubin, Abraham Marsh, Philip Hinz, Caesar Laguna, Arjo Bos, Stefan Kuiper, Max Baeten.

In *Proceedings of AO4ELT7, 2023.*

6.1 Overview of the TNO DM3 & FLASH Prototype Deformable Mirrors

6.1.1 57-Actuator DM3

The DM3 is the third prototype large-format deformable mirror from TNO (Figure 6.1) and was constructed for lab demonstration in 2016. The surface is round (⌀150mm) and flat to within 15.5 um peak-to-valley when the applied actuator current is zero. DM3 was built using 57 actuators of 18mm pitch (Figure 6.2).

The mirror is controlled through a 64 analog output from a Real Time Linux environment. The user can control the shape of the mirror's surface by specifying the value of the current applied to each of the 57 actuators in a remote data access (RDA) interface in Matlab running on an office PC. The actuators are plugged into a breadboard, and the breadboard and control electronics are connected using analog RJ45 ethernet cables . Each ethernet cable controls the signal to four actuators. The electronics can produce an applied voltage of up to +10V on the DAC input. The update rate of this setup is 300Hz.

6.1.2 19-Actuator FLASH

The FLASH is the fourth prototype large-format deformable mirror built by TNO (Figure 6.3). The FLASH was commissioned by the University of California Lab for Adaptive Optics (UCSC-LAO) to verify the performance of the 2020 generation of TNO technology

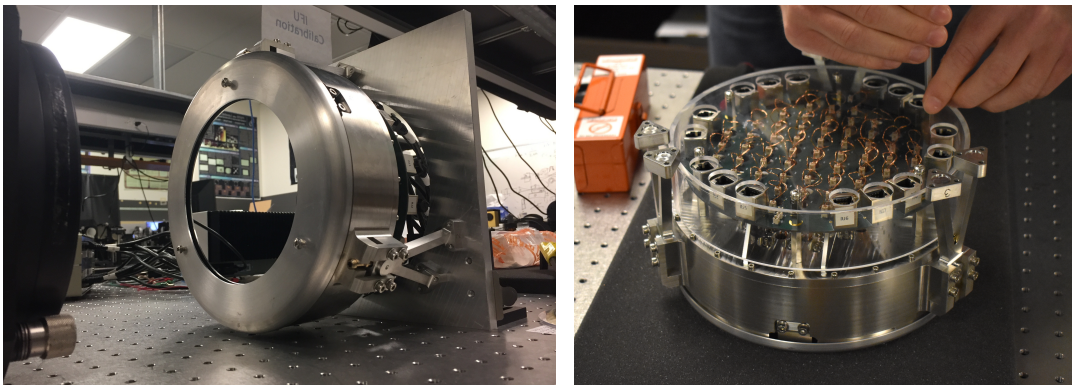

Figure 6.1 **DM3 at the UCSC Lab for Adaptive Optics**. The third prototype large-format deformable mirror from TNO (DM3) contains 57 hybrid variable reluctance actuators.

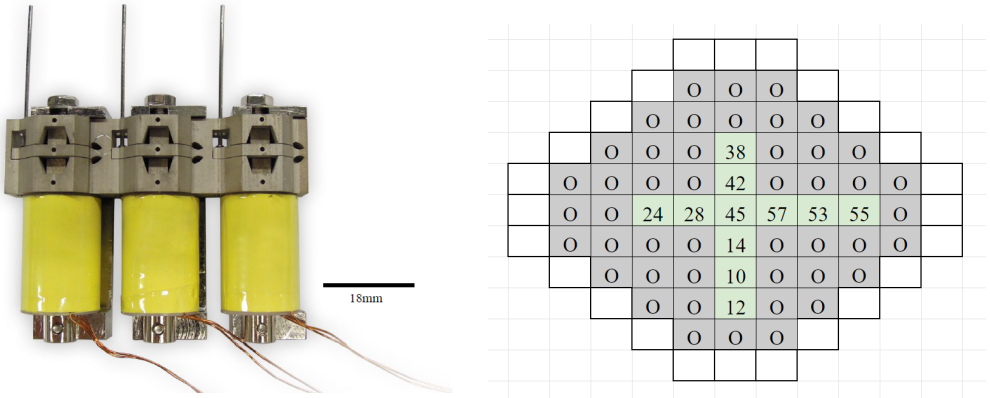

Figure 6.2 **DM3 18mm Pitch Hybrid-Variable Reluctance Actuators** (Left) *The 18mm-pitch TNO actuators used in DM3.* (Right) *Actuator layout in DM3.* The actuators used for the DM3 testing reported in this thesis are labeled by number in the green boxes. The other actuators are shown in the gray boxes, and the channels unoccupied are shown in white.

before the construction of the UH2.2m ASM. It was constructed in 2020 and delivered to the UCSC-LAO in January of 2021. The mirror is a companion to the UH-2.2m adaptive secondary mirror [60] and shares the same facesheet thickness (3.3mm), actuator spacing (39mm), and layout geometry (hexapolar). The UH-2.2m ASM (described in Chapter 7) and FLASH share the same generation of TNO HVR actuator. Figure 6.4 shows the internal designs of the FLASH, and Table 6.1 summarizes the FLASH design specifications.

FLASH shares the same control electronics and Matlab software with DM3, which is described in the previous section.

Table 6.1 **DM3 & FLASH Specifications**

	DM3	**FLASH**
Facesheet Diameter	150mm	150mm
Number of Actuators	57	19
Actuator Spacing	18mm	39mm
Actuator Generation (year)	2016	2020
Actuator Layout Geometry	Rows	Hexapolar
Facesheet Thickness	1mm	3.3mm
Facesheet Material	N/A	Borofloat
Control Electronics Used for Testing	Analog	Analog
Available Capacitive Sensor Locations	0	13

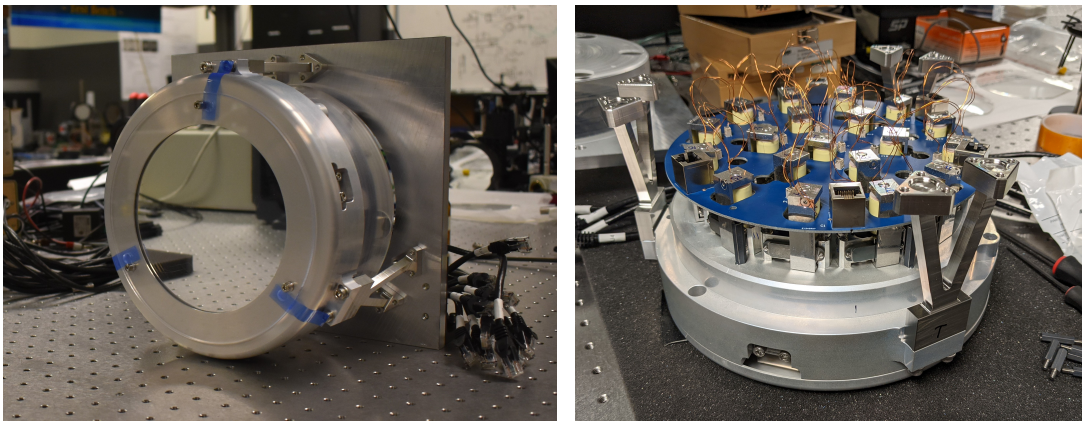

Figure 6.3 **FLASH 19-Actuator Large-Format Deformable Mirror**. (*Left*) The FLASH mounted on the testbench at the UC Santa Cruz Lab for Adaptive Optics. It is pictured here with its protective mirror-facesheet cover on. (*Right*) Back side of the FLASH mirror with the actuators and electronics breadboard.

6.2 Measurement Setups used for Performance Testing

6.2.1 Zygo Interferometer

The large-format deformable mirror testbed at UCSC-LAO utilizes a Zygo laser interferometer that is controlled using Metropro Software (Figure 6.5). The Zygo can perform surface meteorology to measure the shape of the mirror's surface to a precision of 0.6nm of surface error within ⌀140mm. Measurements can be collected at a maximum speed of one image per second.

The Zygo interferometer is not capable of measuring the piston changes in an optical system. To calibrate for piston, we measure the median value of the image and subtract it. We filter the empty pixels (listed in the Zygo data as 'NaN' values) by interpolating

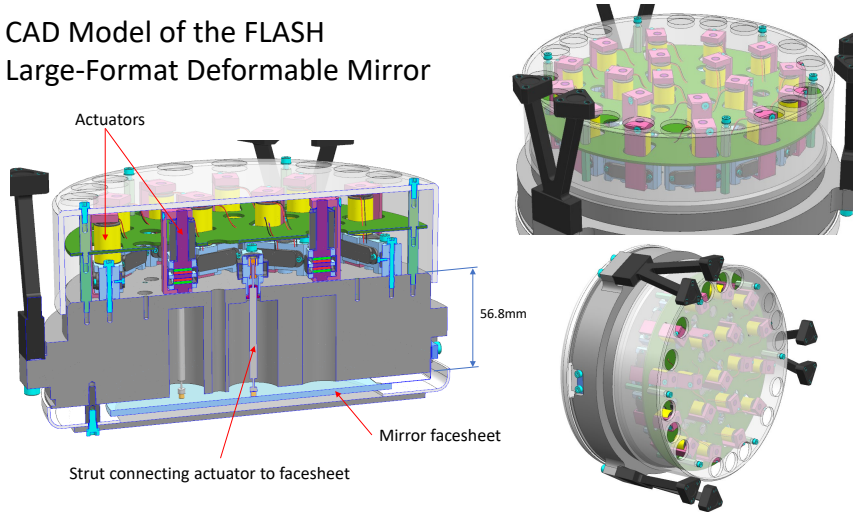

Figure 6.4 **CAD Model of the FLASH Large-Format Deformable Mirror**. FLASH was designed and built by TNO. It has an aluminium backing structure which supports the mirror facesheet, the actuators, and the electronics breadboard. *Figure credit: The Netherlands Organisation for Applied Scientific Research*

the values using nearby pixels. We convert the measurements reported by the Zygo interferometer in units of 'Zygos' to units of nanometers of surface error by

$$PhaseData[nm] = PhaseData[zygos]\frac{\lambda S}{R} \tag{6.1}$$

where the wavelength of the laser in the Zygo interferometer is $\lambda = 632.8$nm, the geometry factor is $S = 0.5$, and the resolution setting (high) is $R = 32768$ (Zygo interferometer manual: zygo-0347M, 12-5 p447). We analyze the Zygo interferometer data using Matlab and load the images using the *LoadZygoBinary* function authored by Massimo Galimberti.

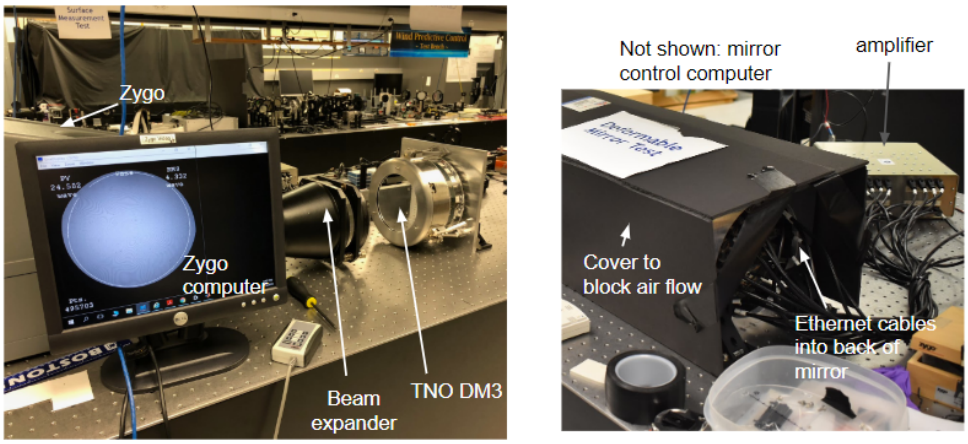

Figure 6.5 **Large-Format Deformable Mirror Testbench at the UCSC Lab for Adaptive Optics**. The testbench utilizes a Zygo Interferometer with MetroPro software to measure the surface shape. A beam expander is used so that the majority of the surface of the FLASH can be measured in a single image (up to ⌀140mm).

6.2.2 Capacitive Sensors

FLASH is the first large-format deformable mirror from TNO to incorporate space for an internal capacitive sensor system. The capacitive sensors are able to detect a change in the surface shape without physical contact by emitting an electrical field. The bottom of the TNO shell is coated with a conductive metal in the locations of the capacitive sensors in order to create a capacitor-effect with the sensor.

While the Zygo interferometer measurement setup can be used to gain an understanding of the full shape of the mirror's surface, it cannot collect time series data. The capacitive sensor system can provide data with a readout speed of 3906Hz over a working range of 50μm. This fast frame rate is needed for evaluating if this technology is suitable for use

in fast adaptive optics correction and high-contrast imaging. However, the capacitive sensor data are limited spatially, capturing displacement information only in the small coverage area that they are located. To determine if having limited access to a few points on the surface is an adequate proxy for the full mirror behavior, the linearity, hysteresis, and drift testing were performed with both the Zygo interferometer measurement setup and capacitive sensor systems side-by-side. Future testing when an interferometer is prohibitively difficult can rely instead on the capacitive sensor system.

The FLASH backing structure has thirteen holes available for capacitive sensors to be mounted. Four Micro Epsilon CS005 capacitive sensors were internally mounted for testing the FLASH at the UCSC-LAO (Figure 6.6, *left*). The sensors were run using the Micro-epsilon capaNCDT 6200 controller and the Micro-epsilon web interface software in an open loop system.

The mounts to position the capacitive sensors directly behind the mirror facesheet were designed by UC Santa Cruz. They were manufactured out of aluminum and are are 60mm in length. The capacitive sensor is glued in place on the mounting tube (Figure 6.6, *right*). To install the capacitive sensor mounts in the FLASH backing structure, the actuators were unplugged from the breadboard and breadboard was removed and reinstalled. The capacitive sensor mount installation was completed in approximately three hours.

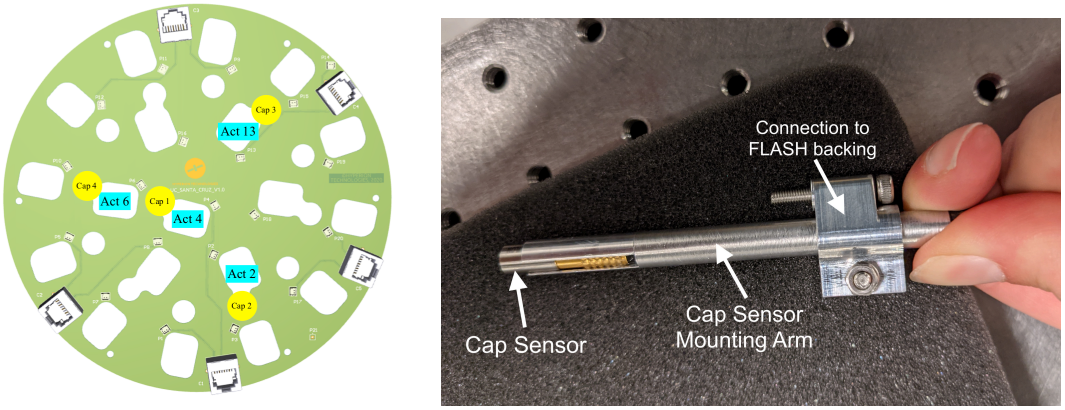

Figure 6.6 **FLASH Capacitive Sensors**. (*Left*) Four capacitive sensors were added to the internal structure of FLASH for testing at UCSC-LAO. The sensors were placed next to the actuators that were used in linearity and hysteresis testing. (*Right*) A capacitive sensor inside its mount before it was installed.

6.2.3 Quadrature Polarization Interferometer Testbench

The layout of the Quadrature Polarization Interferometer (QPI) at the UCSC Lab for Adaptive Optics is shown in Figure 6.7 and described in detail in Laguna et al. 2023 [134]. QPI is a Mach-Zehnder interferometer which can be used to measure the phase of an optic to the spatial resolution of the detector. The testbench uses a polarization based detection technique, unlike the Zygo. A HeNe laser source is polarized by a linear polarizer which converts the laser polarization from linear to circular. The light is then split by 4-inch beam splitter cube to create a test and reference path (traced in red and blue respectively in Figure 6.7). The field of view on the test path is expanded using a one-to-four-inch Zygo beam expander in order to measure a four inch circular patch of the TNO FLASH mirror. The light on the test path is then polarized using a

half waveplate. The light on the reference path is reflected off a reference mirror and then polarized using a quarter waveplate, creating creates a 90° phase offset between the test and reference paths. The light from the paths is combined and then split using a polarized beam splitter to two Thorlabs HT-5000-S Emergent Cameras.

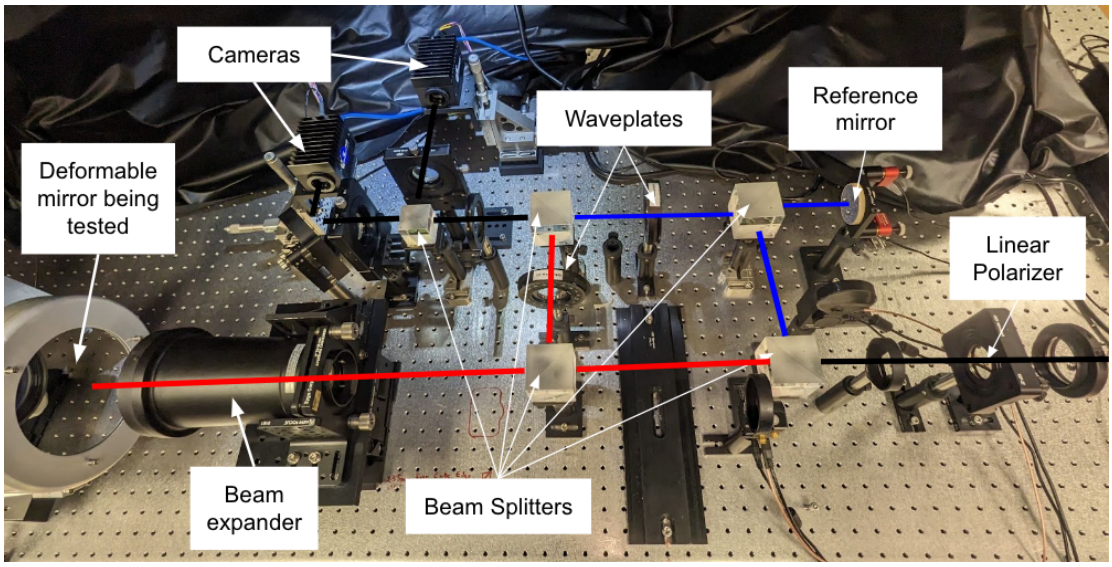

Figure 6.7 **Quadrature polarization interferometer (QPI)**. The QPI testbench is located in the UC Santa Cruz Lab for Adaptive Optics on a vibration isolated floating optical table. The test arm beam path is traced in red and the reference path is traced in blue. FLASH was placed in the test arm beam path to measure its dynamic behavior spatially.

The software for the Thorlabs cameras was modified in-house to allow for subframing to increase the readout speed. Table 6.2 gives a summary of the readout speed achievable as a function of subframe size. The max subframe speed available for the camera in the 16x16 subframing mode was 2800 Hz. The size of 128x128 provided the smallest

Table 6.2 **QPI Camera Readout Speed**

Subframe Size	**Camera Max Readout Speed**
2048	30 Hz
1024	100 Hz
128	1000 Hz
64	1200 Hz
16	2800 Hz

area which could more practically be used for spatial imaging and was usable at 1 kHz speeds.

Although QPI was mounted on a floating optical bench, we found that the stability of the measurements were dependant on the lab acoustics. A cardboard screen was constructed around QPI to minimize the disturbance from sound and air flow. After the overhead filtering fans for the lab's clean room system were were powered down to reduce the noise, the loudest sources of noise near QPI were the fans from the electronics and computers that were needed to power and control FLASH. The sound spectral analysis of the lab at the time that testing was conducted is shown in Figure 6.8. The loudest tone was near 300 Hz.

6.3 Results

6.3.1 Influence Function Actuator Profile

Measurement setup: Zygo Interferometer

The influence function of each actuator were measured to quantify the consistency of

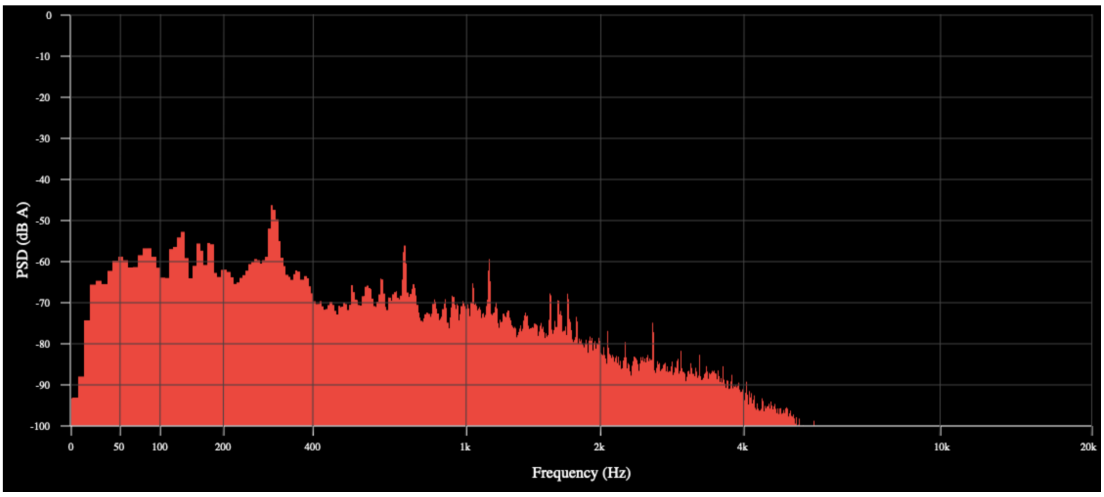

Figure 6.8 **Sound profile of the Lab for Adaptive Optics near the QPI test bench.** This plot was made using the Spectral Analysis tool on checkhearing.org. The sound profile was recorded approximately five minutes before testing was conducted.

the actuator response. To measure the influence functions of the DM3 actuators, a $+20mA$ current was applied in an automated measurement sequence to displace each actuator one-by-one. The displacement of these pokes corresponded to approximately 730nm peak-to-valley. Twenty-one actuators responded to the positive current with a positive displacement, and thirty-six actuators responded with a negative displacement. An example of the influence function measured for Actuator 42 is shown in Figure 6.9. The influence function was measured with the natural shape of the mirror subtracted such that only the displacement is seen. The cross-section of the influence function is plotted in Figure 6.10 with a Gaussian, Moffat, and Cauchy function fit. While each of the three functions can approximate part of the profile, a custom profile would need to be created to correctly fit the actuator cross sections at both the center and tails.

To measure the FLASH influance functions, a +50mA current was applied for a displacement of corresponding to approximately 2200nm peak-to-valley. Eighteen actuators responded to the positive current with a positive displacement, and one actuator responded with a negative displacement. Seven of the actuators had profiles that were fully visible in the field of view of our Zygo interferometer setup: the center actuator (Actuator 4) and the six actuators in the middle ring (Actuators 2, 6, 8, 13, 15, and 17). An example of the influence function measured for Actuator 4 is shown in Figure 6.11.

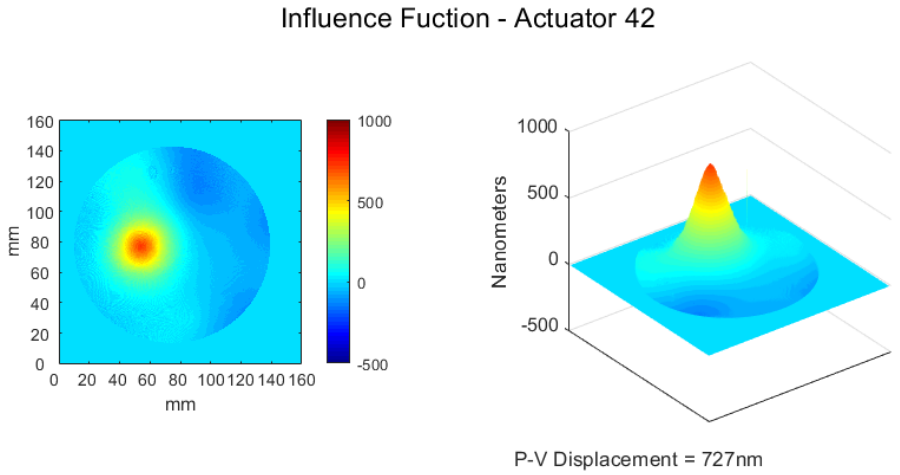

Figure 6.9 **Example Influence Function from DM3**: The influence function for Actuator 42 as measured on April 30th, 2020. An applied voltage of +20mA resulted in an actuator displacement of 727nm. Images are scaled with the x-y axis in millimeters and the color axis and z-displacement in nanometers.

6.3.2 Actuator Cross-Coupling

The "actuator cross-coupling" was measured to quantify how the movement of one actuator will affect its neighbor. By measuring and understanding these coupling effects, it

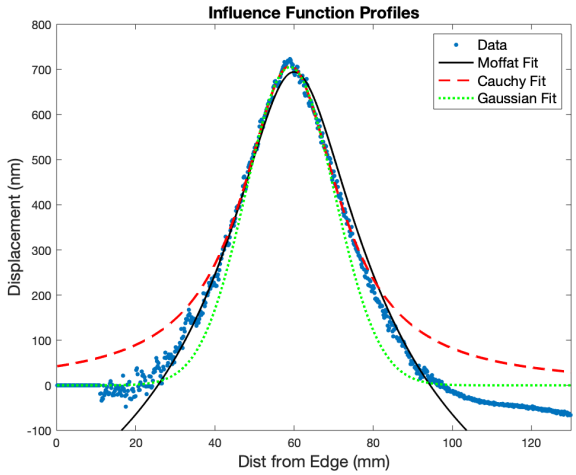

Figure 6.10 **Influence Function Profile for DM3**. A cross-section of the influence function for Actuator 42 was used to determine a profile of best fit. A Moffat, Cauchy, and Gaussian curve were fit to the inner 100 points of the cross section. The Cauchy and Gaussian fit approximate the center well, but do not approximate the width correctly. The Moffat fit can approximate the width to higher precision, but cannot be used to determine the center value. A custom profile is needed to match the greater shape of the cross section. (*Figure credit: Cesar Laguna).*

provides the basis for compensating for the effect when designing the control algorithms.

For DM3, the cross-coupling was measured using the cross section of the influence functions from the center row and center column of actuators (Figure 6.12). The center actuator (45) was used in both samples. The cross sections were corrected for their positive/negative displacement polarity and then normalized. Two measurements were taken per actuator along the line that intersected the neighboring actuator's peak. Using these twenty measurements, we measure an actuator cross-coupling of 37.07 $\pm$ 0.93%.

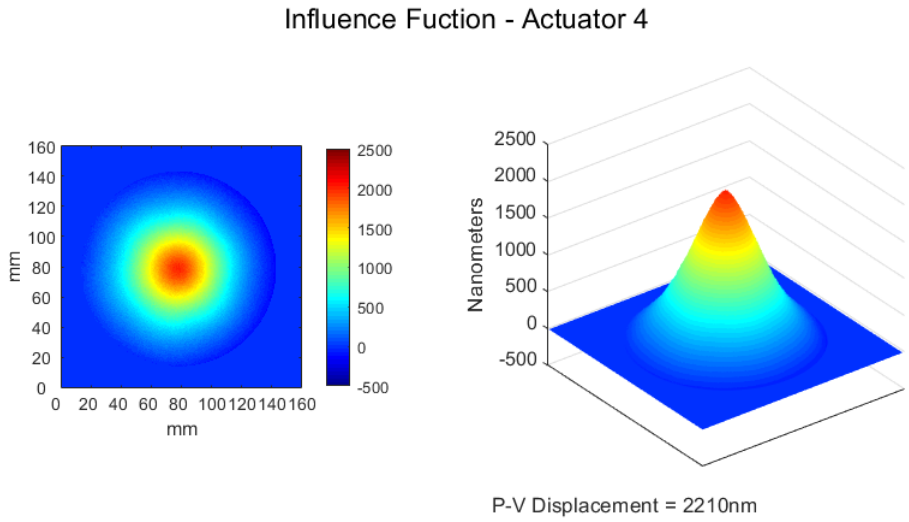

Figure 6.11 **Example Influence Function from FLASH**: An applied voltage of +50mA to Actuator 4 resulted in an actuator displacement of 2210nm. These images are scaled with the x-y axis in millimeters and the color axis and z-displacement in nanometers. The natural shape of the FLASH mirror was subtracted, so only the displacement due to the actuator poke is visible.

For FLASH, the actuator cross-coupling was measured to be 34.2±1%. This value was determined using the influence functions from the seven actuators that were fully visible in the Zygo field of view (Figure 6.13). The location of the center of each of the seven actuators in the image was found using a Gaussian fit. A cross-section of the influence function was then taken in the row and column directions, emanating from the actuator center location. The fourteen cross sections were then normalized and stacked. The average distance between the center actuator to each actuator in the inner ring was then determined using the location of the centers of the actuators and measured to be 39.4 ± 0.4mm. The value of the fourteen normalized cross-sections at the width location

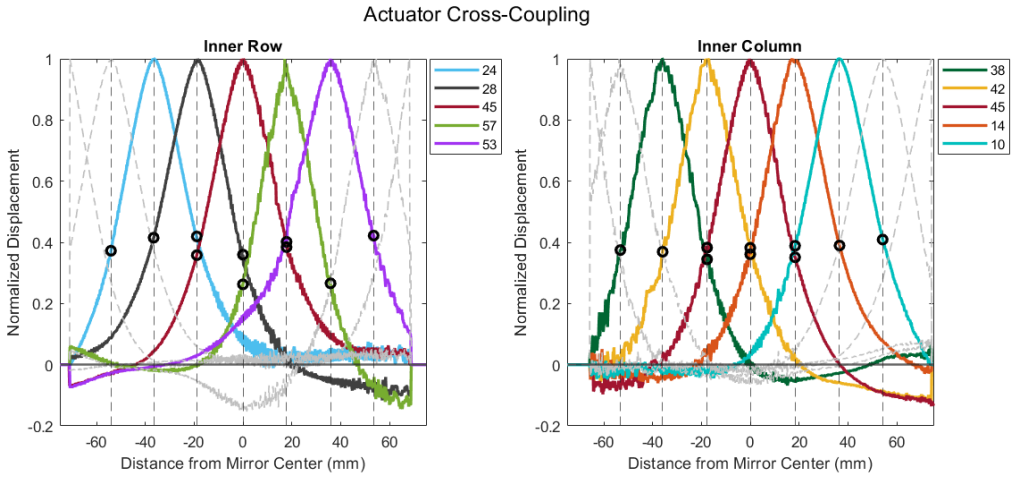

Figure 6.12 **DM3 Actuator Cross-Coupling**. Five actuators from the inner row (24, 28, 45, 57, and 53) and five actuators from the inner column (38, 42, 45, 14, and 10) were used to measure the actuator cross-coupling. The filled lines represent the normalized cross section of the actuators included in the actuator cross-coupling measurement. The black dots indicate the values of the cross-coupling measurements. The dashed lines are the influence functions of the actuators in the row or column not used for the cross-coupling calculation.

of average actuator separation were averaged to yield the cross-coupling measurement. This measurement is consistent with the cross-coupling value expected from the pre-fabrication modeling done by TNO.

6.3.3 Natural-Shape Surface Flattening

Measurement setup: Zygo Interferometer

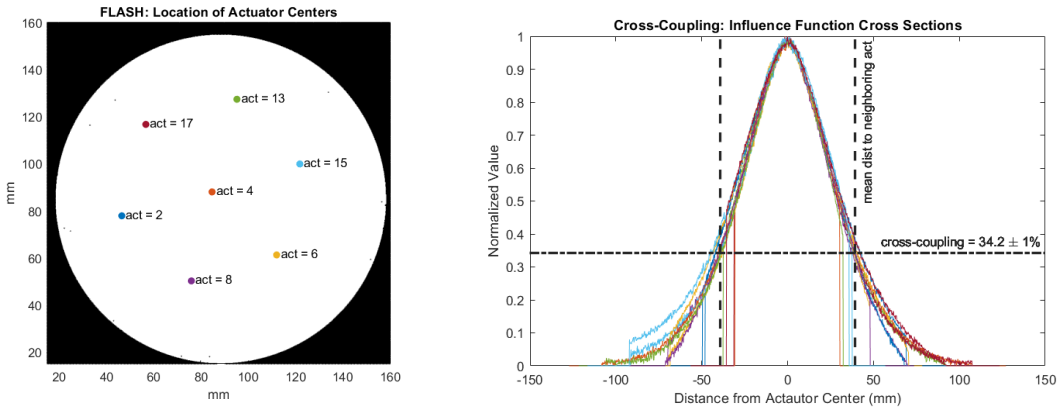

Figure 6.13 **FLASH Actuator Cross-Coupling**. (*Left*) Seven actuators were used to calculate the cross-coupling between actuators. The centers of these actuators were fully visible within the frame of the Zygo interferometer. (*Right*) To measure the cross-coupling the actuator, 14 cross sections from the column and row direction from each visible actuator were aligned at their centers and normalized. The average distance between the middle ring actuators to the center was 39.4 ± 0.4mm. This corresponds to a cross-coupling measurement of 34.2 ± 1%.

The amount of residual wavefront error after natural-shape surface flattening is important to quantify for understanding the static operation of the DM. In cases where AO control is not used but the DM is located in the position of the secondary mirror, the residual wavefronts on the ASM will translate to degradations in image quality.

The natural shape of the TNO DM3 mirror has a peak-to-valley that is 15.5 um with a 2780nm RMS variation (within ⌀140mm). The natural shape of the FLASH mirror facesheet has a peak-to-valley that is 5339.1nm with a 1158.8nm RMS variation.

To bring the surface as flat as possible (as measured by surface RMS), a set of flattening currents was determined using an iterative process. At each step, an image was taken using the Zygo interferometer. The next desired position for the actuators to reproduce in the iteration (i) was set to the negative of the last image taken (S_i). The next set of currents (F_i) to produce the desired shape (S_i) were calculated using the influence functions matrix (P) through the Moore-Penrose inverse:

$$F_i = (P^T P)^{-1} P^T S_i. \tag{6.2}$$

The currents calculated for each iteration were summed with the previous currents applied to find the new values to be applied ($F = \sum_1^{i=n} F_i$).

For the DM3 testing, fifteen iterations of flattening were performed on April 30th 2020 to calculate the optimal flattening currents. The majority of the variation was removed after five iterations. The flattest shape was found on iteration 14 which had an RMS = 27.7nm (within ⌀140mm) with a peak-to-valley of 469nm, demonstrating that it is possible to flatten the surface by two orders of magnitude. Figure 6.14 shows the natural shape of the mirror alongside the shape after this flattening. The total current needed to hold this shape across the 57 actuators was 1967mA, averaging 17.3 ± 3.3mA per actuator. The required power was 94.5mW (1.7 mW/actuator).

For the FLASH flattening, fourteen iterations were completed on April 5th 2021 to calculate the optimal set of flattening currents (Figure 6.15, *top*). The majority of

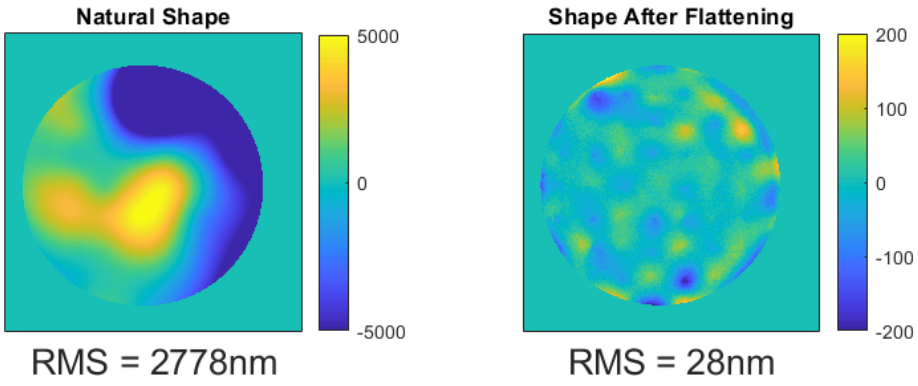

Figure 6.14 **DM3 Natural-Shape Surface Flattening**. *(Left) DM3 Natural Surface Shape.* Unpowered, the shape of the TNO DM3 mirror surface has a peak-to-valley that is 15500nm (RMS = 2780nm within ⌀140mm). *(Right) Surface Shape after Applied Flattening.* After flattening, the surface shape was brought down to 28nm RMS with a peak-to-valley of 469 nm. The colorbar is reported in units of nanometers.

the variation was removed after four iterations. The flattest shape was found on iteration thirteen which had an RMS = 14.7nm (within ⌀140mm) with a peak-to-valley of 260.0nm. The surface RMS was reduced by a factor of 79. Figure 6.15 (*bottom*) shows the natural shape of the mirror alongside the shape after this flattening. The total current needed to hold this shape across the 19 actuators was 323.9mA, averaging 17.0 ± 4.7mA per actuator. The required power was 7.3mW (0.4mW/actuator). This result confirms that the use of a passive air cooling will be appropriate for the UH2.2m adaptive secondary mirror.

6.3.4 Linearity

Measurement setup: Zygo Interferometer & Capacitive Sensors

To quantify the ability for actuators to reproduce the expected position, we quantified the linearity of the HVR actuators in DM3 and FLASH. For this test, we applied current patterns alternating between zero and the value for linearity measurement.

For DM3, linearity testing was performed on five individual actuators (12, 14, 42, 55, and 57). These actuators were run through a fifteen-step current pattern using positive and negative currents, spanning from 0 to +70mA or 0 to -70mA. Although the negative and positive current runs were performed separately, linearity fitting considered the tests jointly for each actuator. The displacement was measured using the mean of the seven points nearest to the actuator center. The average slopes of the linearity fit for the DM3 actuators was $79.32 \pm 1.08\,\mathrm{nm/mA}$.

The percent residuals were calculated using the following formula:

$$Residual(\%) = 100\left(\frac{Data - Fit}{Data}\right). \tag{6.3}$$

The mean of the percent residuals for DM3 across the five actuators was used to quantify the actuator linearity. We measure the actuators to be linear to 99.4% ± 0.33% (nonlinear to 0.6% ± 0.33%). The nonlinearity is most evident at small currents (within ±10mA) where the actuators tend to undershoot their predicted position.

For FLASH, the linearity was measured using both the Zygo interferometer setup like DM3 and FLASH's internal capacitive sensor system. Linearity testing was performed by poking actuators individually (using Actuators 2, 4, 6, and 13 separately) and as a group simultaneously (all actuators). The individual actuator test measured the high spacial order performance. The all-actuator test demonstrated the capabilities of the HVR actuators if minimal inter-actuator and shell deformation forces exist. The actuators were run through two current patterns which applied positive and negative currents from ±150mA and ±300mA (Figure 6.16). The first current pattern probed the HVR actuators quoted linear range, from 0 to ±150mA. The second pattern spanned the maximum possible working range of the HVR actuators when controlled with the analog electronics, from 0 to ±300mA.

Four runs were completed for each configuration. Zygo interferometer data and capacitive sensor data were collected simultaneously during each run. The Zygo interferometer data was used to analyze the individual actuator tests because the capacitive sensors are not able to detect the height of the mirror surface at the actuator's center. The capacitive sensors were used to analyze the all-actuator tests because the Zygo interferometer cannot measure a change in piston.

Table 6.3 summarizes the key results from the FLASH linearity testing. Our testing reveals that within the stated linear range of the actuator, the high-order linearity is $95.2 \pm 0.8\%$ with a max residual of 0.2μm surface error (Figure 6.17). The linearity measured when all-actuators were moved simultaneously was $96.8 \pm 0.5\%$ with a max

residual of 2μm (Figure 6.18). The average displacement measured for the all-actuator movement was roughly 2.5 times larger than the average displacement measured for the individual actuator movements. All testing showed an asymmetry between positive and negative applied currents, with larger movements available when positive currents are applied.

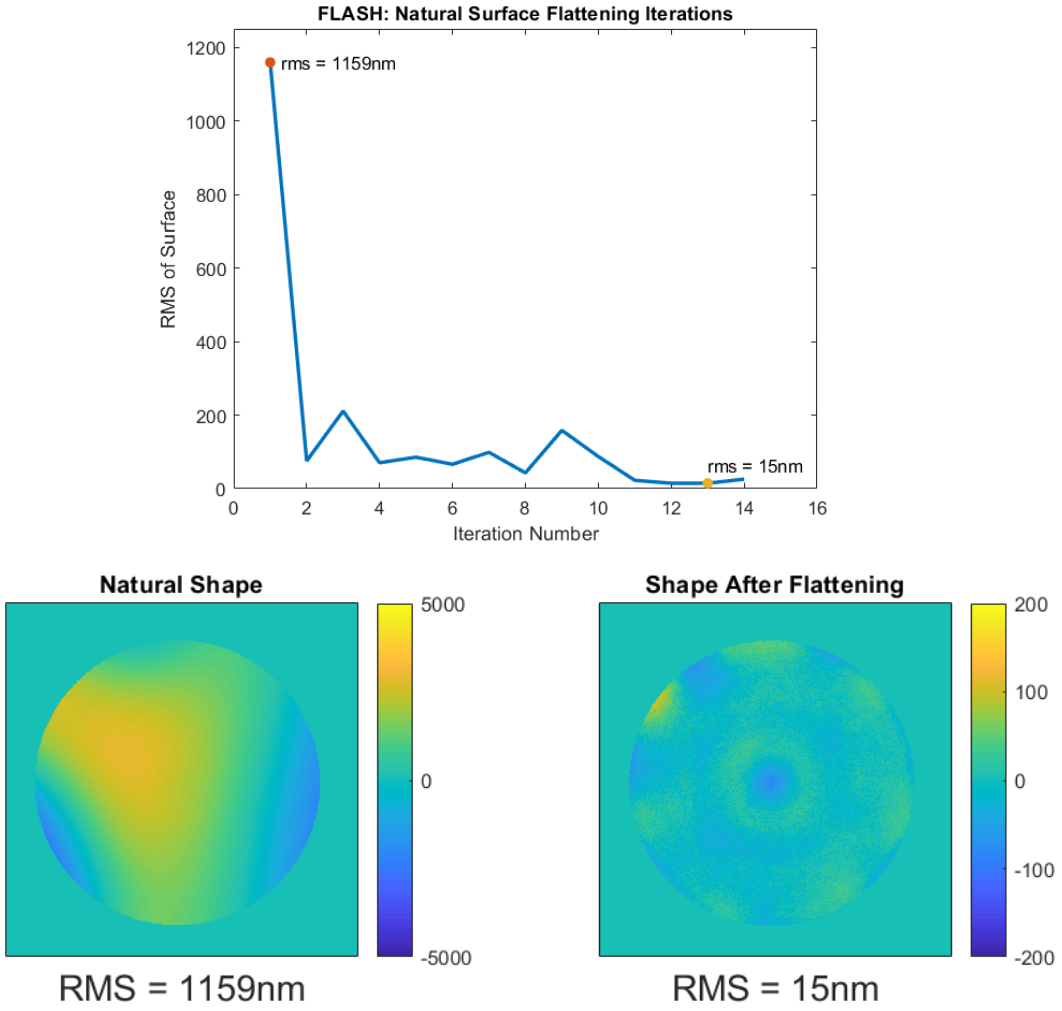

Figure 6.15 **Natural-Shape Surface Flattening**. (*Top*) *RMS of the Mirror Surface Shape during Flattening Iterations.* The best set of flattening currents was determined through an iterative process of 14 steps. (*Bottom left*) *FLASH Natural Surface Shape.* Unpowered, the shape of the TNO FLASH mirror surface has a peak-to-valley that is 5339nm ($RMS = 1159$nm within ⌀140mm). (*Bottom right*) *Surface Shape after Applied Flattening.* After flattening, the surface shape was brought down to 15nm RMS with a peak-to-valley of 261nm. The colorbar is reported in units of nanometers.

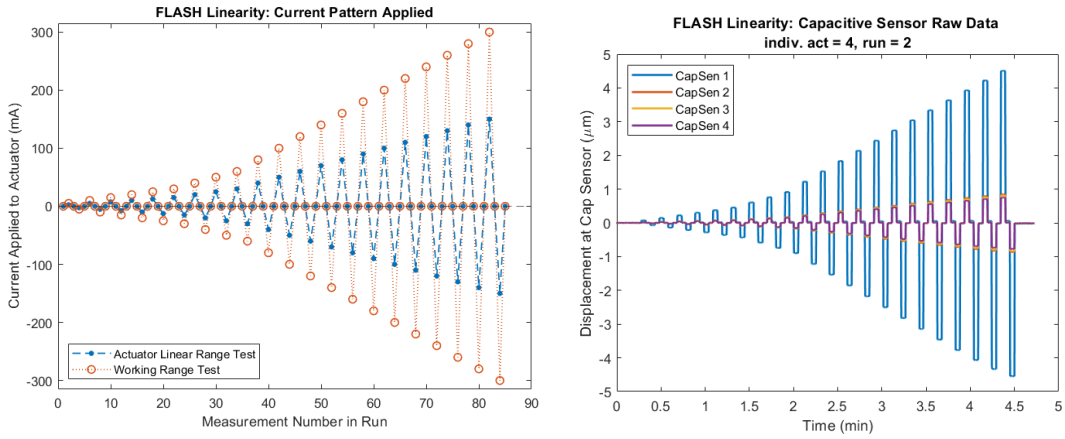

Figure 6.16 **FLASH Linearity Testing** (*Left*) The linearity testing was completed using currents varying across the actuators linear range (±150mA) and full working range (±300mA). (*Right*) The four capacitive sensors were used to collect real time displacement data during the linearity testing. This example data set was taken during an individual actuator run of Actuator 4.

Table 6.3 **FLASH Linearity Results Summary**

Indiv. act./ All act.	**Current Range**	**Act. Used**	**Average Displacement**	**Max Displacement**	**Percent Linearity**
Individual	Linear (±150mA)	2,4,6,13	46.5 ± 1.4 nm/mA	-6.8μm @ ±-150mA 6.8μm @ ±+150mA	$95.2 \pm 0.8\%$
	Working (±300mA)	4	-	-7.2μm @ -300mA 9.4μm @ +300mA	-
All	Linear (±150mA)	all	113.9 ± 1.0 nm/mA	-15.1μm @ -150mA 17.0μm @ +150mA	$96.8 \pm 0.5\%$
	Working (±300mA)	all	-15.3μm @ -300mA 20.5μm @ +300mA	-	

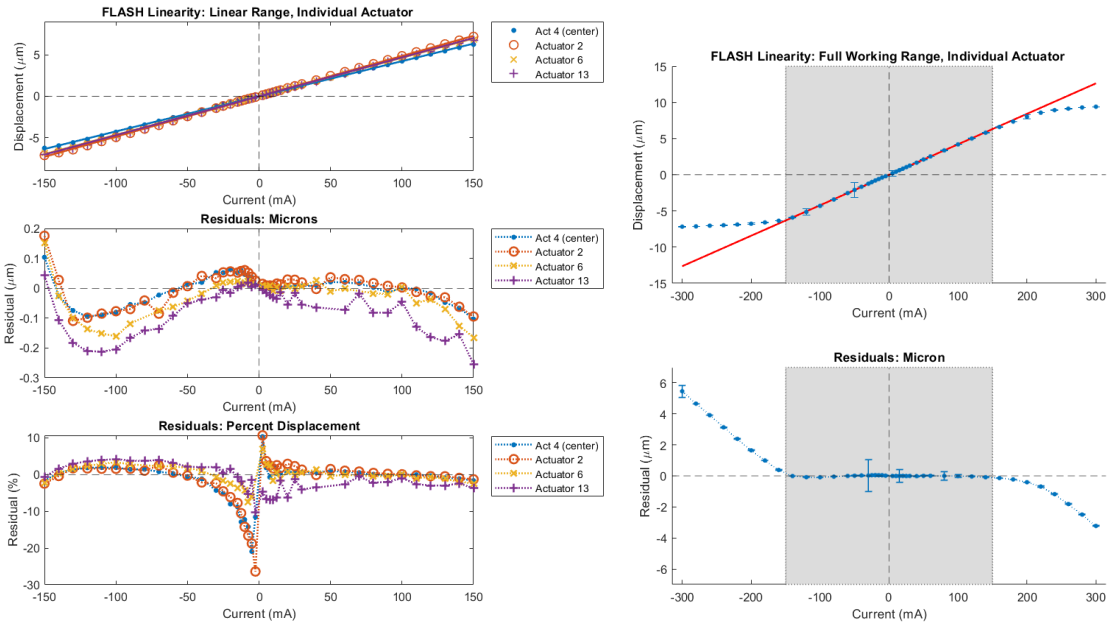

Figure 6.17 **FLASH Linearity Measurements from the Zygo Interferometer for the Actuators Poked Individually**. (*Left*) The linearity measured from the linear-range test (±150mA) for Actuators 2, 4, 6 and 13 was $lin = 95.2 \pm 0.8\%$. The average displacement was 46.5 ± 1.4nm/mA. (*Right*) The displacement measured by the Zygo interferometer data from five runs of Actuator 4 across its working range (blue) was averaged and fit with a zero-intercept linear fit (red). The working range-test confirms that the linear region of the actuators is approximately ±150mA (gray), but the displacements are asymmetric between the positive and negative applied currents.

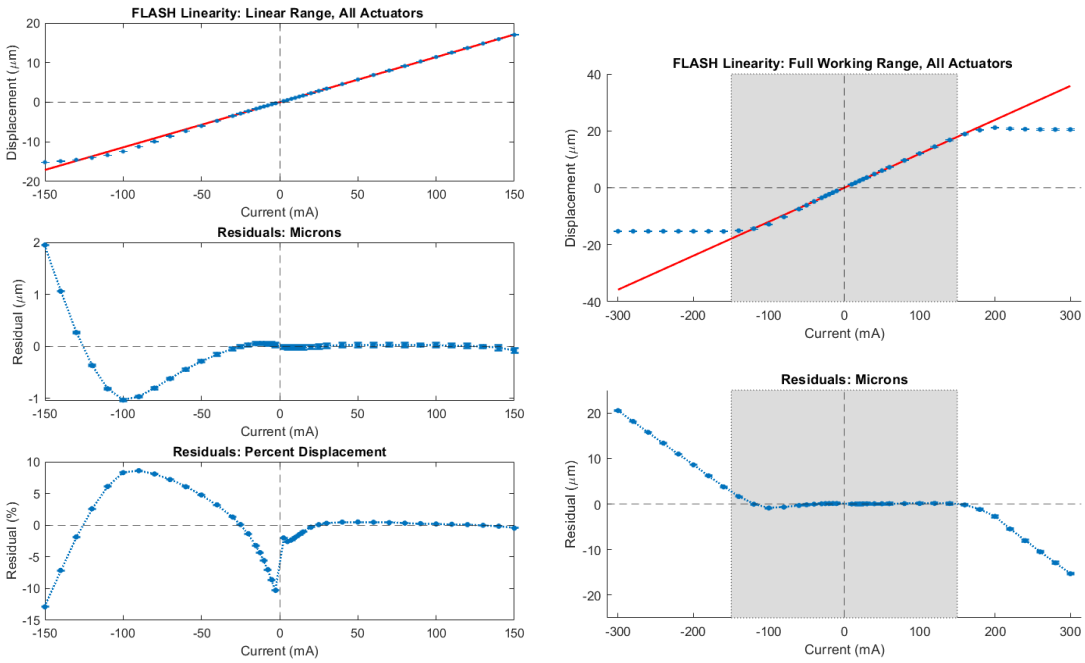

Figure 6.18 **Linearity Measurements from the Capacitive Sensors when All Actuators were Moved Synchronously** (*Left*) The displacement measured by the capacitive sensor data from three runs (blue) was averaged and fit with a zero-intercept linear fit (red). The linearity measured from the linear-range testing (±150mA) when all actuators were moved simultaneously was $lin = 96.8 \pm 0.5\%$. The average displacement was 113.9 ± 1.0 nm/mA. (*Right*) The working-range test (±300mA) when all actuator were moved simultaneously demonstrates that the actuator range cannot extend beyond TNO's quoted linear range ($\pm 150mA$), which is shaded in gray.

6.3.5 Hysteresis

Measurement setup: Zygo Interferometer & Capacitive Sensors

Actuator displacement varies depending on the previous position of the actuator. To quantify this effect, hysteresis testing was performed by stepping individual actuators from measurement value to next measurement value (no return to zero current in between measurements). We measured the hysteresis using the definition:

$$Hyst(\%) = 100\left(\frac{|S3 - S1|}{|S2 - S4|}\right) \tag{6.4}$$

where $S1$ and $S3$ are the displacements measured at an applied current of zero and $S2$ and $S4$ are the displacements measured at the maximum and minimum current applied.

The DM3 hysteresis testing was performed using three actuators (14, 42, and 57) stepped through five independent hysteresis loops. Each loop was done in forty steps between currents of ±2.5mA, ±5mA, ±10mA, ±30mA, ±60mA. Three of these tests occurred in the least linear portions of the actuator displacement curves (±2.5mA, ±5mA, ±20mA) and provide worse-case scenario measurements of the hysteresis. No measurement exceeded a hysteresis value of 3.5%. The average percent hysteresis measured across all fifteen trials was 2.10 ± 0.23%.

For the FLASH hysteresis testing, both the Zygo interferometer and FLASH's internal capacitive sensors measurement setups were used. Four actuators (2, 4, 6, and 13) were

moved individually stepping through five independent hysteresis loops. Each loop was done in eighty steps between currents of ±5mA, ±10mA, ±25mA, ±50mA, ±100mA, ±150mA. Three runs were performed for each actuator at ±5mA, ±10mA, ±150mA and five runs were performed for each actuator at ±25mA, ±50mA, ±100mA. An example of one of these hysteresis loops is shown in Figure 6.19.

The average percent hysteresis for FLASH was measured using the data from the ±25mA, ±50mA, ±100mA runs to be $1.80 \pm 0.13\%$ by the Zygo interferometer and $1.93 \pm 0.04\%$ by the capacitive sensors. This calculation did not include the values measured outside the 20mA-120mA range to assure the hysteresis measurements were taken in the linear range of the actuators. There was no dependency on the actuator tested and the measured hysteresis value.

6.3.6 Repeatablity & Drift

Measurement setup: Zygo Interferometer & Capacitive Sensors

The repeatability and drift testing were performed to evaluate if the TNO deformable mirrors could return and hold the same shape over long duration (8+ hours). For the repeatablity test, we applied the same set of currents from day to day. For drift testing, we hold the same current pattern for hours.

Repeatability testing was run using DM3. The repeatability testing was performed by applying the DM3 flattening current set calculated on April 30th 2020. Five measure-

ments were taken across five days starting from zero currents applied. Images were visually inspected and the RMS was used to quantify the shape. The images passed visual inspection and the RMS did not change to within the precision of the Zygo Interferometer (0.6nm). The same shape was applied after the mirror had been running for unmeasured amounts of times. The RMS differences in these images were observed to fluctuate by up to $\Delta RMS = 33.5$ nm.

DM3 drift testing was performed by applying the same April 30th 2020 current pattern and holding it for twelve hours. Measurements were taken with the applied pattern subtracted such that the Zygo images were more sensitive to any deviations. The tests were repeated three times. The only measurable change came from an added tilt on the order of 1000nm that was believed to be from a shift in the beam expander mounting. Although the data cannot conclusively rule out drift as an issue to <1000nm RMS, there was no evidence for significant drift with DM3.

Nine FLASH drift tests were performed for a duration of 8.5 hours with the goal of determining if the FLASH could hold its surface shape consistently across many hours of applied current. Table 6.4 lists the type of current pattern applied for each drift test. Zygo interferometer and capacitive sensor data were collected simultaneously. The room temperature was also recorded using an Elitech RC-5 USB Temperature Data Logger during two runs.

No drifting above the measurement error of the Zygo interferometer was found on the

surface of the FLASH at the end of the test (Figure 6.20, *top*). The capacitive sensors measured drifting of up to 90nm of change. However, these capacitive sensor drifts have a correlation with the recorded temperature data. These movements are in the range of what could be explained by the thermal expansion change in the 60mm aluminium capacitive sensor mounts. To better calibrate out any movement due to temperature changes, the data from Capacitive Sensors 2-4 were subtracted from the data from Capacitive Sensor 1. After this correction, the biggest change recorded was 20nm of drift (Figure 6.20, *bottom*). Future sensor mount designs should consider using a material with a lower CTE value to increase the measurement precision of the capacitive sensors without this calibration.

Table 6.4 **Drift Testing Runs**

Drift Test	**Pattern**	**Magnitude**	**Note**
1	Checkerboard	+50mA	
2	Checkerboard	+100mA	
3	Piston	+100mA	
4	Piston	-100mA	
5	Piston	+50mA	
6	Flattening Currents found 04-07	–	
7	Flattening Currents found 04-07	–	Taken on 04-08-2021, results shown in Figure 6.20
8	Checkerboard	-50mA	
9	Checkerboard	-100mA	

6.3.7 Zernike Mode Testing

Measurement setup: Zygo Interferometer & Capacitive Sensors

To determine how closely DM3 was able reproduce ideal Zernike shapes, the first 57

Zernike Modes were applied to DM3. The currents needed to reproduce the Zernike modes were calculated using Equation 3.2, where S_i was the shape of each Zernike pattern. No iterations were used in trying to reproduce the Zernike pattern. An example of the side-by-side comparison between DM3 and an ideal Zernike pattern can be viewed in Figure 6.23 for mode 12. A movie of the full test can be watched at the following youtube link: https://youtu.be/dpTzO46zg2Y.

To determine if a trend existed between the Zernike order number and how well DM3 could replicate the pattern, the reduced chi square was calculated for each Zernike frame (Figure 6.22). Modes with a large reduced chi square value could not be replicated to as high precision. Overall, the spherical modes were reproduced the least well (4, 12, 24, 40) of any categorization of mode type. There was not a significant trend between the value of the reduced chi square and low or high order mode number.

To determine how closely the FLASH can reproduce an applied Zernike shape, the first 19 Zernike Modes were applied to FLASH. No iterations were used in trying to reproduce the Zernike pattern. An example of the side-by-side comparison between FLASH and an ideal Zernike pattern can be viewed in Figure 6.23 for mode 6. A movie of the simultaneous capacitive sensor and Zygo interferometer data collection can be watched at the following youtube link: https://youtu.be/scUhmqljJVc.

6.3.8 Lifetime Testing

Measurement setup: Zygo Interferometer

A demonstration to test the working lifetime of the actuators was performed with DM3. The 57 actuators were set to a 34Hz cycle going from -50% to +50% of the maximum stroke. This scenario is a strong worst case for an actual ASM in operation, where the changes in deflection for each cycle will be much lower. Periodically, DM3 was imaged with the Zygo interferometer. At the time of writing, each of the 57 actuators has seen over 110 million cycles with no detectable change in performance.

6.3.9 Settling Time

Measurement setup: Capacitive Sensors

To quantify the response time for an actuator to reach its final position after a current step is applied, we used the capacitive sensor system in FLASH to measure the actuator settling time. A current step of +10mA was applied to Actuator 4 (the center actuator). Our definition of settling time was adopted from Rochette et al. 2018 [207], which began/ended the settling time measurement when the system rose/reached 5% of its final displacement. Ten runs were averaged to measure each settling time value.

We find a settling time of 14.3 $\pm$ 0.1 millisec when the current is applied as a step response (from 0 to 10mA in one step). To overcome the actuators internal eddy-current behavior and speed up the settling time, a lead filter can be implemented when applying

the current step (discussed here in Section 3.7) or the PI control settings can be tuned (discussed in Section 3.8).

We implemented a lead filter using the discrete-space state Matlab Simulink model with zero on the pole location of the measured plant and a pole at 500Hz. This filter applied the current using a spike and then a ramp-down from the peak. It was designed to reach a peak current of 9.058 times the final current; for a step of 10mA, this resulted in a peak current of 90.58mA.

Four tuning values for the lead filter were tried with different decay times (Figure 6.24). The lead filter with the optimal tuning (Lead Filter 2) was set with the parameters of $A = 0.6$, $B = 2.18$, $C = -1.478$, $D = 9.058$. The settling time measured with this lead filter was $t_{set} = 1.08 \pm 0.08$ ms, approximately an order of magnitude faster than the settling time with no lead filter applied.

After the optimal lead-fiter tuning was determined, we performed a diverse set of movements with all-actuator pokes (Figure 6.25, top) and single-actuator pokes (Figure 6.25, bottom) with the following applied currents: 1mA, 2mA, 3mA, 4mA, 5mA, 10mA, 15mA, and 20mA. The measurements were collected with the capacitive sensor system internal to FLASH. The center actuator (actuator 4) was used to perform the single-actuator poke. The capacitive sensors make a good approximation for the displacement in the all-actuator poke but not in the single actuator poke because the captive sensor is located approximately half of an actuator spacing from the center of the actuator. One

trial was performed per displacement step. The displacement measurements of these trials are shown side-by-side in Figure 6.25. Our settling time measurements for each trial are plotted in Figure 6.26.

We find that the lead-filter tuning only holds for single-actuator movements with small current steps ($\leq 5\,\mathrm{mA}$). Curiously, the tuning did not hold for a step size of 10mA where it was originally tuned. The average settling time for the adequately tuned steps was $t_{set} = 1.0 \pm 0.2\,\mathrm{ms}$. The movements for the all-actuators trials and the single-actuator trials with current steps of $\geq 10\,\mathrm{mA}$ display overdamped behavior. It is possible that a better tuned lead filter for each step size could lead to the desired critically damped behavior, but uniform tuning that applies to all movements does not appear to be easily possible.

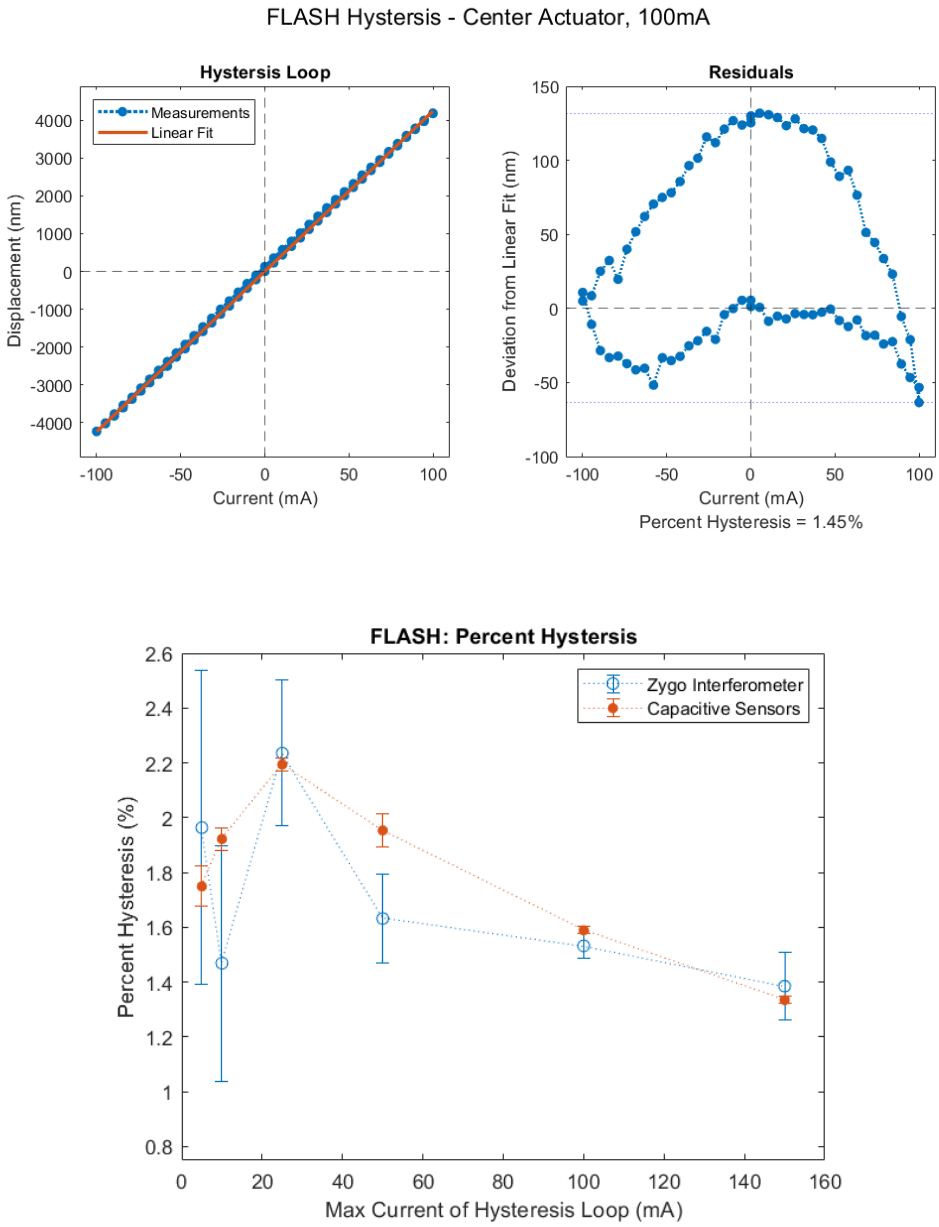

Figure 6.19 **FLASH hysteresis testing results**. (*Top*) *Example Hysteresis Loop* from Actuator 4 with max current of 100mA. (*Bottom*) *Percent Hysteresis*. The data point at each current loop value are an average of the measurements from each the four actuators tested. The average percent hysteresis was measured to be $1.80 \pm 0.13\%$ using the Zygo data and $1.93 \pm 0.04\%$ using the capacitive sensors within the definite linear range of the actuators (20mA - 120mA).

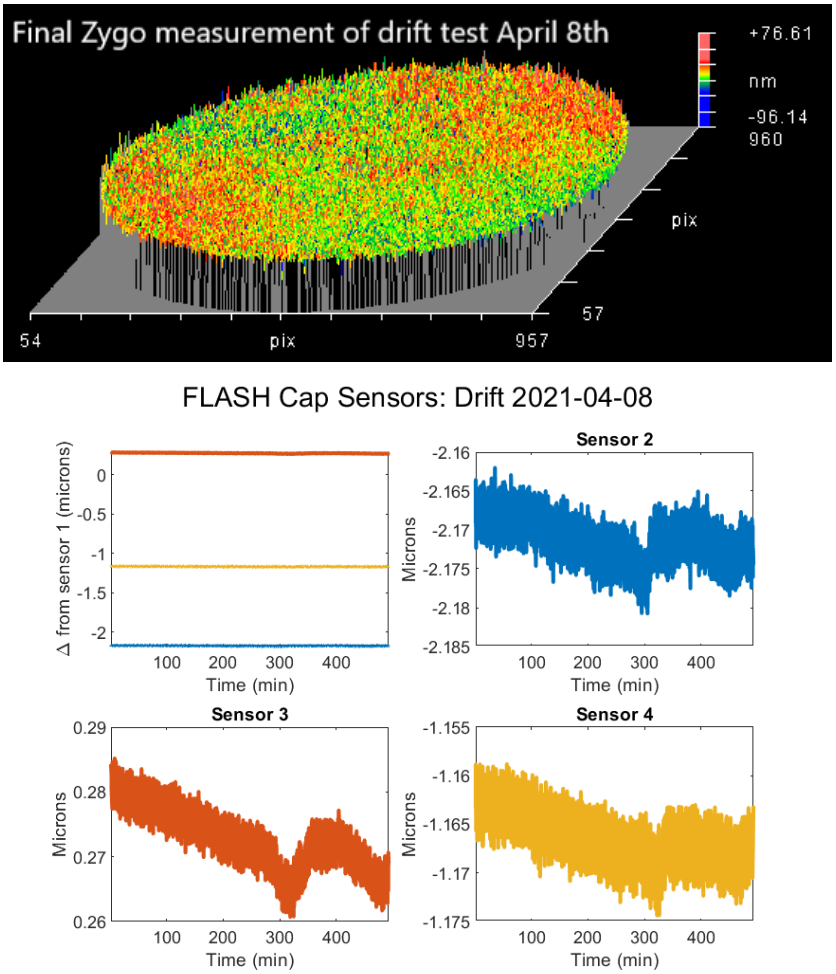

Figure 6.20 **Example Drift Results from Holding the Flattening Currents Pattern on FLASH**. (*Top*) The final Zygo interferometer measurement could not measure drifting outside the measurement error of the Zygo. (*Bottom*) Four capacitive sensors provided real time data over the course of the 8.5hr drift tests. The drifting due to a CTE mismatch of the capacitive sensor mounts was calibrated by subtracting the Capacitive Sensor 1 data from sensors 2-4. In this run, the largest drift measured was 12nm by Capacitive Sensor 3.

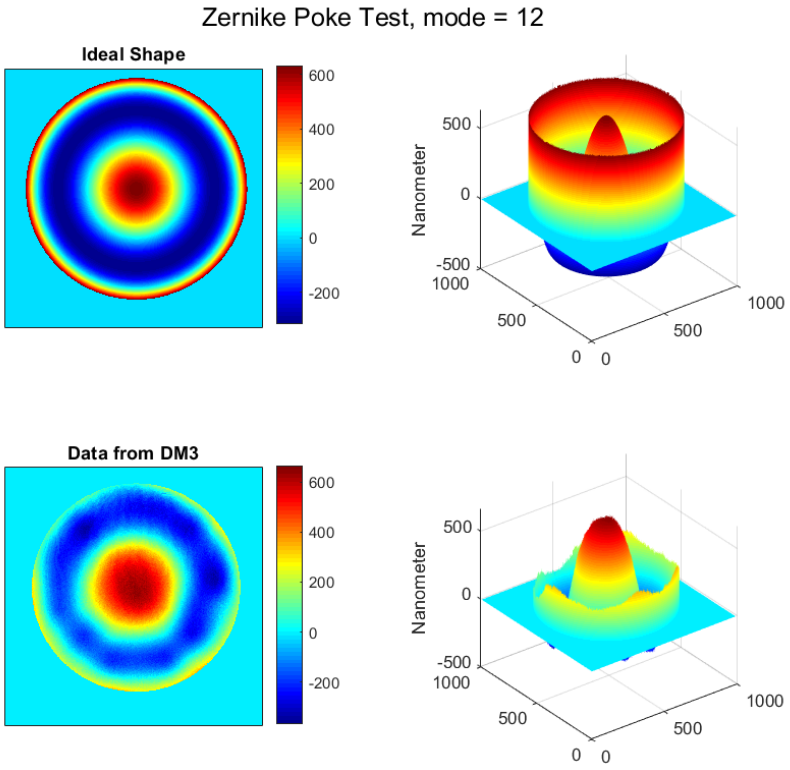

Figure 6.21 **Example Zernike Mode applied on DM3**: Zernike Mode 12. The ideal shape *(top)* is presented with the approximated shape made by DM3 *(bottom)*. A movie of the full Zernike test data from applying modes 1 - 57 to DM3 can be found on youtube.

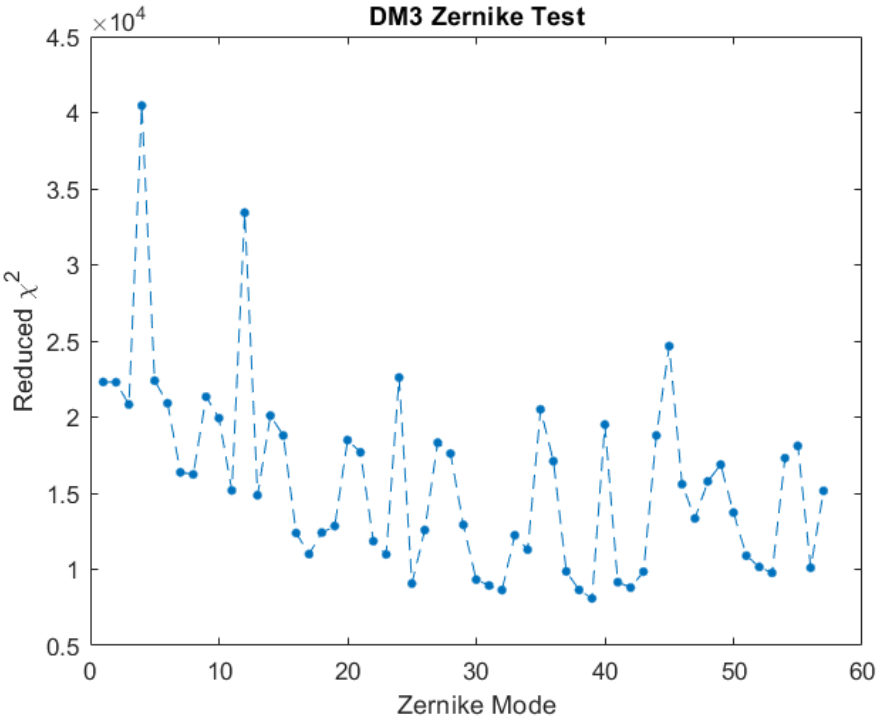

Figure 6.22 **Zernike Mode Test Reduced Chi Square**. The reduced chi square of each Zernike data frame was measured to determine how well each Zernike mode could be reproduced. Four of the spikes in the reduced chi square plot corresponded to the spherical Zernike modes (4, 12, 24, 40), indicating that these shapes were not as precisely replicated as the non-spherical modes.

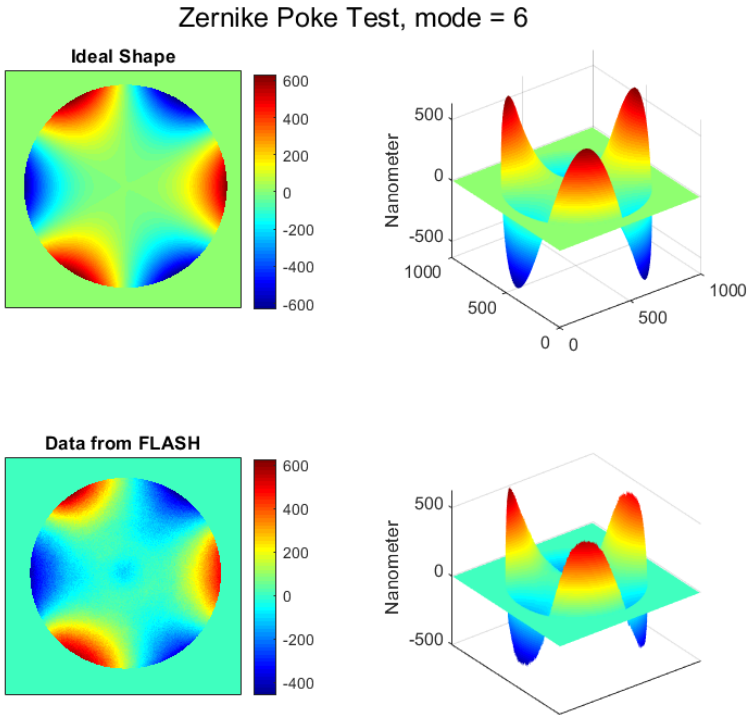

Figure 6.23 **Example Zernike Mode applied on FLASH**: Zernike Mode 6. (*Top*) The Zernike pattern fed to the FLASH. (*Bottom*) The resulting facesheet pattern produced by FLASH.

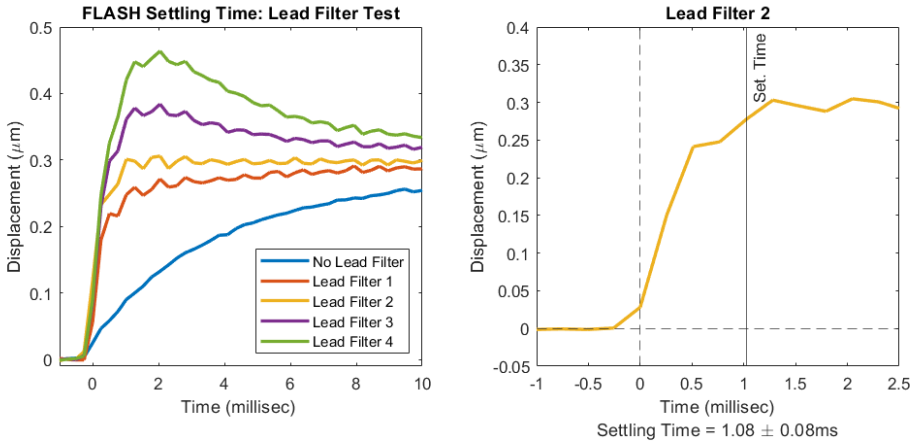

Figure 6.24 **FLASH Settling Time for Lead Filter Tuning.** By applying a lead filter to the actuators, the response time of the actuator was improved by an order of magnitude from $t_{set} = 14.3 \pm 0.1$ms to $t_{set} = 1.08 \pm 0.08$ms.

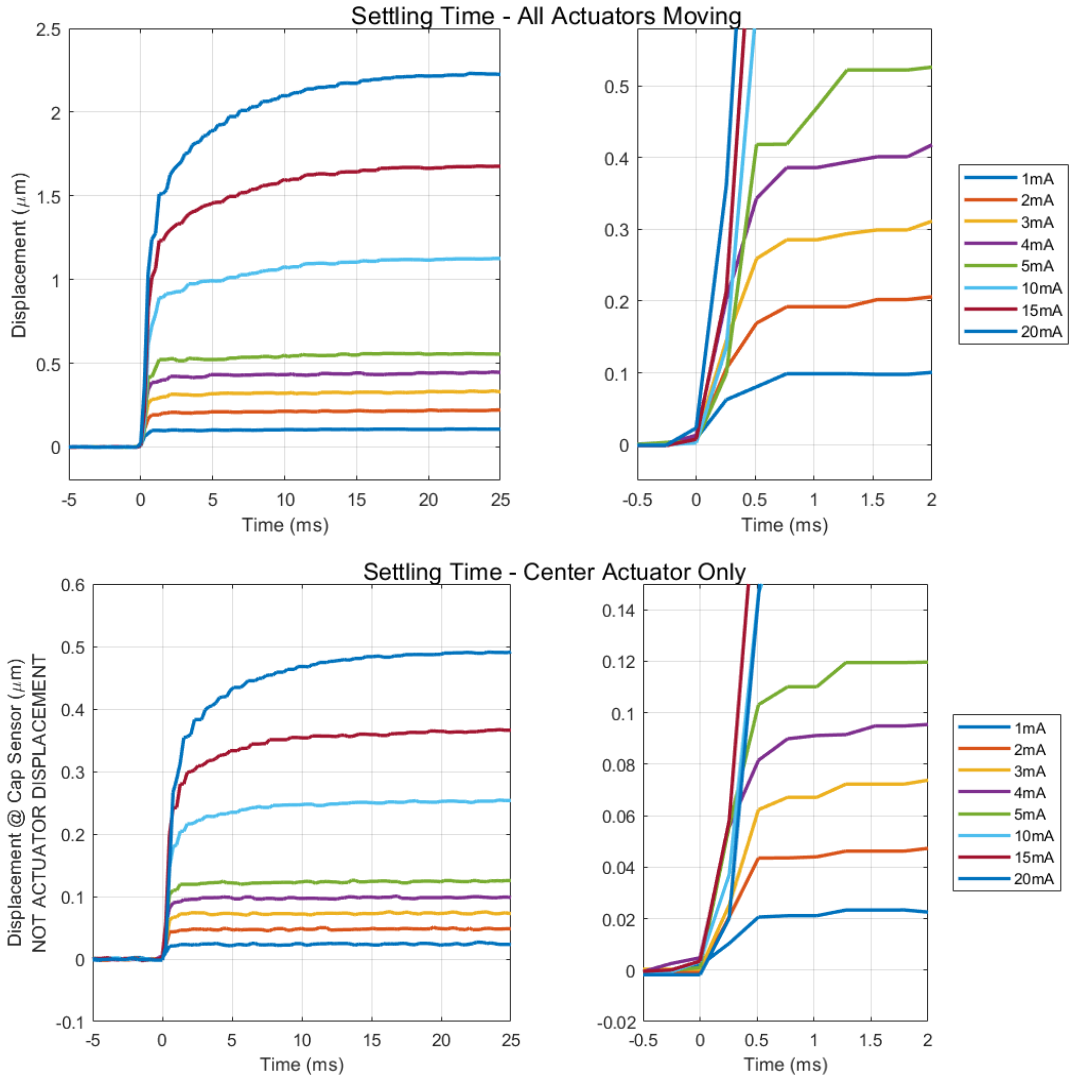

Figure 6.25 **FLASH Settling Time**. Movements were performed with eight applied currents using two styles of movement: all actuators together and the center actuator only. The testing was performed with the "optimal" lead filter applied, however, we find underdamped behavior in all but the smallest single actuator movements. From the linearity measurements, the average displacement shown here with an individual actuator translates to 46.5 ± 1.4nm/mA and the all-actuator displacements translate to 113.9 ± 1.0nm/mA.

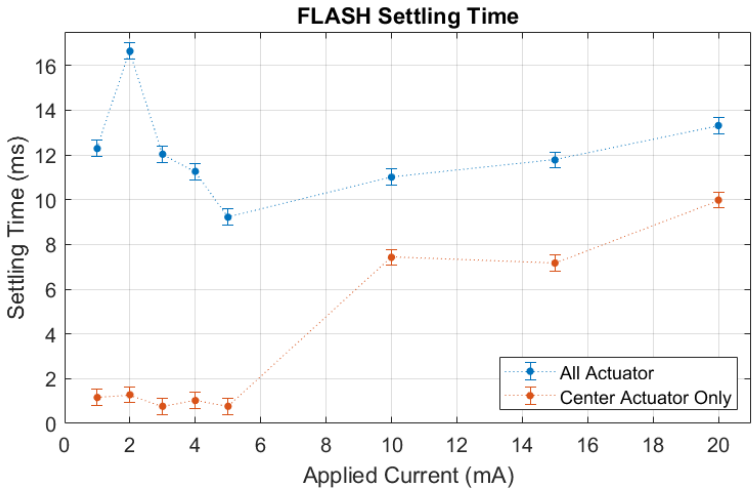

Figure 6.26 **FLASH Settling Time Measurements**. We measured the settling time using the start/stop time at $\pm 5\%$ the total displacement of the poke. The settling times for the small applied currents ($1 - 5\,\mathrm{mA}$) with the single actuator poke were measured to be < 2ms. The larger measurements of the settling time (> 5ms) correspond to runs displaying overdamped behavior.

6.3.10 Dynamic Testing: frequency response transfer function

Measurement setup: External Capacitive Sensor

To verify the dynamic behavior of the FLASH, a non-parametric identification was performed by applying a random input signal to the center actuator and capturing the facesheet displacements. This testing was conducted at TNO using a capacitive sensor system external to the FLASH (separate from the FLASH internal capacitive sensor system described here 6.2.2).

The frequency response of the transfer function measurement reveals a first order drop with a roll-off frequency of ∼40Hz (Figure 6.27). The first second-order mechanical resonance is ∼1.2kHz. The observed first order lowpass response can be explained by the eddy-current behavior within the magnetic circuitry from the fast-changing currents in the coil. The open-loop transfer function shows the dynamical response of a first order parametric model that matches the first order low-passing behavior. A single pole at 42.6Hz and a two-sample delay at 5kHz are present, which is expected from the data acquisition system that was used. The close match between the response of this parametric model and the measurement data in phase and amplitude verify that the low-passing behavior can be characterized as first-order low-pass.

Although the first order low-pass behavior starts at 40Hz, the closed-loop control bandwidth can be pushed to a faster frequency by properly tuning the PI controller. To demonstrate this, a loop-shaping exercise was performed based on the measured fre-

quency responses using a PI controller. Figure 6.28 shows the resulting Loop-gain ($L(j\omega) = H(j\omega)C(j\omega)$) and Sensitivity ($S(j\omega) = 1/(1 + L(j\omega))$) responses when tuning the PI controller to match the pole of the first order low-passing behavior within the actuator. With this PI controller, an open-loop bandwidth of 225Hz and a closed-loop sensitivity bandwidth of around 150Hz (-3dB) is achieved. Higher closed-loop performances are deemed possible when high-order controller design methods are employed.

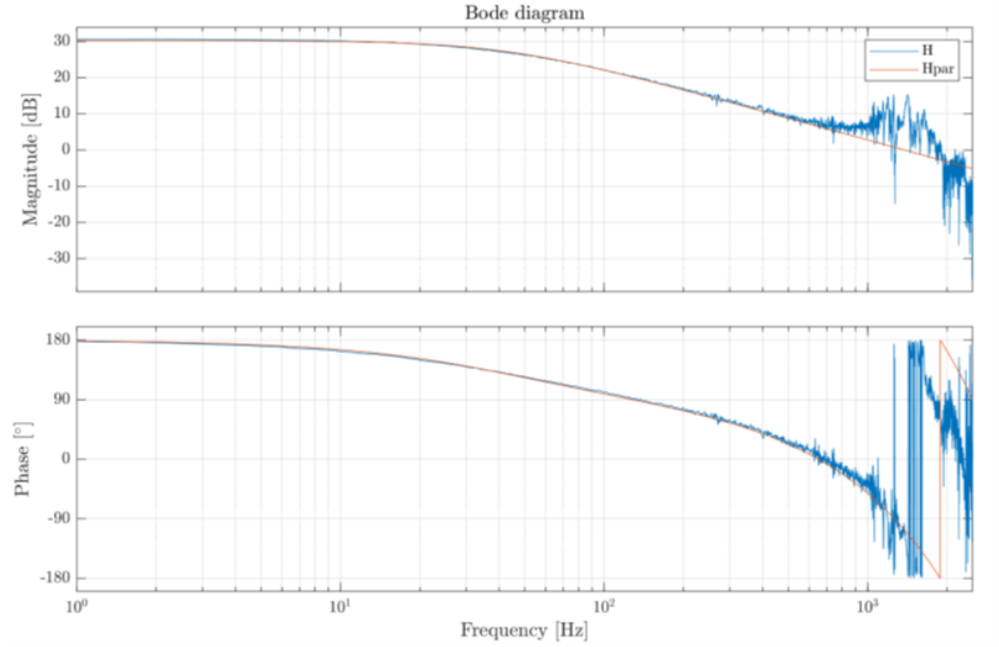

Figure 6.27 **Dynamical Test Bode Plot for FLASH** (*Top*) The non-parametric identification of the transfer function (*Bottom*) The first order parametric model fit to estimate pole location and IO delay. *Figure credit: Stefan Kuiper*

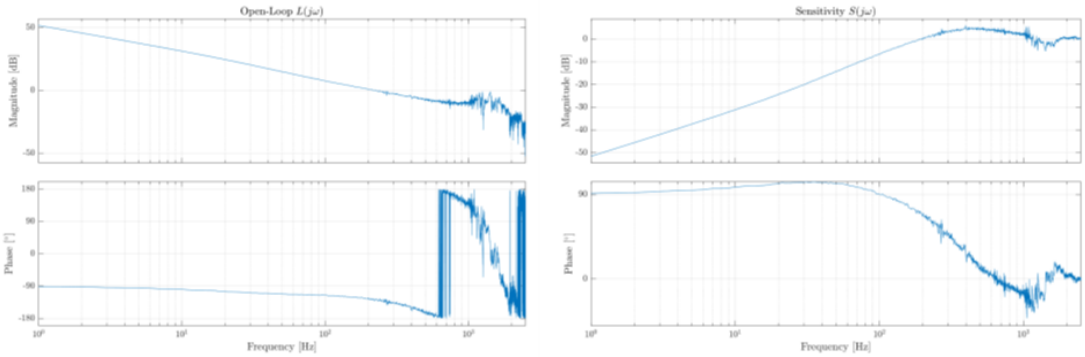

Figure 6.28 **Loop-shaping Exercise for FLASH** (*Left*) Open-Loop Transfer function ($L(j\omega)$) (*Right*) Sensitivity Transfer function ($S(j\omega)$). *Figure credit: Stefan Kuiper*)

6.3.11 Spatial Dynamical Testing

We measured the surface of FLASH using the QPI testbench (described in Section 6.2.3) to evaluate the transient behaviors present after moving an actuator. Testing was completed using the center actuator with applied currents of ±5 mA (±233 nm displacement). The optimally tuned lead-filter (defined in Subsection 6.3.9) was applied to make this testing consistent with the settling time test.

Measurements were performed using the images from the two QPI cameras with subframe sizes of 1024x1024 (speed 100 Hz) and 128x128 (speed 1.0 kHz). Examples of images from Camera 1 at these subframe sizes are shown in Figure 6.29. We were not able to use smaller subframe sizes because we were not able to resolve the sides of a fringe in the subframes smaller than 128x128. We normalized the raw images to account for differences in brightness between the test and reference beams using calibration flats. Each flat was the average of ten images and was obtained by blocking the opposite beam

(i.e. the reference-beam flat was taken with the test beam blocked).

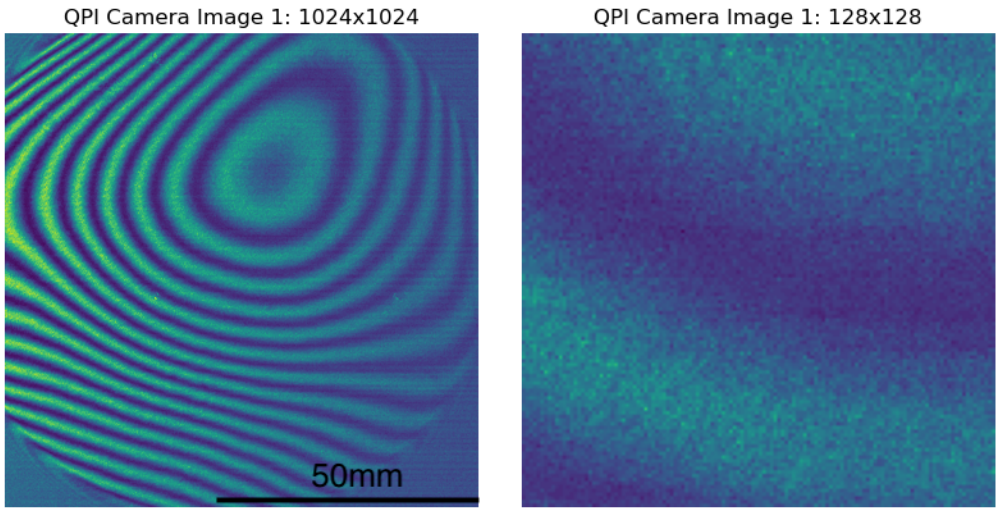

Figure 6.29 **Images from QPI**. (*Left*) An example image with 1024x1024 subframing. (*Right*) An example image with 128x128 subframing.

In our setup's natural steady-state before a move command was applied, we measured a small oscillation at $250 \pm 50\,\text{Hz}$. It is presumed that this vibration is due to the measurement setup and lab environment because the frequency is near the peak of the sound profile of the lab (see Figure 6.8).

We used the 128x128 frames with the speed of 1 ms/frame to study the speed of the actuator movement and the resulting oscillations. The majority of the start and end of the actuator move occurred between two frames, corresponding to a time of $\sim 1\,\text{ms}$. This is consistent with our settling time measurements.

No induced oscillations were detected from the actuator pokes within the frequencies

probed by our testing (slower than 1kHz). This was expected as the FLASH mechanical resonances occur at frequencies $> 1.2\,\text{kHz}$.

6.4 Summary

The key results from the UCSC-LAO initial performance testing of DM3 and FLASH are summarized in Table 6.5. Our linearity, hysteresis, drift, and Zernike mode testing verify that the performance of the 2020 generation of TNO HVR actuators performed as expected and suggest that the performance of the UH2.2m adaptive secondary mirror will behave as TNO's modeling predicts.

The dynamic and settling time measurements provide the first measured results of how the TNO systems perform at kilohertz speeds. Without tuning the profile of the current applied, the TNO deformable mirrors have a settling time of $t_{set} = 14.3 \pm 0.1\text{ms}$. Our testing demonstrates that the correction speed can be improved to $t_{set} = 1.08 \pm 0.08\text{ms}$ using a lead filter. This speed is consistent with the operating speed of the current on-sky adaptive secondary mirrors constructed with voice-coil style actuators. [21] We also identified that the original lead-filter control tuning does not apply universally. We find that no major oscillations were induced by small actuator movements at frequencies $< 1\,\text{kHz}$, as expected.

The Zygo interferometer and capacitive sensor data were consistent when simultaneous data collection was performed. The two data collection methods complemented each

other; the Zygo interferometer provided a holistic view of the mirror shape and the capacitive sensors provided dynamic time response information. The capacitive sensors are capable of measuring displacements at a higher precision than the Zygo interferometer, as long as having limited spatial information is acceptable. In future situations when an interferometer is not possible to use in the testing setup (i.e. in an environmental chamber or on-sky optical system), our testing indicates that the capacitive sensors can accurately provide feedback about the real time performance of the deformable mirror.

Table 6.6 the results presented in this chapter against the requirements from Stroebele et al 2016 [229] for the E-ELT deformable M4 requirements. The TNO technology meets the requirements for linearity, hysteresis, actuator stroke, and actuator replaceability. The technology currently falls short on the necessary actuator count and density/pitch and possibly the small stroke settling time.

Table 6.5: Summary of DM3 and FLASH Testing Results

Section	**Test**	**Takeaway**
6.3.1	Influence functions	The influence function cannot be profiled using a Moffat, Cauchy, or Gaussian. FLASH actuator spacing = 39.4± 0.4mm
6.3.2	Act. Cross Coupling	DM3 cross coupling = 37.07 ± 0.93% FLASH cross-coupling = 34.2± 1.0%
6.3.3	Natural Shape Surface Flat	DM3: Surface went from RMS = 2778nm to RMS = 28nm with an average current per actuator = 17.8 ± 3.3mA and total power = 75mW. FLASH: Surface went from RMS = 1158nm to RMS = 15nm with an average current per actuator = 17.0± 4.7mA and total power = 7.3mW (0.4mW/actuator)

6.3.4	Linearity	DM3 Average Displacement = 79.32 ± 1.08 nm/mA DM3 Linearity = 99.4% ± 0.33% FLASH Individual Actuators: avg disp. = 46.5 ± 1.4nm/mA lin = 95.2 ± 0.8% FLASH All Actuators: avg disp. = 113.9 ± 1.0 nm/mA lin = 96.8 ± 0.5% There are asymmetries between negative and positive currents.
6.3.5	Hysteresis	DM3 Hyst = 2.10 ± 0.23% FLASH Hyst = 1.80 ± 0.13% (zygo), 1.93 ± 0.04% (capacitive sensors)
6.3.6	Repeat. & Drift	DM3: No repeatablity issues to $\Delta RMS = 33.5$ nm No drift measured to 1000nm. FLASH: max drift seen from cap sensors in 9 room-temperature tests: drift < 20nm Some evidence was seen that repeatability could be affected by mirror temperature or working-hours.
6.3.7	Zernike	Additional power is required to reproduce higher order Zernike modes. Spherical modes are the most difficult to reproduce.
6.3.8	Lifetime	DM3: Over 110 million cycles have been completed on each actuator with no change in performance
6.3.9	Settling Time	FLASH: A lead filter can be implemented to lower the actuator response time. A well-tuned lead filter achieved $t_{set} = 1.08 \pm 0.08$ms for a step of 10mA ($\sim 3\mu$m).
6.3.10	Dynamic frequ. response	FLASH: First-order roll-off frequency = 40Hz; Second-order mechanical resonance = 1.2kHz
6.3.11	Spacial Dynamic. Test	FLASH No oscillations induced by an actuator poke of $\sim 230nm$ were detected at frequencies below 1kHz.

Table 6.6 TNO FLASH results as compared to the Stroebele et al 2016 ELT M4 DM requirements [229].

Description	**Specification: ELT XAO-DM M4**	**TNO DM status**
DM clear aperture	⌀150mm-450mm, goal ⌀270mm. Annular shape with 24% central obscuration	Will pass after proof of ASM at mid-sized telescopes
Mirror surface Flatness	10nm rms, goal 5nm rms, after subtraction of few low order modes (Z4-Z11)	Will depend on final ASM designs but not expected to be an issue
Actuators count within the clear aperture	11 000, goal 20 000	Needs development
Actuators pitch (derived information, no specification)	0.9mm – 3.7mm	Needs development
Lowest mechanical resonance frequency (causing a mirror surface deformation)	>1000Hz, goal >2000Hz TBC	Will depend on final ASM designs but not expected to be an issue
Actuators Stroke	>3μm (3 by 3)	Pass; FLASH performed >5μm
Small stroke settling time incl. latency of the drive electronics	50nm settling to ±10% within 150μs, goal 100μs	Only large-scale settling time measured. Cap sensors/QPI did not have sufficient readout speed to complete test.
Hysteresis	5%	Passes; FLASH Hyst = 1.93 ± 0.04% (capacitive sensors)
Actuators non-linearity	<5% Goal <1%	Passes; FLASH lin = 95.2 ± 0.8%
DM surface temp incl. housing: deviation from ambient	<±1C	Depends on implementation of ASM telescope, unknown if it will be an issue
Update frequency of the DM command	2500 Hz goal 4000 Hz	Not explored
Nonfunctioning actuators; depends on failure mode.	5-30, goal 0	Passes; an actuator replacement technique has been proven by TNO

Chapter 7

The Future: Future development of the HVR-based large-format deformable mirror technology and in-progress adaptive secondary mirrors

"Things are only impossible until they're not."

PARTIALLY ADAPTED FROM

An adaptive optics upgrade for the Automated Planet Finder telescope using an adaptive secondary mirror.

Rachel Bowens-Rubin, Arjo Bos, Philip Hinz, Bradford Holden, and Matt Radovan.

In Adaptive Optics Systems VIII, volume 12185 of Society of Photo-Optical Instrumentation Engineers (SPIE) Conference Series, page 121851X, August 2022

7.1 Current barriers in the development of the HVR-actuator based adaptive secondary mirrors

As major observatories (8m+) consider the adoption of an adaptive secondary mirrors as part of their adaptive optics systems, the HVR-based deformable mirrors are currently viewed as higher risk because they have yet to be demonstrated on-sky. This instrumentation development faces several upcoming barriers before it will be ready for adoption at major facilities:

1. The HVR-based technology has yet to be integrated into a full adaptive optics on-sky astronomical application. It is unknown what unpredicted issues will arise. The ASMs that are in development to address this need are overviewed in the following subsections.
2. The actuator spacing and number of actuators operating in a system needs to improve by an order of magnitude. No more than 60 actuators have yet to be built into a deformable mirror by TNO, but major observatories will require deformable mirrors with > 1000 actuators.
3. The manufacturing of a facesheet using free-form glass slumping has not been proven on scales larger than 0.68m. Keck will require a deformable mirror that is 1.4m in diameter.

4. Careful consideration needs to be made to develop the drive electronics. The elctronics used for the testing in Chapter 6 are considered prototyping electronics. Similarly, the control software has yet to be developed beyond the prototyping stages.
5. Driving the actuators at the speeds necessary to be incorporated into an extreme adaptive optics systems ($> 1\,\mathrm{kHz}$) has yet been proven.

Several projects in partnership between TNO, the University of Hawaii, the University of California Observatories, and NASA are underway to try to address these issues and increase the technology readiness of the HVR-based mirrors. Section 7.2 overviews the ASMs currently in planning and construction for five observatories. These ASMs are being designed for a range of telescope sizes from 2.2m to 10m.

7.2 Overview of HVR-based Adaptive Secondary Mirrors in Construction and Planning

The goal of the technology development happening in partnership with TNO is to make the HVR-based ASM technology viable for use at all sizes of observatories. To build towards this goal, there are four adaptive secondary mirrors planned that will demonstrate the reliability of the deformable mirror technology and its ecosystem (i.e. control software, electronics, etc). The state of this development plan is overviewed in Figure 7.1.

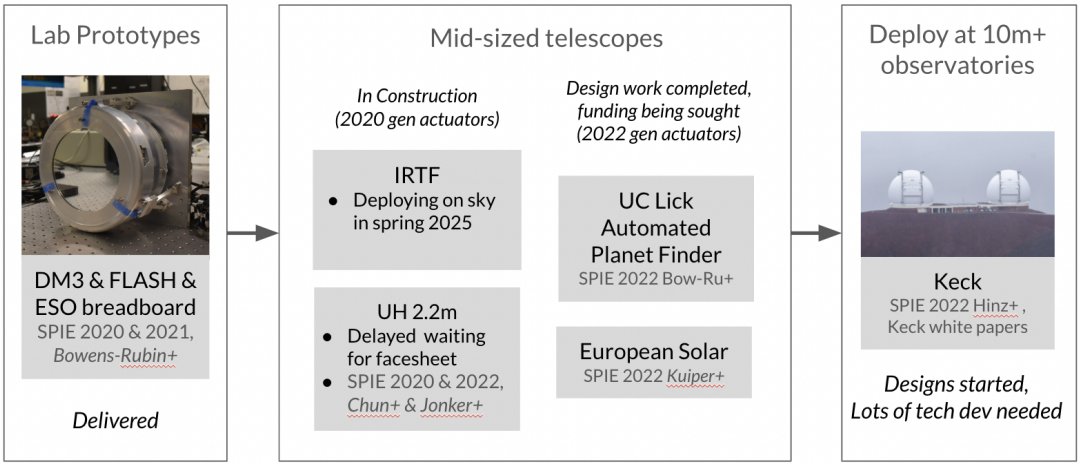

Figure 7.1 **TNO adaptive secondary mirror development plan**

There are currently three lab prototype deformable mirrors that have been built using three different generations of HVR actuators: DM3, FLASH, and the EST DM prototype. Each of these prototype deformable mirrors has a flat surface. The technical specifications of DM3 and FLASH were reviewed in Chapter 6. The third lab prototype was built for the European Solar Telescope using 19 rotationally symmetric actuators from the 2022 generation.

7.2.1 NASA Infrared Telescope Facility ASM

In spring 2024, TNO will deliver its first adaptive secondary mirror for astronomical use to the NASA Infrared Telescope Facility (IRTF). The IRTF is a 3.2m telescope located on Maunakea that is primarily dedicated to the infrared study of solar system objects. It is operated by the University of Hawaii on behalf of NASA [IRTF webpage].

The IRTF ASM was built using a vendor-supplied glass shell and 36 HVR-actuators from the 2020 generation. It will be operated using the DM3 electronics and custom real control software built in-house at the University of Hawaii. After the first demonstration of closed-loop control on sky at the IRTF this spring, the ASM will be decommissioned and undergo an upgrade to increase the actuator count and improve the backing structure. In the future, the IRTF ASM will become a facility active optics system. Additional information about this project can be provided by its PI, Prof. Mark Chun.

7.2.2 University of Hawaii 2.2m Telescope ASM

TNO is currently constructing an adaptive secondary mirror for the University of Hawaii 2.2m telescope (UH-2.2m) (Figure 7.2). This ASM was the first to be conceptualized for a mid-sized telescope in 2018, but its completion has been delayed due to issues in the procurement of the glass facesheet. It incorporates 211 actuators from the 2020 generations within a 620mm diameter. When finished, it will be integrated with the ‘imaka ground-layer demonstrator [61] currently installed at the UH-2.2m Telescope. More information about the UH2.2m ASM can be found in the SPIE paper, Chun et al. 2022 [62].

7.2.3 University of California Automated Planet Finder ASM

The University of California Lick Observatory Automated Planet Finder telescope (APF) is a 2.4m robotic telescope located near San Jose CA. The APF is dedicated to searching

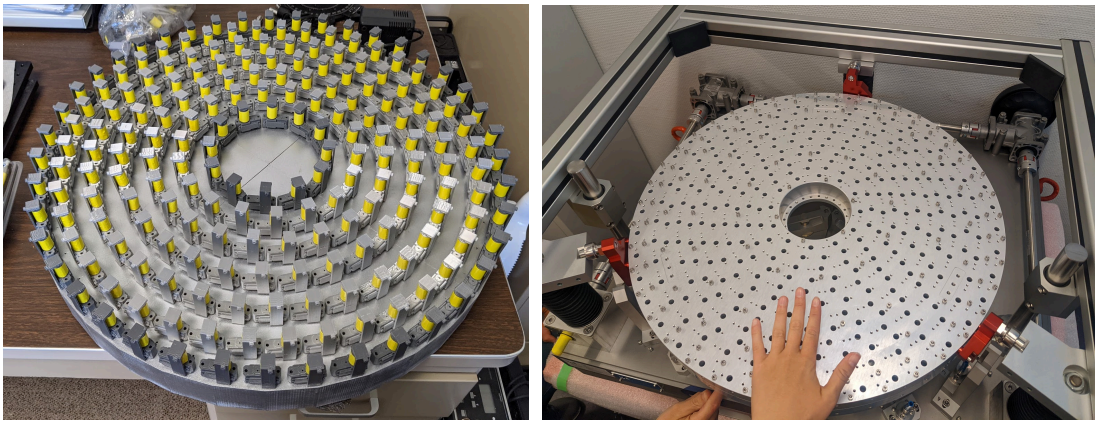

(a) 3D print of the UH-2.2m ASM (b) UH-2.2m ASM backing structure

Figure 7.2 **University of Hawaii 2.2m Telescope Adaptive Secondary Mirror in construction.** The ASM for the UH-2.2m Telescope is currently in construction at TNO. Image *(a)* shows the 3D print that was constructed by Mark Chun at the University of Hawaii to show the actuator layout for the ASM. Image *(b)* shows the aluminum backing structure in the build jig currently located at TNO.

for exoplanets using the radial velocity method. Every night with clear skies, the APF automatically opens its dome and slews across the sky to take precision spectroscopy measurements of stars that could host exoplanet systems. These RV measurements are critical for discovering new planets, constraining an exoplanet's orbital properties, and measuring an exoplanet's masses.

As we enter the era of TESS and JWST, the exoplanet community is facing a shortage in instrumentation that can carry out these critical radial velocity measurements. By adding an adaptive optics system to the APF, the stability of the star's PSF will increase because the light will be better concentrated through the spectrograph slit. Simulations have estimated that we could nearly double the photons collected per second from an efficiency of 23% to 48% (see Section 7.3.5). This efficiency gain is similar to having access to the photon collecting power of a second telescope. More targets could be covered per night and/or the APF could view dimmer targets to alleviate time pressure on RV instruments operating at larger telescopes. An ASM also offers a unique solution of upgrading the APF without disturbing the internals of the spectrograph and disrupting the long-running RV baselines.

The APF ASM is currently seeking funding. If built, it would be the first pairing of an adaptive secondary mirror and a radial velocity instrument. An overview of all the large-format deformable mirror technology development happening at APF is included later in this chapter. Additional information about the APF ASM can be found in the SPIE paper, Bowens-Rubin et al. 2022 [32].

7.2.4 European Solar Telescope ASM

The European Solar Telescope (EST) is yet-to-be-constructed 4 m telescope that will be located at the Roque de los Muchachos Observatory in the Canary Islands, Spain [64]. This telescope will be a dedicated solar observatory and will be equipped with a multi-conjugate AO system [127]. This system will have an adaptive secondary mirror as well as multiple post-focal plane deformable mirrors. Because the EST will be staring at the sun, this ASM requires an active cooling solution.

The EST ASM will represent a dramatic increase in actuator count for the HVR-based technology, designed with 1950 actuators within ⌀80cm arranged in 26 rings. The actuators will be from the 2022 generation, which are rotationally symmetric and have a 16.2mm pitch to allow for the high-density packing required. More information about the EST ASM can be found in the SPIE paper, Kuiper et al. 2022 [127].

7.2.5 W.M. Keck Observatory ASM

The W.M. Keck Observatory is located on Maunakea, Hawaii and consists of two side-by-side 10m telescopes. Together, the two Keck telescopes house ten science instruments. An ASM for one or both of the Keck telescopes could provide ground layer AO correction and improved thermal infrared observations for multiple science instruments [109].

The current Keck instruments that could benefit from an ASM are the following:

- MOSFIRE would benefit from ground-layer AO correction with some minimal

modifications.

- LRIS could benefit from ground-layer AO correction if flexure compensation is added.
- DEIMOS could benefit from ground-layer AO correction if an atmospheric dispersion compensator were added.
- OSIRIS and NIRC2 currently use the AO bench. They could take advantage of an AO system with fewer optics and a higher actuator count if much of the functionality of the current AO bench (wavefront sensor, image rotator, etc) were rebuilt to utilize the ASM.
- KCWI may benefit from ground-layer AO correction.
- HIRES may benefit from increased PSF stability, similar to the case for the APF telescope.

The future Keck instruments that would benefit from an ASM are:

- SCALES is an infrared field spectrograph that will work in the infrared to wavelengths as long as 5μm. It could take advantage of the lower thermal background adaptive optics correction.
- FOBOS is a wide-field fiber fed spectrograph that could conduct science significantly more efficiently if fed with a ground-layer AO correction.
- LRIS2, an upgrade of LRIS, would be more equipped than its predecessor to handle the modifications needed to use the ASM. Like LRIS, it would benefit from ground-layer AO correction.

- IGNIS is an infrared instrument operating out to 2 microns that would benefit from improved thermal background.

The concept drawings for the Keck ASM consider a system with 1000–4000 actuators packed into a secondary mirror that is ⌀1.4 m (projected spacing on the primary between 175–350 mm). A design with a 4000 actuator count could benefit visible light AO correction which is expected to be in demand from ground-based facilities when Hubble retires. The ASM would be housed in a dedicated existing top-end module which can be swapped during day-time operations (Figure 7.3).

A concept study for the Keck ASM was funded in 2020 and the project received Phase A proposal funding in 2021 under the working name Keck Adaptive Secondary Mirror (KASM). More information about KASM can be found in the SPIE paper: Hinz et al 2020 [109], in the Keck White Paper/Phase A proposal, or in the upcoming SPIE paper: Hinz et al 2024.

7.3 Large Format Deformable Mirror Development the Automated Planet Finder Telescope

Two projects are currently being pursued using the APF telescope that will benefit the development of large-format deformable mirror technology: a post-focal plane adaptive optics testbed and an adaptive secondary mirror.

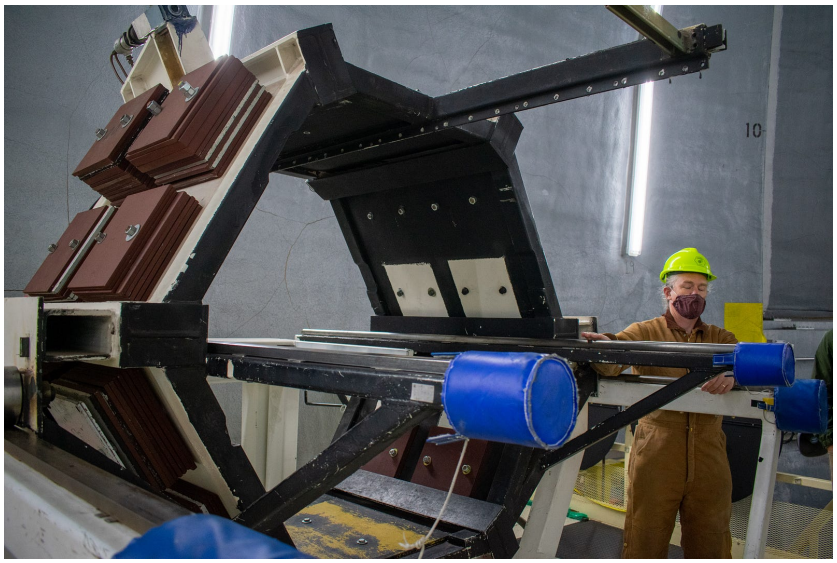

Figure 7.3 **A top-end module for the Keck I Telescope that is currently unused.** This module could be a future home for a 1.4m Keck adaptive secondary mirror. It can be swapped on and off the telescope by the day time crew.

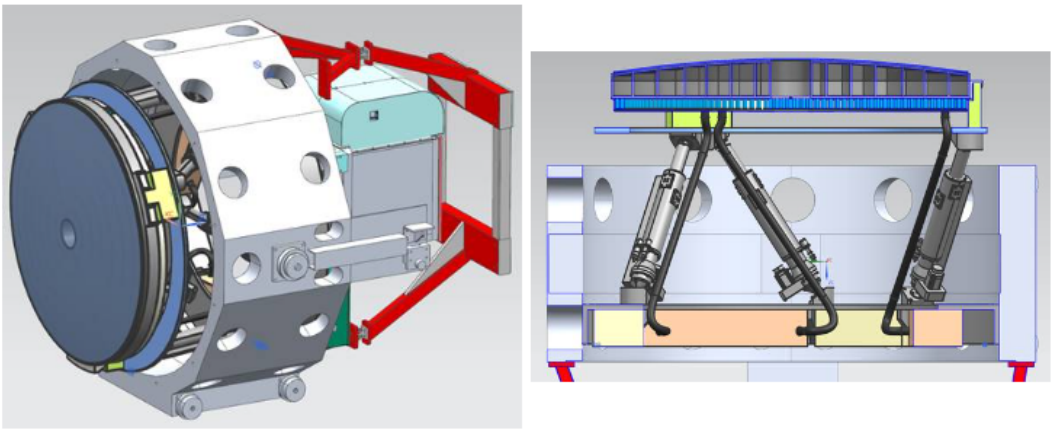

Figure 7.4 **Concept CAD for the Keck Adaptive Secondary Mirror.** This CAD design was completed by TNO. (*Figures retrieved from Hinz et al 2020 [109]*)

The APF is an ideal telescope to conduct this sort of technology development. Because of the style of cadence observations requested by the community, it is easy to negotiate getting observing/engineering time in hour long blocks spread over multiple days. Because of the relative proximity to the UCSC campus, it is also easy for members of the UCO community to travel on site and connect with the observatory staff.

7.3.1 Overview of the Automated Planet Finder Telescope

The Automated Planet Finder (APF) is a 2.4-meter telescope located at the University of California Lick Observatory near San Jose, California that operates fully robotically (Figure 7.5). An overview of the basic properties of the APF and observing site are listed in Table 7.1. A typical value for the seeing at Lick Observatory is 1.5 arcsec with tip/tilt motions of 0.2 arcsec.

The APF was constructed as a dedicated facility to search for extrasolar planets using an optical echelle spectrometer and an iodine gas absorption cell. The spectrometer is optimized to take precision radial velocity measurements around nearby low-mass dwarf stars [42]. Such cooler stars are rich in stellar lines in the iodine region. That high information density combined with the high resolution of the Levy spectrometer yields up to a 1 m/s precision for radial velocities. [41] The APF is optimized for exoplanet science using a spectrometer with spectral resolving power of R≈100,000. For typical observations, the APF uses an image plane slit width of 0.5 arcsec to optimize the achievable spectral resolution.

The APF optical system and the measured on-sky performance is documented on the APF UCO Lick website, in the APF prospectus from July 2013, and in Jennifer Burt's PhD dissertation: The Automated Planet Finder telescope's automation and first three years of planet detections [41].

Figure 7.5 **The 2.4m Automated Planet Finder Telescope** *(Left)* The outside of the APF dome. *(Right)* An inspection of the current APF secondary mirror assembly.

7.3.2 Current limit to the performance of the APF RV measurements

Analysis of guider data for a typical sequence allows us to estimate the slit throughput as 21% with variations of 4% as seen by the guider over 1 second integrations (see Figure 7.10). This throughput is limited by the spread of light because of atmospheric seeing and slow (<1 Hz) tracking variations.

The time-varying line spread function is the largest source of systematic error in the precision of the radial velocity measurements. When using the iodine cell method to measure radial velocities, the most critical component in the measurement accuracy is

Table 7.1 **Overview of the Current APF Telescope and Performance**

Telescope size	2.4 m
Optical prescription	f/15
Location	Mt Hamilton, CA
Typical seeing at site	1.5 arcsec[*]
Type of Spectrograph	Slit Spectrometer[*]
Wavelength Reference	Iodine gas cell in beam[*]
Slit Width Options	0.5-2"[*]
Spectrograph Resolution	R=110,000 (0.5"), R=80,000 (1")[*]
Science spectral range	374 - 680 nm[*]
Magnitude Limit of the Guide Camera	V = 4 - 15[†]
System throughput	$21 \pm 4\%$[†]
Median RV Precision (meas. July 2013-March 2016, V=4.68))	1 m/s[†]

[∗] Vogt et al 2014 [238], [†] Burt et al 2016 [41]

the line shape function [44]. The steeper the absorption features in the star, the more accurate the velocities. For the Levy spectrometer on the APF, the line shape function is modeled with 18 wavelength-dependent free parameters for every exposure. The classical solution to stabilizing the line spread function for an iodine cell spectrometer is retrofitting a fiber scrambling system [225]. When implemented on the HIRES on the Keck I telescope, Spronck et al. (2015) [224] found that their system stabilized the line spread function to such a degree that the highest signal-to-noise data showed errors of 0.5 m/s, less than half of the best values of 1.1-1.2 m/s for the same signal to noise without the scrambling. Further, the line spread function was stable enough that it removed the need for the huge number of wavelength-dependent free parameters per observation. For the APF, Burt et al. (2014) [42] found that the noise floor of the Levy spectrometer was 1.2 m/s, very close to the values found by Spronck et al. (2015) [224]

for HIRES, showing that in principle a similar performance gain is possible. However, the key disadvantage of fiber scrambling is that the additional optics required meant that throughput had decreased by a factor of six. A similar result for the Levy on the APF would mean that the typical exposures would increase from 20 minutes to two hours.

7.3.3 APF adaptive optics on-sky testbench (post-focal plane)

The APF adaptive optics testbench is an adaptive optics instrument designed to be an on-sky demonstration of the TNO technology in the "traditional" post-focal plane position. The goals of this project are to (1) create an on-sky platform that is easily accessible to the UCO community to test the system components related to developing the TNO technology (electronics, controls methods, software, etc), (2) retire technical risks for an future APF ASM adaptive optics upgrade, and (3) train early career scientists in the steps to deploy an adaptive optics instrument from design to finish.

The APF AO on-sky testbench development began in fall 2023 and Dominic Sanchez has been the principle optical designer. This instrument is independent of the spectrograph and will be housed at the opposite Nasmyth port of the Levi spectrometer.

7.3.4 Technical overview of the APF Adaptive Secondary Mirror Concept

As introduced in section 7.2.3, an adaptive secondary mirror upgrade is also being planned for the APF. Funding is currently being sought for this project.

The design of an ASM-based AO system to stabilize the APF PSF can be made with two main additions requiring minimal modifications to the telescope. The first addition is a replacement of the current static secondary mirror (pictured in Figure 7.6) with an adaptive secondary mirror (Figure 7.7). The second is an off-the-shelf wavefront sensor and associated optics for the WFS light path (shown in Figure 7.8).

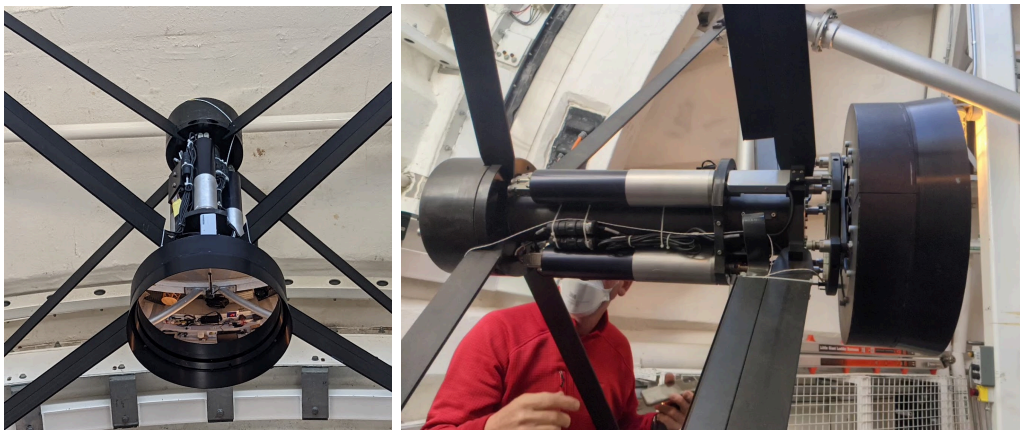

Figure 7.6 **The APF static secondary mirror** mounted on the hexapod that is used to set the focus.

An overview of the proposed AO system is listed in Table 2. The adaptive optics upgrade requires a wavefront sensor that uses light not employed for science observations. A suitable passband is 700-1000 nm, since it is unused in the Levy spectrometer. Since

the spectrometer is observing a bright star, the WFS will be fixed on-axis. We set the spatial sampling at 8 subapertures across the telescope diameter. This will set both the deformable mirror actuator geometry and Shack-Hartmann lenslet size. We arrived at this value after exploring different spatial samplings in the AO simulation. While better samplings improved the Strehl, the coarse slit size resulted in little improvement in throughput above this value.

RV instruments such as the APF/Levy favor observing bright stars to make these precise measurements. As such, there are plenty of photons available to measure and correct the wavefront of the light going into the spectrometer. Further, there is no anisoplanatism effect since the "guide star" used for wavefront control is the science object itself. This allows for a simple implementation of the AO system requiring a natural guide star wavefront sensor on axis. Because the deformable mirror can be integrated into the telescope optics, no new optics are needed beyond a dichroic to extract the light used for the wavefront sensor.

The mirror: Two CAD designs have been completed by TNO for the APF ASM as the project awaits funding. The first design contained 61-actuators and is shown in Figure 7.7. An alternative design was proposed with 180 actuators in order to match the spacing and actuator type in design for the W.M. Keck Observatory ASM. The mirror facesheet will be a 37 cm diameter, convex hyperbola with a radius of curvature of R=1198 mm and a conic constant of -1.49, matching the existing APF optical prescription.

Table 7.2 **Overview of the proposed adaptive secondary mirror AO system for the APF**

Specification	**Value**	**Notes**
DM Location	Secondary mirror	
Number of Actuators	61 (Design 1); 180 (Design 2)	2022-gen, rot. symmetric
Wavefront Sensor	Alpao Sh-Hart EMCCD	
WFS Bandpass	700-1000nm	
WFS Sampling	8 subapertures across diameter	
Operating limit with AO	15 in I band	same as current guider
Corrected Image Width	0.9"	for 1.5" seeing
Corrected Image Jitter	0.05"	improvement of 4X
Expected Throughput	61%	improvement of 2.9X
Expected RV Precision	0.5 m/s	median

Figure 7.7 **The APF ASM secondary assembly model as designed by TNO.** The ASM has 61 actuators laid out in a hexapolar arrangement. The ASM will make use of the existing focus and tip-tilt assembly from the current static secondary mirror assembly. (*Figure credit: Arjo Bos & TNO*)

The Wavefront Sensor: The WFS for the APF ASM adaptive optics system has been designed to be built around an Alpao standard Shack-Hartmann WFS camera placed on-axis. Because the wavefront sensor requires good sensitivity in the red and good noise performance to be able to operate on the faintest stars for an APF observation, the system will use an electron multiplied CCD (EMCCD). Alpao has developed a Shack-Hartmann EMCCD device with low latency and high framerates suitable for our needs. The device has 16x16 sub-apertures and can operate at up to 1004 Hz. The optical design calls for 8x8 sub-apertures, so it will be able to operate the device at up to 1838 Hz with a frame latency of 69μs.

The WFS will be fed by a short pass dichroic that has a cut-on wavelength between 700-750 nm. The dichroic will feed a transmissive reimaging optic that images the APF pupil onto the Alpao Shack-Hartmann lenslet array. The fore optics for the Levy spectrometer are shown in Figure 7.8. They are laid out on an optical breadboard that has suitable space for a dichroic, reimaging lens, and the Alpao WFS module.

The quantum efficiency for the Alpao EMCCD Shack-Hartmann WFS is 50% (Alpao datasheet). Assuming a 30% system throughput (not including the detector) with the specified noise for each subaperture from Alpao, we estimate being able to provide usable stabilization down to guide star magnitudes corresponding to an I-band magnitude of approximately I=11. Simulations with the HCIpy software package [193] confirm this, indicating 1 kHz operation will be optimal to stars as faint as I=9, 300 Hz should be used for stars with 10-12, and that some improvement out to I=15 is possible with corrections

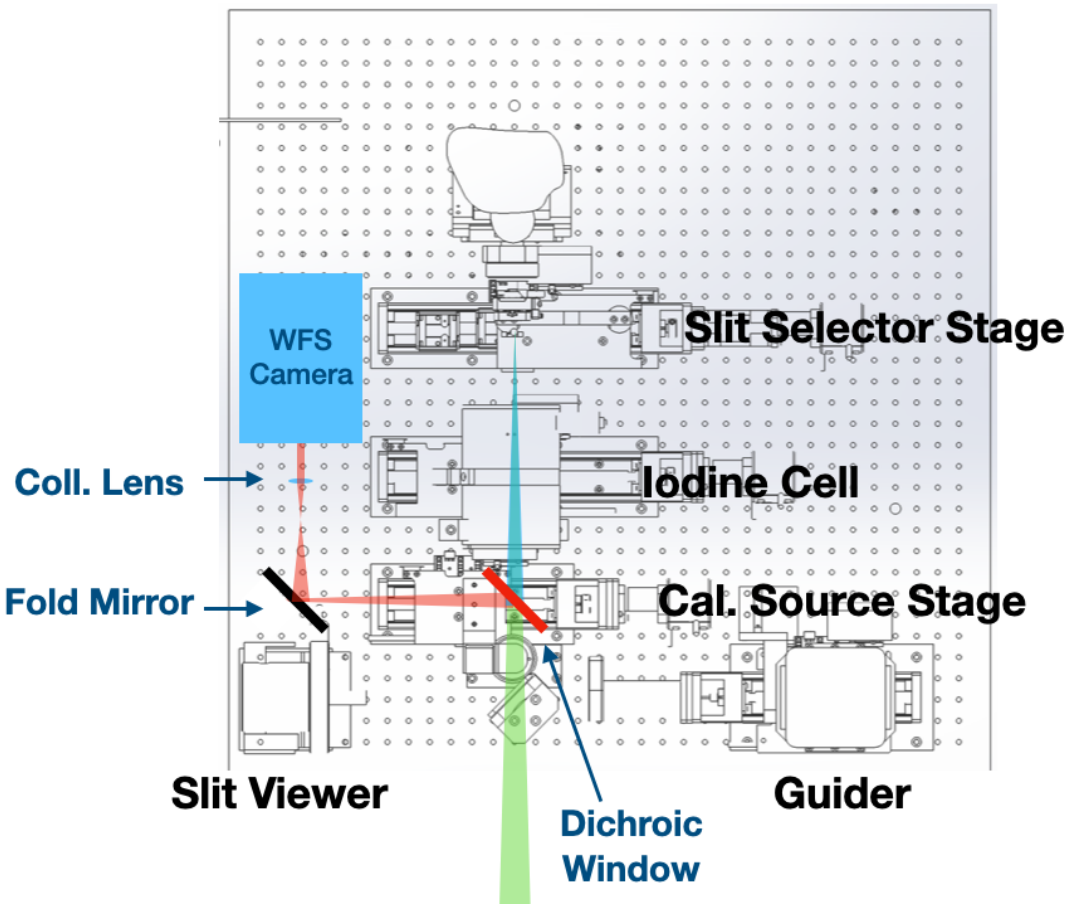

Figure 7.8 **The current APF optics layout with the proposed WFS Camera Location.** The current APF optics bench components are shown in black and white and the additions are shown in color. We will use the calibration source stage to allow insertion of a short-pass dichroic in the beam. The dichroic will reflect long wavelength light to an Alpao SH WFS. A collimating lens is all that is needed to create a pupil image on the SH WFS camera. *(Figure Credit: Phil Hinz & University of California Observatories).*

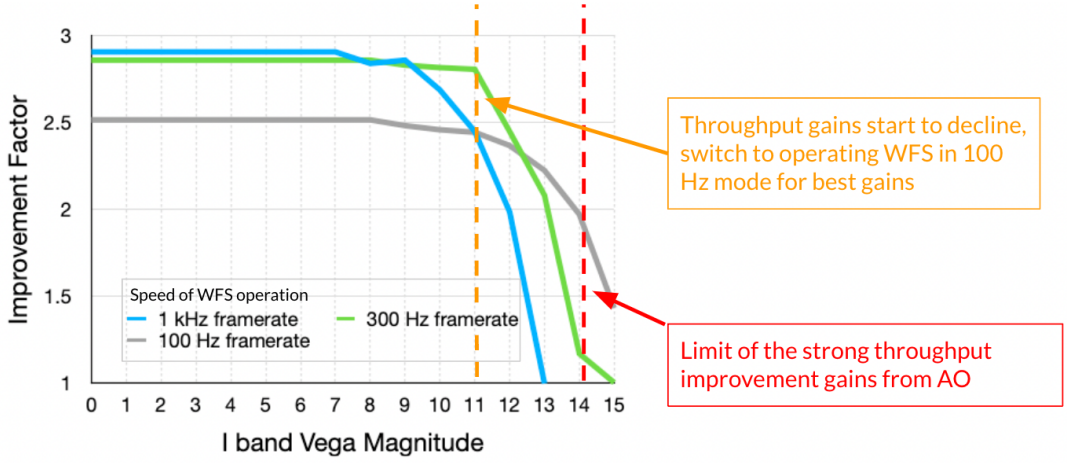

Figure 7.9 **Simulated Efficiency Improvement of an APF enabled by AO.** The throughput improvement factor of the AO upgrade was simulated using HCIpy [192]. For targets brighter than I-mag = 11, the AO system can provide throughput gains to a factor of x2.9 when operating the WFS camera using a speed of 300Hz or 1kHz. For targets with 11>I-mag>14, operating the WFS in 100 Hz mode will lead to improvement factors between $2\times - 2.5\times$.

at 100 Hz, as shown in Figure 7.9.

Integration at the APF: Currently, the APF operates with a guider camera providing pointing information to the telescope at a rate of 1 Hz. This system will be retained and used for an acquisition camera for the system. Once the star is acquired on the WFS, the guiding corrections will be turned off and the AO loop will provide stabilization and pointing offsets for the telescope tracking software. Since the acquisition will be carried out in the same way, it is expected that there will be zero to minor changes to the observing efficiency after the AO system is implemented. A failsafe mode for

seeing-limited operations will be implimented, should conditions be too poor or variable for routine AO-corrected imaging on a particular night.

After validation testing, the existing static secondary mirror will be replaced with the ASM on the APF. The ASM will use the same focus and tip/tilt mechanism used for static positioning in the current APF. The initial tests at the APF will include measurement of the PSF in open loop, refinement of the secondary shape to optimize PSF, measurement of the closed loop performance, refinement of the automated performance, and integration operation into the queue scheduling.

7.3.5 Simulated performance of the improvements possible at the APF with an ASM-based adaptive optics upgrade

Expected Image Stability and Slit Efficiency Improvement:

AO correction is conventionally discussed in terms of diffraction-limited imaging, where correction on the spatial scale of the Fried length (r_0) is required to achieve a decent Strehl ratio. For the APF setup we have more modest goals: (1) improve the fraction of light making it through the slit, and (2) stabilize its variation. Qualitatively, this is similar to ground-layer AO (GLAO) correction, where correction of only the lowest order modes of the atmosphere that dominate the size of the image blur is needed to achieve improvements in the FWHM. We note that other visible light systems have achieved this image sharpening in the visible (see, for example, Chun et al. (2018) [61]). Thus

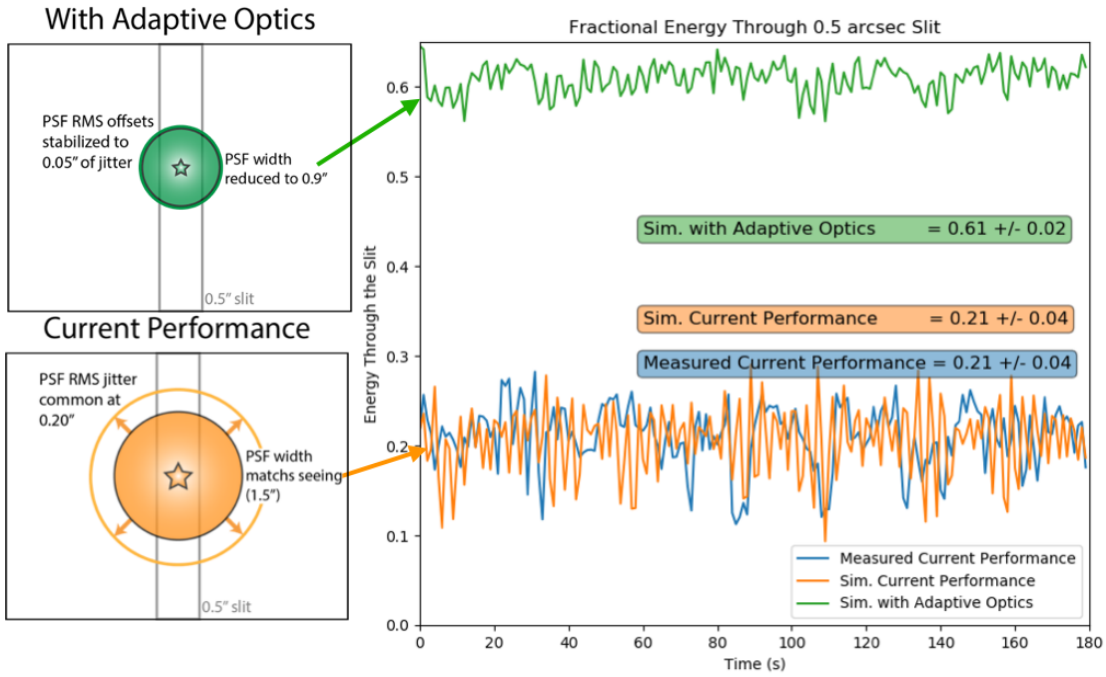

Figure 7.10 **Simulated Improvements to Image Stablity and Throughput**. The APF currently allows for $21 \pm 4\%$ of the light through a 0.5" slit *(blue)*. A simulation was completed using HCIpy [193] by the University of California Observatory in order to estimate the current variability *(orange)* and the variability after an adaptive optics correction (*green*). This modeling suggests that an ASM-based AO system could reduce the PSF width by 40%, leading to an expected improved throughput of $61 \pm 2\%$ (*green*). The RMS offset from the slit is improved by a factor of four resulting in better PSF stability.

the expected improvement is consistent with other AO systems, even if their technical approach (wide-field GLAO correction) is different.

To estimate the system performance, a simulation was made using the python package HCIpy [192] (see Figure 7.10). The atmosphere was modeled with similar image blur to guiding data taken from a typical observing sequence. Slow tracking variations were then added at several frequencies to match the variations we visually see in the guider. The resulting slit efficiency (21%) and variations of 4% are similar to what is seen by the APF guider. We find that the PSF width decreases from 1.5 ± 0.2 arcsec to 0.9 ± 0.05 arcsec in simulation in 1s snapshots. The image jitter is reduced by a factor of four (from 0.20" to 0.05"). With the 0.5-arcsec slit width, this improved light concentration through the slit would lead to a throughput increase of $61 \pm 2\%$ for an improvement factor of 2.9. For the 1-arcsec slit width, the improvement is similar. Without AO correction the efficiency is 40%. After correction, the efficiency improved by a factor of two to 79%.

Even if only the efficiency improvement can be realized, the value of AO for the APF will increase the cadence of nightly observations. The efficiency improvement suggests that we could be able to observe over double the number of stars per night compared to current observations. We expect to provide this improvement on stars as faint as I=14 as shown in Figure 7.9. This dramatic speed-up of observations is equivalent to having a second APF available.

RV Measurement Precision:

The connection between PSF image stability and RV stability is complex and difficult to quantify. We do not attempt to quantify the RV measurement gains, however, we note that there is evidence to suggest that improved image stabilization will indeed lead to higher precision RV measurements.

One example of their correlation is seen in HARPS data where LoCurto et al. (2010) [148] notes that a guider variation of 0.1 arcsec results in approximately 0.3 m/s errors. While this example cannot be used as a direct comparison because HARPS is a different style spectrograph to APF/Levy, it demonstrates that RV and image stability are correlated. We expect the improved stability seen in our simulations to benefit the achieved precision improvement in a similar way to the fiber scrambler retrofit to HIRES [225] without the reduction in throughput.

In total, we may expect to be able to get to the same signal-to-noise thresholds in less than half the time while also doubling the precision of the measurement due to the improvement in image stability. Quantifying the improvement to RV accuracy using the APF AO system on-sky will be informative for future AO-enhanced RV spectrometer designs.

Part III

Conclusions

Chapter 8

Conclusions

"I'm going to miss you. You had such potential. But then again, all good things must come to an end... See you out there."

8.1 Summary

While the majority of exoplanets are currently detected using indirect methods of observation, direct methods of observation offer a way to characterize an exoplanet's atmosphere, chemical composition, density, temperature, and orbit. In the introduction, I overviewed the promise, challenges, and motivation for conducting exoplanet direct imaging. The focus of this thesis was to expand our ability to directly image exoplanets through original research in observational techniques and adaptive optics instrumentation development.

In the first half, I introduced strategies and tools available for conducting targeted direct imaging observations. I demonstrated how a targeted approach to HCI observations could be used by conducting an HCI/RV survey of our fifth closest neighbor, Wolf 359. I quantified the limits of conducting high-contrast imaging with Keck-NIRC2 in the Ms filter (4.7μm) and determined that, even in the case of observing some of the nearest, youngest stars, our current ground-based instrumentation is generally limited to imaging exoplanets larger than $1M_{jup}$. In the final chapter of part 1, I introduced a future JWST survey that outlined a strategy for enabling the direct detection of sub-Jupiter mass exoplanets down to ice-giant size.

The second half of this thesis focused on the development of an adaptive optics technology that could improve the sensitivity of high-contrast imaging in the infrared. TNO recently developed a new style of high-efficiency hybrid-variable reluctance actuator that is the basis of an emerging large-format deformable mirror technology. I completed performance testing using two lab prototype of the TNO deformable mirrors. This testing did not identify any major issues with the TNO technology likely to affect its on-sky use. TNO has designs in progress for building ASMs for four mid-sized telescopes to begin proving this technology on-sky at the NASA IRTF telescope, the UH2.2m telescope, the APF telescope, the European Solar Telescope. This technology is also under consideration for use in an adaptive secondary mirror for Keck observatory which could improve the sensitivity of future infrared high-contrast imaging/spectroscopy instruments by lowering the thermal noise added by the adaptive optics system.

8.2 perspective & Predictions

8.2.1 JWST will unlock our ability to directly detect and take spectra of cold young sub-Jupiter exoplanets

The exoplanet direct imaging community is currently learning how to best unlock the enormous potential of JWST. The door has just opened to determining what sciences cases are possible and which instruments/modes are best suited for that science.

The early release science programs gave us our first glimpse into JWST's unprecedented ability to both directly detect and characterize exoplanets. Carter et al 2023 [50] shared the first direct detection of an exoplanet (HIP 65426b) beyond 5μm using NIRCam (2-5μm) and MIRI (11-16μm). Notably, a detection of the companion was made in all seven filters and the contrast achieved by these observations reached a background limit of 0.3 $Mjup$. Miles et al 2023 [164] presented the highest precision spectra measured to date of a planetary mass object (VHS 1256 b) using the NIRSpec IFU and MIRI MRS modes (1-20μm). Ray et al 2023 [199] and Sallum et al 2023 [212] evaluated the NIRISS aperture masking interferometric mode with the goal of probing separations within the diffraction limit of JWST (down to $0.5\lambda/D$).

Leveraging the success of the early release science observations, a variety of JWST programs have been accepted for Cycle 2 and 3 that focus on directly detecting cold sub-Jupiter mass exoplanets for the first time. The programs capable of sub-Jupiter mass detection fall into two main strategies:

1. **Search young moving groups**: The advantage of searching young (< 300Myr) moving groups is that the age of your targets are well constrained. The disadvantage of this approach is that the known moving groups do not overlap with our nearest neighbors (>∼ 30pc in distance) which limits the sensitivity to finding sub-Jupiter mass exoplanets to wider orbits (>20AU). The JWST programs adopting a moving group focus opt to use NIRCam coronagraphy at 4.44μm to gain access to as tight of an inner working angle as possible. While the occurrence rates of exoplanets have been shown to drop off beyond 10AU for large gas giants, the occurrence rate of smaller giant planets on these wide orbits has yet to be determined. Examples of this style of program include:
    - Cycle 2 GO 4050: *Uncharted Worlds: Towards a Legacy of Direct Imaging of Sub-Jupiter Mass Exoplanets* which calls for NIRCam coronagraphy of targets in the TW-Hya moving group.
    - Cycle 3 GO 5835: *Into The Spotlight: Unveiling Wide-Separation Sub-Jupiters for Future JWST Characterization* which calls for NIRCam coronagraphy of targets in the Beta Pic moving group.
    - Cycle 3 Survey 6005: *Imaging Young Sub-Jupiter Planets down to Solar-System Scales* which calls for NIRCam coronagraphy of FGK stars within 50pc spanning six moving groups.

2. **Search nearby (<10 pc), dim stars with relative youth (<1 Gyr)**: Exoplanets will naturally have a boost in separation and brightness from our vantage

point when they are in nearby systems. Thus, targeting nearby systems opens the detection space to colder exoplanets (< 200K) orbiting closer to the snow line of their system (< 10AU). Because the inner working angle is less critical, these programs can utilize MIRI imaging to gain sensitivity to colder planets. By focusing on observing systems with dim stars (usually M-dwarfs), the contrast with the star is not as critical of an issue and more of the image will be in the background limited regime. Examples of this style of program include:

- Cycle 2 GO 3840: *JWST NIRCam Confirmation of the First Directly Imaged Sub-Saturn Mass Exoplanet*; this program is follow up of a source discovered as part of the Cycle 1 GTO 1184 program to take NIRCam Coronagraphic Imaging Survey of Nearby Young M Dwarfs.
- Cycle 3 GO 6122: *Cool kids on the block: The direct detection of cold ice giants and gas giants orbiting young low-mass neighbors*; This upcoming program was described in Chapter 4 of this thesis that targets 6 M-dwarfs within 6pc with NIRCam coronagraphy and MIRI imaging.

Both strategies currently seem to be viable pathways towards detecting the first cold sub-Jupiter mass exoplanet and may prove complementary. Once giant planets more similar to the ones in our own solar system can be discovered and characterized with JWST, the study of these planets may reveal critical insights to helping us understand the formation mechanisms that were at play in our own solar system. We may soon be able to probe the divide between our own gas giant (Jupiter/Saturn) and ice giant

(Neptune/Uranus) exoplanets: *Is our story of the role giant planets play in formation correct? How binary are the populations of ice and gas giants? Are the atmospheres of giant exoplanets similar to those in our solar system?*

8.2.2 ELTs could face unexpected challenges completing their high-contrast imaging goals unless we improve our understanding of our current infrared high-contrast imaging limits.

In Chapter 3, I quantified the performance gap between the expected background limit when conducting high-contrast imaging with Keck-NIRC2 at 4.7μm. When originally planning the Wolf 359 HCI observation, we did not account for the properties of the vortex coronagraph in the thermal M-band. I quantified the throughput and background glow added due to the vortex, however, the gap could not be fully be explained from the contribution of additional thermal noise from the vortex alone.

Until we understand the full causes of our performance gaps and how to correct them, the HCI programs run at the ELTs should expect to face similar performance issues as experienced by the current 8-10m high-contrast imaging instruments. Less priority has been given to monitoring and improving background noise issues by the HCI community than achieving good contrast, yet both are critical pieces for directly detecting exoplanets. There are new opportunities that are arising for the community to start to track the issues affecting the background sensitivity in the infrared in ground based observatories.

Observers from UC San Deigo are currently exploring the spacial variation of the 4.7μm background of the image rotator in the Keck-II AO system.[1] The image rotator is the first optic in the Keck-II AO system optical path, closest to the telescope.

The NIRC2 electronics upgrade now offers the option of sub-second readout. A full cube of images is generated with each exposure, containing each coadd individually.[2] These cubes offer a chance to test if high-speed variability could be affecting our ability to properly calibrate the background counts. It also opens an opportunity to perform background correction on shorter timescales.

Absil et al 2022 [1] analyzed the possibility of decreased AO performance at the longer IR wavelengths due to the wavefront sensors inability to correct the wavelength dependant aberrations from water vapor. Water vapor is highly chromatic in the infrared, so AO correction at short wavelengths may not apply completely at the longer wavelengths. The authors suggest a plan for METIS to use a focal plane wavefront sensing technique to help mitigate this issue.

SCALES [129, 221] is an integral field spectrograph that will work from 2-5μm that will be commissioned at Keck in 2025. Its commissioning could provide a new understanding of the chromaticity of the systemic errors in the near-infrared at Keck.

The large-format deformable mirror development discussed in Chapters 5-7 could someday offer a solution to diminishing the thermal background noise added by the telescope

[1] Information provided in direct correspondence.
[2] These cubes can be retrieved on the Keck archive with the "unp" extension.

optics at future 30m+ observatories. However, the support of at least one 8-10m facility will be needed in order for the HVR-based DM technology to gain the needed readiness level to someday be adopted more widely.

Overall, if we wish to retire this risks to the ELT exoplanet direct imaging programs, we must continue to trace our infrared performance discrepancies in our current observing.

8.2.3 The expansion of exoplanet direct imaging may enable the important study of exomoons

In the beginning of this thesis, I introduced the three fundamental measurements of observational astronomy (photometry, astrometry, and spectroscopy). When we apply these techniques to a star to learn about an orbiting companion, we are performing an indirect measurement technique (i.e. transit, radial velocity, absolute astrometry, and mircolensing). Once directly detecting an exoplanet becomes a more routine observation with JWST or ELTs, it is not a far stretch of the imagination to think about applying the indirect measurement techniques to *exoplanets* themselves to enable the discovery of companions around the exoplanet and find "exomoons."

Several efforts have already been made to adapt the transit and radial velocity methods for such a purpose. Limbach et al 2021 [143] describes a method for using Spitzer and JWST to detect a transit across isolated planetary-mass objects. Ruffio et al 2023 [210] explored using the Keck Planet Imager and Characterizer to take a timeseries of spectra

of a brown-dwarf companion to hunt for the sign of an exomoon orbiting.

Just like in the early days of exoplanet science where we did not imagine the full diversity of planets, beginning to discover exomoons could reveal an unexpected set of worlds. There may be moons capable of sustaining life, and life on a planet may be vitally influenced by the existence of its moon. Using indirect techniques to find exomoons may also prove critical for interpreting our direct imaging/spectroscopy data of our exoplanets, since photons blended from a moon and planet together may confuse our understanding of both worlds. We may not only be able to soon detect exomoons, we may find it essential to interpreting our final understanding of exoplanets in context.

8.2.4 Direct imaging/spectroscopy will shift to play a central role in exoplanet science within the lifetime of my career

I predict that direct imaging will shift to play a more central role in the discovery of exoplanets within the lifetime of my career. However, it will not look exactly like the direct imaging that I've discussed here.

In this thesis, when I have referred to exoplanet direct imaging I have mostly been discussing *infrared* direct imaging where the self-luminous heat from the exoplanet is detected. There is another branch of direct imaging called *reflected light* direct imaging, where the starlight reflected off of the planet is imaged. This is analogous to how we see the moon in the sky. Reflected light direct imaging is performed at visible

wavelengths, and unlike infrared direct imaging, the brightness of the planet in a reflected light observation is dependant on how close the planet is to its star and the planet's albedo (and it is not dependant on the planet's age).

The Astro2020 report recommended that the next Great Observatory be a 6m infrared/optical/ultraviolet space based observatory optimized to perform reflected light direct imaging/spectroscopy of exoplanets around Sun-like stars. The "Habitable Worlds Observatory" (HWO) will carry out reflected light imaging of at least 25 potentially habitable worlds. While the mission is set to launch in the late 2030s/early 2040s, NASA has called for advancing the technologies required to carryout reflected light observations now in order to reduce the overall mission cost. The exoplanet direct community may begin to see the benefits of this technology push within the next five years.

"Five card stud, nothing wild. And the sky's the limit."

Appendix A

An ode to searching for companions, a 10 minute science play

Synopsis: An observer who is new to the field of exoplanet direct imaging must learn what makes a good observation in order to find a companion.

Setting: Proposal Season, a bar-like establishment full of astronomers and astronomical objects

Character list:

The Astronomers:

OBSERVER – an energetic newcomer with a scientific dream

ADVISOR – a caring mentor

POSTDOC 1 - a rival

POSTDOC 2 - a second rival

The Potential Companions:

HR8799 – a popular, confident system

V833TAU, HIP 6512, and 40 LEO – modern, trendy systems

HD 206893 - a kind system who is not sure how to manage the attention

WOLF 359 - a mysterious neighboring system

Notes on casting:

Many of the characters can be played by the same actor, with the exception of OBSERVER. The minimum cast size is four but five would allow for the easiest doubling (OBSERVER, ADVISOR, and three swings). No characters are required to be doubled if you wish to include as many people as possible.

All characters can be played by actors of any age, race, and/or gender.

If the cast includes work colleagues, such as a cohort of professional astronomers, care should be given to make sure that there are no power differences between the characters that have any implied intimate relationships. Because there is a large metaphor included comparing "searching for companions" to dating, it is not appropriate to mix people of differing seniority levels in particular parts.

An OBSERVER walks into a bar. Their ADVISOR is the bartender.

OBSERVER

Oh my stars! What is this place?

ADVISOR

This dark little miserable hole of an establishment? Welcome to Proposal Season!

> *A light up sign illuminates indicating that they are indeed in a bar called "Proposal Season"*

OBSERVER

Proposal Season? Cool! That sounds like so much fun!

ADVISOR

Sure... I take it you're new to these parts?

OBSERVER

I am. In undergrad I lived in the Theory neighborhood, but there's something that was just calling to me about this part of town when I came to grad school. It feels like there's so much history here!

ADVISOR

Many great minds has gotten their start here. I'd say all observers seem to find themselves in Proposal Season one to four times per year. For some observers, coming here is their favorite time of the year, but for most, honestly, it's hell.

OBSERVER

I can sense it now. It's the aura of longing and despair and a slight zest of... hope!

ADVISOR

Now you're getting it.

OBSERVER

Smells sort of like Pop-Tarts.

ADVISOR

So what can I get you?

OBSERVER

Four Keck half-nights, please.

ADVISOR

No.

OBSERVER

What?

ADVISOR

I'm sorry, you can't just walk in and get something that big here! You need to justify it.

OBSERVER

What do you mean?

ADVISOR

To get something like four Keck half-nights, you need a good reason. You need to prepare a proposal PDF containing a scientific justification, figures, technical comments, a catchy title, and the results from previous Keck runs. Then you have to proceed to the Keck Observer Login Page in a supported browser, enter the e-mail address of the PI or a Co-I as listed on the Keck Cover Sheet, then the Keck Cover Sheet ID, and click the "Proposer Login" button to upload –

(getting cut off)

OBSERVER

Whoa, whoa whoa! That all sounds sort of overwhelming.

ADVISOR serves OBSERVER a cup of coffee.

ADVISOR

Here, you're going to need this. So, have you got a good reason to propose for so much Keck time?

OBSERVER

Well, I think it's a good reason! I mean, I hope it's a good reason? It actually feels sort of embarrassing.

ADVISOR

Oh, come on, whatever it is can't be that bad. This one time I did a 100 night campaign to measure the level of background dust. Exozodical dust. It doesn't sound very flashy, but it was very important NASA business. So tell me, what's the question you want to stay up night after night trying to answer?

OBSERVER

Well, I know I'm not a real astronomer... but I want to find a companion.

ADVISOR

That's nothing to be ashamed of. All of us exoplanet observers want to find a companion someday! Most of us want to find as many companions as we can.

OBSERVER

It's not actually just that I want to *find* a companion, I want to make a real connection with a companion, you know? I want to really understand its nature! Its character. Its bulk density. I want to find a companion where I can study the chemicals in its atmosphere and learn what makes it tick. I want to know everything about its *life*! Do you think I'm weird?

ADVISOR

Not at all, but you should know that this is not going to be an easy observation. That sort of question asking will require *direct* observations. If you want low hanging fruit, this isn't it.

OBSERVER

Other students might be satisfied by being part of a radial velocity survey or doing something safe like analyzing exoplanet transit data, but that's just not who I am. My family might end up hating me for it, but I think I've always known since that first week of intro to astronomy... deep down in my heart of Pluto's heart... I'm an exoplanet direct imager.

ADVISOR

When you know, you know.

OBSERVER

Will you help me find the perfect companion to publish with?

ADVISOR

Okay. I'll mentor you.

OBSERVER

Yes! How do I *star*-t?

ADVISOR

Take a look over there. You see that time-honored star system?

> *ADVISOR points towards HR8799. They're sitting with POSTDOC 1 in one arm & POSTDOC 2 in the other.*

That's HR8799. They're quite popular with the direct imagers.

OBSERVER

Wow, they're hot!

ADVISOR

Indeed! The planets in the HR 8799 system are massive and still cooling from the heat of their formation, so the companions are quite hot in temperature. They were one

of the first planetary systems to be directly imaged because the planets are spaced far enough from their star to be accessible by instrumentation at eight to ten meter class telescopes. Despite their popularity, they're still published with all the time because they are so multifaceted.

OBSERVER

HR 8799 is absolutely glowing!

ADVISOR

They really do know how to get along with all sorts of science programs. Go see if they feel like a good match!

OBSERVER walks up to HR8799 and the POSTDOCs scatter. Tango music starts.

HR 8799

(*Flirtatiously)*

Why hello there, I'm HR 8799.

OBSERVER

You're looking absolutely radiant tonight.

HR 8799

Are you up for some exploration?

OBSERVER

Yes!

HR 8799 pulls observer into a tango, leading. OBSERVER can hardly keep up with HR 8799's elegance and grace as they talk and dance.

OBSERVER

Do you think we could slow down a little? I'm sort of new to this and I'm — ahh!

HR 8799 sweeps OBSERVER off their feet.

HR 8799

I've been studied for decades. Can you see the motion of my four big... bright... beautiful planets?

(whispering in OBSERVERS ear)

And who knows, maybe there's even another one at tighter separation angles... would you like to see?

(Pulling OBSERVER in with confidence.)

Want to make a discovery together?

OBSERVER

I'm sorry, you seem like a perfect system. It's just that I don't really think this observing mode is going to work for me.

OBSERVER steps back, and OBSERVER and HR8799 stop their dance.

HR 8799

Your loss!

POSTDOC 1 and POSTDOC 2 swoop in and dance away with HR 8799. OBSERVER returns to their coffee to talk with ADVISOR.

OBSERVER

Wow... that wasn't what I was expecting at all.

ADVISOR

Often the best things in science are unexpected.

OBSERVER

It's just that I felt like such a mess out there! There's no way I can be an astronomer with that sort of performance.

ADVISOR

Don't let HR 8799 get to you, okay? We all have some fond memories with them, but alas, they're not a system for everyone.

(beat)

Wait, I know another system you could try! Why don't you try checking out some of the accelerators?

OBSERVER

What are the accelerators?

ADVISOR

There are these two space missions, you see. One mission was called Hipparcos and the other is called Gaia. They've been measuring the precise position of the stars for decades, and their precision is so exact that you can use the astrometry data to tell which stars are moving and accelerating! And you know what an acceleration means?

OBSERVER

They're going in little circles? Which means... that they might be hosting an unseen companion!

ADVISOR

Exactly!

OBSERVER

Wow, super *trendy*! I'll go check them out!

Modern electronic dance music is playing. Lights come up on 3 systems: V833TAU, HIP 6512, and 40 LEO. OBSERVER approaches V833 TAU who is dancing.

Hey there, V833 Tau! Are you hosting an L-type brown dwarf? Because you are a beacon of warmth and comfort in this cold expanse of the universe.

V833 TAU

Nope, sorry.

V833 TAU dances away. OBSERVER then approaches to dance with HIP 6512.

OBSERVER

HIP 6512! In the constellation of my heart, you and I could be the binary stars, forever intertwined in a cosmic story.

HIP 6512

How rude! I'm in a triple system.

HD 8375 dances away. OBSERVER then approaches to dance with 40 LEO.

OBSERVER

40 Leo! Are you a Habitable Worlds Observatory target or a cosmic anomaly who is capturing my attention?

Go sink into a black hole.

OBSERVER

Harsh, but fair.

OBSERVER returns to sit with ADVISOR. The music fades.

OBSERVER

I wasn't getting the sense that I understood any of those systems.

ADVISOR

Just because a system looks like an accelerator doesn't mean you'll find the type of companion you're looking for. You see, there's a degeneracy in mass-separation space for what type of companions is in the system. The star could be accelerating for three reasons. It could be the type of companion your looking for, but it could also be a short period planet that's so guarded that you'll never be able to learn about it. Or even worse, the system is with some faraway star that barely has anything to do with the system you care about at all.

(beat)

Also, your pickup lines were terrible.

OBSERVER

Sorry. It's just that... I'm scared that I'm not good enough.

ADVISOR

Let me teach you a new technique then! It's a post-processing method called principle component analysis! You can use PCA to cut through the starlight to help you focus in on the things that really matter about a companion. The trick is to look for commonalities and identify the underlying patterns in a system. Once you reveal the hidden correlations, you can uncover the deeper connections. Try slowing down and looking for the shared values, but also appreciate the differences.

OBSERVER

I really hope I'm qualified for all of this.

ADVISOR

Go talk to HD 206893. I sense there's something about that system that they might be ready to share with the universe. I don't know their secrets, but maybe you can be the one to help them.

OBSERVER approaches HD 206893, who is alone. Swing music starts to play.

OBSERVER

Okay I got this... PCA ... look for the commonalities... but appreciate where you see the difference...

HD 206893

(shyly)

Hi.

OBSERVER

Hi! Can I join you?

HD 206893

Oh! Me, really? Well, okay.

They start to swing dance together while talking and smile shyly at each other.

OBSERVER

I'm new here to the Proposal Season. Have you been around here much before?

HD 206893

I've started to come around here a more often lately, but I'm still feeling a little dusty.

OBSERVER

"Dusty" you say? Want to tell me a little about yourself?

HD 206893

Well my star is a yellow-white main sequence star of spectral type F-five-V. I'm between fifty and seven-hundred million years old.

OBSERVER

Do you have a disk?

HD 206893

Oh yes of course, with a gap! And when I'm bored, I like to go for long drifts across the milky way with my companions.

OBSERVER

Hey, I like drifting across the milky way too! Do you want to *drift together* sometime?

HD 206893

I like the way you're looking at me, which makes me feel like I need to tell you something.

OBSERVER

Oh? I'd really like to get to know you better.

HD 206893

You're so kind. It's just that well... you see... I just published with another observer, and I'm not really ready for another survey right now. I'm with GRAVITY.

OBSERVER

What?

HD 206893

The paper just came out. I thought you knew, it was such big news!

OBSERVER

Oh...

HD 206893

I'm so sorry. Maybe in another epoch?

POSTDOC 1 comes by and taps OBSERVER to cut in on the dance. POSTDOC 1 and HD 206893 leave.

OBSERVER

Was I just scooped?

ADVISOR

Got to watch out for those cut-throat postdocs! They might not be able to hold grants

yet, but they sure know how to get telescope time.

OBSERVER

I was making a real connection there! I thought that the HD 206893 might have really been the one. I'm probably just lucky to have gotten this far. It's only a matter of time before people realize I'm a fraud.

OBSERVER slams back the end of their coffee and dejectedly lays their head on the bar.

ADVISOR

Hey look, I know that the Proposal Season can make you feel like you don't belong or that you're not good enough. It makes everyone feel that way at some point, and it can be overwhelming, especially for newcomers. But I'm here to tell you that you are not alone.

OBSERVER

I feel like nothing I do will ever be enough.

ADVISOR

Those feelings are just that: feelings, not facts. I don't know you that well yet, but I do know that you've achieved so much to get to where you are today. You are unique, with your own set of skills, experiences, and perspectives. You bring something valuable and

irreplaceable to the table, something that no one else can replicate.

(beat)

I think I may have been holding you back by telling you what systems you might connect with. Those systems have worked for others, but I think I've learned enough to evaluate your own contrast and limits. Look around, what is it that *you* want to explore?

> *OBSERVER stands up. The scene shifts to outside the Proposal Season. WOLF 359 is standing looking at the stars. WOLF 359 has the aesthetic that they could be smoking a cigarette but they're so cool they don't even need to. OBSERVER walks up to WOLF 359. An acoustic guitar track of a Vampire Weekend song (or another punk song) starts to play.*

OBSERVER

Mind if I join you for some fresh air? Oh hey, it's you!

WOLF 359

(gruffly)

Sorry, do I know you?

OBSERVER

Don't you live next door to me? I just moved into the neighborhood. I think you're five stars down the block from me! Who are you?

WOLF 359

Everyone seems to call me something different. Simbad lists 57 identifiers for me.

OBSERVER

Well, what do your friends call you?

WOLF 359

Wolf 359. But don't think that makes you my friend. Who are you?

OBSERVER

An astronomer.

OBSERVER moves closer to give WOLF 359 a look over. Astronomers usually don't look at them that closely.

WOLF 359

Why are you looking at me like that?

OBSERVER

I can tell by your appearance that you are a pretty active M-star system, but I have no idea how old you are.

WOLF 359

It's best not to make any assumptions with me.

OBSERVER

I never do when it comes to an *attractive* star system like you.

(OBSERVER catches themselves and tries to backtrack)

Ah! I mean... not *attractive* in the *gravitational* sense because you're a *low mass* star system and low mass stars aren't attractive like that and I know that... but I mean...you are very attractive!

WOLF 359

(winking)

It's my strong magnetic field, stargazer. It's hundreds of times stronger than the Sun.

WOLF 359 and OBSERVER move closer, but then WOLF 359 pulls back.

Look. I can tell I find your scientific question asking compelling, but there are some things you should probably know about me before I get your hopes up.

OBSERVER

There's so much I'd like to know ... strictly as your neighbor, of course!

WOLF 359

You see my star is a rapid rotator. It flares a lot, and when it does, it's ugly. I don't have any openly public companions, and I don't even know if I'm capable of having

companions at all. I know what you exoplanet hunters are looking for, and you're probably not going to find it here. It's really best if you move your survey along.

OBSERVER

How do you know what I'm looking for in my survey? It's best not to make any assumptions with *me*.

WOLF 359

Fine, I'll bite. What is it you're looking for then?

OBSERVER

Propose for four Keck half-nights with me and find out.

WOLF 359

Pfft, just because you're clever and charming doesn't mean I'm about to change who I am for you.

OBSERVER

Give me a chance to measure the *real* you, not the system you're pretending to be. Let me be the astronomer who faces faulty wavefront sensors, global pandemics, and ice storms for you!

WOLF 359

That's really flattering, but I'm not the type of system that folks want to analyze.

OBSERVER

Eventually I want to find a system who will be there for me through the end of my thesis, but there's so many different ways that chapter can look. No expectations here. I just want to have a chance to see how this observation evolves, because if we are alone in the universe, it sure seems like an awful waste of space.

OBSERVER gets down on one knee.

So, will you propose with me?

WOLF 359

By the moons of Neptune, let's do it! Who knows, there might be something between us...

OBSERVER

Literally... like a transiting planet!

WOLF 359

So how do we *star*-t?

OBSERVER and WOLF 359 start to exit, arm over shoulder plotting.

OBSERVER

Well first I need to prepare the proposal PDF containing a scientific justification, figures, technical comments, a catchy title, and the results from previous Keck runs. Then I have to proceed to the Keck Observer Login Page and — *(continuing the line from earlier as is needed to exit)*

The music takes over cutting off OBSERVER's final line. WOLF 359 and OBSERVER exit together.

End of Play.

Bibliography

[1] Olivier Absil, Christian Delacroix, Gilles Orban de Xivry, Prashant Pathak, Matthew Willson, Philippe Berio, Roy van Boekel, Alexis Matter, Denis Defrère, Leo Burtscher, Julien Woillez, and Bernhard Brandl. Impact of water vapor seeing on mid-infrared high-contrast imaging at ELT scale. In Laura Schreiber, Dirk Schmidt, and Elise Vernet, editors, *Adaptive Optics Systems VIII*, volume 12185 of *Society of Photo-Optical Instrumentation Engineers (SPIE) Conference Series*, page 1218511, August 2022.

[2] Joseph M. Akana Murphy, Molly R. Kosiarek, Natalie M. Batalha, Erica J. Gonzales, Howard Isaacson, Erik A. Petigura, Lauren M. Weiss, Samuel K. Grunblatt, David R. Ciardi, Benjamin Fulton, Lea A. Hirsch, Aida Behmard, and Lee J. Rosenthal. Another Superdense Sub-Neptune in K2-182 b and Refined Mass Measurements for K2-199 b and c. , 162(6):294, December 2021.

[3] F. Allard. The PHOENIX Model Atmosphere Grid for Stars. In C. Reylé, J. Richard, L. Cambrésy, M. Deleuil, E. Pécontal, L. Tresse, and I. Vauglin, editors,

SF2A-2016: Proceedings of the Annual meeting of the French Society of Astronomy and Astrophysics, pages 223–227, December 2016.

[4] Adam Amara and Sascha P. Quanz. PYNPOINT: an image processing package for finding exoplanets. , 427(2):948–955, December 2012.

[5] Guillem Anglada-Escudé and R. Paul Butler. The HARPS-TERRA Project. I. Description of the Algorithms, Performance, and New Measurements on a Few Remarkable Stars Observed by HARPS. , 200(2):15, June 2012.

[6] Ruth Angus, Timothy D. Morton, Daniel Foreman-Mackey, Jennifer van Saders, Jason Curtis, Stephen R. Kane, Megan Bedell, Rocio Kiman, David W. Hogg, and John Brewer. Toward Precise Stellar Ages: Combining Isochrone Fitting with Empirical Gyrochronology. , 158(5):173, November 2019.

[7] Astropy Collaboration, A. M. Price-Whelan, B. M. Sipőcz, H. M. Günther, P. L. Lim, S. M. Crawford, S. Conseil, D. L. Shupe, M. W. Craig, N. Dencheva, A. Ginsburg, J. T. VanderPlas, L. D. Bradley, D. Pérez-Suárez, M. de Val-Borro, T. L. Aldcroft, K. L. Cruz, T. P. Robitaille, E. J. Tollerud, C. Ardelean, T. Babej, Y. P. Bach, M. Bachetti, A. V. Bakanov, S. P. Bamford, G. Barentsen, P. Barmby, A. Baumbach, K. L. Berry, F. Biscani, M. Boquien, K. A. Bostroem, L. G. Bouma, G. B. Brammer, E. M. Bray, H. Breytenbach, H. Buddelmeijer, D. J. Burke, G. Calderone, J. L. Cano Rodríguez, M. Cara, J. V. M. Cardoso, S. Cheedella, Y. Copin, L. Corrales, D. Crichton, D. D'Avella, C. Deil, É. Depagne, J. P. Di-

etrich, A. Donath, M. Droettboom, N. Earl, T. Erben, S. Fabbro, L. A. Ferreira, T. Finethy, R. T. Fox, L. H. Garrison, S. L. J. Gibbons, D. A. Goldstein, R. Gommers, J. P. Greco, P. Greenfield, A. M. Groener, F. Grollier, A. Hagen, P. Hirst, D. Homeier, A. J. Horton, G. Hosseinzadeh, L. Hu, J. S. Hunkeler, Ž. Ivezić, A. Jain, T. Jenness, G. Kanarek, S. Kendrew, N. S. Kern, W. E. Kerzendorf, A. Khvalko, J. King, D. Kirkby, A. M. Kulkarni, A. Kumar, A. Lee, D. Lenz, S. P. Littlefair, Z. Ma, D. M. Macleod, M. Mastropietro, C. McCully, S. Montagnac, B. M. Morris, M. Mueller, S. J. Mumford, D. Muna, N. A. Murphy, S. Nelson, G. H. Nguyen, J. P. Ninan, M. Nöthe, S. Ogaz, S. Oh, J. K. Parejko, N. Parley, S. Pascual, R. Patil, A. A. Patil, A. L. Plunkett, J. X. Prochaska, T. Rastogi, V. Reddy Janga, J. Sabater, P. Sakurikar, M. Seifert, L. E. Sherbert, H. Sherwood-Taylor, A. Y. Shih, J. Sick, M. T. Silbiger, S. Singanamalla, L. P. Singer, P. H. Sladen, K. A. Sooley, S. Sornarajah, O. Streicher, P. Teuben, S. W. Thomas, G. R. Tremblay, J. E. H. Turner, V. Terrón, M. H. van Kerkwijk, A. de la Vega, L. L. Watkins, B. A. Weaver, J. B. Whitmore, J. Woillez, V. Zabalza, and Astropy Contributors. The Astropy Project: Building an Open-science Project and Status of the v2.0 Core Package. , 156(3):123, September 2018.

[8] Astropy Collaboration, Adrian M. Price-Whelan, Pey Lian Lim, Nicholas Earl, Nathaniel Starkman, Larry Bradley, David L. Shupe, Aarya A. Patil, Lia Corrales, C. E. Brasseur, Maximilian Nöthe, Axel Donath, Erik Tollerud, Brett M. Morris, Adam Ginsburg, Eero Vaher, Benjamin A. Weaver, James Tocknell,

William Jamieson, Marten H. van Kerkwijk, Thomas P. Robitaille, Bruce Merry, Matteo Bachetti, H. Moritz Günther, Thomas L. Aldcroft, Jaime A. Alvarado-Montes, Anne M. Archibald, Attila Bódi, Shreyas Bapat, Geert Barentsen, Juanjo Bazán, Manish Biswas, Médéric Boquien, D. J. Burke, Daria Cara, Mihai Cara, Kyle E. Conroy, Simon Conseil, Matthew W. Craig, Robert M. Cross, Kelle L. Cruz, Francesco D'Eugenio, Nadia Dencheva, Hadrien A. R. Devillepoix, Jörg P. Dietrich, Arthur Davis Eigenbrot, Thomas Erben, Leonardo Ferreira, Daniel Foreman-Mackey, Ryan Fox, Nabil Freij, Suyog Garg, Robel Geda, Lauren Glattly, Yash Gondhalekar, Karl D. Gordon, David Grant, Perry Greenfield, Austen M. Groener, Steve Guest, Sebastian Gurovich, Rasmus Handberg, Akeem Hart, Zac Hatfield-Dodds, Derek Homeier, Griffin Hosseinzadeh, Tim Jenness, Craig K. Jones, Prajwel Joseph, J. Bryce Kalmbach, Emir Karamehmetoglu, Mikołaj Kałuszyński, Michael S. P. Kelley, Nicholas Kern, Wolfgang E. Kerzendorf, Eric W. Koch, Shankar Kulumani, Antony Lee, Chun Ly, Zhiyuan Ma, Conor MacBride, Jakob M. Maljaars, Demitri Muna, N. A. Murphy, Henrik Norman, Richard O'Steen, Kyle A. Oman, Camilla Pacifici, Sergio Pascual, J. Pascual-Granado, Rohit R. Patil, Gabriel I. Perren, Timothy E. Pickering, Tanuj Rastogi, Benjamin R. Roulston, Daniel F. Ryan, Eli S. Rykoff, Jose Sabater, Parikshit Sakurikar, Jesús Salgado, Aniket Sanghi, Nicholas Saunders, Volodymyr Savchenko, Ludwig Schwardt, Michael Seifert-Eckert, Albert Y. Shih, Anany Shrey Jain, Gyanendra Shukla, Jonathan Sick, Chris Simpson, Sudheesh Singanamalla, Leo P. Singer, Jaladh Singhal, Manodeep Sinha, Brigitta M. Sipőcz, Lee R. Spitler,

David Stansby, Ole Streicher, Jani Šumak, John D. Swinbank, Dan S. Taranu, Nikita Tewary, Grant R. Tremblay, Miguel de Val-Borro, Samuel J. Van Kooten, Zlatan Vasović, Shresth Verma, José Vinícius de Miranda Cardoso, Peter K. G. Williams, Tom J. Wilson, Benjamin Winkel, W. M. Wood-Vasey, Rui Xue, Peter Yoachim, Chen Zhang, Andrea Zonca, and Astropy Project Contributors. The Astropy Project: Sustaining and Growing a Community-oriented Open-source Project and the Latest Major Release (v5.0) of the Core Package. , 935(2):167, August 2022.

[9] Astropy Collaboration, Thomas P. Robitaille, Erik J. Tollerud, Perry Greenfield, Michael Droettboom, Erik Bray, Tom Aldcroft, Matt Davis, Adam Ginsburg, Adrian M. Price-Whelan, Wolfgang E. Kerzendorf, Alexander Conley, Neil Crighton, Kyle Barbary, Demitri Muna, Henry Ferguson, Frédéric Grollier, Madhura M. Parikh, Prasanth H. Nair, Hans M. Unther, Christoph Deil, Julien Woillez, Simon Conseil, Roban Kramer, James E. H. Turner, Leo Singer, Ryan Fox, Benjamin A. Weaver, Victor Zabalza, Zachary I. Edwards, K. Azalee Bostroem, D. J. Burke, Andrew R. Casey, Steven M. Crawford, Nadia Dencheva, Justin Ely, Tim Jenness, Kathleen Labrie, Pey Lian Lim, Francesco Pierfederici, Andrew Pontzen, Andy Ptak, Brian Refsdal, Mathieu Servillat, and Ole Streicher. Astropy: A community Python package for astronomy. , 558:A33, October 2013.

[10] I. Baraffe, G. Chabrier, T. S. Barman, F. Allard, and P. H. Hauschildt. Evolutionary models for cool brown dwarfs and extrasolar giant planets. The case of HD

209458. , 402:701–712, May 2003.

[11] I. Baraffe, G. Chabrier, T. S. Barman, F. Allard, and P. H. Hauschildt. Evolutionary models for cool brown dwarfs and extrasolar giant planets. The case of HD 209458. , 402:701–712, May 2003.

[12] I. Baraffe, D. Homeier, F. Allard, and G. Chabrier. New evolutionary models for pre-main sequence and main sequence low-mass stars down to the hydrogen-burning limit. , 577:A42, May 2015.

[13] Madyson G. Barber and Andrew W. Mann. Using the Gaia Excess Uncertainty as a Proxy for Stellar Variability and Age. , 953(2):127, August 2023.

[14] Mauro Barbieri. ESO/HARPS Radial Velocities Catalog. *arXiv e-prints*, page arXiv:2312.06586, December 2023.

[15] Sydney A. Barnes and Yong-Cheol Kim. Angular Momentum Loss from Cool Stars: An Empirical Expression and Connection to Stellar Activity. , 721(1):675–685, September 2010.

[16] D. Barrado y Navascues. The Castor moving group. The age of Fomalhaut and VEGA. , 339:831–839, November 1998.

[17] Natasha E. Batalha, Mark S. Marley, Nikole K. Lewis, and Jonathan J. Fortney. Exoplanet Reflected-light Spectroscopy with PICASO. , 878(1):70, June 2019.

[18] Travis Allen Berger. *Precise Demographics of Kepler Exoplanets in the Gaia Era*. PhD thesis, University of Hawai'i at Manoa, January 2021.

[19] Michael S. Bessell. Standard Photometric Systems. , 43(1):293–336, September 2005.

[20] R. Biasi, M. Andrighettoni, G. Angerer, C. Mair, D. Pescoller, P. Lazzarini, E. Anaclerio, M. Mantegazza, D. Gallieni, E. Vernet, R. Arsenault, P. Y. Madec, P. Duhoux, A. Riccardi, M. Xompero, R. Briguglio, M. Manetti, and M. Morandini. VLT deformable secondary mirror: integration and electromechanical tests results. In Brent L. Ellerbroek, Enrico Marchetti, and Jean-Pierre Véran, editors, *Adaptive Optics Systems III*, volume 8447 of *Society of Photo-Optical Instrumentation Engineers (SPIE) Conference Series*, page 84472G, July 2012.

[21] Roberto Biasi, Daniele Gallieni, Piero Salinari, Armando Riccardi, and Paolo Mantegazza. Contactless thin adaptive mirror technology: past, present, and future. In Brent L. Ellerbroek, Michael Hart, Norbert Hubin, and Peter L. Wizinowich, editors, *Adaptive Optics Systems II*, volume 7736 of *Society of Photo-Optical Instrumentation Engineers (SPIE) Conference Series*, page 77362B, July 2010.

[22] Beth A. Biller, Laird M. Close, Elena Masciadri, Eric Nielsen, Rainer Lenzen, Wolfgang Brandner, Donald McCarthy, Markus Hartung, Stephan Kellner, Eric Mamajek, Thomas Henning, Douglas Miller, Matthew Kenworthy, and Craig Kulesa. An Imaging Survey for Extrasolar Planets around 45 Close, Young Stars with

the Simultaneous Differential Imager at the Very Large Telescope and MMT. , 173(1):143–165, November 2007.

[23] Beth A. Biller, Michael C. Liu, Zahed Wahhaj, Eric L. Nielsen, Thomas L. Hayward, Jared R. Males, Andrew Skemer, Laird M. Close, Mark Chun, Christ Ftaclas, Fraser Clarke, Niranjan Thatte, Evgenya L. Shkolnik, I. Neill Reid, Markus Hartung, Alan Boss, Douglas Lin, Silvia H. P. Alencar, Elisabete de Gouveia Dal Pino, Jane Gregorio-Hetem, and Douglas Toomey. The Gemini/NICI Planet-Finding Campaign: The Frequency of Planets around Young Moving Group Stars. , 777(2):160, November 2013.

[24] Sarah Blunt, Jason J. Wang, Isabel Angelo, Henry Ngo, Devin Cody, Robert J. De Rosa, James R. Graham, Lea Hirsch, Vighnesh Nagpal, Eric L. Nielsen, Logan Pearce, Malena Rice, and Roberto Tejada. orbitize!: A Comprehensive Orbit-fitting Software Package for the High-contrast Imaging Community. , 159(3):89, March 2020.

[25] M. Bonavita, G. Chauvin, S. Desidera, R. Gratton, M. Janson, J. L. Beuzit, M. Kasper, and C. Mordasini. MESS (multi-purpose exoplanet simulation system). A Monte Carlo tool for the statistical analysis and prediction of exoplanet search results. , 537:A67, January 2012.

[26] M. Bonavita, C. Fontanive, R. Gratton, K. Mužić, S. Desidera, D. Mesa, B. Biller, A. Scholz, A. Sozzetti, and V. Squicciarini. Results from The COPAINS Pilot

Survey: four new BDs and a high companion detection rate for accelerating stars. , 513(4):5588–5605, July 2022.

[27] Mariangela Bonavita. Exo-DMC: Exoplanet Detection Map Calculator. Astrophysics Source Code Library, record ascl:2010.008, October 2020.

[28] Charlotte Z. Bond, Sylvain Cetre, Scott Lilley, Peter Wizinowich, Dimitri Mawet, Mark Chun, Edward Wetherell, Shane Jacobson, Charles Lockhart, Eric Warmbier, Sam Ragland, Carlos Alvarez, Olivier Guyon, Sean Goebel, Jacques-Robert Delorme, Nemanja Jovanovic, Donald N. Hall, James K. Wallace, Mojtaba Taheri, Cedric Plantet, and Vincent Chambouleyron. Adaptive optics with an infrared pyramid wavefront sensor at Keck. *Journal of Astronomical Telescopes, Instruments, and Systems*, 6:039003, July 2020.

[29] M. Bonnefoy, A. Zurlo, J. L. Baudino, P. Lucas, D. Mesa, A. L. Maire, A. Vigan, R. Galicher, D. Homeier, F. Marocco, R. Gratton, G. Chauvin, F. Allard, S. Desidera, M. Kasper, C. Moutou, A. M. Lagrange, J. Antichi, A. Baruffolo, J. Baudrand, J. L. Beuzit, A. Boccaletti, F. Cantalloube, M. Carbillet, J. Charton, R. U. Claudi, A. Costille, K. Dohlen, C. Dominik, D. Fantinel, P. Feautrier, M. Feldt, T. Fusco, P. Gigan, J. H. Girard, L. Gluck, C. Gry, T. Henning, M. Janson, M. Langlois, F. Madec, Y. Magnard, D. Maurel, D. Mawet, M. R. Meyer, J. Milli, O. Moeller-Nilsson, D. Mouillet, A. Pavlov, D. Perret, P. Pujet, S. P. Quanz, S. Rochat, G. Rousset, A. Roux, B. Salasnich, G. Salter, J. F. Sauvage,

H. M. Schmid, A. Sevin, C. Soenke, E. Stadler, M. Turatto, S. Udry, F. Vakili, Z. Wahhaj, and F. Wildi. First light of the VLT planet finder SPHERE. IV. Physical and chemical properties of the planets around HR8799. , 587:A58, March 2016.

[30] Jo Bovy. galpy: A python Library for Galactic Dynamics. , 216(2):29, February 2015.

[31] Rachel Bowens-Rubin, Joseph M. Akana Murphy, Philip M. Hinz, Mary Anne Limbach, Andreas Seifahrt, Rocio Kiman, Maïssa Salama, Sagnick Mukherjee, Madison Brady, Aarynn L. Carter, Rebecca Jensen-Clem, Maaike A. M. van Kooten, Howard Isaacson, Molly Kosiarek, Jacob L. Bean, David Kasper, Rafael Luque, Gudmundur Stefánsson, and Julian Stürmer. A Wolf 359 in Sheep's Clothing: Hunting for Substellar Companions in the Fifth-closest System Using Combined High-contrast Imaging and Radial Velocity Analysis. , 166(6):260, December 2023.

[32] Rachel Bowens-Rubin, Arjo Bos, Philip Hinz, Bradford Holden, and Matt Radovan. An adaptive optics upgrade for the Automated Planet Finder telescope using an adaptive secondary mirror. In Laura Schreiber, Dirk Schmidt, and Elise Vernet, editors, *Adaptive Optics Systems VIII*, volume 12185 of *Society of Photo-Optical Instrumentation Engineers (SPIE) Conference Series*, page 121851X, August 2022.

[33] Brendan P. Bowler. Imaging Extrasolar Giant Planets. , 128(968):102001, October

2016.

[34] Brendan P. Bowler and Eric L. Nielsen. Occurrence Rates from Direct Imaging Surveys. In Hans J. Deeg and Juan Antonio Belmonte, editors, *Handbook of Exoplanets*, page 155. 2018.

[35] Brendan P. Bowler, Evgenya L. Shkolnik, Michael C. Liu, Joshua E. Schlieder, Andrew W. Mann, Trent J. Dupuy, Sasha Hinkley, Justin R. Crepp, John Asher Johnson, Andrew W. Howard, Laura Flagg, Alycia J. Weinberger, Kimberly M. Aller, Katelyn N. Allers, William M. J. Best, Michael C. Kotson, Benjamin T. Montet, Gregory J. Herczeg, Christoph Baranec, Reed Riddle, Nicholas M. Law, Eric L. Nielsen, Zahed Wahhaj, Beth A. Biller, and Thomas L. Hayward. Planets Around Low-mass Stars (PALMS). V. Age-dating Low-mass Companions to Members and Interlopers of Young Moving Groups. , 806(1):62, June 2015.

[36] Wolfgang Brandner, Per Calissendorff, and Taisiya Kopytova. Benchmarking MESA isochrones against the Hyades single star sequence. , 518(1):662–668, January 2023.

[37] Timothy D. Brandt. The Hipparcos-Gaia Catalog of Accelerations: Gaia EDR3 Edition. , 254(2):42, June 2021.

[38] Timothy D. Brandt. The Hipparcos-Gaia Catalog of Accelerations: Gaia EDR3 Edition. , 254(2):42, June 2021.

[39] Timothy D. Brandt, Masayuki Kuzuhara, Michael W. McElwain, Joshua E. Schlieder, John P. Wisniewski, Edwin L. Turner, J. Carson, T. Matsuo, B. Biller, M. Bonnefoy, C. Dressing, M. Janson, G. R. Knapp, A. Moro-Martín, C. Thalmann, T. Kudo, N. Kusakabe, J. Hashimoto, L. Abe, W. Brandner, T. Currie, S. Egner, M. Feldt, T. Golota, M. Goto, C. A. Grady, O. Guyon, Y. Hayano, M. Hayashi, S. Hayashi, T. Henning, K. W. Hodapp, M. Ishii, M. Iye, R. Kandori, J. Kwon, K. Mede, S. Miyama, J. I. Morino, T. Nishimura, T. S. Pyo, E. Serabyn, T. Suenaga, H. Suto, R. Suzuki, M. Takami, Y. Takahashi, N. Takato, H. Terada, D. Tomono, M. Watanabe, T. Yamada, H. Takami, T. Usuda, and M. Tamura. The Moving Group Targets of the SEEDS High-contrast Imaging Survey of Exoplanets and Disks: Results and Observations from the First Three Years. , 786(1):1, May 2014.

[40] Runa Briguglio, Giorgio Pariani, Marco Xompero, Beatrice Tofani, Marco Rossetti, Paolo Calabretto, and Armando Riccardi. The crystal ball, the spider and other stories: a journey around the test tower of the M4 adaptive mirror. In Laird M. Close, Laura Schreiber, and Dirk Schmidt, editors, *Adaptive Optics Systems VI*, volume 10703 of *Society of Photo-Optical Instrumentation Engineers (SPIE) Conference Series*, page 1070373, July 2018.

[41] Jennifer Burt. *The Automated Planet Finder telescope's automation and first three years of planet detections*. PhD thesis, University of California, Santa Cruz, August 2016.

[42] Jennifer Burt, Steven S. Vogt, R. Paul Butler, Russell Hanson, Stefano Meschiari, Eugenio J. Rivera, Gregory W. Henry, and Gregory Laughlin. The Lick-Carnegie Exoplanet Survey: Gliese 687 b—A Neptune-mass Planet Orbiting a Nearby Red Dwarf. *apj*, 789(2):114, July 2014.

[43] R. P. Butler, G. W. Marcy, E. Williams, C. McCarthy, P. Dosanjh, and S. S. Vogt. Attaining doppler precision of 3 m s-1. *Publications of the Astronomical Society of the Pacific*, 108:500, jun 1996.

[44] R. P. Butler, G. W. Marcy, E. Williams, C. McCarthy, P. Dosanjh, and S. S. Vogt. Attaining Doppler Precision of 3 M s-1. *pasp*, 108:500, June 1996.

[45] R. Paul Butler, Steven S. Vogt, Gregory Laughlin, Jennifer A. Burt, Eugenio J. Rivera, Mikko Tuomi, Johanna Teske, Pamela Arriagada, Matias Diaz, Brad Holden, and Sandy Keiser. The LCES HIRES/Keck Precision Radial Velocity Exoplanet Survey. , 153(5):208, May 2017.

[46] I. Carleo, L. Malavolta, A. F. Lanza, M. Damasso, S. Desidera, F. Borsa, M. Mallonn, M. Pinamonti, R. Gratton, E. Alei, S. Benatti, L. Mancini, J. Maldonado, K. Biazzo, M. Esposito, G. Frustagli, E. González-Álvarez, G. Micela, G. Scandariato, A. Sozzetti, L. Affer, A. Bignamini, A. S. Bonomo, R. Claudi, R. Cosentino, E. Covino, A. F. M. Fiorenzano, P. Giacobbe, A. Harutyunyan, G. Leto, A. Maggio, E. Molinari, V. Nascimbeni, I. Pagano, M. Pedani, G. Piotto, E. Poretti, M. Rainer, S. Redfield, C. Baffa, A. Baruffolo, N. Buchschacher, V. Billotti,

M. Cecconi, G. Falcini, D. Fantinel, L. Fini, A. Galli, A. Ghedina, F. Ghinassi, E. Giani, C. Gonzalez, M. Gonzalez, J. Guerra, M. Hernandez Diaz, N. Hernandez, M. Iuzzolino, M. Lodi, E. Oliva, L. Origlia, H. Perez Ventura, A. Puglisi, C. Riverol, L. Riverol, J. San Juan, N. Sanna, S. Scuderi, U. Seemann, M. Sozzi, and A. Tozzi. The GAPS Programme at TNG. XXI. A GIARPS case study of known young planetary candidates: confirmation of HD 285507 b and refutation of AD Leonis b. , 638:A5, June 2020.

[47] Aarynn Carter, William Balmer, Beth Biller, Ell Bogat, Mariangela Bonavita, Brendan Bowler, Per Calissendorff, Clemence Fontanive, Kyle Franson, Jonathan Gagne, Julien Girard, Sasha Hinkley, Kielan K. W. Hoch, Jens Kammerer, Grant Kennedy, Jarron Michael Leisenring, Bruce A. Macintosh, Elisabeth C. Matthews, Michael R. Meyer, Maxwell Andrew Millar-Blanchaer, Caroline Morley, Marshall Perrin, Laurent Pueyo, Shrishmoy Ray, Isabel Rebollido, Emily Rickman, Andrew Skemer, and Jason J. Wang. Uncharted Worlds: Towards a Legacy of Direct Imaging of Sub-Jupiter Mass Exoplanets. JWST Proposal. Cycle 2, ID. #4050, May 2023.

[48] Aarynn L. Carter, Sasha Hinkley, Jens Kammerer, Andrew Skemer, Beth A. Biller, Jarron M. Leisenring, Maxwell A. Millar-Blanchaer, Simon Petrus, Jordan M. Stone, Kimberly Ward-Duong, Jason J. Wang, Julien H. Girard, Dean C. Hines, Marshall D. Perrin, Laurent Pueyo, William O. Balmer, Mariangela Bonavita, Mickael Bonnefoy, Gael Chauvin, Elodie Choquet, Valentin Christi-

aens, Camilla Danielski, Grant M. Kennedy, Elisabeth C. Matthews, Brittany E. Miles, Polychronis Patapis, Shrishmoy Ray, Emily Rickman, Steph Sallum, Karl R. Stapelfeldt, Niall Whiteford, Yifan Zhou, Olivier Absil, Anthony Boccaletti, Mark Booth, Brendan P. Bowler, Christine H. Chen, Thayne Currie, Jonathan J. Fortney, Carol A. Grady, Alexandra Z. Greebaum, Thomas Henning, Kielan K. W. Hoch, Markus Janson, Paul Kalas, Matthew A. Kenworthy, Pierre Kervella, Adam L. Kraus, Pierre-Olivier Lagage, Michael C. Liu, Bruce Macintosh, Sebastian Marino, Mark S. Marley, Christian Marois, Brenda C. Matthews, Dimitri Mawet, Michael W. McElwain, Stanimir Metchev, Michael R. Meyer, Paul Molliere, Sarah E. Moran, Caroline V. Morley, Sagnick Mukherjee, Eric Pantin, Andreas Quirrenbach, Isabel Rebollido, Bin B. Ren, Glenn Schneider, Malavika Vasist, Kadin Worthen, Mark C. Wyatt, Zackery W. Briesemeister, Marta L. Bryan, Per Calissendorff, Faustine Cantalloube, Gabriele Cugno, Matthew De Furio, Trent J. Dupuy, Samuel M. Factor, Jacqueline K. Faherty, Michael P. Fitzgerald, Kyle Franson, Eileen C. Gonzales, Callie E. Hood, Alex R. Howe, Masayuki Kuzuhara, Anne-Marie Lagrange, Kellen Lawson, Cecilia Lazzoni, Ben W. P. Lew, Pengyu Liu, Jorge Llop-Sayson, James P. Lloyd, Raquel A. Martinez, Johan Mazoyer, Paulina Palma-Bifani, Sascha P. Quanz, Jea Adams Redai, Matthias Samland, Joshua E. Schlieder, Motohide Tamura, Xianyu Tan, Taichi Uyama, Arthur Vigan, Johanna M. Vos, Kevin Wagner, Schuyler G. Wolff, Marie Ygouf, Xi Zhang, Keming Zhang, and Zhoujian Zhang. The JWST Early Release Science Program for Direct Observations of Exoplanetary Systems I: High-contrast Imaging of the

Exoplanet HIP 65426 b from 2 to 16 μm. , 951(1):L20, July 2023.

[49] Aarynn L. Carter, Sasha Hinkley, Jens Kammerer, Andrew Skemer, Beth A. Biller, Jarron M. Leisenring, Maxwell A. Millar-Blanchaer, Simon Petrus, Jordan M. Stone, Kimberly Ward-Duong, Jason J. Wang, Julien H. Girard, Dean C. Hines, Marshall D. Perrin, Laurent Pueyo, William O. Balmer, Mariangela Bonavita, Mickael Bonnefoy, Gael Chauvin, Elodie Choquet, Valentin Christiaens, Camilla Danielski, Grant M. Kennedy, Elisabeth C. Matthews, Brittany E. Miles, Polychronis Patapis, Shrishmoy Ray, Emily Rickman, Steph Sallum, Karl R. Stapelfeldt, Niall Whiteford, Yifan Zhou, Olivier Absil, Anthony Boccaletti, Mark Booth, Brendan P. Bowler, Christine H. Chen, Thayne Currie, Jonathan J. Fortney, Carol A. Grady, Alexandra Z. Greenbaum, Thomas Henning, Kielan K. W. Hoch, Markus Janson, Paul Kalas, Matthew A. Kenworthy, Pierre Kervella, Adam L. Kraus, Pierre-Olivier Lagage, Michael C. Liu, Bruce Macintosh, Sebastian Marino, Mark S. Marley, Christian Marois, Brenda C. Matthews, Dimitri Mawet, Michael W. McElwain, Stanimir Metchev, Michael R. Meyer, Paul Molliere, Sarah E. Moran, Caroline V. Morley, Sagnick Mukherjee, Eric Pantin, Andreas Quirrenbach, Isabel Rebollido, Bin B. Ren, Glenn Schneider, Malavika Vasist, Kadin Worthen, Mark C. Wyatt, Zackery W. Briesemeister, Marta L. Bryan, Per Calissendorff, Faustine Cantalloube, Gabriele Cugno, Matthew De Furio, Trent J. Dupuy, Samuel M. Factor, Jacqueline K. Faherty, Michael P. Fitzgerald, Kyle Franson, Eileen C. Gonzales, Callie E. Hood, Alex R. Howe, Masayuki

Kuzuhara, Anne-Marie Lagrange, Kellen Lawson, Cecilia Lazzoni, Ben W. P. Lew, Pengyu Liu, Jorge Llop-Sayson, James P. Lloyd, Raquel A. Martinez, Johan Mazoyer, Sascha P. Quanz, Jea Adams Redai, Matthias Samland, Joshua E. Schlieder, Motohide Tamura, Xianyu Tan, Taichi Uyama, Arthur Vigan, Johanna M. Vos, Kevin Wagner, Schuyler G. Wolff, Marie Ygouf, Xi Zhang, Keming Zhang, and Zhoujian Zhang. The JWST Early Release Science Program for Direct Observations of Exoplanetary Systems I: High Contrast Imaging of the Exoplanet HIP 65426 b from 2-16 μm. *arXiv e-prints*, page arXiv:2208.14990, August 2022.

[50] Aarynn L. Carter, Sasha Hinkley, Jens Kammerer, Andrew Skemer, Beth A. Biller, Jarron M. Leisenring, Maxwell A. Millar-Blanchaer, Simon Petrus, Jordan M. Stone, Kimberly Ward-Duong, Jason J. Wang, Julien H. Girard, Dean C. Hines, Marshall D. Perrin, Laurent Pueyo, William O. Balmer, Mariangela Bonavita, Mickael Bonnefoy, Gael Chauvin, Elodie Choquet, Valentin Christiaens, Camilla Danielski, Grant M. Kennedy, Elisabeth C. Matthews, Brittany E. Miles, Polychronis Patapis, Shrishmoy Ray, Emily Rickman, Steph Sallum, Karl R. Stapelfeldt, Niall Whiteford, Yifan Zhou, Olivier Absil, Anthony Boccaletti, Mark Booth, Brendan P. Bowler, Christine H. Chen, Thayne Currie, Jonathan J. Fortney, Carol A. Grady, Alexandra Z. Greebaum, Thomas Henning, Kielan K. W. Hoch, Markus Janson, Paul Kalas, Matthew A. Kenworthy, Pierre Kervella, Adam L. Kraus, Pierre-Olivier Lagage, Michael C. Liu, Bruce Macintosh, Sebastian Marino, Mark S. Marley, Christian Marois, Brenda C. Matthews, Dim-

itri Mawet, Michael W. McElwain, Stanimir Metchev, Michael R. Meyer, Paul Molliere, Sarah E. Moran, Caroline V. Morley, Sagnick Mukherjee, Eric Pantin, Andreas Quirrenbach, Isabel Rebollido, Bin B. Ren, Glenn Schneider, Malavika Vasist, Kadin Worthen, Mark C. Wyatt, Zackery W. Briesemeister, Marta L. Bryan, Per Calissendorff, Faustine Cantalloube, Gabriele Cugno, Matthew De Furio, Trent J. Dupuy, Samuel M. Factor, Jacqueline K. Faherty, Michael P. Fitzgerald, Kyle Franson, Eileen C. Gonzales, Callie E. Hood, Alex R. Howe, Masayuki Kuzuhara, Anne-Marie Lagrange, Kellen Lawson, Cecilia Lazzoni, Ben W. P. Lew, Pengyu Liu, Jorge Llop-Sayson, James P. Lloyd, Raquel A. Martinez, Johan Mazoyer, Paulina Palma-Bifani, Sascha P. Quanz, Jea Adams Redai, Matthias Samland, Joshua E. Schlieder, Motohide Tamura, Xianyu Tan, Taichi Uyama, Arthur Vigan, Johanna M. Vos, Kevin Wagner, Schuyler G. Wolff, Marie Ygouf, Xi Zhang, Keming Zhang, and Zhoujian Zhang. The JWST Early Release Science Program for Direct Observations of Exoplanetary Systems I: High-contrast Imaging of the Exoplanet HIP 65426 b from 2 to 16 μm. , 951(1):L20, July 2023.

[51] Aarynn L. Carter, Andrew J. I. Skemer, Camilla Danielski, Jarron Leisenring, Jason J. Wang, Kyle Van Gorkom, Brian York, Jea Adams, Beth Biller, Julien H. Girard, Sasha Hinkley, Bryony Nickson, Marshall Perrin, and Laurent Pueyo. Simulating JWST high contrast observations with PanCAKE. In Stuart B. Shaklan and Garreth J. Ruane, editors, *Techniques and Instrumentation for Detection of Exoplanets X*, volume 11823 of *Society of Photo-Optical Instrumentation Engineers*

(SPIE) Conference Series, page 118230H, September 2021.

[52] Aarynn L. Carter, Andrew J. I. Skemer, Camilla Danielski, Jarron Leisenring, Jason J. Wang, Kyle Van Gorkom, Brian York, Jea Adams, Beth Biller, Julien H. Girard, Sasha Hinkley, Bryony Nickson, Marshall Perrin, and Laurent Pueyo. Simulating JWST high contrast observations with PanCAKE. In *Society of Photo-Optical Instrumentation Engineers (SPIE) Conference Series*, volume 11823 of *Society of Photo-Optical Instrumentation Engineers (SPIE) Conference Series*, page 118230H, September 2021.

[53] A. Cassan, D. Kubas, J. P. Beaulieu, M. Dominik, K. Horne, J. Greenhill, J. Wambsganss, J. Menzies, A. Williams, U. G. Jørgensen, A. Udalski, D. P. Bennett, M. D. Albrow, V. Batista, S. Brillant, J. A. R. Caldwell, A. Cole, Ch. Coutures, K. H. Cook, S. Dieters, D. Dominis Prester, J. Donatowicz, P. Fouqué, K. Hill, N. Kains, S. Kane, J. B. Marquette, R. Martin, K. R. Pollard, K. C. Sahu, C. Vinter, D. Warren, B. Watson, M. Zub, T. Sumi, M. K. Szymański, M. Kubiak, R. Poleski, I. Soszynski, K. Ulaczyk, G. Pietrzyński, and Ł. Wyrzykowski. One or more bound planets per Milky Way star from microlensing observations. , 481(7380):167–169, January 2012.

[54] G. Chabrier, I. Baraffe, F. Allard, and P. Hauschildt. Evolutionary Models for Very Low-Mass Stars and Brown Dwarfs with Dusty Atmospheres. , 542(1):464–472, October 2000.

[55] G. Chabrier, I. Baraffe, F. Allard, and P. Hauschildt. Evolutionary Models for Very Low-Mass Stars and Brown Dwarfs with Dusty Atmospheres. , 542(1):464–472, October 2000.

[56] G. Chauvin, A. M. Lagrange, M. Bonavita, B. Zuckerman, C. Dumas, M. S. Bessell, J. L. Beuzit, M. Bonnefoy, S. Desidera, J. Farihi, P. Lowrance, D. Mouillet, and I. Song. Deep imaging survey of young, nearby austral stars . VLT/NACO near-infrared Lyot-coronographic observations. , 509:A52, January 2010.

[57] G. Chauvin, A. Vigan, M. Bonnefoy, S. Desidera, M. Bonavita, D. Mesa, A. Boccaletti, E. Buenzli, J. Carson, P. Delorme, J. Hagelberg, G. Montagnier, C. Mordasini, S. P. Quanz, D. Segransan, C. Thalmann, J. L. Beuzit, B. Biller, E. Covino, M. Feldt, J. Girard, R. Gratton, T. Henning, M. Kasper, A. M. Lagrange, S. Messina, M. Meyer, D. Mouillet, C. Moutou, M. Reggiani, J. E. Schlieder, and A. Zurlo. The VLT/NaCo large program to probe the occurrence of exoplanets and brown dwarfs at wide orbits. II. Survey description, results, and performances. , 573:A127, January 2015.

[58] A. Cheetham, D. Ségransan, S. Peretti, J. B. Delisle, J. Hagelberg, J. L. Beuzit, T. Forveille, M. Marmier, S. Udry, and F. Wildi. Direct imaging of an ultracool substellar companion to the exoplanet host star HD 4113 A. , 614:A16, June 2018.

[59] Jieun Choi, Aaron Dotter, Charlie Conroy, Matteo Cantiello, Bill Paxton, and Benjamin D. Johnson. Mesa Isochrones and Stellar Tracks (MIST). I. Solar-scaled

Models. , 823(2):102, June 2016.

[60] Mark Chun, Christoph Baranec, Olivier Lai, Jessica R. Lu, Ruihan Zhang, Stefan Kuiper, Wouter Jonker, and Matthew Maniscalco. A new adaptive secondary mirror for astronomy on the University of Hawaii 2.2-meter telescope. In *Society of Photo-Optical Instrumentation Engineers (SPIE) Conference Series*, volume 11448 of *Society of Photo-Optical Instrumentation Engineers (SPIE) Conference Series*, page 114481E, December 2020.

[61] Mark Chun, Jessica Lu, Olivier Lai, Fatima Abdurrahman, Maxwell Service, Douglas Toomey, Dora Fohring, Christoph Baranec, Yutaka Hayano, and Shin Oya. On-sky results from the wide-field ground-layer adaptive optics demonstrator 'imaka. In Laird M. Close, Laura Schreiber, and Dirk Schmidt, editors, *Adaptive Optics Systems VI*, volume 10703 of *Society of Photo-Optical Instrumentation Engineers (SPIE) Conference Series*, page 107030J, July 2018.

[62] Mark R. Chun, Alan Ryan, Ruihan Zhang, Stefan Kuiper, Gilles Ackaert, Christoph Baranec, M. J. J. Baeten, Arjo Bos, Rachel Bowens-Rubin, Bert Dekker, Ryan Dungee, Taavishe Gupta, Phil Hinz, Wouter Jonker, Fred Kamphues, Olivier Lai, Jessica Lu, Matt Maniscalco, Bert Monna, Manav Nair, Jan Nijenhuis, Hans Priem, and Paul-Alexander Vogel. Progress on the University of Hawaii 2.2-meter adaptive secondary mirror. In Laura Schreiber, Dirk Schmidt, and Elise Vernet, editors, *Adaptive Optics Systems VIII*, volume 12185 of *Society of Photo-Optical*

Instrumentation Engineers (SPIE) Conference Series, page 121857U, August 2022.

[63] Laird M. Close, Jared R. Males, Katie M. Morzinski, Simone Esposito, Armando Riccardi, Runa Briguglio, Kate B. Follette, Ya-Lin Wu, Enrico Pinna, Alfio Puglisi, Marco Xompero, Fernando Quiros, and Phil M. Hinz. Status of MagAO and review of astronomical science with visible light adaptive optics. In Laird M. Close, Laura Schreiber, and Dirk Schmidt, editors, *Adaptive Optics Systems VI*, volume 10703 of *Society of Photo-Optical Instrumentation Engineers (SPIE) Conference Series*, page 107030L, July 2018.

[64] M. Collados, F. Bettonvil, L. Cavaller, I. Ermolli, B. Gelly, A. Pérez, H. Socas-Navarro, D. Soltau, R. Volkmer, and EST Team. The European Solar Telescope. , 84:379, January 2013.

[65] Justin R. Crepp, Erica J. Gonzales, Eric B. Bechter, Benjamin T. Montet, John Asher Johnson, Danielle Piskorz, Andrew W. Howard, and Howard Isaacson. The TRENDS High-contrast Imaging Survey. VI. Discovery of a Mass, Age, and Metallicity Benchmark Brown Dwarf. , 831(2):136, December 2016.

[66] Justin R. Crepp, Erica J. Gonzales, Brendan P. Bowler, Farisa Morales, Jordan Stone, Eckhart Spalding, Amali Vaz, Philip Hinz, Steve Ertel, Andrew Howard, and Howard Isaacson. The TRENDS High-contrast Imaging Survey. VII. Discovery of a Nearby Sirius-like White Dwarf System (HD 169889). , 864(1):42, September 2018.

[67] Thayne Currie, G. Mirek Brandt, Timothy D. Brandt, Brianna Lacy, Adam Burrows, Olivier Guyon, Motohide Tamura, Ranger Y. Liu, Sabina Sagynbayeva, Taylor Tobin, Jeffrey Chilcote, Tyler Groff, Christian Marois, William Thompson, Simon J. Murphy, Masayuki Kuzuhara, Kellen Lawson, Julien Lozi, Vincent Deo, Sebastien Vievard, Nour Skaf, Taichi Uyama, Nemanja Jovanovic, Frantz Martinache, N. Jeremy Kasdin, Tomoyuki Kudo, Michael McElwain, Markus Janson, John Wisniewski, Klaus Hodapp, Jun Nishikawa, Krzysztof Hełminiak, Jungmi Kwon, and Masahiko Hayashi. Direct imaging and astrometric detection of a gas giant planet orbiting an accelerating star. *Science*, 380(6641):198–203, April 2023.

[68] Jason Lee Curtis, Marcel A. Agüeros, Sean P. Matt, Kevin R. Covey, Stephanie T. Douglas, Ruth Angus, Steven H. Saar, Ann Marie Cody, Andrew Vanderburg, Nicholas M. Law, Adam L. Kraus, David W. Latham, Christoph Baranec, Reed Riddle, Carl Ziegler, Mikkel N. Lund, Guillermo Torres, Søren Meibom, Victor Silva Aguirre, and Jason T. Wright. When Do Stalled Stars Resume Spinning Down? Advancing Gyrochronology with Ruprecht 147. , 904(2):140, December 2020.

[69] R. M. Cutri, M. F. Skrutskie, S. van Dyk, C. A. Beichman, J. M. Carpenter, T. Chester, L. Cambresy, T. Evans, J. Fowler, J. Gizis, E. Howard, J. Huchra, T. Jarrett, E. L. Kopan, J. D. Kirkpatrick, R. M. Light, K. A. Marsh, H. McCallon, S. Schneider, R. Stiening, M. Sykes, M. Weinberg, W. A. Wheaton, S. Wheelock, and N. Zacarias. VizieR Online Data Catalog: 2MASS All-Sky Catalog of Point

Sources (Cutri+ 2003). *VizieR Online Data Catalog*, page II/246, June 2003.

[70] Paul A. Dalba, Benjamin Fulton, Howard Isaacson, Stephen R. Kane, and Andrew W. Howard. Multiple Explanations for the Single Transit of KIC 5951458 Based on Radial Velocity Measurements Extracted with a Novel Matched-template Technique. , 160(3):149, September 2020.

[71] Robert J. De Rosa, Eric L. Nielsen, Zahed Wahhaj, Jean-Baptiste Ruffio, Paul G. Kalas, Anne E. Peck, Lea A. Hirsch, and William Roberson. Direct imaging discovery of a super-Jovian around the young Sun-like star AF Leporis. , 672:A94, April 2023.

[72] C. Desgrange, J. Milli, G. Chauvin, Th. Henning, A. Luashvili, M. Read, M. Wyatt, G. Kennedy, R. Burn, M. Schlecker, F. Kiefer, V. D'Orazi, S. Messina, P. Rubini, A. M. Lagrange, C. Babusiaux, L. Matrà, B. Bitsch, M. Bonavita, P. Delorme, E. Matthews, P. Palma-Bifani, and A. Vigan. Planetary system architectures with low-mass inner planets. Direct imaging exploration of mature systems beyond 1 au. , 680:A64, December 2023.

[73] Aaron Dotter. MESA Isochrones and Stellar Tracks (MIST) 0: Methods for the Construction of Stellar Isochrones. , 222(1):8, January 2016.

[74] Ryan Dungee, Jennifer van Saders, Eric Gaidos, Mark Chun, Rafael A. García, Eugene A. Magnier, Savita Mathur, and Ângela R. G. Santos. A 4 Gyr M-dwarf

Gyrochrone from CFHT/MegaPrime Monitoring of the Open Cluster M67. , 938(2):118, October 2022.

[75] Ryan Dungee, Jennifer van Saders, Eric Gaidos, Mark Chun, Rafael A. García, Eugene A. Magnier, Savita Mathur, and Ângela R. G. Santos. A 4 Gyr M-dwarf Gyrochrone from CFHT/MegaPrime Monitoring of the Open Cluster M67. , 938(2):118, October 2022.

[76] Scott G. Engle and Edward F. Guinan. The Rotation-Age Relationship of M Dwarfs: A Progress Report of the Living with a Red Dwarf Program. *Research Notes of the American Astronomical Society*, 2(1):34, February 2018.

[77] Linn E. J. Eriksson, Marit A. S. Mol Lous, Sho Shibata, and Ravit Helled. Can Uranus and Neptune form concurrently via pebble, gas and planetesimal accretion? , October 2023.

[78] 1997 Esa. VizieR Online Data Catalog: The Hipparcos and Tycho Catalogues (ESA 1997). VizieR On-line Data Catalog: I/239. Originally published in: 1997HIP...C.....0E, February 1997.

[79] Simone Esposito, Armando Riccardi, Luca Fini, Alfio T. Puglisi, Enrico Pinna, Marco Xompero, Runa Briguglio, Fernando Quirós-Pacheco, Paolo Stefanini, Juan C. Guerra, Lorenzo Busoni, Andrea Tozzi, Francesca Pieralli, Guido Agapito, Guido Brusa-Zappellini, Richard Demers, Joar Brynnel, Carmelo Arcidiacono, and

Piero Salinari. First light AO (FLAO) system for LBT: final integration, acceptance test in Europe, and preliminary on-sky commissioning results. In Brent L. Ellerbroek, Michael Hart, Norbert Hubin, and Peter L. Wizinowich, editors, *Adaptive Optics Systems II*, volume 7736 of *Society of Photo-Optical Instrumentation Engineers (SPIE) Conference Series*, page 773609, July 2010.

[80] Rachel B. Fernandes, Gijs D. Mulders, Ilaria Pascucci, Christoph Mordasini, and Alexandre Emsenhuber. Hints for a Turnover at the Snow Line in the Giant Planet Occurrence Rate. , 874(1):81, March 2019.

[81] Debra A. Fischer, Geoffrey W. Marcy, and Julien F. P. Spronck. The Twenty-five Year Lick Planet Search. , 210(1):5, January 2014.

[82] Katherine B. Follette. An Introduction to High Contrast Differential Imaging of Exoplanets and Disks. , 135(1051):093001, September 2023.

[83] Kyle Franson, Brendan P. Bowler, Mariangela Bonavita, Timothy D. Brandt, Minghan Chen, Matthias Samland, Zhoujian Zhang, Anna Lueber, Kevin Heng, Daniel Kitzmann, Trevor Wolf, Brandon A. Jones, Quang H. Tran, Daniella C. Bardalez Gagliuffi, Beth Biller, Jeffrey Chilcote, Justin R. Crepp, Trent J. Dupuy, Jacqueline Faherty, Clémence Fontanive, Tyler D. Groff, Raffaele Gratton, Olivier Guyon, Rebecca Jensen-Clem, Nemanja Jovanovic, N. Jeremy Kasdin, Julien Lozi, Eugene A. Magnier, Koraljka Mužić, Aniket Sanghi, and Christopher A. Theissen. Astrometric Accelerations as Dynamical Beacons: Discovery and Characterization

of HIP 21152 B, the First T-dwarf Companion in the Hyades. , 165(2):39, February 2023.

[84] Kyle Franson, Brendan P. Bowler, Yifan Zhou, Tim D. Pearce, Daniella C. Bardalez Gagliuffi, Lauren I. Biddle, Timothy D. Brandt, Justin R. Crepp, Trent J. Dupuy, Jacqueline Faherty, Rebecca Jensen-Clem, Marvin Morgan, Aniket Sanghi, Christopher A. Theissen, Quang H. Tran, and Trevor N. Wolf. Astrometric Accelerations as Dynamical Beacons: A Giant Planet Imaged inside the Debris Disk of the Young Star AF Lep. , 950(2):L19, June 2023.

[85] B. Fuhrmeister, J. H. M. M. Schmitt, and P. H. Hauschildt. PHOENIX model chromospheres of mid- to late-type M dwarfs. , 439(3):1137–1148, September 2005.

[86] Benjamin J. Fulton, Erik A. Petigura, Sarah Blunt, and Evan Sinukoff. RadVel: The Radial Velocity Modeling Toolkit. , 130(986):044504, April 2018.

[87] Benjamin J. Fulton, Lee J. Rosenthal, Lea A. Hirsch, Howard Isaacson, Andrew W. Howard, Cayla M. Dedrick, Ilya A. Sherstyuk, Sarah C. Blunt, Erik A. Petigura, Heather A. Knutson, Aida Behmard, Ashley Chontos, Justin R. Crepp, Ian J. M. Crossfield, Paul A. Dalba, Debra A. Fischer, Gregory W. Henry, Stephen R. Kane, Molly Kosiarek, Geoffrey W. Marcy, Ryan A. Rubenzahl, Lauren M. Weiss, and Jason T. Wright. California Legacy Survey. II. Occurrence of Giant Planets beyond the Ice Line. , 255(1):14, July 2021.

[88] Jonathan Gagné, Jacqueline K. Faherty, Leslie Moranta, and Mark Popinchalk. A Number of nearby Moving Groups May Be Fragments of Dissolving Open Clusters. , 915(2):L29, July 2021.

[89] Jonathan Gagné, Leslie Moranta, Jacqueline K. Faherty, Rocio Kiman, Dominic Couture, Arnaud René Larochelle, Mark Popinchalk, and Daniella Morrone. The Oceanus Moving Group: A New 500 Myr Old Host for the Nearest Brown Dwarf. , 945(2):119, March 2023.

[90] Gaia Collaboration, A. G. A. Brown, A. Vallenari, T. Prusti, J. H. J. de Bruijne, C. Babusiaux, M. Biermann, O. L. Creevey, D. W. Evans, L. Eyer, A. Hutton, F. Jansen, C. Jordi, S. A. Klioner, U. Lammers, L. Lindegren, X. Luri, F. Mignard, C. Panem, D. Pourbaix, S. Randich, P. Sartoretti, C. Soubiran, N. A. Walton, F. Arenou, C. A. L. Bailer-Jones, U. Bastian, M. Cropper, R. Drimmel, D. Katz, M. G. Lattanzi, F. van Leeuwen, J. Bakker, C. Cacciari, J. Castañeda, F. De Angeli, C. Ducourant, C. Fabricius, M. Fouesneau, Y. Frémat, R. Guerra, A. Guerrier, J. Guiraud, A. Jean-Antoine Piccolo, E. Masana, R. Messineo, N. Mowlavi, C. Nicolas, K. Nienartowicz, F. Pailler, P. Panuzzo, F. Riclet, W. Roux, G. M. Seabroke, R. Sordo, P. Tanga, F. Thévenin, G. Gracia-Abril, J. Portell, D. Teyssier, M. Altmann, R. Andrae, I. Bellas-Velidis, K. Benson, J. Berthier, R. Blomme, E. Brugaletta, P. W. Burgess, G. Busso, B. Carry, A. Cellino, N. Cheek, G. Clementini, Y. Damerdji, M. Davidson, L. Delchambre, A. Dell'Oro, J. Fernández-Hernández, L. Galluccio, P. García-Lario, M. Garcia-

Reinaldos, J. González-Núñez, E. Gosset, R. Haigron, J. L. Halbwachs, N. C. Hambly, D. L. Harrison, D. Hatzidimitriou, U. Heiter, J. Hernández, D. Hestroffer, S. T. Hodgkin, B. Holl, K. Janßen, G. Jevardat de Fombelle, S. Jordan, A. Krone-Martins, A. C. Lanzafame, W. Löffler, A. Lorca, M. Manteiga, O. Marchal, P. M. Marrese, A. Moitinho, A. Mora, K. Muinonen, P. Osborne, E. Pancino, T. Pauwels, J. M. Petit, A. Recio-Blanco, P. J. Richards, M. Riello, L. Rimoldini, A. C. Robin, T. Roegiers, J. Rybizki, L. M. Sarro, C. Siopis, M. Smith, A. Sozzetti, A. Ulla, E. Utrilla, M. van Leeuwen, W. van Reeven, U. Abbas, A. Abreu Aramburu, S. Accart, C. Aerts, J. J. Aguado, M. Ajaj, G. Altavilla, M. A. Álvarez, J. Álvarez Cid-Fuentes, J. Alves, R. I. Anderson, E. Anglada Varela, T. Antoja, M. Audard, D. Baines, S. G. Baker, L. Balaguer-Núñez, E. Balbinot, Z. Balog, C. Barache, D. Barbato, M. Barros, M. A. Barstow, S. Bartolomé, J. L. Bassilana, N. Bauchet, A. Baudesson-Stella, U. Becciani, M. Bellazzini, M. Bernet, S. Bertone, L. Bianchi, S. Blanco-Cuaresma, T. Boch, A. Bombrun, D. Bossini, S. Bouquillon, A. Bragaglia, L. Bramante, E. Breedt, A. Bressan, N. Brouillet, B. Bucciarelli, A. Burlacu, D. Busonero, A. G. Butkevich, R. Buzzi, E. Caffau, R. Cancelliere, H. Cánovas, T. Cantat-Gaudin, R. Carballo, T. Carlucci, M. I. Carnerero, J. M. Carrasco, L. Casamiquela, M. Castellani, A. Castro-Ginard, P. Castro Sampol, L. Chaoul, P. Charlot, L. Chemin, A. Chiavassa, M. R. L. Cioni, G. Comoretto, W. J. Cooper, T. Cornez, S. Cowell, F. Crifo, M. Crosta, C. Crowley, C. Dafonte, A. Dapergolas, M. David, P. David, P. de Laverny, F. De Luise, R. De March, J. De Ridder, R. de Souza, P. de Teodoro, A. de Torres,

E. F. del Peloso, E. del Pozo, M. Delbo, A. Delgado, H. E. Delgado, J. B. Delisle, P. Di Matteo, S. Diakite, C. Diener, E. Distefano, C. Dolding, D. Eappachen, B. Edvardsson, H. Enke, P. Esquej, C. Fabre, M. Fabrizio, S. Faigler, G. Fedorets, P. Fernique, A. Fienga, F. Figueras, C. Fouron, F. Fragkoudi, E. Fraile, F. Franke, M. Gai, D. Garabato, A. Garcia-Gutierrez, M. García-Torres, A. Garofalo, P. Gavras, E. Gerlach, R. Geyer, P. Giacobbe, G. Gilmore, S. Girona, G. Giuffrida, R. Gomel, A. Gomez, I. Gonzalez-Santamaria, J. J. González-Vidal, M. Granvik, R. Gutiérrez-Sánchez, L. P. Guy, M. Hauser, M. Haywood, A. Helmi, S. L. Hidalgo, T. Hilger, N. Hładczuk, D. Hobbs, G. Holland, H. E. Huckle, G. Jasniewicz, P. G. Jonker, J. Juaristi Campillo, F. Julbe, L. Karbevska, P. Kervella, S. Khanna, A. Kochoska, M. Kontizas, G. Kordopatis, A. J. Korn, Z. Kostrzewa-Rutkowska, K. Kruszyńska, S. Lambert, A. F. Lanza, Y. Lasne, J. F. Le Campion, Y. Le Fustec, Y. Lebreton, T. Lebzelter, S. Leccia, N. Leclerc, I. Lecoeur-Taibi, S. Liao, E. Licata, E. P. Lindstrøm, T. A. Lister, E. Livanou, A. Lobel, P. Madrero Pardo, S. Managau, R. G. Mann, J. M. Marchant, M. Marconi, M. M. S. Marcos Santos, S. Marinoni, F. Marocco, D. J. Marshall, L. Martin Polo, J. M. Martín-Fleitas, A. Masip, D. Massari, A. Mastrobuono-Battisti, T. Mazeh, P. J. McMillan, S. Messina, D. Michalik, N. R. Millar, A. Mints, D. Molina, R. Molinaro, L. Molnár, P. Montegriffo, R. Mor, R. Morbidelli, T. Morel, D. Morris, A. F. Mulone, D. Munoz, T. Muraveva, C. P. Murphy, I. Musella, L. Noval, C. Ordénovic, G. Orrù, J. Osinde, C. Pagani, I. Pagano, L. Palaversa, P. A. Palicio, A. Panahi, M. Pawlak, X. Peñalosa Esteller, A. Penttilä, A. M. Piersimoni, F. X.

Pineau, E. Plachy, G. Plum, E. Poggio, E. Poretti, E. Poujoulet, A. Prša, L. Pulone, E. Racero, S. Ragaini, M. Rainer, C. M. Raiteri, N. Rambaux, P. Ramos, M. Ramos-Lerate, P. Re Fiorentin, S. Regibo, C. Reylé, V. Ripepi, A. Riva, G. Rixon, N. Robichon, C. Robin, M. Roelens, L. Rohrbasser, M. Romero-Gómez, N. Rowell, F. Royer, K. A. Rybicki, G. Sadowski, A. Sagristà Sellés, J. Sahlmann, J. Salgado, E. Salguero, N. Samaras, V. Sanchez Gimenez, N. Sanna, R. Santoveña, M. Sarasso, M. Schultheis, E. Sciacca, M. Segol, J. C. Segovia, D. Ségransan, D. Semeux, S. Shahaf, H. I. Siddiqui, A. Siebert, L. Siltala, E. Slezak, R. L. Smart, E. Solano, F. Solitro, D. Souami, J. Souchay, A. Spagna, F. Spoto, I. A. Steele, H. Steidelmüller, C. A. Stephenson, M. Süveges, L. Szabados, E. Szegedi-Elek, F. Taris, G. Tauran, M. B. Taylor, R. Teixeira, W. Thuillot, N. Tonello, F. Torra, J. Torra, C. Turon, N. Unger, M. Vaillant, E. van Dillen, O. Vanel, A. Vecchiato, Y. Viala, D. Vicente, S. Voutsinas, M. Weiler, T. Wevers, Ł. Wyrzykowski, A. Yoldas, P. Yvard, H. Zhao, J. Zorec, S. Zucker, C. Zurbach, and T. Zwitter. Gaia Early Data Release 3. Summary of the contents and survey properties. , 649:A1, May 2021.

[91] Gaia Collaboration, A. Vallenari, A. G. A. Brown, T. Prusti, J. H. J. de Bruijne, F. Arenou, C. Babusiaux, M. Biermann, O. L. Creevey, C. Ducourant, D. W. Evans, L. Eyer, R. Guerra, A. Hutton, C. Jordi, S. A. Klioner, U. L. Lammers, L. Lindegren, X. Luri, F. Mignard, C. Panem, D. Pourbaix, S. Randich, P. Sartoretti, C. Soubiran, P. Tanga, N. A. Walton, C. A. L. Bailer-Jones, U. Bastian,

R. Drimmel, F. Jansen, D. Katz, M. G. Lattanzi, F. van Leeuwen, J. Bakker, C. Cacciari, J. Castañeda, F. De Angeli, C. Fabricius, M. Fouesneau, Y. Frémat, L. Galluccio, A. Guerrier, U. Heiter, E. Masana, R. Messineo, N. Mowlavi, C. Nicolas, K. Nienartowicz, F. Pailler, P. Panuzzo, F. Riclet, W. Roux, G. M. Seabroke, R. Sordoørcit, F. Thévenin, G. Gracia-Abril, J. Portell, D. Teyssier, M. Altmann, R. Andrae, M. Audard, I. Bellas-Velidis, K. Benson, J. Berthier, R. Blomme, P. W. Burgess, D. Busonero, G. Busso, H. Cánovas, B. Carry, A. Cellino, N. Cheek, G. Clementini, Y. Damerdji, M. Davidson, P. de Teodoro, M. Nuñez Campos, L. Delchambre, A. Dell'Oro, P. Esquej, J. Fernández-Hernández, E. Fraile, D. Garabato, P. García-Lario, E. Gosset, R. Haigron, J. L. Halbwachs, N. C. Hambly, D. L. Harrison, J. Hernández, D. Hestroffer, S. T. Hodgkin, B. Holl, K. Janßen, G. Jevardat de Fombelle, S. Jordan, A. Krone-Martins, A. C. Lanzafame, W. Löffler, O. Marchal, P. M. Marrese, A. Moitinho, K. Muinonen, P. Osborne, E. Pancino, T. Pauwels, A. Recio-Blanco, C. Reylé, M. Riello, L. Rimoldini, T. Roegiers, J. Rybizki, L. M. Sarro, C. Siopis, M. Smith, A. Sozzetti, E. Utrilla, M. van Leeuwen, U. Abbas, P. Ábrahám, A. Abreu Aramburu, C. Aerts, J. J. Aguado, M. Ajaj, F. Aldea-Montero, G. Altavilla, M. A. Álvarez, J. Alves, F. Anders, R. I. Anderson, E. Anglada Varela, T. Antoja, D. Baines, S. G. Baker, L. Balaguer-Núñez, E. Balbinot, Z. Balog, C. Barache, D. Barbato, M. Barros, M. A. Barstow, S. Bartolomé, J. L. Bassilana, N. Bauchet, U. Becciani, M. Bellazzini, A. Berihuete, M. Bernet, S. Bertone, L. Bianchi, A. Binnenfeld, S. Blanco-Cuaresma, A. Blazere, T. Boch, A. Bombrun, D. Bossini, S. Bouquillon, A. Bragaglia, L. Bramante,

E. Breedt, A. Bressan, N. Brouillet, E. Brugaletta, B. Bucciarelli, A. Burlacu, A. G. Butkevich, R. Buzzi, E. Caffau, R. Cancelliere, T. Cantat-Gaudin, R. Carballo, T. Carlucci, M. I. Carnerero, J. M. Carrasco, L. Casamiquela, M. Castellani, A. Castro-Ginard, L. Chaoul, P. Charlot, L. Chemin, V. Chiaramida, A. Chiavassa, N. Chornay, G. Comoretto, G. Contursi, W. J. Cooper, T. Cornez, S. Cowell, F. Crifo, M. Cropper, M. Crosta, C. Crowley, C. Dafonte, A. Dapergolas, M. David, P. David, P. de Laverny, F. De Luise, R. De March, J. De Ridder, R. de Souza, A. de Torres, E. F. del Peloso, E. del Pozo, M. Delbo, A. Delgado, J. B. Delisle, C. Demouchy, T. E. Dharmawardena, P. Di Matteo, S. Diakite, C. Diener, E. Distefano, C. Dolding, B. Edvardsson, H. Enke, C. Fabre, M. Fabrizio, S. Faigler, G. Fedorets, P. Fernique, A. Fienga, F. Figueras, Y. Fournier, C. Fouron, F. Fragkoudi, M. Gai, A. Garcia-Gutierrez, M. Garcia-Reinaldos, M. García-Torres, A. Garofalo, A. Gavel, P. Gavras, E. Gerlach, R. Geyer, P. Giacobbe, G. Gilmore, S. Girona, G. Giuffrida, R. Gomel, A. Gomez, J. González-Núñez, I. González-Santamaría, J. J. González-Vidal, M. Granvik, P. Guillout, J. Guiraud, R. Gutiérrez-Sánchez, L. P. Guy, D. Hatzidimitriou, M. Hauser, M. Haywood, A. Helmer, A. Helmi, M. H. Sarmiento, S. L. Hidalgo, T. Hilger, N. Hładczuk, D. Hobbs, G. Holland, H. E. Huckle, K. Jardine, G. Jasniewicz, A. Jean-Antoine Piccolo, Ó. Jiménez-Arranz, A. Jorissen, J. Juaristi Campillo, F. Julbe, L. Karbevska, P. Kervella, S. Khanna, M. Kontizas, G. Kordopatis, A. J. Korn, Á Kóspál, Z. Kostrzewa-Rutkowska, K. Kruszyńska, M. Kun, P. Laizeau, S. Lambert, A. F. Lanza, Y. Lasne, J. F. Le Campion, Y. Lebreton, T. Lebzelter, S. Leccia, N. Leclerc, I. Lecoeur-Taibi,

S. Liao, E. L. Licata, H. E. P. Lindstrøm, T. A. Lister, E. Livanou, A. Lobel, A. Lorca, C. Loup, P. Madrero Pardo, A. Magdaleno Romeo, S. Managau, R. G. Mann, M. Manteiga, J. M. Marchant, M. Marconi, J. Marcos, M. M. S. Marcos Santos, D. Marín Pina, S. Marinoni, F. Marocco, D. J. Marshall, L. Martin Polo, J. M. Martín-Fleitas, G. Marton, N. Mary, A. Masip, D. Massari, A. Mastrobuono-Battisti, T. Mazeh, P. J. McMillan, S. Messina, D. Michalik, N. R. Millar, A. Mints, D. Molina, R. Molinaro, L. Molnár, G. Monari, M. Monguió, P. Montegriffo, A. Montero, R. Mor, A. Mora, R. Morbidelli, T. Morel, D. Morris, T. Muraveva, C. P. Murphy, I. Musella, Z. Nagy, L. Noval, F. Ocaña, A. Ogden, C. Ordenovic, J. O. Osinde, C. Pagani, I. Pagano, L. Palaversa, P. A. Palicio, L. Pallas-Quintela, A. Panahi, S. Payne-Wardenaar, X. Peñalosa Esteller, A. Penttilä, B. Pichon, A. M. Piersimoni, F. X. Pineau, E. Plachy, G. Plum, E. Poggio, A. Prša, L. Pulone, E. Racero, S. Ragaini, M. Rainer, C. M. Raiteri, N. Rambaux, P. Ramos, M. Ramos-Lerate, P. Re Fiorentin, S. Regibo, P. J. Richards, C. Rios Diaz, V. Ripepi, A. Riva, H. W. Rix, G. Rixon, N. Robichon, A. C. Robin, C. Robin, M. Roelens, H. R. O. Rogues, L. Rohrbasser, M. Romero-Gómez, N. Rowell, F. Royer, D. Ruz Mieres, K. A. Rybicki, G. Sadowski, A. Sáez Núñez, A. Sagristà Sellés, J. Sahlmann, E. Salguero, N. Samaras, V. Sanchez Gimenez, N. Sanna, R. Santoveña, M. Sarasso, M. Schultheis, E. Sciacca, M. Segol, J. C. Segovia, D. Ségransan, D. Semeux, S. Shahaf, H. I. Siddiqui, A. Siebert, L. Siltala, A. Silvelo, E. Slezak, I. Slezak, R. L. Smart, O. N. Snaith, E. Solano, F. Solitro, D. Souami, J. Souchay, A. Spagna, L. Spina, F. Spoto, I. A. Steele, H. Stei-

delmüller, C. A. Stephenson, M. Süveges, J. Surdej, L. Szabados, E. Szegedi-Elek, F. Taris, M. B. Taylo, R. Teixeira, L. Tolomei, N. Tonello, F. Torra, J. Torra, G. Torralba Elipe, M. Trabucchi, A. T. Tsounis, C. Turon, A. Ulla, N. Unger, M. V. Vaillant, E. van Dillen, W. van Reeven, O. Vanel, A. Vecchiato, Y. Viala, D. Vicente, S. Voutsinas, M. Weiler, T. Wevers, L. Wyrzykowski, A. Yoldas, P. Yvard, H. Zhao, J. Zorec, S. Zucker, and T. Zwitter. Gaia Data Release 3: Summary of the content and survey properties. *arXiv e-prints*, page arXiv:2208.00211, July 2022.

[92] R. Galicher, C. Marois, B. Macintosh, B. Zuckerman, T. Barman, Q. Konopacky, I. Song, J. Patience, D. Lafrenière, R. Doyon, and E. L. Nielsen. The International Deep Planet Survey. II. The frequency of directly imaged giant exoplanets with stellar mass. , 594:A63, October 2016.

[93] Daniele Gallieni, Matteo Tintori, Pierluigi Fumi, Lorenzo Crimella, Roberto Biasi, Gerald Angerer, Mauro Manetti, Antonin Bouchez, Glenn Brossus, Frank Groark, and Peter M. Thompson. GMT adaptive secondary mirrors subsystem final design. In Laura Schreiber, Dirk Schmidt, and Elise Vernet, editors, *Adaptive Optics Systems VII*, volume 11448 of *Society of Photo-Optical Instrumentation Engineers (SPIE) Conference Series*, page 114485K, December 2020.

[94] Bartosz Gauza, Víctor J. S. Béjar, Rafael Rebolo, Carlos Álvarez, María Rosa Zapatero Osorio, Gabriel Bihain, José A. Caballero, David J. Pinfield, Charles M.

Telesco, and Christopher Packham. GTC/CanariCam Deep Mid-infrared Imaging Survey of Northern Stars within 5 pc. , 923(1):119, December 2021.

[95] N. P. Gentile Fusillo, P. E. Tremblay, E. Cukanovaite, A. Vorontseva, R. Lallement, M. Hollands, B. T. Gänsicke, K. B. Burdge, J. McCleery, and S. Jordan. A catalogue of white dwarfs in Gaia EDR3. , 508(3):3877–3896, December 2021.

[96] Nikolaos Georgakarakos, Siegfried Eggl, and Ian Dobbs-Dixon. Giant Planets: Good Neighbors for Habitable Worlds? , 856(2):155, April 2018.

[97] Gregory J. Gilbert and Daniel C. Fabrycky. An Information Theoretic Framework for Classifying Exoplanetary System Architectures. , 159(6):281, June 2020.

[98] Julien H. Girard, William Blair, Brian Brooks, Keira Brooks, Robert Brown, Howard Bushouse, Alicia Canipe, Christine Chen, Matteo Correnti, J. Brendan Hagan, Bryan Hilbert, Dean Hines, Jarron Leisenring, Joseph Long, Bryony Nickson, Marshall D. Perrin, Klaus Pontoppidan, Laurent Pueyo, Abhijith Rajan, Adric Riedel, Remi Soummer, John Stansberry, Christopher Stark, Kyle Van Gorkom, and Brian York. Making good use of JWST's coronagraphs: tools and strategies from a user's perspective. In Makenzie Lystrup, Howard A. MacEwen, Giovanni G. Fazio, Natalie Batalha, Nicholas Siegler, and Edward C. Tong, editors, *Space Telescopes and Instrumentation 2018: Optical, Infrared, and Millimeter Wave*, volume 10698 of *Society of Photo-Optical Instrumentation Engineers (SPIE) Conference Series*, page 106983V, August 2018.

[99] C. A. Gomez Gonzalez, O. Absil, P. A. Absil, M. Van Droogenbroeck, D. Mawet, and J. Surdej. Low-rank plus sparse decomposition for exoplanet detection in direct-imaging ADI sequences. The LLSG algorithm. , 589:A54, May 2016.

[100] Carlos Alberto Gomez Gonzalez, Olivier Wertz, Olivier Absil, Valentin Christiaens, Denis Defrère, Dimitri Mawet, Julien Milli, Pierre-Antoine Absil, Marc Van Droogenbroeck, Faustine Cantalloube, Philip M. Hinz, Andrew J. Skemer, Mikael Karlsson, and Jean Surdej. VIP: Vortex Image Processing Package for High-contrast Direct Imaging. , 154(1):7, July 2017.

[101] Carlos Alberto Gomez Gonzalez, Olivier Wertz, Olivier Absil, Valentin Christiaens, Denis Defrère, Dimitri Mawet, Julien Milli, Pierre-Antoine Absil, Marc Van Droogenbroeck, Faustine Cantalloube, Philip M. Hinz, Andrew J. Skemer, Mikael Karlsson, and Jean Surdej. VIP: Vortex Image Processing Package for High-contrast Direct Imaging. , 154(1):7, July 2017.

[102] Gravity Collaboration, M. Nowak, S. Lacour, P. Mollière, J. Wang, B. Charnay, E. F. van Dishoeck, R. Abuter, A. Amorim, J. P. Berger, H. Beust, M. Bonnefoy, H. Bonnet, W. Brandner, A. Buron, F. Cantalloube, C. Collin, F. Chapron, Y. Clénet, V. Coudé Du Foresto, P. T. de Zeeuw, R. Dembet, J. Dexter, G. Duvert, A. Eckart, F. Eisenhauer, N. M. Förster Schreiber, P. Fédou, R. Garcia Lopez, F. Gao, E. Gendron, R. Genzel, S. Gillessen, F. Haußmann, T. Henning, S. Hippler, Z. Hubert, L. Jocou, P. Kervella, A. M. Lagrange, V. Lapeyrère, J. B.

Le Bouquin, P. Léna, A. L. Maire, T. Ott, T. Paumard, C. Paladini, K. Perraut, G. Perrin, L. Pueyo, O. Pfuhl, S. Rabien, C. Rau, G. Rodríguez-Coira, G. Rousset, S. Scheithauer, J. Shangguan, O. Straub, C. Straubmeier, E. Sturm, L. J. Tacconi, F. Vincent, F. Widmann, E. Wieprecht, E. Wiezorrek, J. Woillez, S. Yazici, and D. Ziegler. Peering into the formation history of β Pictoris b with VLTI/GRAVITY long-baseline interferometry. , 633:A110, January 2020.

[103] Edward F. Guinan and Scott G. Engle. New Perspectives of our Nearby Red Dwarf Neighbor Wolf 359 from the Kepler K2 Mission. *Research Notes of the American Astronomical Society*, 2(2):1, April 2018.

[104] Caleb K. Harada, Courtney D. Dressing, Stephen R. Kane, and Bahareh Adami Ardestani. Setting the stage for the search for life with the Habitable Worlds Observatory: Properties of 164 promising planet survey targets. *arXiv e-prints*, page arXiv:2401.03047, January 2024.

[105] Matthias Y. He and Lauren M. Weiss. Inner Planetary System Gap Complexity is a Predictor of Outer Giant Planets. , 166(1):36, July 2023.

[106] A. N. Heinze, Philip M. Hinz, Suresh Sivanandam, Matthew Kenworthy, Michael Meyer, and Douglas Miller. Constraints on Long-period Planets from an L'- and M-band Survey of Nearby Sun-like Stars: Observations. , 714(2):1551–1569, May 2010.

[107] S. Hinkley, S. Lacour, G. D. Marleau, A. M. Lagrange, J. J. Wang, J. Kammerer, A. Cumming, M. Nowak, L. Rodet, T. Stolker, W. O. Balmer, S. Ray, M. Bonnefoy, P. Mollière, C. Lazzoni, G. Kennedy, C. Mordasini, R. Abuter, S. Aigrain, A. Amorim, R. Asensio-Torres, C. Babusiaux, M. Benisty, J. P. Berger, H. Beust, S. Blunt, A. Boccaletti, A. Bohn, H. Bonnet, G. Bourdarot, W. Brandner, F. Cantalloube, P. Caselli, B. Charnay, G. Chauvin, A. Chomez, E. Choquet, V. Christiaens, Y. Clénet, V. Coudé du Foresto, A. Cridland, P. Delorme, R. Dembet, P. T. de Zeeuw, A. Drescher, G. Duvert, A. Eckart, F. Eisenhauer, H. Feuchtgruber, F. Galland, P. Garcia, R. Garcia Lopez, T. Gardner, E. Gendron, R. Genzel, S. Gillessen, J. H. Girard, A. Grandjean, X. Haubois, G. Heißel, Th. Henning, S. Hippler, M. Horrobin, M. Houllé, Z. Hubert, L. Jocou, M. Keppler, P. Kervella, L. Kreidberg, V. Lapeyrère, J. B. Le Bouquin, P. Léna, D. Lutz, A. L. Maire, F. Mang, A. Mérand, N. Meunier, J. D. Monnier, C. Mordasini, D. Mouillet, E. Nasedkin, T. Ott, G. P. P. L. Otten, C. Paladini, T. Paumard, K. Perraut, G. Perrin, F. Philipot, O. Pfuhl, N. Pourré, L. Pueyo, J. Rameau, E. Rickman, P. Rubini, Z. Rustamkulov, M. Samland, J. Shangguan, T. Shimizu, D. Sing, C. Straubmeier, E. Sturm, L. J. Tacconi, E. F. van Dishoeck, A. Vigan, F. Vincent, K. Ward-Duong, F. Widmann, E. Wieprecht, E. Wiezorrek, J. Woillez, S. Yazici, A. Young, N. Zicher, and the GRAVITY Collaboration. Direct Discovery of the Inner Exoplanet in the HD206893 System. *arXiv e-prints*, page arXiv:2208.04867, August 2022.

[108] Sasha Hinkley, Beth Biller, Andrew Skemer, Aarynn L. Carter, Julien Girard, Dean Hines, Jens Kammerer, Jarron Leisenring, William Balmer, Elodie Choquet, Maxwell A. Millar-Blanchaer, Marshall Perrin, Laurent Pueyo, Jason Wang, Kimberly Ward-Duong, Anthony Boccaletti, Brittany Miles, Polychronis Patapis, Isabel Rebollido, Emily Rickman, B. Sargent, Kadin Worthen, Kielan Hoch, Christine Chen, Stephanie Sallum, Shrishmoy Ray, Karl Stapelfeldt, Yifan Zhou, Michael Meyer, Mickael Bonnefoy, Camilla Danielski, Elisabeth C. Matthews, Anand Sivaramakrishnan, Jordan Stone, and Malavika Vasist. The JWST Early Release Science Program for Direct Observations of Exoplanetary Systems: Best Practices for Data Collection in Cycle 2 and Beyond. *arXiv e-prints*, page arXiv:2301.07199, January 2023.

[109] Philip M. Hinz, Rachel Bowens-Rubin, Christoph Baranec, Kevin Bundy, Mark Chun, Daren Dillon, Brad Holden, Wouter Jonker, Molly Kosiarek, Renate Kupke, Stefan Kuiper, Olivier Lai, Jessica R. Lu, Matthew Maniscalco, Matthew Radovan, Sam Ragland, Stephanie Sallum, Andrew Skemer, and Peter Wizinowich. Developing adaptive secondary mirror concepts for the APF and W.M. Keck Observatory based on HVR technology. In Laura Schreiber, Dirk Schmidt, and Elise Vernet, editors, *Adaptive Optics Systems VII*, volume 11448 of *Society of Photo-Optical Instrumentation Engineers (SPIE) Conference Series*, page 114485U, December 2020.

[110] Philip M. Hinz, Matt Radovan, and Daren Dillon. Generating curved deformable

facesheets via free form slumping. In *Society of Photo-Optical Instrumentation Engineers (SPIE) Conference Series*, volume 12188 of *Society of Photo-Optical Instrumentation Engineers (SPIE) Conference Series*, page 121880T, August 2022.

[111] Andrew W. Howard, John Asher Johnson, Geoffrey W. Marcy, Debra A. Fischer, Jason T. Wright, David Bernat, Gregory W. Henry, Kathryn M. G. Peek, Howard Isaacson, Kevin Apps, Michael Endl, William D. Cochran, Jeff A. Valenti, Jay Anderson, and Nikolai E. Piskunov. THE CALIFORNIA PLANET SURVEY. i. FOUR NEW GIANT EXOPLANETS. *The Astrophysical Journal*, 721(2):1467–1481, sep 2010.

[112] Steve B Howell, Charlie Sobeck, Michael Haas, Martin Still, Thomas Barclay, Fergal Mullally, John Troeltzsch, Suzanne Aigrain, Stephen T Bryson, Doug Caldwell, et al. The k2 mission: characterization and early results. *Publications of the Astronomical Society of the Pacific*, 126(938):398, 2014.

[113] E. Huby, M. Bottom, B. Femenia, H. Ngo, D. Mawet, E. Serabyn, and O. Absil. On-sky performance of the QACITS pointing control technique with the Keck-/NIRC2 vortex coronagraph. , 600:A46, April 2017.

[114] E. Huby, M. Bottom, B. Femenia, H. Ngo, D. Mawet, E. Serabyn, and O. Absil. On-sky performance of the QACITS pointing control technique with the Keck-/NIRC2 vortex coronagraph. , 600:A46, April 2017.

[115] S. Hunziker, S. P. Quanz, A. Amara, and M. R. Meyer. PCA-based approach for subtracting thermal background emission in high-contrast imaging data. , 611:A23, March 2018.

[116] T. O. Husser, S. Wende-von Berg, S. Dreizler, D. Homeier, A. Reiners, T. Barman, and P. H. Hauschildt. A new extensive library of PHOENIX stellar atmospheres and synthetic spectra. , 553:A6, May 2013.

[117] Jonathan Irwin, Zachory K. Berta, Christopher J. Burke, David Charbonneau, Philip Nutzman, Andrew A. West, and Emilio E. Falco. On the Angular Momentum Evolution of Fully Convective Stars: Rotation Periods for Field M-dwarfs from the MEarth Transit Survey. , 727(1):56, January 2011.

[118] Markus Janson, Timothy D. Brandt, Amaya Moro-Martín, Tomonori Usuda, Christian Thalmann, Joseph C. Carson, Miwa Goto, Thayne Currie, M. W. McElwain, Yoichi Itoh, Misato Fukagawa, Justin Crepp, Masayuki Kuzuhara, Jun Hashimoto, Tomoyuki Kudo, Nobuhiko Kusakabe, Lyu Abe, Wolfgang Brandner, Sebastian Egner, Markus Feldt, Carol A. Grady, Olivier Guyon, Yutaka Hayano, Masahiro Hayashi, Saeko Hayashi, Thomas Henning, Klaus W. Hodapp, Miki Ishii, Masanori Iye, Ryo Kandori, Gillian R. Knapp, Jungmi Kwon, Taro Matsuo, Shoken Miyama, Jun-Ichi Morino, Tetsuro Nishimura, Tae-Soo Pyo, Eugene Serabyn, Takuya Suenaga, Hiroshi Suto, Ryuji Suzuki, Yasuhiro Takahashi, Michihiro Takami, Naruhisa Takato, Hiroshi Terada, Daego Tomono, Edwin L. Turner,

Makoto Watanabe, John Wisniewski, Toru Yamada, Hideki Takami, and Motohide Tamura. The SEEDS Direct Imaging Survey for Planets and Scattered Dust Emission in Debris Disk Systems. , 773(1):73, August 2013.

[119] Aïssa Jolivet, Gilles Orban de Xivry, Elsa Huby, Pierre Piron, Ernesto Vargas Catalan, Serge Habraken, Jean Surdej, Mikael Karlsson, and Oliver Absil. L- and M-band annular groove phase mask in lab performance assessment on the vortex optical demonstrator for coronagraphic applications. *Journal of Astronomical Telescopes, Instruments, and Systems*, 5:025001, April 2019.

[120] Jens Kammerer, Julien Girard, Aarynn L. Carter, Marshall D. Perrin, Rachel Cooper, Deepashri Thatte, Thomas Vandal, Jarron Leisenring, Jason Wang, William O. Balmer, Anand Sivaramakrishnan, Laurent Pueyo, Kimberly Ward-Duong, Ben Sunnquist, and Jéa. Adams Redai. Performance of near-infrared high-contrast imaging methods with JWST from commissioning. In Laura E. Coyle, Shuji Matsuura, and Marshall D. Perrin, editors, *Space Telescopes and Instrumentation 2022: Optical, Infrared, and Millimeter Wave*, volume 12180 of *Society of Photo-Optical Instrumentation Engineers (SPIE) Conference Series*, page 121803N, August 2022.

[121] Pierre Kervella, Frédéric Arenou, and Frédéric Thévenin. Stellar and substellar companions from Gaia EDR3. Proper-motion anomaly and resolved common proper-motion pairs. , 657:A7, January 2022.

[122] Aurora Y. Kesseli, J. Davy Kirkpatrick, Sergio B. Fajardo-Acosta, Matthew T. Penny, B. Scott Gaudi, Mark Veyette, Patricia C. Boeshaar, Calen B. Henderson, Michael C. Cushing, Sebastiano Calchi-Novati, Y. Shvartzvald, and Philip S. Muirhead. Radii of 88 M Subdwarfs and Updated Radius Relations for Low-metallicity M-dwarf Stars. , 157(2):63, February 2019.

[123] Rocio Kiman, Sarah J. Schmidt, Ruth Angus, Kelle L. Cruz, Jacqueline K. Faherty, and Emily Rice. Exploring the Age-dependent Properties of M and L Dwarfs Using Gaia and SDSS. , 157(6):231, June 2019.

[124] Rocio Kiman, Siyi Xu, Jacqueline K. Faherty, Jonathan Gagné, Ruth Angus, Timothy D. Brandt, Sarah L. Casewell, and Kelle L. Cruz. wdwarfdate: A Python Package to Derive Bayesian Ages of White Dwarfs. , 164(2):62, August 2022.

[125] Rocio Ayelen Kiman. *A Unified Approach to M Dwarf Ages.* PhD thesis, City University of New York, January 2021.

[126] Molly R. Kosiarek, David A. Berardo, Ian J. M. Crossfield, Cesar Laguna, Caroline Piaulet, Joseph M. Akana Murphy, Steve B. Howell, Gregory W. Henry, Howard Isaacson, Benjamin Fulton, Lauren M. Weiss, Erik A. Petigura, Aida Behmard, Lea A. Hirsch, Johanna Teske, Jennifer A. Burt, Sean M. Mills, Ashley Chontos, Teo Močnik, Andrew W. Howard, Michael Werner, John H. Livingston, Jessica Krick, Charles Beichman, Varoujan Gorjian, Laura Kreidberg, Caroline Morley, Jessie L. Christiansen, Farisa Y. Morales, Nicholas J. Scott, Jeffrey D. Crane,

Sharon Xuesong Wang, Stephen A. Shectman, Lee J. Rosenthal, Samuel K. Grunblatt, Ryan A. Rubenzahl, Paul A. Dalba, Steven Giacalone, Chiara Dane Villanueva, Qingtian Liu, Fei Dai, Michelle L. Hill, Malena Rice, Stephen R. Kane, and Andrew W. Mayo. Physical Parameters of the Multiplanet Systems HD 106315 and GJ 9827. , 161(1):47, January 2021.

[127] Stefan Kuiper, Arjo Bos, Jan de Vreugd, Gert Witvoet, Bert Dekker, Fred Kamphues, Geert Slegtenhorst, Wouter Jonker, Matthew Maniscalco, Bruno Femenía-Castella, Miguel Núñez Cagigal, Jonai Bienes Pérez, Juan Cózar-Castellano, Jose Manuel González-Cava, Angel Mato, Alejandro Mahy Soler Trujillo, and Nauzet Vega Reyes. Preliminary design of the Adaptive Secondary Mirror for the European Solar Telescope. In Laura Schreiber, Dirk Schmidt, and Elise Vernet, editors, *Adaptive Optics Systems VIII*, volume 12185 of *Society of Photo-Optical Instrumentation Engineers (SPIE) Conference Series*, page 1218528, August 2022.

[128] Stefan Kuiper, Niek Doelman, Jet Human, Rudolf Saathof, Wimar Klop, and Matthew Maniscalco. Advances of TNO's electromagnetic deformable mirror development. In Ramón Navarro and Roland Geyl, editors, *Advances in Optical and Mechanical Technologies for Telescopes and Instrumentation III*, volume 10706 of *Society of Photo-Optical Instrumentation Engineers (SPIE) Conference Series*, page 1070619, July 2018.

[129] Renate Kupke, R. Deno Stelter, Amirul Hasan, Arun Surya, Isabel Kain, Zackery

Briesemeister, Jialin Li, Phil Hinz, Andrew Skemer, Benjamin Gerard, Daren Dillon, and Christopher Ratliff. SCALES on Keck: optical design. In Christopher J. Evans, Julia J. Bryant, and Kentaro Motohara, editors, *Ground-based and Airborne Instrumentation for Astronomy IX*, volume 12184 of *Society of Photo-Optical Instrumentation Engineers (SPIE) Conference Series*, page 121844A, August 2022.

[130] Masayuki Kuzuhara, Thayne Currie, Takuya Takarada, Timothy D. Brandt, Bun'ei Sato, Taichi Uyama, Markus Janson, Jeffrey Chilcote, Taylor Tobin, Kellen Lawson, Yasunori Hori, Olivier Guyon, Tyler D. Groff, Julien Lozi, Sebastien Vievard, Ananya Sahoo, Vincent Deo, Nemanja Jovanovic, Kyohoon Ahn, Frantz Martinache, Nour Skaf, Eiji Akiyama, Barnaby R. Norris, Mickaël Bonnefoy, Krzysztof G. Hełminiak, Tomoyuki Kudo, Michael W. McElwain, Matthias Samland, Kevin Wagner, John Wisniewski, Gillian R. Knapp, Jungmi Kwon, Jun Nishikawa, Eugene Serabyn, Masahiko Hayashi, and Motohide Tamura. Direct-imaging Discovery and Dynamical Mass of a Substellar Companion Orbiting an Accelerating Hyades Sun-like Star with SCExAO/CHARIS. , 934(2):L18, August 2022.

[131] S. Lacour, J. J. Wang, M. Nowak, L. Pueyo, F. Eisenhauer, A. M. Lagrange, P. Mollière, R. Abuter, A. Amorin, R. Asensio-Torres, M. Bauböck, M. Benisty, J. P. Berger, H. Beust, S. Blunt, A. Boccaletti, A. Bohn, M. Bonnefoy, H. Bonnet, W. Brandner, F. Cantalloube, P. Caselli, B. Charnay, G. Chauvin, E. Choquet, V. Christiaens, Y. Clénet, A. Cridland, P. T. de Zeeuw, R. Dembet, J. Dexter,

A. Drescher, G. Duvert, F. Gao, P. Garcia, R. Garcia Lopez, T. Gardner, E. Gendron, R. Genzel, S. Gillessen, J. H. Girard, X. Haubois, G. Heißel, T. Henning, S. Hinkley, S. Hippler, M. Horrobin, M. Houllé, Z. Hubert, A. Jiménez-Rosales, L. Jocou, J. Kammerer, M. Keppler, P. Kervella, L. Kreidberg, V. Lapeyrère, J. B. Le Bouquin, P. Léna, D. Lutz, A. L. Maire, A. Mérand, J. D. Monnier, D. Mouillet, A. Muller, E. Nasedkin, T. Ott, G. P. P. L. Otten, C. Paladini, T. Paumard, K. Perraut, G. Perrin, O. Pfuhl, J. Rameau, L. Rodet, G. Rodriguez-Coira, G. Rousset, J. Shangguan, T. Shimizu, J. Stadler, O. Straub, C. Straubmeier, E. Sturm, T. Stolker, E. F. van Dishoeck, A. Vigan, F. Vincent, S. D. von Fellenberg, K. Ward-Duong, F. Widmann, E. Wieprecht, E. Wiezorrek, and J. Woillez. The ExoGRAVITY project: using single mode interferometry to characterize exoplanets. In Peter G. Tuthill, Antoine Mérand, and Stephanie Sallum, editors, *Optical and Infrared Interferometry and Imaging VII*, volume 11446 of *Society of Photo-Optical Instrumentation Engineers (SPIE) Conference Series*, page 114460O, December 2020.

[132] M. Lafarga, I. Ribas, A. Reiners, A. Quirrenbach, P. J. Amado, J. A. Caballero, M. Azzaro, V. J. S. Béjar, M. Cortés-Contreras, S. Dreizler, A. P. Hatzes, Th. Henning, S. V. Jeffers, A. Kaminski, M. Kürster, D. Montes, J. C. Morales, M. Oshagh, C. Rodríguez-López, P. Schöfer, A. Schweitzer, and M. Zechmeister. The CARMENES search for exoplanets around M dwarfs. Mapping stellar activity indicators across the M dwarf domain. , 652:A28, August 2021.

[133] David Lafrenière, René Doyon, Christian Marois, Daniel Nadeau, Ben R. Oppenheimer, Patrick F. Roche, François Rigaut, James R. Graham, Ray Jayawardhana, Doug Johnstone, Paul G. Kalas, Bruce Macintosh, and René Racine. The Gemini Deep Planet Survey. , 670(2):1367–1390, December 2007.

[134] Cesar Laguna. Analyzing Variation in Phase Delays Across Phase Plates With a Quadrature Polarization Interferometer. *arXiv e-prints*, page arXiv:2310.07737, October 2023.

[135] M. Lambrechts, A. Johansen, and A. Morbidelli. Separating gas-giant and ice-giant planets by halting pebble accretion. , 572:A35, December 2014.

[136] Arlo U. Landolt. UBVRI Photometric Standard Stars Around the Celestial Equator: Updates and Additions. , 137(5):4186–4269, May 2009.

[137] J. Lannier, P. Delorme, A. M. Lagrange, S. Borgniet, J. Rameau, J. E. Schlieder, J. Gagné, M. A. Bonavita, L. Malo, G. Chauvin, M. Bonnefoy, and J. H. Girard. MASSIVE: A Bayesian analysis of giant planet populations around low-mass stars. , 596:A83, December 2016.

[138] S. K. Leggett, Ben Burningham, D. Saumon, M. S. Marley, S. J. Warren, R. L. Smart, H. R. A. Jones, P. W. Lucas, D. J. Pinfield, and Motohide Tamura. Mid-Infrared Photometry of Cold Brown Dwarfs: Diversity in Age, Mass, and Metallicity. , 710(2):1627–1640, February 2010.

[139] J. F. Lestrade, M. C. Wyatt, F. Bertoldi, W. R. F. Dent, and K. M. Menten. Search for cold debris disks around M-dwarfs. , 460(3):733–741, December 2006.

[140] Yiting Li, Timothy D. Brandt, G. Mirek Brandt, Qier An, Kyle Franson, Trent J. Dupuy, Minghan Chen, Rachel Bowens-Rubin, Briley L. Lewis, Brendan P. Bowler, Aidan Gibbs, Rocio Kiman, Jacqueline Faherty, Thayne Currie, Rebecca Jensen-Clem, Hengyue Zhang, Ezequiel Contreras-Martinez, Michael P. Fitzgerald, Benjamin A. Mazin, and Maxwell Millar-Blanchaer. Surveying nearby brown dwarfs with HGCA: direct imaging discovery of a faint, high-mass brown dwarf orbiting HD 176535 A. , 522(4):5622–5637, July 2023.

[141] Mary Anne Limbach, Andrew Vanderburg, Kevin B. Stevenson, Simon Blouin, Caroline Morley, Jacob Lustig-Yaeger, Melinda Soares-Furtado, and Markus Janson. A new method for finding nearby white dwarfs exoplanets and detecting biosignatures. , 517(2):2622–2638, December 2022.

[142] Mary Anne Limbach, Andrew Vanderburg, Kevin B. Stevenson, Simon Blouin, Caroline Morley, Jacob Lustig-Yaeger, Melinda Soares-Furtado, and Markus Janson. A new method for finding nearby white dwarfs exoplanets and detecting biosignatures. *MNRAS*, 517(2):2622–2638, December 2022.

[143] Mary Anne Limbach, Johanna M. Vos, Joshua N. Winn, René Heller, Jeffrey C. Mason, Adam C. Schneider, and Fei Dai. On the Detection of Exomoons Transiting Isolated Planetary-mass Objects. , 918(2):L25, September 2021.

[144] Chia-Lung Lin, Wen-Ping Chen, Wing-Huen Ip, Dániel Apai, Alex Bixel, Richard Boyle, Jose Perez Chavez, Nestor Espinoza, Aidan Gibbs, Paul Gabor, Thomas Henning, Luigi Mancini, Benjamin V. Rackham, Martin Schlecker, Jeremy Dietrich, Quentin Jay Socia, Miriam Keppler, Asmita Bhandare, and Maximilian Häberle. EDEN: Flare Activity of the Nearby Exoplanet-hosting M Dwarf Wolf 359 Based on K2 and EDEN Light Curves. , 162(1):11, July 2021.

[145] Han-Tang Lin, Wen-Ping Chen, Jinzhong Liu, Xuan Zhang, Yu Zhang, Andrew Wang, Shiang-Yu Wang, Matthew J. Lehner, C. Y. Wen, J. K. Guo, Y. H. Chang, M. H. Chang, Anli Tsai, Chia-Lung Lin, C. Y. Hsu, and Wing Ip. Simultaneous Detection of Optical Flares of the Magnetically Active M-dwarf Wolf359. , 163(4):164, April 2022.

[146] Esther F. Linder, Christoph Mordasini, Paul Mollière, Gabriel-Dominique Marleau, Matej Malik, Sascha P. Quanz, and Michael R. Meyer. Evolutionary models of cold and low-mass planets: cooling curves, magnitudes, and detectability. , 623:A85, March 2019.

[147] Jorge Llop-Sayson, Jason J. Wang, Jean-Baptiste Ruffio, Dimitri Mawet, Sarah Blunt, Olivier Absil, Charlotte Bond, Casey Brinkman, Brendan P. Bowler, Michael Bottom, Ashley Chontos, Paul A. Dalba, B. J. Fulton, Steven Giacalone, Michelle Hill, Lea A. Hirsch, Andrew W. Howard, Howard Isaacson, Mikael Karlsson, Jack Lubin, Alex Madurowicz, Keith Matthews, Evan Morris, Marshall Per-

rin, Bin Ren, Malena Rice, Lee J. Rosenthal, Garreth Ruane, Ryan Rubenzahl, He Sun, Nicole Wallack, Jerry W. Xuan, and Marie Ygouf. Constraining the Orbit and Mass of epsilon Eridani b with Radial Velocities, Hipparcos IAD-Gaia DR2 Astrometry, and Multiepoch Vortex Coronagraphy Upper Limits. , 162(5):181, November 2021.

[148] Gaspare Lo Curto, Christophe Lovis, Tobias Wilken, Gerardo Avila, Bruno Chazelas, Massimiliano Esposito, Theodor W. Hänsch, Jonay Gonzáez-Hernández, Ronald Holzwarth, Gerardo Ihle, Antonio Manescau, Luca Pasquini, Francesco Pepe, Rafael Rebolo, Alex Segovia, Peter Sinclaire, Tilo Steinmetz, Thomas Udem, and François Wildi. Along the path towards extremely precise radial velocity measurements. In Ian S. McLean, Suzanne K. Ramsay, and Hideki Takami, editors, *Ground-based and Airborne Instrumentation for Astronomy III*, volume 7735 of *Society of Photo-Optical Instrumentation Engineers (SPIE) Conference Series*, page 77350Z, July 2010.

[149] Yuxi Lucy Lu, Ruth Angus, Jason L. Curtis, Trevor J. David, and Rocio Kiman. Gyro-kinematic Ages for around 30,000 Kepler Stars. , 161(4):189, April 2021.

[150] K. L. Luhman, K. N. Allers, D. T. Jaffe, M. C. Cushing, K. A. Williams, C. L. Slesnick, and W. D. Vacca. Ophiuchus 1622-2405: Not a Planetary-Mass Binary. , 659(2):1629–1636, April 2007.

[151] Nikku Madhusudhan. Exoplanetary Atmospheres: Key Insights, Challenges, and

Prospects. , 57:617–663, August 2019.

[152] Eric E. Mamajek and Lynne A. Hillenbrand. Improved Age Estimation for Solar-Type Dwarfs Using Activity-Rotation Diagnostics. , 687(2):1264–1293, November 2008.

[153] Andrew W. Mann, Gregory A. Feiden, Eric Gaidos, Tabetha Boyajian, and Kaspar von Braun. How to Constrain Your M Dwarf: Measuring Effective Temperature, Bolometric Luminosity, Mass, and Radius. , 804(1):64, May 2015.

[154] M. S. Marley, C. Gelino, D. Stephens, J. I. Lunine, and R. Freedman. Reflected Spectra and Albedos of Extrasolar Giant Planets. I. Clear and Cloudy Atmospheres. *ApJ*, 513:879–893, March 1999.

[155] Mark Marley, Nikole Lewis, Giada Arney, Vanessa Bailey, Natasha Batalha, Charles Beichman, Björn Benneke, Jasmina Blecic, Kerri Cahoy, Jeffrey Chilcote, Shawn Domagal-Goldman, Courtney Dressing, Michael Fitzgerald, Jonathan Fortney, Richard Freedman, Dawn Gelino, John Gizis, Olivier Guyon, Thomas Greene, Heidi Hammel, Yasuhiro Hasegawa, Nemanja Jovanovic, Quinn Konopacky, Ravi Kopparapu, Michael Liu, Eric Lopez, Jonathan Lunine, Roxana Lupu, Bruce Macintosh, Kathleen Mandt, Christian Marois, Dimitri Mawet, Laura Mayorga, Caroline Morley, Eric Nielsen, Aki Roberge, Eugene Serabyn, Andrew Skemer, Karl Stapelfeldt, Channon Vischer, and Jason Wang. Imaging Cool Giant Planets in Reflected Light: Science Investigations and Synergy with Habitable Planets. ,

51(3):345, May 2019.

[156] Mark Marley, Didier Saumon, Caroline Morley, Jonathan Fortney, Channon Visscher, Richard Freedman, and Roxana Lupu. Sonora Bobcat: cloud-free, substellar atmosphere models, spectra, photometry, evolution, and chemistry, July 2021.

[157] Christian Marois, David Lafrenière, René Doyon, Bruce Macintosh, and Daniel Nadeau. Angular Differential Imaging: A Powerful High-Contrast Imaging Technique. , 641(1):556–564, April 2006.

[158] Dimitri Mawet, Lea Hirsch, Eve J. Lee, Jean-Baptiste Ruffio, Michael Bottom, Benjamin J. Fulton, Olivier Absil, Charles Beichman, Brendan Bowler, Marta Bryan, Elodie Choquet, David Ciardi, Valentin Christiaens, Denis Defrère, Carlos Alberto Gomez Gonzalez, Andrew W. Howard, Elsa Huby, Howard Isaacson, Rebecca Jensen-Clem, Molly Kosiarek, Geoff Marcy, Tiffany Meshkat, Erik Petigura, Maddalena Reggiani, Garreth Ruane, Eugene Serabyn, Evan Sinukoff, Ji Wang, Lauren Weiss, and Marie Ygouf. Deep Exploration of Eridani with Keck Ms-band Vortex Coronagraphy and Radial Velocities: Mass and Orbital Parameters of the Giant Exoplanet. , 157(1):33, January 2019.

[159] M. Mayor, F. Pepe, D. Queloz, F. Bouchy, G. Rupprecht, G. Lo Curto, G. Avila, W. Benz, J. L. Bertaux, X. Bonfils, Th. Dall, H. Dekker, B. Delabre, W. Eckert, M. Fleury, A. Gilliotte, D. Gojak, J. C. Guzman, D. Kohler, J. L. Lizon, A. Longinotti, C. Lovis, D. Megevand, L. Pasquini, J. Reyes, J. P. Sivan, D. Sos-

nowska, R. Soto, S. Udry, A. van Kesteren, L. Weber, and U. Weilenmann. Setting New Standards with HARPS. *The Messenger*, 114:20–24, December 2003.

[160] Michel Mayor and Didier Queloz. A Jupiter-mass companion to a solar-type star. , 378(6555):355–359, November 1995.

[161] Amber A. Medina, Jennifer G. Winters, Jonathan M. Irwin, and David Charbonneau. Galactic Kinematics and Observed Flare Rates of a Volume-complete Sample of Mid-to-late M Dwarfs: Constraints on the History of the Stellar Radiation Environment of Planets Orbiting Low-mass Stars. , 935(2):104, August 2022.

[162] D. Mesa, R. Gratton, P. Kervella, M. Bonavita, S. Desidera, V. D'Orazi, S. Marino, A. Zurlo, and E. Rigliaco. AF Lep b: The lowest-mass planet detected by coupling astrometric and direct imaging data. , 672:A93, April 2023.

[163] Tiffany Meshkat, Dimitri Mawet, Marta L. Bryan, Sasha Hinkley, Brendan P. Bowler, Karl R. Stapelfeldt, Konstantin Batygin, Deborah Padgett, Farisa Y. Morales, Eugene Serabyn, Valentin Christiaens, Timothy D. Brandt, and Zahed Wahhaj. A Direct Imaging Survey of Spitzer-detected Debris Disks: Occurrence of Giant Planets in Dusty Systems. , 154(6):245, December 2017.

[164] Brittany E. Miles, Beth A. Biller, Polychronis Patapis, Kadin Worthen, Emily Rickman, Kielan K. W. Hoch, Andrew Skemer, Marshall D. Perrin, Niall White-

ford, Christine H. Chen, B. Sargent, Sagnick Mukherjee, Caroline V. Morley, Sarah E. Moran, Mickael Bonnefoy, Simon Petrus, Aarynn L. Carter, Elodie Choquet, Sasha Hinkley, Kimberly Ward-Duong, Jarron M. Leisenring, Maxwell A. Millar-Blanchaer, Laurent Pueyo, Shrishmoy Ray, Steph Sallum, Karl R. Stapelfeldt, Jordan M. Stone, Jason J. Wang, Olivier Absil, William O. Balmer, Anthony Boccaletti, Mariangela Bonavita, Mark Booth, Brendan P. Bowler, Gael Chauvin, Valentin Christiaens, Thayne Currie, Camilla Danielski, Jonathan J. Fortney, Julien H. Girard, Carol A. Grady, Alexandra Z. Greenbaum, Thomas Henning, Dean C. Hines, Markus Janson, Paul Kalas, Jens Kammerer, Grant M. Kennedy, Matthew A. Kenworthy, Pierre Kervella, Pierre-Olivier Lagage, Ben W. P. Lew, Michael C. Liu, Bruce Macintosh, Sebastian Marino, Mark S. Marley, Christian Marois, Elisabeth C. Matthews, Brenda C. Matthews, Dimitri Mawet, Michael W. McElwain, Stanimir Metchev, Michael R. Meyer, Paul Molliere, Eric Pantin, Andreas Quirrenbach, Isabel Rebollido, Bin B. Ren, Glenn Schneider, Malavika Vasist, Mark C. Wyatt, Yifan Zhou, Zackery W. Briesemeister, Marta L. Bryan, Per Calissendorff, Faustine Cantalloube, Gabriele Cugno, Matthew De Furio, Trent J. Dupuy, Samuel M. Factor, Jacqueline K. Faherty, Michael P. Fitzgerald, Kyle Franson, Eileen C. Gonzales, Callie E. Hood, Alex R. Howe, Adam L. Kraus, Masayuki Kuzuhara, Anne-Marie Lagrange, Kellen Lawson, Cecilia Lazzoni, Pengyu Liu, Jorge Llop-Sayson, James P. Lloyd, Raquel A. Martinez, Johan Mazoyer, Sascha P. Quanz, Jea Adams Redai, Matthias Samland, Joshua E. Schlieder, Motohide Tamura, Xianyu Tan, Taichi Uyama, Arthur Vi-

gan, Johanna M. Vos, Kevin Wagner, Schuyler G. Wolff, Marie Ygouf, Xi Zhang, Keming Zhang, and Zhoujian Zhang. The JWST Early-release Science Program for Direct Observations of Exoplanetary Systems II: A 1 to 20 μm Spectrum of the Planetary-mass Companion VHS 1256-1257 b. , 946(1):L6, March 2023.

[165] Julien Milli, Dimitri Mawet, David Mouillet, Markus Kasper, and Julien H. Girard. Adaptive Optics in High-Contrast Imaging. In Henri M. J. Boffin, Gaitee Hussain, Jean-Philippe Berger, and Linda Schmidtobreick, editors, *Astronomy at High Angular Resolution*, volume 439 of *Astrophysics and Space Science Library*, page 17, January 2016.

[166] P. Mollière, T. Stolker, S. Lacour, G. P. P. L. Otten, J. Shangguan, B. Charnay, T. Molyarova, M. Nowak, Th. Henning, G. D. Marleau, D. A. Semenov, E. van Dishoeck, F. Eisenhauer, P. Garcia, R. Garcia Lopez, J. H. Girard, A. Z. Greenbaum, S. Hinkley, P. Kervella, L. Kreidberg, A. L. Maire, E. Nasedkin, L. Pueyo, I. A. G. Snellen, A. Vigan, J. Wang, P. T. de Zeeuw, and A. Zurlo. Retrieving scattering clouds and disequilibrium chemistry in the atmosphere of HR 8799e. , 640:A131, August 2020.

[167] Paul Mollière, Tamara Molyarova, Bertram Bitsch, Thomas Henning, Aaron Schneider, Laura Kreidberg, Christian Eistrup, Remo Burn, Evert Nasedkin, Dmitry Semenov, Christoph Mordasini, Martin Schlecker, Kamber R. Schwarz, Sylvestre Lacour, Mathias Nowak, and Matthäus Schulik. Interpreting the Atmo-

spheric Composition of Exoplanets: Sensitivity to Planet Formation Assumptions. , 934(1):74, July 2022.

[168] C. V. Morley, J. J. Fortney, M. S. Marley, C. Visscher, D. Saumon, and S. K. Leggett. Neglected Clouds in T and Y Dwarf Atmospheres. *ApJ*, 756:172, September 2012.

[169] C. V. Morley, M. S. Marley, J. J. Fortney, R. Lupu, D. Saumon, T. Greene, and K. Lodders. Water Clouds in Y Dwarfs and Exoplanets. *ApJ*, 787:78, May 2014.

[170] Caroline V. Morley, Andrew J. Skemer, Katelyn N. Allers, Mark. S. Marley, Jacqueline K. Faherty, Channon Visscher, Samuel A. Beiler, Brittany E. Miles, Roxana Lupu, Richard S. Freedman, Jonathan J. Fortney, Thomas R. Geballe, and Gordon L. Bjoraker. An L Band Spectrum of the Coldest Brown Dwarf. , 858(2):97, May 2018.

[171] Katie M. Morzinski, Laird M. Close, Jared R. Males, Phil M. Hinz, Simone Esposito, Armando Riccardi, Runa Briguglio, Katherine B. Follette, Enrico Pinna, Alfio Puglisi, Jennifer Vezilj, Marco Xompero, and Ya-Lin Wu. MagAO: status and science. In Enrico Marchetti, Laird M. Close, and Jean-Pierre Véran, editors, *Adaptive Optics Systems V*, volume 9909 of *Society of Photo-Optical Instrumentation Engineers (SPIE) Conference Series*, page 990901, July 2016.

[172] Sagnick Mukherjee, Natasha E. Batalha, Jonathan J. Fortney, and Mark S. Marley.

PICASO 3.0: A One-dimensional Climate Model for Giant Planets and Brown Dwarfs. , 942(2):71, January 2023.

[173] Gijs D. Mulders, Fred J. Ciesla, Michiel Min, and Ilaria Pascucci. The Snow Line in Viscous Disks around Low-mass Stars: Implications for Water Delivery to Terrestrial Planets in the Habitable Zone. , 807(1):9, July 2015.

[174] A. Müller, M. Keppler, Th. Henning, M. Samland, G. Chauvin, H. Beust, A. L. Maire, K. Molaverdikhani, R. van Boekel, M. Benisty, A. Boccaletti, M. Bonnefoy, F. Cantalloube, B. Charnay, J. L. Baudino, M. Gennaro, Z. C. Long, A. Cheetham, S. Desidera, M. Feldt, T. Fusco, J. Girard, R. Gratton, J. Hagelberg, M. Janson, A. M. Lagrange, M. Langlois, C. Lazzoni, R. Ligi, F. Ménard, D. Mesa, M. Meyer, P. Mollière, C. Mordasini, T. Moulin, A. Pavlov, N. Pawellek, S. P. Quanz, J. Ramos, D. Rouan, E. Sissa, E. Stadler, A. Vigan, Z. Wahhaj, L. Weber, and A. Zurlo. Orbital and atmospheric characterization of the planet within the gap of the PDS 70 transition disk. , 617:L2, September 2018.

[175] Marie-Eve Naud, Étienne Artigau, René Doyon, Lison Malo, Jonathan Gagné, David Lafrenière, Christian Wolf, and Eugene A. Magnier. PSYM-WIDE: A Survey for Large-separation Planetary-mass Companions to Late Spectral Type Members of Young Moving Groups. , 154(3):129, September 2017.

[176] Elisabeth R. Newton, Jonathan Irwin, David Charbonneau, Perry Berlind, Michael L. Calkins, and Jessica Mink. The Hα Emission of Nearby M Dwarfs

and its Relation to Stellar Rotation. , 834(1):85, January 2017.

[177] Elisabeth R. Newton, Nicholas Mondrik, Jonathan Irwin, Jennifer G. Winters, and David Charbonneau. New Rotation Period Measurements for M Dwarfs in the Southern Hemisphere: An Abundance of Slowly Rotating, Fully Convective Stars. , 156(5):217, November 2018.

[178] John Niclasen. The lapse rate atmospheric model. 07 2015.

[179] Eric L. Nielsen, Michael C. Liu, Zahed Wahhaj, Beth A. Biller, Thomas L. Hayward, Laird M. Close, Jared R. Males, Andrew J. Skemer, Mark Chun, Christ Ftaclas, Silvia H. P. Alencar, Pawel Artymowicz, Alan Boss, Fraser Clarke, Elisabete de Gouveia Dal Pino, Jane Gregorio-Hetem, Markus Hartung, Shigeru Ida, Marc Kuchner, Douglas N. C. Lin, I. Neill Reid, Evgenya L. Shkolnik, Matthias Tecza, Niranjan Thatte, and Douglas W. Toomey. The Gemini NICI Planet-Finding Campaign: The Frequency of Giant Planets around Young B and A Stars. , 776(1):4, October 2013.

[180] Emily K. Pass, David Charbonneau, Jonathan M. Irwin, and Jennifer G. Winters. Constraints on the Spindown of Fully Convective M Dwarfs Using Wide Field Binaries. , 936(2):109, September 2022.

[181] V. M. Passegger, A. Schweitzer, D. Shulyak, E. Nagel, P. H. Hauschildt, A. Reiners, P. J. Amado, J. A. Caballero, M. Cortés-Contreras, A. J. Domínguez-Fernández,

A. Quirrenbach, I. Ribas, M. Azzaro, G. Anglada-Escudé, F. F. Bauer, V. J. S. Béjar, S. Dreizler, E. W. Guenther, T. Henning, S. V. Jeffers, A. Kaminski, M. Kürster, M. Lafarga, E. L. Martín, D. Montes, J. C. Morales, J. H. M. M. Schmitt, and M. Zechmeister. The CARMENES search for exoplanets around M dwarfs. Photospheric parameters of target stars from high-resolution spectroscopy. II. Simultaneous multiwavelength range modeling of activity insensitive lines. , 627:A161, July 2019.

[182] Ya. V. Pavlenko, H. R. A. Jones, Yu. Lyubchik, J. Tennyson, and D. J. Pinfield. Spectral energy distribution for GJ406. , 447(2):709–717, February 2006.

[183] Logan Pearce and Rachel Bowens-Rubin. Exoplanet occurrence rates plot, August 2023.

[184] F. Pepe, M. Mayor, G. Rupprecht, G. Avila, P. Ballester, J. L. Beckers, W. Benz, J. L. Bertaux, F. Bouchy, B. Buzzoni, C. Cavadore, S. Deiries, H. Dekker, B. Delabre, S. D'Odorico, W. Eckert, J. Fischer, M. Fleury, M. George, A. Gilliotte, D. Gojak, J. C. Guzman, F. Koch, D. Kohler, H. Kotzlowski, D. Lacroix, J. Le Merrer, J. L. Lizon, G. Lo Curto, A. Longinotti, D. Megevand, L. Pasquini, P. Petitpas, M. Pichard, D. Queloz, J. Reyes, P. Richaud, J. P. Sivan, D. Sosnowska, R. Soto, S. Udry, E. Ureta, A. van Kesteren, L. Weber, U. Weilenmann, A. Wicenec, G. Wieland, J. Christensen-Dalsgaard, D. Dravins, A. Hatzes, M. Kürster, F. Paresce, and A. Penny. HARPS: ESO's coming planet searcher.

Chasing exoplanets with the La Silla 3.6-m telescope. *The Messenger*, 110:9–14, December 2002.

[185] Marshall D. Perrin, Laurent Pueyo, Kyle Van Gorkom, Keira Brooks, Abhijith Rajan, Julien Girard, and Charles-Philippe Lajoie. Updated optical modeling of JWST coronagraph performance contrast, stability, and strategies. In Makenzie Lystrup, Howard A. MacEwen, Giovanni G. Fazio, Natalie Batalha, Nicholas Siegler, and Edward C. Tong, editors, *Space Telescopes and Instrumentation 2018: Optical, Infrared, and Millimeter Wave*, volume 10698 of *Society of Photo-Optical Instrumentation Engineers (SPIE) Conference Series*, page 1069809, August 2018.

[186] Michael Perryman, Joel Hartman, Gáspár Á. Bakos, and Lennart Lindegren. Astrometric Exoplanet Detection with Gaia. , 797(1):14, December 2014.

[187] M. W. Phillips, P. Tremblin, I. Baraffe, G. Chabrier, N. F. Allard, F. Spiegelman, J. M. Goyal, B. Drummond, and E. Hébrard. A new set of atmosphere and evolution models for cool T-Y brown dwarfs and giant exoplanets. , 637:A38, May 2020.

[188] J. Sebastian Pineda, Allison Youngblood, and Kevin France. The M-dwarf Ultraviolet Spectroscopic Sample. I. Determining Stellar Parameters for Field Stars. , 918(1):40, September 2021.

[189] R. Poleski, J. Skowron, P. Mróz, A. Udalski, M. K. Szymański, P. Pietrukowicz,

K. Ulaczyk, K. Rybicki, P. Iwanek, M. Wrona, and M. Gromadzki. Wide-Orbit Exoplanets are Common. Analysis of Nearly 20 Years of OGLE Microlensing Survey Data. , 71(1):1–23, March 2021.

[190] Mark Popinchalk, Jacqueline K. Faherty, Rocio Kiman, Jonathan Gagné, Jason L. Curtis, Ruth Angus, Kelle L. Cruz, and Emily L. Rice. Evaluating Rotation Periods of M Dwarfs across the Ages. , 916(2):77, August 2021.

[191] Mark Popinchalk, Jacqueline K. Faherty, Rocio Kiman, Jonathan Gagné, Jason L. Curtis, Ruth Angus, Kelle L. Cruz, and Emily L. Rice. Evaluating Rotation Periods of M Dwarfs across the Ages. , 916(2):77, August 2021.

[192] E. H. Por, S. Y. Haffert, V. M. Radhakrishnan, D. S. Doelman, M. Van Kooten, and S. P. Bos. High Contrast Imaging for Python (HCIPy): an open-source adaptive optics and coronagraph simulator. In *Adaptive Optics Systems VI*, volume 10703 of *Proc. SPIE*, 2018.

[193] Emiel H. Por, Sebastiaan Y. Haffert, Vikram M. Radhakrishnan, David S. Doelman, Maaike van Kooten, and Steven P. Bos. High Contrast Imaging for Python (HCIPy): an open-source adaptive optics and coronagraph simulator. In Laird M. Close, Laura Schreiber, and Dirk Schmidt, editors, *Adaptive Optics Systems VI*, volume 10703 of *Society of Photo-Optical Instrumentation Engineers (SPIE) Conference Series*, page 1070342, July 2018.

[194] A. Quirrenbach, P. J. Amado, J. A. Caballero, R. Mundt, A. Reiners, I. Ribas, W. Seifert, M. Abril, J. Aceituno, F. J. Alonso-Floriano, H. Anwand-Heerwart, M. Azzaro, F. Bauer, D. Barrado, S. Becerril, V. J. S. Bejar, D. Benitez, Z. M. Berdinas, M. Brinkmöller, M. C. Cardenas, E. Casal, A. Claret, J. Colomé, M. Cortes-Contreras, S. Czesla, M. Doellinger, S. Dreizler, C. Feiz, M. Fernandez, I. M. Ferro, B. Fuhrmeister, D. Galadi, I. Gallardo, M. C. Gálvez-Ortiz, A. Garcia-Piquer, R. Garrido, L. Gesa, V. Gómez Galera, J. I. González Hernández, R. Gonzalez Peinado, U. Grözinger, J. Guàrdia, E. W. Guenther, E. de Guindos, H. J. Hagen, A. P. Hatzes, P. H. Hauschildt, J. Helmling, T. Henning, D. Hermann, R. Hernández Arabi, L. Hernández Castaño, F. Hernández Hernando, E. Herrero, A. Huber, K. F. Huber, P. Huke, S. V. Jeffers, E. de Juan, A. Kaminski, M. Kehr, M. Kim, R. Klein, J. Klüter, M. Kürster, M. Lafarga, L. M. Lara, A. Lamert, W. Laun, R. Launhardt, U. Lemke, R. Lenzen, M. Llamas, M. Lopez del Fresno, M. López-Puertas, J. López-Santiago, J. F. Lopez Salas, H. Magan Madinabeitia, U. Mall, H. Mandel, L. Mancini, J. A. Marin Molina, D. Maroto Fernández, E. L. Martín, S. Martín-Ruiz, C. Marvin, R. J. Mathar, E. Mirabet, D. Montes, J. C. Morales, R. Morales Muñoz, E. Nagel, V. Naranjo, G. Nowak, E. Palle, J. Panduro, V. M. Passegger, A. Pavlov, S. Pedraz, E. Perez, D. Pérez-Medialdea, M. Perger, M. Pluto, A. Ramón, R. Rebolo, P. Redondo, S. Reffert, S. Reinhart, P. Rhode, H. W. Rix, F. Rodler, E. Rodríguez, C. Rodríguez López, R. R. Rohloff, A. Rosich, M. A. Sanchez Carrasco, J. Sanz-Forcada, P. Sarkis, L. F. Sarmiento, S. Schäfer, J. Schiller, C. Schmidt, J. H. M. M. Schmitt, P. Schöfer, A. Schweitzer, D. Shulyak,

E. Solano, O. Stahl, C. Storz, H. M. Tabernero, M. Tala, L. Tal-Or, R. G. Ulbrich, G. Veredas, J. I. Vico Linares, F. Vilardell, K. Wagner, J. Winkler, M. R. Zapatero Osorio, M. Zechmeister, M. Ammler-von Eiff, G. Anglada-Escudé, C. del Burgo, M. L. Garcia-Vargas, A. Klutsch, J. L. Lizon, M. Lopez-Morales, A. Ofir, A. Pérez-Calpena, M. A. C. Perryman, E. Sánchez-Blanco, J. B. P. Strachan, J. Stürmer, J. C. Suárez, T. Trifonov, S. M. Tulloch, and W. Xu. CARMENES: an overview six months after first light. In Christopher J. Evans, Luc Simard, and Hideki Takami, editors, *Ground-based and Airborne Instrumentation for Astronomy VI*, volume 9908 of *Society of Photo-Optical Instrumentation Engineers (SPIE) Conference Series*, page 990812, August 2016.

[195] Abhijith Rajan, Travis Barman, Rémi Soummer, J. Brendan Hagan, Jennifer Patience, Laurent Pueyo, Élodie Choquet, Quinn Konopacky, Bruce Macintosh, and Christian Marois. Characterizing the Atmospheres of the HR8799 Planets with HST/WFC3. , 809(2):L33, August 2015.

[196] Abhijith Rajan, Julien Rameau, Robert J. De Rosa, Mark S. Marley, James R. Graham, Bruce Macintosh, Christian Marois, Caroline Morley, Jennifer Patience, Laurent Pueyo, Didier Saumon, Kimberly Ward-Duong, S. Mark Ammons, Pauline Arriaga, Vanessa P. Bailey, Travis Barman, Joanna Bulger, Adam S. Burrows, Jeffrey Chilcote, Tara Cotten, Ian Czekala, Rene Doyon, Gaspard Duchêne, Thomas M. Esposito, Michael P. Fitzgerald, Katherine B. Follette, Jonathan J. Fortney, Stephen J. Goodsell, Alexandra Z. Greenbaum, Pascale Hibon, Li-Wei

Hung, Patrick Ingraham, Mara Johnson-Groh, Paul Kalas, Quinn Konopacky, David Lafrenière, James E. Larkin, Jérôme Maire, Franck Marchis, Stanimir Metchev, Maxwell A. Millar-Blanchaer, Katie M. Morzinski, Eric L. Nielsen, Rebecca Oppenheimer, David Palmer, Rahul I. Patel, Marshall Perrin, Lisa Poyneer, Fredrik T. Rantakyrö, Jean-Baptiste Ruffio, Dmitry Savransky, Adam C. Schneider, Anand Sivaramakrishnan, Inseok Song, Rémi Soummer, Sandrine Thomas, Gautam Vasisht, J. Kent Wallace, Jason J. Wang, Sloane Wiktorowicz, and Schuyler Wolff. Characterizing 51 Eri b from 1 to 5 μm: A Partly Cloudy Exoplanet. , 154(1):10, July 2017.

[197] J. Rameau, G. Chauvin, A. M. Lagrange, H. Klahr, M. Bonnefoy, C. Mordasini, M. Bonavita, S. Desidera, C. Dumas, and J. H. Girard. A survey of young, nearby, and dusty stars conducted to understand the formation of wide-orbit giant planets. VLT/NaCo adaptive optics thermal and angular differential imaging. , 553:A60, May 2013.

[198] Heike Rauer, Michel Blanc, Julia Venturini, Véronique Dehant, Brice Demory, Caroline Dorn, Shawn Domagal-Goldman, Bernard Foing, B. Scott Gaudi, Ravit Helled, Kevin Heng, Daniel Kitzman, Eiichiro Kokubo, Louis Le Sergeant d'Hendecourt, Christoph Mordasini, David Nesvorny, Lena Noack, Merav Opher, James Owen, Chris Paranicas, Sascha Quanz, Liping Qin, Ignas Snellen, Leonardo Testi, Stéphane Udry, Joachim Wambsganss, Frances Westall, Philippe Zarka, and Qiugang Zong. Solar System/Exoplanet Science Synergies in a multidecadal per-

spective. In *Planetary Exploration Horizon 2061. Edited by Michel Blano et al. ISBN: 978-0-323-90226-7. Elsevier*, pages 17–64. 2023.

[199] Shrishmoy Ray, Steph Sallum, Sasha Hinkley, Anand Sivamarakrishnan, Rachel Cooper, Jens Kammerer, Alexandra Z. Greebaum, Deepashri Thatte, Cecilia Lazzoni, Andrei Tokovinin, Matthew de Furio, Samuel Factor, Michael Meyer, Jordan M. Stone, Aarynn Carter, Beth Biller, Andrew Skemer, Genaro Suarez, Jarron M. Leisenring, Marshall D. Perrin, Adam L. Kraus, Olivier Absil, William O. Balmer, Mickael Bonnefoy, Marta L. Bryan, Sarah K. Betti, Anthony Boccaletti, Mariangela Bonavita, Mark Booth, Brendan P. Bowler, Zackery W. Briesemeister, Faustine Cantalloube, Gael Chauvin, Valentin Christiaens, Gabriele Cugno, Thayne Currie, Camilla Danielski, Trent J. Dupuy, Jacqueline K. Faherty, Christine H. Chen, Per Calissendorff, Elodie Choquet, Michael P. Fitzgerald, Jonathan J. Fortney, Kyle Franson, Julien H. Girard, Carol A. Grady, Eileen C. Gonzales, Thomas Henning, Dean C. Hines, Kielan K. W. Hoch, Callie E. Hood, Alex R. Howe, Markus Janson, Paul Kalas, Grant M. Kennedy, Matthew A. Kenworthy, Pierre Kervella, Daniel Kitzmann, Masayuki Kuzuhara, Anne-Marie Lagrange, Pierre-Olivier Lagage, Kellen Lawson, Ben W. P. Lew, Michael C. Liu, Pengyu Liu, Jorge Llop-Sayson, James P. Lloyd, Anna Lueber, Bruce Macintosh, Elena Manjavacas, Sebastian Marino, Mark S. Marley, Christian Marois, Raquel A. Martinez, Brenda C. Matthews, Elisabeth C. Matthews, Dimitri Mawet, Johan Mazoyer, Michael W. McElwain, Stanimir Metchev, Brittany E. Miles,

Maxwell A. Millar-Blanchaer, Paul Molliere, Sarah E. Moran, Caroline V. Morley, Sagnick Mukherjee, Paulina Palma-Bifani, Eric Pantin, Polychronis Patapis, Simon Petrus, Laurent Pueyo, Sascha P. Quanz, Andreas Quirrenbach, Isabel Rebollido, Jea Adams Redai, Bin B. Ren, Emily Rickman, Matthias Samland, B. A. Sargent, Joshua E. Schlieder, Glenn Schneider, Karl R. Stapelfeldt, Ben J. Sutlieff, Motohide Tamura, Xianyu Tan, Christopher A. Theissen, Taichi Uyama, Arthur Vigan, Malavika Vasist, Johanna M. Vos, Kevin Wagner, Jason J. Wang, Kimberly Ward-Duong, Niall Whiteford, Schuyler G. Wolff, Kadin Worthen, Mark C. Wyatt, Marie Ygouf, Xi Zhang, Keming Zhang, Zhoujian Zhang, and Yifan Zhou. The {JWST} Early Release Science Program for Direct Observations of Exoplanetary Systems III: Aperture Masking Interferometric Observations of the star HIP\,65426 at **3.8 μm**. *arXiv e-prints*, page arXiv:2310.11508, October 2023.

[200] A. Reiners, M. Zechmeister, J. A. Caballero, I. Ribas, J. C. Morales, S. V. Jeffers, P. Schöfer, L. Tal-Or, A. Quirrenbach, P. J. Amado, A. Kaminski, W. Seifert, M. Abril, J. Aceituno, F. J. Alonso-Floriano, M. Ammler-von Eiff, R. Antona, G. Anglada-Escudé, H. Anwand-Heerwart, B. Arroyo-Torres, M. Azzaro, D. Baroch, D. Barrado, F. F. Bauer, S. Becerril, V. J. S. Béjar, D. Benítez, Z. M. Berdinas, G. Bergond, M. Blümcke, M. Brinkmöller, C. del Burgo, J. Cano, M. C. Cárdenas Vázquez, E. Casal, C. Cifuentes, A. Claret, J. Colomé, M. Cortés-Contreras, S. Czesla, E. Díez-Alonso, S. Dreizler, C. Feiz, M. Fernández, I. M. Ferro, B. Fuhrmeister, D. Galadí-Enríquez, A. Garcia-Piquer, M. L. García Var-

gas, L. Gesa, V. Gómez Galera, J. I. González Hernández, R. González-Peinado, U. Grözinger, S. Grohnert, J. Guàrdia, E. W. Guenther, A. Guijarro, E. de Guindos, J. Gutiérrez-Soto, H. J. Hagen, A. P. Hatzes, P. H. Hauschildt, R. P. Hedrosa, J. Helmling, Th. Henning, I. Hermelo, R. Hernández Arabí, L. Hernández Castaño, F. Hernández Hernando, E. Herrero, A. Huber, P. Huke, E. N. Johnson, E. de Juan, M. Kim, R. Klein, J. Klüter, A. Klutsch, M. Kürster, M. Lafarga, A. Lamert, M. Lampón, L. M. Lara, W. Laun, U. Lemke, R. Lenzen, R. Launhardt, M. López del Fresno, J. López-González, M. López-Puertas, J. F. López Salas, J. López-Santiago, R. Luque, H. Magán Madinabeitia, U. Mall, L. Mancini, H. Mandel, E. Marfil, J. A. Marín Molina, D. Maroto Fernández, E. L. Martín, S. Martín-Ruiz, C. J. Marvin, R. J. Mathar, E. Mirabet, D. Montes, M. E. Moreno-Raya, A. Moya, R. Mundt, E. Nagel, V. Naranjo, L. Nortmann, G. Nowak, A. Ofir, R. Oreiro, E. Pallé, J. Panduro, J. Pascual, V. M. Passegger, A. Pavlov, S. Pedraz, A. Pérez-Calpena, D. Pérez Medialdea, M. Perger, M. A. C. Perryman, M. Pluto, O. Rabaza, A. Ramón, R. Rebolo, P. Redondo, S. Reffert, S. Reinhart, P. Rhode, H. W. Rix, F. Rodler, E. Rodríguez, C. Rodríguez-López, A. Rodríguez Trinidad, R. R. Rohloff, A. Rosich, S. Sadegi, E. Sánchez-Blanco, M. A. Sánchez Carrasco, A. Sánchez-López, J. Sanz-Forcada, P. Sarkis, L. F. Sarmiento, S. Schäfer, J. H. M. M. Schmitt, J. Schiller, A. Schweitzer, E. Solano, O. Stahl, J. B. P. Strachan, J. Stürmer, J. C. Suárez, H. M. Tabernero, M. Tala, T. Trifonov, S. M. Tulloch, R. G. Ulbrich, G. Veredas, J. I. Vico Linares, F. Vilardell, K. Wagner, J. Winkler, V. Wolthoff, W. Xu, F. Yan, and M. R. Zapatero Osorio.

The CARMENES search for exoplanets around M dwarfs. High-resolution optical and near-infrared spectroscopy of 324 survey stars. , 612:A49, April 2018.

[201] Bin Ren, Laurent Pueyo, Guangtun Ben Zhu, John Debes, and Gaspard Duchêne. Non-negative Matrix Factorization: Robust Extraction of Extended Structures. , 852(2):104, January 2018.

[202] I. Ribas, A. Reiners, M. Zechmeister, J. A. Caballero, J. C. Morales, S. Sabotta, D. Baroch, P. J. Amado, A. Quirrenbach, M. Abril, J. Aceituno, G. Anglada-Escudé, M. Azzaro, D. Barrado, V. J. S. Béjar, D. Benítez de Haro, G. Bergond, P. Bluhm, R. Calvo Ortega, C. Cardona Guillén, P. Chaturvedi, C. Cifuentes, J. Colomé, D. Cont, M. Cortés-Contreras, S. Czesla, E. Díez-Alonso, S. Dreizler, C. Duque-Arribas, N. Espinoza, M. Fernández, B. Fuhrmeister, D. Galadí-Enríquez, A. García-López, E. González-Álvarez, J. I. González Hernández, E. W. Guenther, E. de Guindos, A. P. Hatzes, Th. Henning, E. Herrero, D. Hintz, Á. L. Huelmo, S. V. Jeffers, E. N. Johnson, E. de Juan, A. Kaminski, J. Kemmer, J. Khaimova, S. Khalafinejad, D. Kossakowski, M. Kürster, F. Labarga, M. Lafarga, S. Lalitha, M. Lampón, J. Lillo-Box, N. Lodieu, M. J. López González, M. López-Puertas, R. Luque, H. Magán, L. Mancini, E. Marfil, E. L. Martín, S. Martín-Ruiz, K. Molaverdikhani, D. Montes, E. Nagel, L. Nortmann, G. Nowak, E. Pallé, V. M. Passegger, A. Pavlov, S. Pedraz, V. Perdelwitz, M. Perger, A. Ramón-Ballesta, S. Reffert, D. Revilla, E. Rodríguez, C. Rodríguez-López, S. Sadegi, M. Á. Sánchez Carrasco, A. Sánchez-López, J. Sanz-Forcada, S. Schäfer,

M. Schlecker, J. H. M. M. Schmitt, P. Schöfer, A. Schweitzer, W. Seifert, Y. Shan, S. L. Skrzypinski, E. Solano, O. Stahl, M. Stangret, S. Stock, J. Stürmer, H. M. Tabernero, L. Tal-Or, T. Trifonov, S. Vanaverbeke, F. Yan, and M. R. Zapatero Osorio. The CARMENES search for exoplanets around M dwarfs. Guaranteed time observations Data Release 1 (2016-2020). *arXiv e-prints*, page arXiv:2302.10528, February 2023.

[203] Armando Riccardi, Guido Brusa, Ciro Del Vecchio, Roberto Baisi, M. Andrighettoni, Daneile Gallieni, F. Zocchi, Michael Lloyd-Hart, Hubert M. Martin, and François Wildi. The adaptive secondary mirror for the 6.5 conversion of the Multiple Mirror Telescope. In *European Southern Observatory Conference and Workshop Proceedings*, volume 58 of *European Southern Observatory Conference and Workshop Proceedings*, page 55, January 2002.

[204] Armando Riccardi, Guido Brusa, Piero Salinari, Daniele Gallieni, Roberto Biasi, Mario Andrighettoni, and Hubert M. Martin. Adaptive secondary mirrors for the Large Binocular Telescope. In Peter L. Wizinowich and Domenico Bonaccini, editors, *Adaptive Optical System Technologies II*, volume 4839 of *Society of Photo-Optical Instrumentation Engineers (SPIE) Conference Series*, pages 721–732, February 2003.

[205] E. L. Rickman, D. Ségransan, M. Marmier, S. Udry, F. Bouchy, C. Lovis, M. Mayor, F. Pepe, D. Queloz, N. C. Santos, R. Allart, V. Bonvin, P. Bratschi,

F. Cersullo, B. Chazelas, A. Choplin, U. Conod, A. Deline, J. B. Delisle, L. A. Dos Santos, P. Figueira, H. A. C. Giles, M. Girard, B. Lavie, D. Martin, F. Motalebi, L. D. Nielsen, H. Osborn, G. Ottoni, M. Raimbault, J. Rey, T. Roger, J. V. Seidel, M. Stalport, A. Suárez Mascareño, A. Triaud, O. Turner, L. Weber, and A. Wyttenbach. The CORALIE survey for southern extrasolar planets. XVIII. Three new massive planets and two low-mass brown dwarfs at greater than 5 AU separation. , 625:A71, May 2019.

[206] Marcia J. Rieke, Douglas M. Kelly, Karl Misselt, John Stansberry, Martha Boyer, Thomas Beatty, Eiichi Egami, Michael Florian, Thomas P. Greene, Kevin Hainline, Jarron Leisenring, Thomas Roellig, Everett Schlawin, Fengwu Sun, Lee Tinnin, Christina C. Williams, Christopher N. A. Willmer, Debra Wilson, Charles R. Clark, Scott Rohrbach, Brian Brooks, Alicia Canipe, Matteo Correnti, Audrey DiFelice, Mario Gennaro, Julian Girard, George Hartig, Bryan Hilbert, Anton M. Koekemoer, Nikolay K. Nikolov, Norbert Pirzkal, Armin Rest, Massimo Robberto, Ben Sunnquist, Randal Telfer, Chi Rai Wu, Malcolm Ferry, Dan Lewis, Stefi Baum, Charles Beichman, René Doyon, Alan Dressler, Daniel J. Eisenstein, Laura Ferrarese, Klaus Hodapp, Scott Horner, Daniel T. Jaffe, Doug Johnstone, John Krist, Peter Martin, Donald W. McCarthy, Michael Meyer, George H. Rieke, John Trauger, and Erick T. Young. Performance of NIRCam on JWST in Flight. , 135(1044):028001, February 2023.

[207] Maxime Rochette, Ermanno F. Borra, Jean-Philippe Déry, and Anna M. Ritcey.

Dynamic response of ferrofluidic deformable mirrors using elastomer membrane and overdrive techniques. *International Journal of Optomechatronics*, 12(1):20–30, January 2018.

[208] Lee J. Rosenthal, Benjamin J. Fulton, Lea A. Hirsch, Howard T. Isaacson, Andrew W. Howard, Cayla M. Dedrick, Ilya A. Sherstyuk, Sarah C. Blunt, Erik A. Petigura, Heather A. Knutson, Aida Behmard, Ashley Chontos, Justin R. Crepp, Ian J. M. Crossfield, Paul A. Dalba, Debra A. Fischer, Gregory W. Henry, Stephen R. Kane, Molly Kosiarek, Geoffrey W. Marcy, Ryan A. Rubenzahl, Lauren M. Weiss, and Jason T. Wright. The California Legacy Survey. I. A Catalog of 178 Planets from Precision Radial Velocity Monitoring of 719 Nearby Stars over Three Decades. , 255(1):8, July 2021.

[209] Lee J. Rosenthal, Benjamin J. Fulton, Lea A. Hirsch, Howard T. Isaacson, Andrew W. Howard, Cayla M. Dedrick, Ilya A. Sherstyuk, Sarah C. Blunt, Erik A. Petigura, Heather A. Knutson, Aida Behmard, Ashley Chontos, Justin R. Crepp, Ian J. M. Crossfield, Paul A. Dalba, Debra A. Fischer, Gregory W. Henry, Stephen R. Kane, Molly Kosiarek, Geoffrey W. Marcy, Ryan A. Rubenzahl, Lauren M. Weiss, and Jason T. Wright. The California Legacy Survey. I. A Catalog of 178 Planets from Precision Radial Velocity Monitoring of 719 Nearby Stars over Three Decades. , 255(1):8, July 2021.

[210] Jean-Baptiste Ruffio, Katelyn Horstman, Dimitri Mawet, Lee J. Rosenthal, Kon-

stantin Batygin, Jason J. Wang, Maxwell Millar-Blanchaer, Ji Wang, Benjamin J. Fulton, Quinn M. Konopacky, Shubh Agrawal, Lea A. Hirsch, Andrew W. Howard, Sarah Blunt, Eric Nielsen, Ashley Baker, Randall Bartos, Charlotte Z. Bond, Benjamin Calvin, Sylvain Cetre, Jacques-Robert Delorme, Greg Doppmann, Daniel Echeverri, Luke Finnerty, Michael P. Fitzgerald, Nemanja Jovanovic, Ronald López, Emily C. Martin, Evan Morris, Jacklyn Pezzato, Garreth Ruane, Ben Sappey, Tobias Schofield, Andrew Skemer, Taylor Venenciano, J. Kent Wallace, Nicole L. Wallack, Peter Wizinowich, and Jerry W. Xuan. Detecting Exomoons from Radial Velocity Measurements of Self-luminous Planets: Application to Observations of HR 7672 B and Future Prospects. , 165(3):113, March 2023.

[211] C. Saffe, M. Gómez, and C. Chavero. On the ages of exoplanet host stars. , 443(2):609–626, November 2005.

[212] Steph Sallum, Shrishmoy Ray, Jens Kammerer, Anand Sivaramakrishnan, Rachel Cooper, Alexandra Z. Greebaum, Deepashri Thatte, Matthew De Furio, Samuel M. Factor, Michael R. Meyer, Jordan M. Stone, Aarynn Carter, Beth Biller, Sasha Hinkley, Andrew Skemer, Genaro Suárez, Jarron M. Leisenring, Marshall D. Perrin, Adam L. Kraus, Olivier Absil, William O. Balmer, Sarah K. Betti, Anthony Boccaletti, Mariangela Bonavita, Mickael Bonnefoy, Mark Booth, Brendan P. Bowler, Zackery W. Briesemeister, Marta L. Bryan, Per Calissendorff, Faustine Cantalloube, Gael Chauvin, Christine H. Chen, Elodie Choquet, Valentin Christiaens, Gabriele Cugno, Thayne Currie, Camilla Danielski, Trent J. Dupuy,

Jacqueline K. Faherty, Michael P. Fitzgerald, Jonathan J. Fortney, Kyle Franson, Julien H. Girard, Carol A. Grady, Eileen C. Gonzales, Thomas Henning, Dean C. Hines, Kielan K. W. Hoch, Callie E. Hood, Alex R. Howe, Markus Janson, Paul Kalas, Grant M. Kennedy, Matthew A. Kenworthy, Pierre Kervella, Daniel Kitzmann, Masayuki Kuzuhara, Anne-Marie Lagrange, Pierre-Olivier Lagage, Kellen Lawson, Cecilia Lazzoni, Ben W. P. Lew, Michael C. Liu, Pengyu Liu, Jorge Llop-Sayson, James P. Lloyd, Anna Lueber, Bruce Macintosh, Elena Manjavacas, Sebastian Marino, Mark S. Marley, Christian Marois, Raquel A. Martinez, Brenda C. Matthews, Elisabeth C. Matthews, Dimitri Mawet, Johan Mazoyer, Michael W. McElwain, Stanimir Metchev, Brittany E. Miles, Maxwell A. Millar-Blanchaer, Paul Molliere, Sarah E. Moran, Caroline V. Morley, Sagnick Mukherjee, Paulina Palma-Bifani, Eric Pantin, Polychronis Patapis, Simon Petrus, Laurent Pueyo, Sascha P. Quanz, Andreas Quirrenbach, Isabel Rebollido, Jea Adams Redai, Bin B. Ren, Emily Rickman, Matthias Samland, B. A. Sargent, Joshua E. Schlieder, Glenn Schneider, Karl R. Stapelfeldt, Ben J. Sutlieff, Motohide Tamura, Xianyu Tan, Christopher A. Theissen, Taichi Uyama, Arthur Vigan, Malavika Vasist, Johanna M. Vos, Kevin Wagner, Jason J. Wang, Kimberly Ward-Duong, Niall Whiteford, Schuyler G. Wolff, Kadin Worthen, Mark C. Wyatt, Marie Ygouf, Xi Zhang, Keming Zhang, Zhoujian Zhang, Yifan Zhou, and Alice Zurlo. The JWST Early Release Science Program for Direct Observations of Exoplanetary Systems. IV. NIRISS Aperture Masking Interferometry Performance and Lessons Learned. , 963(1):L2, March 2024.

[213] D. Saumon and M. S. Marley. The Evolution of L and T Dwarfs in Color-Magnitude Diagrams. *ApJ*, 689:1327–1344, December 2008.

[214] Joshua Schlieder, Charles A. Beichman, Jarron Michael Leisenring, Michael R. Meyer, and Marie Ygouf. Survey of Nearby Young M Stars. JWST Proposal. Cycle 1, ID. #1184, June 2017.

[215] Andreas Seifahrt, Jacob L. Bean, David Kasper, Julian Stürmer, Madison Brady, Robert Liu, Mathias Zechmeister, Gudmundur K. Stefánsson, Ben Montet, John White, Eduardo Tapia, Teo Mocnik, Siyi Xu, and Christian Schwab. MAROON-X: the first two years of EPRVs from Gemini North. In Christopher J. Evans, Julia J. Bryant, and Kentaro Motohara, editors, *Ground-based and Airborne Instrumentation for Astronomy IX*, volume 12184 of *Society of Photo-Optical Instrumentation Engineers (SPIE) Conference Series*, page 121841G, August 2022.

[216] E. Serabyn, E. Huby, K. Matthews, D. Mawet, O. Absil, B. Femenia, P. Wizinowich, M. Karlsson, M. Bottom, R. Campbell, B. Carlomagno, D. Defrère, C. Delacroix, P. Forsberg, C. Gomez Gonzalez, S. Habraken, A. Jolivet, K. Liewer, S. Lilley, P. Piron, M. Reggiani, J. Surdej, H. Tran, E. Vargas Catalán, and O. Wertz. The W. M. Keck Observatory Infrared Vortex Coronagraph and a First Image of HIP 79124 B. , 153(1):43, January 2017.

[217] E. Serabyn, E. Huby, K. Matthews, D. Mawet, O. Absil, B. Femenia, P. Wizinowich, M. Karlsson, M. Bottom, R. Campbell, B. Carlomagno, D. Defrère,

C. Delacroix, P. Forsberg, C. Gomez Gonzalez, S. Habraken, A. Jolivet, K. Liewer, S. Lilley, P. Piron, M. Reggiani, J. Surdej, H. Tran, E. Vargas Catalán, and O. Wertz. The W. M. Keck Observatory Infrared Vortex Coronagraph and a First Image of HIP 79124 B. , 153(1):43, January 2017.

[218] Evgenya Shkolnik, Michael C. Liu, and I. Neill Reid. Identifying the Young Low-mass Stars within 25 pc. I. Spectroscopic Observations. , 699(1):649–666, July 2009.

[219] Nour Skaf. *Self-optimization of adaptive optics and characterization of exoplanetary systems*. Theses, Université Paris sciences et lettres, March 2023.

[220] Andrew J. Skemer, Caroline V. Morley, Katelyn N. Allers, Thomas R. Geballe, Mark S. Marley, Jonathan J. Fortney, Jacqueline K. Faherty, Gordon L. Bjoraker, and Roxana Lupu. The First Spectrum of the Coldest Brown Dwarf. , 826(2):L17, August 2016.

[221] Andrew J. Skemer, R. Deno Stelter, Stephanie Sallum, Nicholas MacDonald, Renate Kupke, Christopher Ratliff, Ravinder Banyal, Amirul Hasan, Hari Mohan Varshney, Arun Surya, Ajin Prakaesh, Sivarani Thirupathi, Ramya Sethuram, Govinda K. V., Michael P. Fitzgerald, Eric Wang, Marc Kassis, Olivier Absil, Carlos Alvarez, Natasha Batalha, Marc-André Boucher, Cyril Bourgenot, Timothy Brandt, Zackery Briesemeister, Katherine de Kleer, Imke de Pater, William Deich, Devika Divakar, Guillaume Filion, Étienne Gauvin, Michael Gonzales, Thomas

Greene, Philip Hinz, Rebecca Jensen-Clem, Christopher Johnson, Isabel Kain, Gabriel Kruglikov, Mackenzie Lach, Jean-Thomas Landry, Jialin Li, Michael C. Liu, James Lyke, Kenneth Magnone, Eduardo Marin, Emily Martin, Raquel Martinez, Dimitri Mawet, Brittany Miles, Dale Sandford, Patrick Sheehan, Ji Man Sohn, and Jordan Stone. Design of SCALES: a 2-5 micron coronagraphic integral field spectrograph for Keck Observatory. In Christopher J. Evans, Julia J. Bryant, and Kentaro Motohara, editors, *Ground-based and Airborne Instrumentation for Astronomy IX*, volume 12184 of *Society of Photo-Optical Instrumentation Engineers (SPIE) Conference Series*, page 121840I, August 2022.

[222] A. Skumanich. Time Scales for Ca II Emission Decay, Rotational Braking, and Lithium Depletion. , 171:565, February 1972.

[223] Rémi Soummer, Laurent Pueyo, and James Larkin. Detection and Characterization of Exoplanets and Disks Using Projections on Karhunen-Loève Eigenimages. , 755(2):L28, August 2012.

[224] Julien F. P. Spronck, Debra A. Fischer, Zachary Kaplan, Colby A. Jurgenson, Jeff Valenti, John Moriarty, and Andrew E. Szymkowiak. Fiber Scrambling for High-Resolution Spectrographs. II. A Double Fiber Scrambler for Keck Observatory. *pasp*, 127(956):1027, October 2015.

[225] Julien F. P. Spronck, Debra A. Fischer, Zachary A. Kaplan, Christian Schwab, and Andrew Szymkowiak. Fiber Scrambling for High-Resolution Spectrographs.

I. Lick Observatory. *pasp*, 125(927):511, May 2013.

[226] Daniel J. Stevens and B. Scott Gaudi. A Posteriori Transit Probabilities. , 125(930):933, August 2013.

[227] T. Stolker, S. P. Quanz, K. O. Todorov, J. Kühn, P. Mollière, M. R. Meyer, T. Currie, S. Daemgen, and B. Lavie. MIRACLES: atmospheric characterization of directly imaged planets and substellar companions at 4-5 μm. I. Photometric analysis of β Pic b, HIP 65426 b, PZ Tel B, and HD 206893 B. , 635:A182, March 2020.

[228] S. Ströbele, M. Kasper, and P. Y. Madec. Overview on wavefront corrector technologies for astronomy and solar adaptive optics systems. In Laura Schreiber, Dirk Schmidt, and Elise Vernet, editors, *Adaptive Optics Systems VII*, volume 11448 of *Society of Photo-Optical Instrumentation Engineers (SPIE) Conference Series*, page 114481B, December 2020.

[229] Stefan Stroebele, Elise Vernet, Martin Brinkmann, Gerd Jakob, Paul Lilley, Mark Casali, Pierre-Yves Madec, and Markus Kasper. Deformable mirrors development program at ESO. In Enrico Marchetti, Laird M. Close, and Jean-Pierre Véran, editors, *Adaptive Optics Systems V*, volume 9909 of *Society of Photo-Optical Instrumentation Engineers (SPIE) Conference Series*, page 99090O, July 2016.

[230] D. Suzuki, D. P. Bennett, T. Sumi, I. A. Bond, L. A. Rogers, F. Abe, Y. Asakura,

A. Bhattacharya, M. Donachie, M. Freeman, A. Fukui, Y. Hirao, Y. Itow, N. Koshimoto, M. C. A. Li, C. H. Ling, K. Masuda, Y. Matsubara, Y. Muraki, M. Nagakane, K. Onishi, H. Oyokawa, N. Rattenbury, To. Saito, A. Sharan, H. Shibai, D. J. Sullivan, P. J. Tristram, A. Yonehara, and MOA Collaboration. The Exoplanet Mass-ratio Function from the MOA-II Survey: Discovery of a Break and Likely Peak at a Neptune Mass. , 833(2):145, December 2016.

[231] Taylor L. Tobin, Thayne Currie, Yiting Li, Jeffrey Chilcote, Timothy D. Brandt, Brianna Lacy, Masayuki Kuzuhara, Maria Vincent, Mona El Morsy, Vincent Deo, Jonathan P. Williams, Olivier Guyon, Julien Lozi, Sebastien Vievard, Nour Skaf, Kyohoon Ahn, Tyler Groff, N. Jeremy Kasdin, Taichi Uyama, Motohide Tamura, Aidan Gibbs, Briley L. Lewis, Rachel Bowens-Rubin, Maïssa Salama, Qier An, and Minghan Chen. Direct-imaging Discovery of a Substellar Companion Orbiting the Accelerating Variable Star HIP 39017. , 167(5):205, May 2024.

[232] T. Trifonov, J. A. Caballero, J. C. Morales, A. Seifahrt, I. Ribas, A. Reiners, J. L. Bean, R. Luque, H. Parviainen, E. Pallé, S. Stock, M. Zechmeister, P. J. Amado, G. Anglada-Escudé, M. Azzaro, T. Barclay, V. J. S. Béjar, P. Bluhm, N. Casasayas-Barris, C. Cifuentes, K. A. Collins, K. I. Collins, M. Cortés-Contreras, J. de Leon, S. Dreizler, C. D. Dressing, E. Esparza-Borges, N. Espinoza, M. Fausnaugh, A. Fukui, A. P. Hatzes, C. Hellier, Th. Henning, C. E. Henze, E. Herrero, S. V. Jeffers, J. M. Jenkins, E. L. N. Jensen, A. Kaminski, D. Kasper, D. Kossakowski, M. Kürster, M. Lafarga, D. W. Latham, A. W. Mann, K. Molaverdikhani,

D. Montes, B. T. Montet, F. Murgas, N. Narita, M. Oshagh, V. M. Passegger, D. Pollacco, S. N. Quinn, A. Quirrenbach, G. R. Ricker, C. Rodríguez López, J. Sanz-Forcada, R. P. Schwarz, A. Schweitzer, S. Seager, A. Shporer, M. Stangret, J. Stürmer, T. G. Tan, P. Tenenbaum, J. D. Twicken, R. Vanderspek, and J. N. Winn. A nearby transiting rocky exoplanet that is suitable for atmospheric investigation. *Science*, 371(6533):1038–1041, March 2021.

[233] Trifon Trifonov, Lev Tal-Or, Mathias Zechmeister, Adrian Kaminski, Shay Zucker, and Tsevi Mazeh. Public HARPS radial velocity database corrected for systematic errors. , 636:A74, April 2020.

[234] M. Tuomi, H. R. A. Jones, R. P. Butler, P. Arriagada, S. S. Vogt, J. Burt, G. Laughlin, B. Holden, S. A. Shectman, J. D. Crane, I. Thompson, S. Keiser, J. S. Jenkins, Z. Berdiñas, M. Diaz, M. Kiraga, and J. R. Barnes. Frequency of planets orbiting M dwarfs in the Solar neighbourhood. *arXiv e-prints*, page arXiv:1906.04644, June 2019.

[235] S. Udry, M. Mayor, D. Naef, F. Pepe, D. Queloz, N. C. Santos, M. Burnet, B. Confino, and C. Melo. The CORALIE survey for southern extra-solar planets. II. The short-period planetary companions to <ASTROBJ>HD 75289</ASTROBJ> and <ASTROBJ>HD 130322</ASTROBJ>. , 356:590–598, April 2000.

[236] Taichi Uyama, Jun Hashimoto, Masayuki Kuzuhara, Satoshi Mayama, Eiji Akiyama, Thayne Currie, John Livingston, Tomoyuki Kudo, Nobuhiko Kusak-

abe, Lyu Abe, Wolfgang Brandner, Timothy D. Brandt, Joseph C. Carson, Sebastian Egner, Markus Feldt, Miwa Goto, Carol A. Grady, Olivier Guyon, Yutaka Hayano, Masahiko Hayashi, Saeko S. Hayashi, Thomas Henning, Klaus W. Hodapp, Miki Ishii, Masanori Iye, Markus Janson, Ryo Kandori, Gillian R. Knapp, Jungmi Kwon, Taro Matsuo, Michael W. Mcelwain, Shoken Miyama, Jun-Ichi Morino, Amaya Moro-Martin, Tetsuo Nishimura, Tae-Soo Pyo, Eugene Serabyn, Takuya Suenaga, Hiroshi Suto, Ryuji Suzuki, Yasuhiro H. Takahashi, Michihiro Takami, Naruhisa Takato, Hiroshi Terada, Christian Thalmann, Edwin L. Turner, Makoto Watanabe, John Wisniewski, Toru Yamada, Hideki Takami, Tomonori Usuda, and Motohide Tamura. The SEEDS High-Contrast Imaging Survey of Exoplanets Around Young Stellar Objects. , 153(3):106, March 2017.

[237] A. Vigan, J. Patience, C. Marois, M. Bonavita, R. J. De Rosa, B. Macintosh, I. Song, R. Doyon, B. Zuckerman, D. Lafrenière, and T. Barman. The International Deep Planet Survey. I. The frequency of wide-orbit massive planets around A-stars. , 544:A9, August 2012.

[238] Steven S. Vogt, Matthew Radovan, Robert Kibrick, R. Paul Butler, Barry Alcott, Steve Allen, Pamela Arriagada, Mike Bolte, Jennifer Burt, Jerry Cabak, Kostas Chloros, David Cowley, William Deich, Brian Dupraw, Wayne Earthman, Harland Epps, Sandra Faber, Debra Fischer, Elinor Gates, David Hilyard, Brad Holden, Ken Johnston, Sandy Keiser, Dick Kanto, Myra Katsuki, Lee Laiterman, Kyle Lanclos, Greg Laughlin, Jeff Lewis, Chris Lockwood, Paul Lynam, Geoffrey

Marcy, Maureen McLean, Joe Miller, Tony Misch, Michael Peck, Terry Pfister, Andrew Phillips, Eugenio Rivera, Dale Sandford, Mike Saylor, Richard Stover, Matthew Thompson, Bernie Walp, James Ward, John Wareham, Mingzhi Wei, and Chris Wright. APF—The Lick Observatory Automated Planet Finder. *pasp*, 126(938):359, April 2014.

[239] K. Wagner, A. Boehle, P. Pathak, M. Kasper, R. Arsenault, G. Jakob, U. Käufl, S. Leveratto, A. L. Maire, E. Pantin, R. Siebenmorgen, G. Zins, O. Absil, N. Ageorges, D. Apai, A. Carlotti, É. Choquet, C. Delacroix, K. Dohlen, P. Duhoux, P. Forsberg, E. Fuenteseca, S. Gutruf, O. Guyon, E. Huby, D. Kampf, M. Karlsson, P. Kervella, J. P. Kirchbauer, P. Klupar, J. Kolb, D. Mawet, M. N'Diaye, G. Orban de Xivry, S. P. Quanz, A. Reutlinger, G. Ruane, M. Riquelme, C. Soenke, M. Sterzik, A. Vigan, and T. de Zeeuw. Imaging low-mass planets within the habitable zone of α Centauri. *Nature Communications*, 12:922, January 2021.

[240] Zahed Wahhaj, Michael C. Liu, Beth A. Biller, Eric L. Nielsen, Laird M. Close, Thomas L. Hayward, Markus Hartung, Mark Chun, Christ Ftaclas, and Douglas W. Toomey. The Gemini NICI Planet-Finding Campaign: The Companion Detection Pipeline. , 779(1):80, December 2013.

[241] Jason J. Wang, Jean-Baptise Ruffio, Robert J. De Rosa, Jonathan Aguilar, Schuyler G. Wolff, and Laurent Pueyo. pyKLIP: PSF Subtraction for Exoplanets

and Disks. Astrophysics Source Code Library, record ascl:1506.001, June 2015.

[242] B. J. Wargelin, V. L. Kashyap, J. J. Drake, D. García-Alvarez, and P. W. Ratzlaff. X-Ray Flaring on the dMe Star, Ross 154. , 676(1):610–627, March 2008.

[243] Marc L. Whiting, Joshua B. Hill, Benjamin C. Bromley, and Scott J. Kenyon. A Catalog of Nearby Accelerating Star Candidates in Gaia DR3. , 165(5):193, May 2023.

[244] Francois P. Wildi, Guido Brusa, Armando Riccardi, Michael Lloyd-Hart, Hubert M. Martin, and Laird M. Close. Towards 1^{st} light of the 6.5m MMT adaptive optics system with deformable secondary mirror. In Peter L. Wizinowich and Domenico Bonaccini, editors, *Adaptive Optical System Technologies II*, volume 4839 of *Society of Photo-Optical Instrumentation Engineers (SPIE) Conference Series*, pages 155–163, February 2003.

[245] P. Wizinowich, D. S. Acton, C. Shelton, P. Stomski, J. Gathright, K. Ho, W. Lupton, K. Tsubota, O. Lai, C. Max, J. Brase, J. An, K. Avicola, S. Olivier, D. Gavel, B. Macintosh, A. Ghez, and J. Larkin. First Light Adaptive Optics Images from the Keck II Telescope: A New Era of High Angular Resolution Imagery. , 112(769):315–319, March 2000.

[246] Gillian S. Wright, George H. Rieke, Alistair Glasse, Michael Ressler, Macarena García Marín, Jonathan Aguilar, Stacey Alberts, Javier Álvarez-Márquez, Ioannis

Argyriou, Kimberly Banks, Pierre Baudoz, Anthony Boccaletti, Patrice Bouchet, Jeroen Bouwman, Bernard R. Brandl, David Breda, Stacey Bright, Steven Cale, Luis Colina, Christophe Cossou, Alain Coulais, Misty Cracraft, Wim De Meester, Daniel Dicken, Michael Engesser, Mireya Etxaluze, Ori D. Fox, Scott Friedman, Henry Fu, Danny Gasman, András Gáspár, René Gastaud, Vincent Geers, Adrian Michael Glauser, Karl D. Gordon, Thomas Greene, Thomas R. Greve, Timothy Grundy, Manuel Güdel, Pierre Guillard, Peter Haderlein, Ryan Hashimoto, Thomas Henning, Dean Hines, Bryan Holler, Örs Hunor Detre, Amir Jahromi, Bryan James, Olivia C. Jones, Kay Justtanont, Patrick Kavanagh, Sarah Kendrew, Pamela Klaassen, Oliver Krause, Alvaro Labiano, Pierre-Olivier Lagage, Scott Lambros, Kirsten Larson, David Law, David Lee, Mattia Libralato, Jose Lorenzo Alverez, Margaret Meixner, Jane Morrison, Migo Mueller, Katherine Murray, Matthew Mycroft, Richard Myers, Omnarayani Nayak, Bret Naylor, Bryony Nickson, Alberto Noriega-Crespo, Göran Östlin, Brian O'Sullivan, Richard Ottens, Polychronis Patapis, Konstantin Penanen, Martin Pietraszkiewicz, Tom Ray, Michael Regan, Anthony Roteliuk, Pierre Royer, Piyal Samara-Ratna, Bridget Samuelson, Beth A. Sargent, Silvia Scheithauer, Analyn Schneider, Jürgen Schreiber, Bryan Shaughnessy, Evan Sheehan, Irene Shivaei, G. C. Sloan, Laszlo Tamas, Kelly Teague, Tea Temim, Tuomo Tikkanen, Samuel Tustain, Ewine F. van Dishoeck, Bart Vandenbussche, Mark Weilert, Paul Whitehouse, and Schuyler Wolff. The Mid-infrared Instrument for JWST and Its In-flight Performance. , 135(1046):048003, April 2023.

[247] Nicholas J. Wright, Jeremy J. Drake, Eric E. Mamajek, and Gregory W. Henry. The Stellar-activity-Rotation Relationship and the Evolution of Stellar Dynamos. , 743(1):48, December 2011.

[248] W. Jerry Xuan, Dimitri Mawet, Henry Ngo, Garreth Ruane, Vanessa P. Bailey, Élodie Choquet, Olivier Absil, Carlos Alvarez, Marta Bryan, Therese Cook, Bruno Femenía Castellá, Carlos Gomez Gonzalez, Elsa Huby, Heather A. Knutson, Keith Matthews, Sam Ragland, Eugene Serabyn, and Zoë Zawol. Characterizing the Performance of the NIRC2 Vortex Coronagraph at W. M. Keck Observatory. , 156(4):156, October 2018.

[249] Kodai Yamamoto, Taro Matsuo, Hiroshi Shibai, Yoichi Itoh, Mihoko Konishi, Jun Sudo, Ryoko Tanii, Misato Fukagawa, Takahiro Sumi, Tomoyuki Kudo, Jun Hashimoto, Nobuhiko Kusakabe, Lyu Abe, Wolfgang Brandner, Timothy D. Brandt, Joseph Carson, Thayne Currie, Sebastian E. Egner, Markus Feldt, Miwa Goto, Carol Grady, Olivier Guyon, Yutaka Hayano, Masahiko Hayashi, Saeko Hayashi, Thomas Henning, Klaus Hodapp, Miki Ishii, Masanori Iye, Markus Janson, Ryo Kandori, Gillian R. Knapp, Masayuki Kuzuhara, Jungmi Kwon, Mike McElwain, Shoken Miyama, Jun-Ichi Morino, Amaya Moro-Martin, June Nishikawa, Tetsuo Nishimura, Tae-Soo Pyo, Eugene Serabyn, Hiroshi Suto, Ryuji Suzuki, Michihiro Takami, Naruhisa Takato, Hiroshi Terada, Christian Thalmann, Daigo Tomono, Edwin L. Turner, John Wisniewski, Makoto Watanabe, Toru Yamada, Hideki Takami, and Tomonori Usuda. Direct Imaging Search for Extrasolar

Planets in the Pleiades. , 65:90, August 2013.

[250] Jincheng Yu and Chao Liu. The age-velocity dispersion relation of the Galactic discs from LAMOST-Gaia data. , 475(1):1093–1103, March 2018.

[251] Olga V. Zakhozhay, Ralf Launhardt, Andre Müller, Stefan S. Brems, Paul Eigenthaler, Mario Gennaro, Angela Hempel, Maren Hempel, Thomas Henning, Grant M. Kennedy, Sam Kim, Martin Kürster, Régis Lachaume, Yashodhan Manerikar, Jayshil A. Patel, Alexey Pavlov, Sabine Reffert, and Trifon Trifonov. Radial Velocity Survey for Planets around Young stars (RVSPY). Target characterisation and high-cadence survey. , 667:A63, November 2022.

[252] M. Zechmeister, A. Reiners, P. J. Amado, M. Azzaro, F. F. Bauer, V. J. S. Béjar, J. A. Caballero, E. W. Guenther, H. J. Hagen, S. V. Jeffers, A. Kaminski, M. Kürster, R. Launhardt, D. Montes, J. C. Morales, A. Quirrenbach, S. Reffert, I. Ribas, W. Seifert, L. Tal-Or, and V. Wolthoff. Spectrum radial velocity analyser (SERVAL). High-precision radial velocities and two alternative spectral indicators. , 609:A12, January 2018.

[253] Jingwen Zhang, Lauren M. Weiss, Daniel Huber, Eric L. N. Jensen, Timothy D. Brandt, Karen Collins, Dennis M. Conti, Howard Isaacson, Pablo Lewin, Giuseppe Marino, Bob Massey, Felipe Murgas, Enric Palle, Don J. Radford, Howard M. Relles, Gregor Srdoc, Chris Stockdale, Thiam-Guan Tan, and Gavin Wang. Dynamical Architectures of S-type Transiting Planets in Binaries. I. Target Selection

Using Hipparcos and Gaia Proper Motion Anomalies. , 167(3):89, March 2024.

[254] Zhoujian Zhang, Michael C. Liu, Zachary R. Claytor, William M. J. Best, Trent J. Dupuy, and Robert J. Siverd. The Second Discovery from the COCONUTS Program: A Cold Wide-orbit Exoplanet around a Young Field M Dwarf at 10.9 pc. , 916(2):L11, August 2021.